UNIVERSITY OF CALIFORNIA, SAN DIEGO

Observation of matter–antimatter asymmetry in the B^0 meson system

A dissertation submitted in partial satisfaction of the
requirements for the degree Doctor of Philosophy in
Physics

by

Shahram Rahatlou

Committee in charge:

Professor Vivek Sharma, Chairperson
Professor James Branson
Professor Aneesh Manohar
Professor Xuong Nguyen-Huu
Professor John Wheeler

2002

DEDICATION

In a country torn by war, where people were fighting for their lives, my parents taught me the importance of education and of human values. The monthly trips to the bookstores across the street from the University of Tehran introduced me to science.

This dissertation is dedicated to my mom and dad, for their relentless efforts through the years and continents. They have dedicated their life to provide the best of everything to my brother and me. I owe them my education and my love for what I do today.

TABLE OF CONTENTS

LIST OF FIGURES

LIST OF TABLES

Acknowledgments

I have shared the journey through the graduate school with many friends. Their company in the good times and their advice in times of trouble have been invaluable.

In the last four years my adviser Vivek has been an endless and constant source of guidance and advice. I am very thankful to Vivek and Poornima for their kindness from the moment I arrived to the day I finished.

I have had the fortune and the pleasure of working with Riccardo, Sören, and Gerhard. Their enthusiasm and passion are contagious, and working with them a lot of fun.

Working on $\sin 2\beta$ has been a great learning and professional experience, but above all a great team effort. This measurements relies on the work of many people in *BABAR*, from those responsible for data taking in IR-2 to those providing the analysis tools. But in particular I would like to thank Owen, Steve, and David. We shared the joy of many "unblindings", and the pain of getting there.

In the final hectic days, when my brain was pretty much dead, I could rely on the careful reading of Max, the miracalous ntuples and histograms of Patrick, and the colorful CKM plots from Sandrine.

The *BABAR* computing is, if nothing else, quite challenging. I am grateful to Adil, Yury, Stephen, and Peter for their infinite support at any time of the day and night.

I have had the opportunity to meet some very special people in my three years in the Bay Area: Amir and Haleh, my only Persian friends; Eric, my guide to the nightlife in San Francisco; Owen, who knows almost all good local rock bands in the area, and a big Giants

fan; David and Sylvie, my crazy Canadian friends; Sandrine, who reintroduced me to Tintin and Asterix after almost 2 decades.

Although far away in time, my memories from the beautiful years in Rome and Italy are kept alive thanks to Cristina, Francesca, Gloria, Fulvio, Luca, Daniele, and Cecilia. I am specially grateful to Nando for introducing me to *BABAR* in 1996 and his support when everything seemed to be going wrong in 1998.

The first year in San Diego was one of the hardest ones in my life. I left 24 years and 2 continents behind to jump into a new adventure. Discovering the new culture and reality was made easy by Defne, Omar, Nobu, Blake, Tom, Jonathan, Mike, Chris, Brian, and Phil. We shared the panic and the 99c fish tacos at Rubio's while preparing for the qualifier.

My brother Shahriar is my source of inspiration. His strength and courage in facing life and its obstacles encourage me to improve everyday and go forward.

I will never be able to thank my parents enough. Their support in these years has been priceless. We are far apart, but they are always with me with their wisdom.

VITA

1998	Laurea in Fisica, Universitá degli Studi di Roma ”La Sapienza”
1998–1999	Teaching Assistant, Department of Physics, University of California, San Diego
1999–2002	Research Assistant, University of California, San Diego
2002	Ph.D., University of California, San Diego

ABSTRACT OF THE DISSERTATION

Observation of matter–antimatter asymmetry in the B^0 meson system

by

Shahram Rahatlou

Doctor of Philosophy in Physics

University of California, San Diego, 2002

Professor Vivek A. Sharma, Chair

In this dissertation, a measurement of CP-violating effects in decays of neutral B meson is presented. The data sample for this measurement consists of about 88 million $\Upsilon(4S) \rightarrow B\bar{B}$ decays collected between 1999 and 2002 with the *BABAR* detector at the PEP-II asymmetric-energy e^+e^- collider, located at the Stanford Linear Accelerator Center. One neutral B meson is fully reconstructed in the CP eigenstates $J/\psi K^0_S$, $\psi(2S)K^0_S$, $\chi_{c1}K^0_S$, and $\eta_c K^0_S$, or in the flavor eigenstates $D^{(*)-}\pi^+/\rho^+/a_1^+$ and $J/\psi K^{*0}$ ($K^{*0} \rightarrow K^+\pi^-$). The other B meson is determined to be either a B^0 or a $\overline{B}^0$, at the time of its decay, from the properties of its decay products. The proper time Δt elapsed between the decay of the two mesons is determined by reconstructing their decay vertices, and by measuring the distance between them. The CP asymmetry amplitude $\sin 2\beta$ is determined by the distributions of Δt in events with a reconstructed B meson in CP eigenstates. The detector resolution and the b-flavor–tagging parameters are constrained by the Δt distributions of events with a fully reconstructed flavor eigenstate. From a simultaneous maximum-likelihood fit to the Δt distributions of all selected events in CP and flavor eigenstates, the value of $\sin 2\beta$ is measured to be $0.755 \pm 0.074\,(\mathrm{stat}) \pm 0.030\,(\mathrm{syst})$. This value is in agreement with the Standard Model prediction, and represents a successful test of the Kobayashi-Maskawa mechanism of CP violation.

Chapter 1

Introduction

Symmetries and conservation laws are an important aspect of physical theories. Search for symmetries and symmetry violations in nature has been one of the major goals of particle physics in the last fifty years.

Transformations that leave the laws of a theory unchanged are called symmetries of that theory. For example, equations of motion in classical mechanics are invariant under spatial translations and rotations as well as time translations. Laws of nature are valid in all regions of space and time. For each symmetry of a theory, there is a conserved quantity as implied by Nöther's theorem [1]. In classical mechanics, invariance under spatial translations and rotations result in conservation of three-momentum $\vec{p} = m\,\mathrm{d}\vec{x}/\mathrm{d}t$ and angular momentum $\vec{L} = \vec{x} \times \vec{p}$, where m is the mass and $\vec{x}$ are the coordinates of a particle. Similarly, conservation of energy E is a consequence of the invariance of physical laws under time translations. In particle physics three discrete symmetries, *time reversal* T, *parity* P, and *charge conjugation* C, are of particular interest [2]. The effect of these transformations on momentum $\vec{p}$ and spin $\vec{s}$ of particles is illustrated in Figure 1.1. T changes the sign of the time coordinate ($t \rightarrow -t$) while P inverts the space coordinates ($\vec{x} \rightarrow -\vec{x}$) of a particle. C transforms a particle in its antiparticle by changing its electrical charge and other *quantum numbers*, but leaves its space-time coordinates unchanged. Maxwell equations of electrodynamics are a good example of invariance of classical physics laws under these transformation.

Invariance of classical mechanics and electrodynamics suggested the invariance of all interactions under discrete transformations. This assumption was not supported, nor contradicted, by experimental evidence. In 1956, T. D. Lee and C. N. Yang [3] suggested the possibility of invariance under P being violated in weak interactions. They also discussed experimental methods to observe the effects of P violation. Soon after in 1957, violation of P was observed in the nuclear

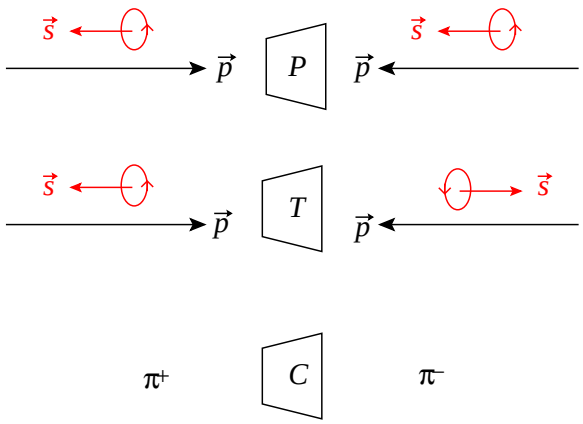

Figure 1.1: Transformation of momentum $\vec{p}$ and spin $\vec{s}$, under discrete transformations P, T, and C.

β-decays of ^{60}Co nuclei [4] by C. Wu *et al.*.

Measurement of neutrino helicity in 1958 by M. Goldhaber *et al.* provided evidence of C violation in weak interactions [5]. They observed that electron neutrinos ν_e are left-handed ($\vec{s}$ anti-parallel to $\vec{p}$), while antineutrinos are right-handed ($\vec{s}$ parallel to $\vec{p}$). This result was later confirmed with the measurement of the helicity of muon neutrinos ν_μ [6–8]. Transformation of neutrinos under P and C is shown schematically in Figure 1.2. Left-handed neutrinos ν_ℓ are transformed by C into left-handed antineutrinos $\overline{\nu}_\ell$ which do not exist in nature. Therefore, the C invariance is maximally violated.

Measurement of helicity also provided another evidence of P violation. Since neutrinos are left-handed, and antineutrinos right-handed, violation of C occurs simultaneously with violation of P. Hence, the combined transformation CP was believed to be a symmetry of the weak interactions. This assumption was certainly valid for neutrinos (see Figure 1.2), and was supported by measurements of other physical observables such as cross sections and decay rates mediated by weak interactions.

Violation of the CP symmetry was discovered in 1964 by J. Christenson, J. Cronin, V. Fitch, and R. Turlay in the decays of *strange* particles, known as kaons [9]. Existence of CP violation is particularly important, because it allows to distinguish unequivocally matter from antimatter.

Following the discovery of CP violation, M. Kobayashi and T. Maskawa proposed an elegant explanation of this phenomenon [10] within the framework of what is now known as the Standard Model of interactions in particle physics [11]. The Standard Model describes the hundreds of observed elementary particles in terms of three generations of quarks and leptons, as well as the weak, electromagnetic, and strong interactions between them. At the time of discovery, only two genera-

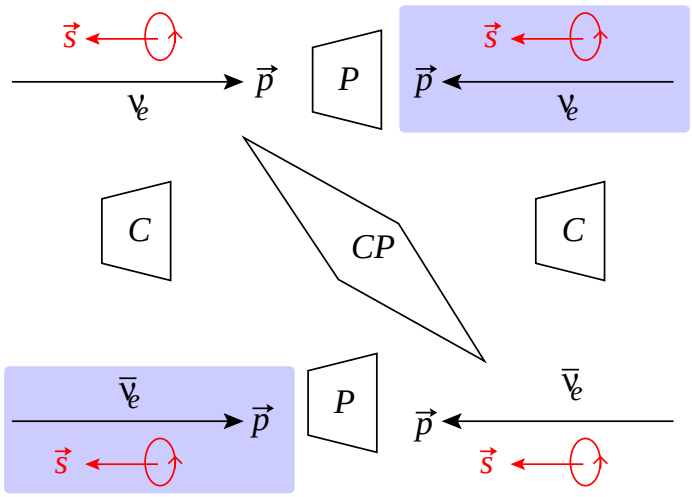

Figure 1.2: Discrete transformations C, P, and CP for neutrinos ν_ℓ and antineutrinos $\overline{\nu}_\ell$. Right-handed ν_ℓ and left-handed $\overline{\nu}_\ell$ (shaded areas) do not exist in nature and imply the maximal violation of C and P in weak interactions.

tions of quarks were known: up quark (u) and down quark (d) in the first generation, and strange quark (s) in the second. The theory of weak interactions with these two generations could not explain the presence of CP violation. The model proposed by Kobayashi and Maskawa pointed out, that existence of a third generation of quarks could accommodate, in an elegant and natural fashion, the presence of CP violation in weak interactions. The first member of the third generation, beauty quark (b), was discovered in 1977 [12, 13] while the discovery of the top quark (t) did not occur until 1995 [14, 15].

The strength of the weak interactions between quarks is regulated by the complex coupling constants that are parameterized as a function of three real parameters and one irreducible complex phase. The magnitude of CP violating effects in the Standard Model is proportional to this complex phase. Processes involving particles containing an s quark (kaons) or a b quark (B mesons) can exhibit CP violating effects. However, while the magnitude of CP violation in kaons is of the order $\mathcal{O}(10^{-3})$, the predicted asymmetry in the B meson system is expected to be of the order of unity.

Violation of CP is also of great interest for modern theories of cosmology [16, 17]. According to these theories, an equal amount of matter and antimatter was present in the early universe after the Big Bang. Today, our universe exhibits a very large asymmetry between matter and antimatter. There is basically no antimatter, and very little matter compared to photons:

$$N << \overline{N} << N_\gamma$$
$$N \sim 10^{-19}\, N_\gamma$$

with N, $\overline{N}$, and N_γ, respectively, the number of baryons, antibaryons, and photons in the universe [18].

In our galaxy, the heavy primary cosmic-ray nuclei are invariably nuclei rather than antinuclei. The existence of big masses of antimatter could be detected through intense emission of γ rays, following the annihilation of such masses with the galactic matter. No such phenomenon has been observed yet. The abundance of matter and the absence of antimatter is therefore one of the most puzzling questions in modern cosmology. In 1967, Sakharov emphasized that three elements are essential in any theory that attempts to explain the present cosmic matter-antimatter asymmetry [19]:

- processes that change the baryon number must occur;
- CP can not be conserved in these processes; and
- they must proceed outside thermal equilibrium.

Therefore CP violation is a key element in the understanding of our universe. Study of CP violation at the microscopic level of particle interactions could shed light on the abundance of matter over antimatter. The predicted CP violation in the Standard Model can not account for the absence of antimatter, and is a hint that sources of CP violation beyond the Standard Model are worth probing [20, 21].

In this dissertation, a measurement of the CP asymmetry amplitude $\sin 2\beta$ in the decays of B mesons is presented. As mentioned earlier, the expected magnitude of CP violation for kaons and B mesons differ by three orders of magnitude. Therefore, this measurement is an important test of the Standard Model, and represents the first observation of CP violation beyond the kaon system.

This dissertation is organized as the following:

- The theory of CP violation and the CP violating observables in the time evolution of B mesons are discussed in Chapter 2.
- The experimental ingredients required for a time-dependent measurement of CP violation with B mesons are discussed in Chapter 3. The key elements are 1) reconstruction of B meson in CP and flavor eigenstates, 2) determination of the quark composition of B mesons from their decay products, and 3) reconstruction of their decay vertices.
- The large data sample used in this analysis was produced at the PEP-II collider and recorded with the *BABAR* detector. The main characteristics of PEP-II and *BABAR* are described in Chapter 4.

- Event selection and exclusive reconstruction of B mesons in CP and flavor eigenstates are described in Chapter 5.
- The flavor (quark composition) of B mesons can be determined by identifying leptons and kaons in the final state. The flavor-tagging algorithm used in this analysis is described in Chapter 6.
- Reconstruction of B decay vertices and the measurement of decay-time intervals are described in Chapter 7.
- Value of $\sin 2\beta$ is measured with a likelihood fit to the decay-time distributions of B mesons. The fit procedure is described in Chapter 8.
- The results of this analysis and the evaluation of the systematic uncertainty are discussed in Chapter 9.
- The discussion of the impact of this measurement, in terms of the Standard Model parameters, and prospects for future measurements conclude this dissertation in Chapter 10.

Chapter 2

CP violation

In this chapter a brief outline of CP violation in the Standard Model of weak interactions is presented. The discussion is mainly focused on CP-violating effects in decays of the B mesons, relevant for the analysis presented in this dissertation. An excellent discussion of all aspects of CP violation can be found in References [22, 23].

Section 2.1 begins by discussing the way CP violation appears in the Lagrangian of a quantum field theory. Violation of CP symmetry occurs in field theories with complex coupling constants in the Lagrangian, which cannot be removed by an arbitrary phase redefinition of the fields. A complete discussion of this subject can be found in References [24–26].

The inclusion of CP violation in the Standard Model through the quark-mixing matrix, commonly known as the Cabibbo-Kobayashi-Maskawa (CKM) matrix, follows in Section 2.2. The unitarity of this matrix is expressed as constraints among its elements and displayed graphically as triangles in the complex plane, which are discussed in Section 2.3.

An excellent testing ground for the study of CP violation and measurement of the CKM-matrix elements is provided by neutral B mesons, described in Section 2.4. The phenomenon of flavor oscillation, that occurs in systems of neutral B mesons, is described in Section 2.4.1 and represents an important ingredient for the analysis of CP-violating effects.

As explained in Section 2.4.3, pairs of B^0 $\overline{B}^0$ mesons are produced in a coherent state, in decays of the $\Upsilon(4S)$ resonance. The time evolution of this coherent state is described in Section 2.4.4.

Three types of CP-violating effects are discussed in Section 2.4.5. One type is due to the quantum mechanical interference between the decay amplitude of B mesons to CP eigenstates, and the amplitude of B^0 $\overline{B}^0$ oscillation. This type of CP violation is discussed in Section 2.4.6 and is investigated in this thesis.

Finally, Section 2.5 concludes this Chapter with an overview of the B decay modes that can be utilized to measure the complex parameter of the CKM matrix. In Section 2.5.2, it is shown how the time-evolution of B mesons, decaying to the CP-eigenstate $B^0 \to J/\psi\, K^0_S$, offers a theoretically clean measurement of the CP asymmetry $\sin 2\beta$.

2.1 CP violation in field theories

Three discrete operations are potential symmetries of a field theory Lagrangian. Two of them, *parity* and *time reversal* are space-time transformations. Parity $\mathbf{P}$ changes the sign of the space coordinates, $(t, \mathbf{x}) \to (t, -\mathbf{x})$, while time reversal $\mathbf{T}$ inverts the sign of the time coordinate, $(t, \mathbf{x}) \to (-t, \mathbf{x})$. A third discrete transformation, called *charge conjugation* $\mathbf{C}$ is not related to spacetime coordinates. This transformation interchanges particles and antiparticles. The combined transformation $\mathbf{CP}$ replaces a particle with its antiparticles, and reverses its momentum and spin (see Figure 1.1 and 1.2).

So far there is no experimental evidence for violation of $\mathbf{P}$, $\mathbf{C}$, or $\mathbf{T}$ symmetries in electromagnetic and strong interactions. On the contrary, violation of all these symmetries have been observed in the weak interactions (Chapter 1).

A theory is invariant under $\mathbf{CP}$ if its Lagrangian $\mathcal{L}$ satisfies the condition

$$\mathbf{CP}\, \mathcal{L}(t, \vec{x})\, \mathbf{CP}^\dagger = \mathcal{L}(t, -\vec{x})\ . \tag{2.1}$$

In order to determine whether this requirement is met in a theory, one needs to know the transformation properties of the fields which $\mathcal{L}$ depends upon [27]. Table 2.1 summarizes these properties for the scalar, pseudoscalar, vector, and axial boson fields. Since $\mathcal{L}$ is a Lorentz scalar, it can only depend on bilinear functions of fermion field ψ. The properties of the bilinear terms are similar to those for bosons, and are listed in Table 2.1 as well. Now, consider a simple interaction Lagrangian

Fermion bilinear	Boson field F	$\mathbf{P}\, F\, \mathbf{P}^\dagger$	$\mathbf{C}\, F\, \mathbf{C}^\dagger$	$\mathbf{CP}\, F\, \mathbf{CP}^\dagger$
$\overline{\psi}\psi$	Scalar $S^+(t, \vec{x})$	$S^+(t, -\vec{x})$	$S^-(t, \vec{x})$	$S^-(t, -\vec{x})$
$\overline{\psi}\gamma^5\psi$	Pseudoscalar $P^+(t, \vec{x})$	$-P^+(t, -\vec{x})$	$P^-(t, \vec{x})$	$-P^-(t, -\vec{x})$
$\overline{\psi}\gamma_\mu\psi$	Vector $V^+_\mu(t, \vec{x})$	$V^+_\mu(t, -\vec{x})$	$-V^-_\mu(t, \vec{x})$	$-V^-_\mu(t, -\vec{x})$
$\overline{\psi}\gamma_\mu\gamma^5\psi$	Axial $A^+_\mu(t, \vec{x})$	$-A^+_\mu(t, -\vec{x})$	$A^-_\mu(t, \vec{x})$	$-A^-_\mu(t, -\vec{x})$

Table 2.1: Properties of charged boson fields and corresponding fermion bilinear terms under $\mathbf{P}$, $\mathbf{C}$, and $\mathbf{CP}$. γ^5 and γ^μ are the Dirac matrices.

$$\begin{aligned}\mathcal{L} &= a\, V_\mu^+(t,\vec{x})V^{\mu-}(t,\vec{x}) + b\, A_\mu^+(t,\vec{x})A^{\mu-}(t,\vec{x}) + \\ &\quad c\, V_\mu^+(t,\vec{x})A^{\mu-}(t,\vec{x}) + c^*\, A_\mu^+(t,\vec{x})V^{\mu-}(t,\vec{x})\end{aligned}$$

where the coupling constants a and b are real, while c is complex. Under $\mathbf{CP}$, $\mathcal{L}$ transforms as

$$\begin{aligned}\mathbf{CP}\mathcal{L}\mathbf{CP}^\dagger &= a\, V_\mu^-(t,-\vec{x})V^{\mu+}(t,-\vec{x}) + b\, A_\mu^-(t,-\vec{x})A^{\mu+}(t,-\vec{x}) + \\ &\quad c\, V_\mu^-(t,-\vec{x})A^{\mu+}(t,-\vec{x}) + c^*\, A_\mu^-(t,-\vec{x})V^{\mu+}(t,-\vec{x})\ .\end{aligned}$$

One observes that $\mathcal{L}$ is invariant under $\mathbf{CP}$ only if $c = c^*$, that is if all coupling constants are real. Therefore, theories with complex coupling constants accommodate can accommodate CP violation.

It must be said that CP can be conserved in a theory with complex coupling constants. The physical observables are invariant under global phase redefinitions of the fields, e.g.

$$V_\mu^+(t,\vec{x}) \to e^{i\phi}V_\mu^+(t,\vec{x})\ .$$

These transformations can be used to absorb the phase of the complex coupling constants. A theory is not invariant under the $\mathbf{CP}$ if after an arbitrary number of phase redefinitions of the fields, there is still a complex coupling constant. This is shown explicitly in the next Section for the Lagrangian of the Standard Model.

2.2 Kobayashi-Maskawa mechanism of CP violation

The Standard Model of particle physics [11] is a field theory, with local gauge symmetry $SU(3)_C \times SU(2)_L \times U(1)_Y$, and describes the strong, weak, and electromagnetic interactions between the known elementary particles. The electromagnetic and weak interactions are discussed in detail in References [25, 26], while a very good introduction to the strong interaction can be found in Reference [28]. So far, there is no experimental evidence for CP violation in strong and electromagnetic interactions. Hence, the discussion here will focus on the weak interactions within the Standard Model.

The fundamental ingredients of the Standard Model are six leptons and six quarks divided in three generations. Each of these particles has an antiparticle, with the same mass but opposite electrical charge and *quantum numbers*, e.g. strangeness and beauty. Each quark generation, commonly called a quark flavor, consists of three multiplets:

$$Q_L^I = \begin{pmatrix} U_L^I \\ D_L^I \end{pmatrix} = (3,2)_{+1/6}, \quad u_R^I = (3,1)_{+2/3}, \quad d_R^I = (3,1)_{-1/3}, \tag{2.2}$$

where $(3,2)_{+1/6}$ denotes a triplet of $SU(3)_C$, doublet of $SU(2)_L$ with hypercharge $Y = Q - T_3 = +1/6$, and similarly for the other representations.

The interactions of quarks with the $SU(2)_L$ gauge bosons are described by the Lagrangian

$$\mathcal{L}_W = -\frac{1}{2} g \overline{Q^I_{Li}} \gamma^\mu \tau^a \mathbf{1}_{ij} Q^I_{Lj} W^a_\mu + \text{Hermitian conjugate}\,, \tag{2.3}$$

where g is the weak coupling constant, γ^μ operates in Lorentz space, τ^a operates in $SU(2)_L$ space, and $\mathbf{1}$ is the unit matrix operating in generation (flavor) space. This unit matrix is written explicitly to make the transformation to mass eigenbasis clearer.

The Standard Model includes also a single Higgs scalar doublet field $\phi(1,2)_{+1/2}$. The interactions between the quarks and this field generate the fermion masses through the spontaneous symmetry breaking mechanism [29]. The Lagrangian for these interactions is given by

$$\mathcal{L}_Y = -\mathbf{G}_{ij} \overline{Q^I_{Li}} \phi d^I_{Rj} - \mathbf{F}_{ij} \overline{Q^I_{Li}} \tilde{\phi} u^I_{Rj} + \text{H.c.}, \tag{2.4}$$

where $\mathbf{G}$ and $\mathbf{F}$ are general *complex* 3×3 matrices. Their complex nature is the source of CP violation in the Standard Model. Due to the non-zero expectation value of the Higgs field in the vacuum, $\langle \phi \rangle = 1/\sqrt{2}(v, 0)$, the spontaneous symmetry breaking transforms $SU(2)_L \otimes U(1)_Y$ in $U(1)_{\text{EM}}$, and the two components of the quark doublet become distinguishable, as are the three members of the W^μ triplet. The charged current interaction in (2.3) is given by

$$\mathcal{L}_W = -\sqrt{\frac{1}{2}} g \overline{u^I_{Li}} \gamma^\mu \mathbf{1}_{ij} d^I_{Lj} W^+_\mu + \text{h.c.}. \tag{2.5}$$

The mass terms for the quarks arise from the replacement $\mathcal{R}e(\phi^0) \rightarrow \sqrt{\frac{1}{2}}(v + H^0)$ in (2.4) of the ϕ field near its minimum $\langle \phi \rangle$, and are given by

$$\mathcal{L}_M = -\sqrt{\frac{1}{2}} v \mathbf{G}_{ij} \overline{d^I_{Li}} d^I_{Rj} - \sqrt{\frac{1}{2}} v \mathbf{F}_{ij} \overline{u^I_{Li}} u^I_{Rj} + \text{H.c.}\,, \tag{2.6}$$

with

$$\mathbf{M}_d = \mathbf{G} v/\sqrt{2}, \quad \mathbf{M}_u = \mathbf{F} v/\sqrt{2}. \tag{2.7}$$

The quark fields in (2.2) are eigenstates of the weak interaction but do not correspond to the quark states in nature with definite mass. This is commonly referred to as the mass eigenstates being *rotated* with respect to the eigenstates of the weak interactions [30].

Since the two eigenbases are not identical, the mass matrices $\mathbf{M}_d$ and $\mathbf{M}_u$ do not correspond to the physical masses of the quarks. These matrices can be transformed to the mass eigenbasis by defining four unitary matrices such that

$$\mathbf{V}_{dL} \mathbf{M}_d \mathbf{V}^\dagger_{dR} = \mathbf{M}^{\text{diag}}_d, \quad \mathbf{V}_{uL} \mathbf{M}_u \mathbf{V}^\dagger_{uR} = \mathbf{M}^{\text{diag}}_u, \tag{2.8}$$

where $\mathbf{M}_q^{\rm diag}$ are diagonal and real, while $\mathbf{V}_{qL}$ and $\mathbf{V}_{qR}$ are complex. In the mass basis the charged current interactions (2.5) can be rewritten as

$$\mathcal{L}_W = -\sqrt{\frac{1}{2}} g \overline{u_{Li}} \gamma^\mu \overline{\mathbf{V}}_{ij} d_{Lj} W_\mu^+ + \text{h.c.}. \tag{2.9}$$

Here the quark fields are in the mass eigenbasis. The matrix $\overline{\mathbf{V}} = \mathbf{V}_{uL}\mathbf{V}_{dL}^\dagger$ is the unitary mixing matrix for three quark generations.

A unitary $n \times n$ complex matrix generally depends on $2n^2$ parameters. The condition of unitarity reduces this number to a total of n^2 independent parameter. Using the properties of orthogonal matrices, these parameters can be divided in

- $\frac{1}{2}n(n-1)$ real angles, and
- $n^2 - \frac{1}{2}n(n-1) = \frac{1}{2}n(n+1)$ complex phases

For n families of quarks, there are $2n$ quark fields. As stated earlier, physical observables are invariant under phase redefinitions of the fields. One can remove $2n-1$ of the complex phases by redefining the quark fields. Therefore, there are

- $\frac{1}{2}n(n+1) - (2n-1 = \frac{1}{2}(n-1)(n-2)$ irreducible complex phases

in the unitary $n \times n$ complex matrix.

In case of the mass matrices, there are three real angles and six total complex phases. The number of phases in $\bar{V}$ is reduced by a transformation

$$\overline{\mathbf{V}} \implies \mathbf{V} = \mathbf{P}_u \overline{\mathbf{V}} \mathbf{P}_d^*, \tag{2.10}$$

where $\mathbf{P}_u$ and $\mathbf{P}_d$ are diagonal matrices of pure complex phases. This is a legitimate transformation and, as described in Section 2.1, corresponds to redefining the phases of the quark fields in the mass eigenbasis:

$$q_{Li} \to (\mathbf{P}_q)_{ij} q_{Lj}, \quad q_{Ri} \to (\mathbf{P}_q)_{ij} q_{Rj}, \tag{2.11}$$

which does not change the real diagonal mass matrix $\mathbf{M}_q^{\rm diag}$. The five phase differences among the elements of $\mathbf{P}_u$ and $\mathbf{P}_d$ can be chosen so that the transformation (2.10) eliminates five of the six independent phases from $\overline{\mathbf{V}}$. The new matrix $\mathbf{V}$ is left with three real angles and one irreducible complex phase. This phase is called the Kobayashi-Maskawa phase [10], $\delta_{\rm KM}$, and the mixing matrix is called the Cabibbo-Kobayashi-Maskawa (CKM) matrix [10, 32].

It is important to note that the existence of the third generation of quarks is a necessary ingredient for the presence of the complex phase, and therefore CP violation in the Standard Model. In

a Standard Model with only two generations of quarks, the procedure described above removes all the complex phases and the 2×2 mixing matrix $\mathbf{V}$ is left with only one real parameter which is the Cabibbo angle. It was this observation that led Kobayashi and Maskawa to suggest a third quark generation in 1973 long before the discovery of the beauty quark b in 1977 [12, 13] and of the top quark t in 1995 [14, 15].

The presence of only one complex phase in the CKM model implies that all CP-violating effects are closely related. Therefore different physical processes, such as decays of Kaons and B mesons, can be used to probe the same source of CP violation.

The CKM matrix $\mathbf{V}$ can be symbolically written as

$$\mathbf{V} \equiv \begin{pmatrix} V_{ud} & V_{us} & V_{ub} \\ V_{cd} & V_{cs} & V_{cb} \\ V_{td} & V_{ts} & V_{tb} \end{pmatrix} , \tag{2.12}$$

which explicitly shows the flavor-changing aspect of the weak interactions. Each element $\mathbf{V}_{q_i q_j}$ determines the amplitude of interactions between quarks q_i and q_j. The magnitude of all nine elements of this matrix have now been measured in the weak decays of hadrons containing the relevant quarks, and in some cases in the deep inelastic neutrino–nucleon scattering [33]. The precision on these elements reflects both the experimental limitations and the theoretical uncertainties associated with the imprecise knowledge of the hadronic quantities required to analyze the experimental data [30]. Present knowledge of the magnitude $|V_{ij}|$ of the matrix elements can be summarized as [33]

$$|\mathbf{V}| \equiv \begin{pmatrix} 0.9741 - 0.9756 & 0.219 - 0.226 & 0.0025 - 0.0048 \\ 0.219 - 0.226 & 0.9732 - 0.9748 & 0.038 - 0.044 \\ 0.004 - 0.014 & 0.037 - 0.044 & 0.9990 - 0.9993 \end{pmatrix} . \tag{2.13}$$

where the values are the 90% confidence limits on $|V_{ij}|$.

2.3 Unitarity of the CKM matrix

There are several parameterizations of the CKM matrix $\mathbf{V}$ that exhibit its unitarity explicitly. A clear and complete discussion of the parameterizations of the CKM matrix can be found in Reference [34].

One of these is considered commonly the “standard” parameterization [35] and utilizes three

angles θ_{12}, θ_{23}, θ_{13}, and a complex phase $\delta \equiv \delta_{\rm KM}$

$$\mathbf{V} = \begin{pmatrix} c_{12}c_{13} & s_{12}c_{13} & s_{13}e^{-i\delta} \\ -s_{12}c_{23} - c_{12}s_{23}s_{13}e^{i\delta} & c_{12}c_{23} - s_{12}s_{23}s_{13}e^{i\delta} & s_{23}c_{13} \\ s_{12}s_{23} - c_{12}c_{23}s_{13}e^{i\delta} & -c_{12}s_{23} - s_{12}c_{23}s_{13}e^{i\delta} & c_{23}c_{13} \end{pmatrix}, \tag{2.14}$$

with $c_{ij} \equiv \cos\theta_{ij}$ and $s_{ij} \equiv \sin\theta_{ij}$, and indices $i, j = 1, 2, 3$ corresponding to the three quark generations. In this parameterization, the angles θ_{ij} are related to the amount of "mixing" between two generations i and j. For example θ_{12} corresponds to the Cabibbo angle [32]. It can be shown that eight conditions on the angles and the complex phase

$$\theta_{ij} \neq 0, \frac{\pi}{2}\,, \quad \delta \neq 0, \pi\,, \quad j = 1, 2, 3\,, \tag{2.15}$$

are necessary for having CP violation, in the Standard Model, with three quark generations [34].

The unitarity of $\mathbf{V}$ implies nine constraint between its elements. Three of these constraints are relative to the elements of each row

$$\begin{aligned} |V_{ud}|^2 &+ |V_{us}|^2 + |V_{ub}|^2 = 1\,, \\ |V_{cd}|^2 &+ |V_{cs}|^2 + |V_{cb}|^2 = 1\,, \\ |V_{td}|^2 &+ |V_{ts}|^2 + |V_{tb}|^2 = 1\,, \end{aligned} \tag{2.16}$$

while the other six express the condition of orthogonality between any pair of rows or any pair of columns of the matrix. A review of all these constraints is given in Reference [36]. The six orthogonality conditions require the sum of three complex terms to vanish and can be represented graphically as triangles in the complex plane [35, 37, 38]. All these triangles have the same area $|J|/2$, with $J = c_{12}c_{23}c_{13}^2 s_{12}s_{23}s_{13}\sin\delta$. One observes that all eight conditions in (2.15) are unified in the single requirement that $J \neq 0$.

Three of these triangles, defined by

$$V_{ud}V_{us}^* + V_{cd}V_{cs}^* + V_{td}V_{ts}^* = 0, \tag{2.17}$$

$$V_{us}V_{ub}^* + V_{cs}V_{cb}^* + V_{ts}V_{tb}^* = 0, \tag{2.18}$$

$$V_{ud}V_{ub}^* + V_{cd}V_{cb}^* + V_{td}V_{tb}^* = 0\,, \tag{2.19}$$

are very useful in understanding the Standard Model predictions for CP violation, and are shown in Figure 2.1.

The length of the sides of these triangles can be measured from the decay rates of, respectively, $K \equiv (\bar{s}d)$, $B_s \equiv (\bar{b}s)$, and $B_d \equiv (\bar{b}d)$ mesons.

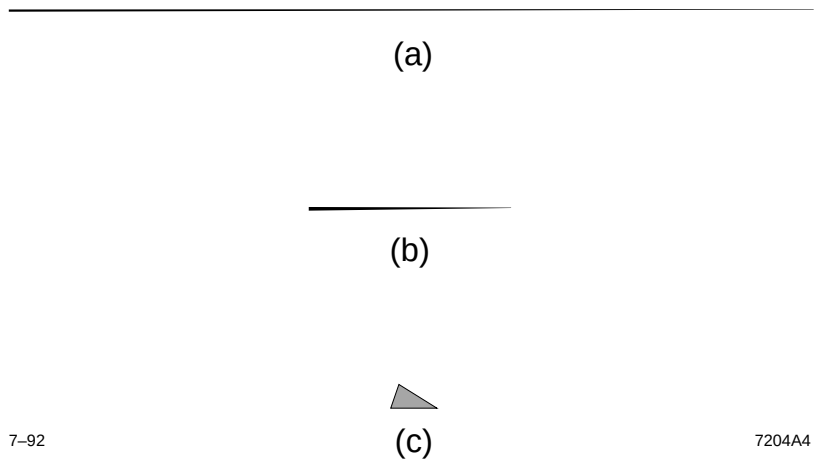

Figure 2.1: The unitarity triangles defined by (2.17) in a), (2.18) in b), and (2.19) in c). The same scale has been used for all triangles.

The size of the angles are proportional to the magnitude of CP-violating effects in the decays of, respectively, K, B_s, and B_d mesons. In case of the K and B_s mesons, the experimental precision needs to be high in order to be able to resolve the structure of the flat triangles.

On the contrary, the third triangle, related to the B_d mesons, is expected to have large angles, which result in large CP-violating effects, discussed later in Section 2.5.2. The remainder of the discussion is devoted to CP violation in B_d mesons, which, unless specified, are simply referred to as B mesons. Similarly, Equation (2.19), illustrated in Figure 2.1c, is referred to as the "Unitarity Triangle".

It is customary to study the Unitarity Triangle with the Wolfenstein parametrization [39] of the CKM matrix. In this parameterization, matrix $\mathbf{V}$ is written as [35]

$$\mathbf{V} = \begin{pmatrix} 1-\frac{\lambda^2}{2} & \lambda & A\lambda^3(\rho-i\eta) \\ -\lambda & 1-\frac{\lambda^2}{2} & A\lambda^2 \\ A\lambda^3(1-\rho-i\eta) & -A\lambda^2 & 1 \end{pmatrix} + \mathcal{O}(\lambda^4)\ , \tag{2.20}$$

with $\lambda = |V_{us}| = 0.22$ playing the role of the expansion parameter, and A, ρ, and η real numbers of the order of unity. The parameters of the standard parameterization (2.14) are related to the Wolfenstein parameters in (2.20) by

$$s_{12} \equiv \lambda, \quad s_{23} \equiv A\lambda^2, \quad s_{13}e^{-i\delta} \equiv A\lambda^3(\rho - i\eta)\ . \tag{2.21}$$

The CKM elements can be written in terms of the Wolfenstein parameters A, ρ, and η, by using relation (2.21), as

$$V_{us} = \lambda, \quad V_{cb} = A\lambda^2, \quad V_{ub} = A\lambda^3(\rho - i\eta), \tag{2.22}$$

$$V_{td} = A\lambda^3(1 - \bar{\rho} - i\bar{\eta}), \tag{2.23}$$

$$\mathcal{I}mV_{cd} = -A^2\lambda^5\eta, \quad \mathcal{I}mV_{ts} = -A\lambda^4\eta, \tag{2.24}$$

with

$$\bar{\rho} = \rho(1 - \lambda^2/2), \quad \bar{\eta} = \eta(1 - \lambda^2/2)\ . \tag{2.25}$$

These expressions are valid up to $\mathcal{O}(\lambda^6)$ corrections and turn out to be excellent approximations to their exact expressions [40].

The rescaled Unitarity Triangle in Figure 2.2b is derived from (2.19) by dividing the lengths of all sides by $V_{cd}V_{cb}^*$, which, in the Wolfenstein parameterization, is a real number. Two vertices of the rescaled Unitarity Triangle are thus fixed at (0,0) and (1,0), while the coordinates of the remaining vertex are denoted by $(\bar{\rho}, \bar{\eta})$. In the $(\bar{\rho}, \bar{\eta})$ plane, the lengths of the sides of the triangle are given by

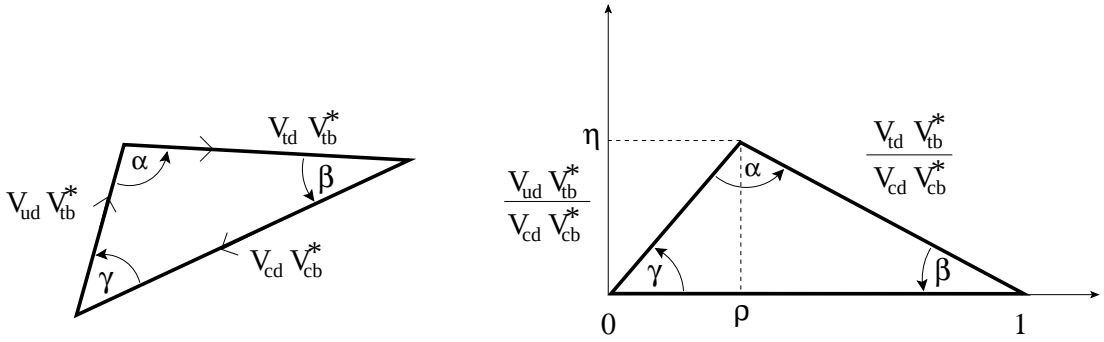

Figure 2.2: (a) The Unitarity triangle as defined in relation (2.19), and (b) the rescaled triangle, where all sides are divided by $V_{cb}^*V_{cd}$.

$$R_b \equiv \sqrt{\bar{\rho}^2 + \bar{\eta}^2} = \frac{1 - \lambda^2/2}{\lambda}\left|\frac{V_{ub}}{V_{cb}}\right|, \quad R_t \equiv \sqrt{(1 - \bar{\rho})^2 + \bar{\eta}^2} = \frac{1}{\lambda}\left|\frac{V_{td}}{V_{cb}}\right|\ , \tag{2.26}$$

and can be measured experimentally. Similarly, the three angles α, β, and γ are defined by

$$\alpha \equiv \arg\left[-\frac{V_{td}V_{tb}^*}{V_{ud}V_{ub}^*}\right], \quad \beta \equiv \arg\left[-\frac{V_{cd}V_{cb}^*}{V_{td}V_{tb}^*}\right], \quad \gamma \equiv \arg\left[-\frac{V_{ud}V_{ub}^*}{V_{cd}V_{cb}^*}\right] \equiv \pi - \alpha - \beta\ . \tag{2.27}$$

Knowledge of the sides of the triangles allows to measure the angles. On the other hand, these angles can be measured directly through observation of CP violation in several decays of the B mesons. The consistency of the independent measurements provides an important test of the Standard Model.

Figure 2.3 shows the current indirect constraints on the position of the apex of the Unitarity Triangle, from the measurements of CP violation in kaons (ϵ_K), oscillation frequencies in B^0 and

B_s mesons (Δm_d and Δm_s), and the ratio $|V_{ub}/V_{cb}|$. The measurement of $\sin 2\beta$ provides a direct constraint on the position of the apex and is discussed in Section 10.2.

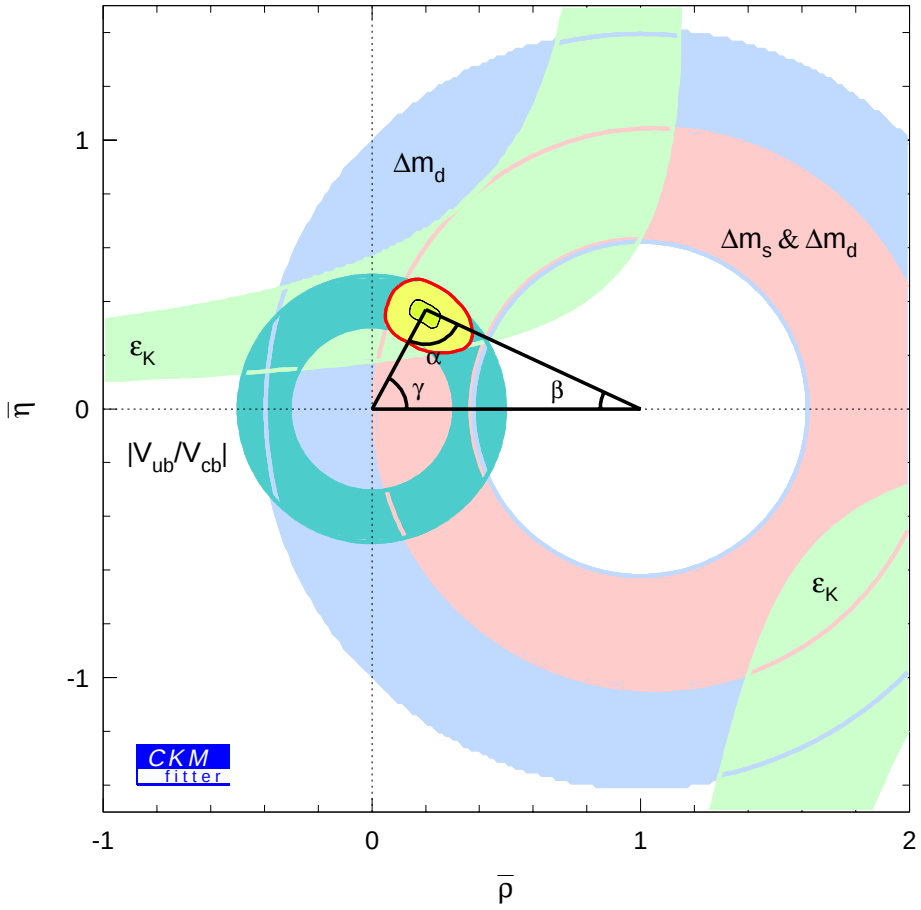

Figure 2.3: Existing constraints on the position of the apex of the Unitarity Triangle.

2.4 CP violation in B decays

The interest in the physics of the B mesons lies in that several of their decays can be used to test the paradigm of CP violation in the Standard Model. In particular some decays modes of neutral B mesons provide theoretically clean information about the angles of the Unitarity Triangle.

The $\overline{B}^0$ mesons [1] are made out of a b quark and an antiquark $\bar{d}$ and were first discovered in the decays of the bound state $\Upsilon(4S) \equiv (b\bar{b})$ in 1977 [12, 13]. The $\overline{B}^0$ meson has also an isospin partner

[1] Charge conjugation is implied through out this discussion unless explicitly specified.

B^- which contains a b quark and a $\bar{u}$ antiquark. The masses and the lifetimes of the B mesons are summarized in Table 2.2.

Meson	Mass (MeV/c^2)	Lifetime (ps)
$B_d^0 \equiv \bar{b}d$	5279.4 ± 0.5	1.542 ± 0.016
$B^+ \equiv \bar{b}u$	5279.0 ± 0.5	1.674 ± 0.018
$B_s^0 \equiv \bar{b}s$	5369.6 ± 2.4	1.461 ± 0.057

Table 2.2: Properties of B mesons.

Two aspects of the B^0 mesons are important for the study of CP violation

1. Presence of final CP eigenstates accessible to both B^0 and $\overline{B}^0$.

2. Phenomenon of B^0 $\overline{B}^0$ oscillation that allows a $|B^0\rangle$ state at time t_1 to become $|\overline{B}^0\rangle$ at a later time $t_2 > t_1$.

2.4.1 Phenomenology of B^0-$\overline{B}^0$ oscillations

B^0 $\overline{B}^0$ oscillations were first observed in 1987 by the ARGUS [42] and UA1 [41] collaborations. The B^0 and $\overline{B}^0$ mesons have a definite quark composition and are therefore commonly called flavor eigenstates. They, however, are not eigenstates of the weak interactions. Figure 2.4 shows the diagram of the second-order weak interaction that allows a $\overline{B}^0$ meson to change its flavor, and become a B^0 meson. This process is commonly called the B^0 $\overline{B}^0$ oscillation. The probability of oscillation depends on the decay-time of the B meson and is discussed in Section 2.4.4.

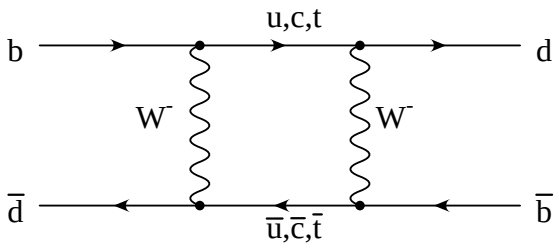

Figure 2.4: Feynman diagram of the second-order weak interaction responsible for the flavor oscillation $\overline{B}^0 \to B^0$.

The phenomenology of the B^0-$\overline{B}^0$ oscillation [43] is discussed in the framework of a two-state quantum-mechanical system. In such a system, an arbitrary pair of linearly-independent states is used to form a basis. For the self-conjugate system formed by a B^0 and a $\overline{B}^0$, there are three bases of interest:

- Flavor eigenstates $|B^0\rangle$ and $|\overline{B}^0\rangle$: physical states with definite quark structure and are produced as a consequence of the quark-level strong interactions.
- CP eigenstates $|B_{CP=1}\rangle$ and $|B_{CP=-1}\rangle$: eigenstates of the the CP operation

$$\begin{aligned} CP|B_{CP=1}\rangle &= +|B_{CP=1}\rangle \\ CP|B_{CP=-1}\rangle &= -|B_{CP=-1}\rangle \end{aligned}$$

- Mass eigenstates $|B_L\rangle$ and $|B_H\rangle$: eigenstates of the full Hamiltonian and, hence, with definite mass M and decay width $\Gamma \equiv 1/\tau$. These states evolve in time in a definite fashion according to

$$|B_L, t\rangle = \mathrm{e}^{-\Gamma_L t}\mathrm{e}^{-iM_L t}|B_L, t=0\rangle \tag{2.28}$$

$$|B_H, t\rangle = \mathrm{e}^{-\Gamma_H t}\mathrm{e}^{-iM_H t}|B_H, t=0\rangle\ . \tag{2.29}$$

The B^0-$\overline{B}^0$ oscillation represents an example of the superposition principle in this two-state system. The oscillation occurs because the flavor and mass eigenstates are not identical, as discussed below. Since CP is not a good symmetry of the Hamiltonian, that is $[CP, H] \neq 0$, the CP eigenstates could be different from the mass eigenstates and, therefore, from the flavor eigenstates.

In order to see the relation between the mass and flavor eigenstates, consider an arbitrary linear combination of the flavor eigenstates,

$$|\psi\rangle \equiv a|B^0\rangle + b|\overline{B}^0\rangle, \tag{2.30}$$

which is governed by a time-dependent Schrödinger equation

$$i\frac{d}{dt}\begin{pmatrix} a \\ b \end{pmatrix} = \mathbf{H}\begin{pmatrix} a \\ b \end{pmatrix} \equiv (\mathbf{M} - \frac{i}{2}\mathbf{\Gamma})\begin{pmatrix} a \\ b \end{pmatrix} \tag{2.31}$$

where $\mathbf{H}$ is the Hamiltonian, and $\mathbf{M}$ and $\mathbf{\Gamma}$ are 2×2 complex matrices. Conservation of probability requires $\mathbf{H}$ to be a unitary matrix. This implies that $\mathbf{M}$ and $\mathbf{\Gamma}$ be Hermitian, that is $\mathbf{M} = \mathbf{M}^\dagger$ and $\mathbf{\Gamma} = \mathbf{\Gamma}^\dagger$. Under the assumption of CPT invariance, CPT invariance, assumed throughout this discussion, guarantees that $H_{11} = H_{22}$.

The expression of matrices $\mathbf{M}$ and $\mathbf{\Gamma}$, in second-order perturbation theory, is given by

$$\begin{aligned} M_{ij} &= m_B\delta_{ij} + \langle i|H_W^{\Delta B=2}|j\rangle + P\sum_n \frac{1}{m_B - E_n}\langle i|H_W^{\Delta B=1}|n\rangle\langle n|H_W^{\Delta B=1}|j\rangle \\ \Gamma_{ij} &= 2\pi\sum_n \delta(E_n - m_B)\langle i|H_W^{\Delta B=1}|n\rangle\langle n|H_W^{\Delta B=1}|j\rangle \ . \end{aligned}$$

The virtual (off-shell) intermediate states contribute to $\mathbf{M}$, while those contributing to $\mathbf{\Gamma}$ are physical states (on-shell) to which both B^0 and $\overline{B}^0$ can decay. The off-diagonal terms M_{ij} and Γ_{ij} are called, respectively, the dispersive and the absorptive transition amplitude between B^0 and $\overline{B}^0$ states, and play an important role in CP-violating effects.

Since $\mathbf{H}$ is not Hermitian solving the eigenvalue equation $\mathbf{H}|\psi\rangle = \lambda|\psi\rangle$ yields two complex solutions

$$\lambda_\pm = M - \frac{i}{2}\Gamma - \sqrt{(M_{12} - \frac{i}{2}\Gamma_{12})(M_{12}^* - \frac{i}{2}\Gamma_{12})} \tag{2.32}$$

with $\Gamma \equiv \Gamma_{11} \equiv \Gamma_{22}$ and $M \equiv M_{11} \equiv M_{22}$. It is customary to define the mass difference Δm_d and decay width difference $\Delta\Gamma$ ($\Gamma \equiv 1/\tau$) as

$$\Delta m_d \equiv m_H - m_L \equiv \mathcal{R}e(\lambda_+ - \lambda_-) \tag{2.33}$$

$$\Delta\Gamma \equiv \Gamma_H - \Gamma_L \equiv 2\mathcal{I}m(\lambda_+ - \lambda_-) \tag{2.34}$$

to deduce the following relations from (2.32)

$$(\Delta m_d)^2 - \frac{1}{4}(\Delta\Gamma)^2 = 4(|M_{12}|^2 - \frac{1}{4}|\Gamma_{12}|^2), \tag{2.35}$$

$$\Delta m_d \Delta\Gamma = 4\mathcal{R}e(M_{12}\Gamma_{12}^*). \tag{2.36}$$

The mass eigenstates can then be expressed as

$$|B_L\rangle \ = \ p|B^0\rangle + q|\bar{B}^0\rangle, \tag{2.37}$$

$$|B_H\rangle \ = \ p|B^0\rangle - q|\bar{B}^0\rangle \ , \tag{2.38}$$

with the complex coefficients q and p defined as

$$p = \sqrt{(M_{12} - \frac{i}{2}\Gamma_{12})(M_{12}^* - \frac{i}{2}\Gamma_{12})} \tag{2.39}$$

$$q = (M_{12}^* - \frac{i}{2}\Gamma_{12}) \ , \tag{2.40}$$

obeying the normalization condition

$$|q|^2 + |p|^2 = 1. \tag{2.41}$$

Although both q and p are complex, the phase of eigenstates $|B_L\rangle$ and $|B_H\rangle$ can be redefined in order to make one between q and p real. Only the phase difference between them is physically meaningful. This can be stated explicitly by defining the ratio

$$\frac{q}{p} = \frac{\sqrt{M_{12}^* - \frac{i}{2}\Gamma_{12}^*}}{\sqrt{M_{12} - \frac{i}{2}\Gamma_{12}}} = -\frac{\Delta m_d - \frac{i}{2}\Delta\Gamma}{2(M_{12} - \frac{i}{2}\Gamma_{12})} = -\frac{2(M_{12}^* - \frac{i}{2}\Gamma_{12}^*)}{\Delta m_d - \frac{i}{2}\Delta\Gamma} \,. \tag{2.42}$$

Its magnitude $|q/p|$, and the complex phase $\arg(q/p)$ have physical significance, as discussed later in Section 2.4.5.

Relations (2.35), (2.36), and (2.42) can be further simplified by the following considerations. The difference $\Delta\Gamma$ is produced by decay channels common to B^0 and $\overline{B}^0$, e.g. $B^0, \overline{B}^0 \to D\bar{D}$. Typically, these decay modes are at least CKM suppressed, and their branching fractions are of the order $\mathcal{O}(10^{-3})$ or below. Although not measured yet, $\Delta\Gamma$ is expected to be negligible [44]

$$\Delta\Gamma/\Gamma \lesssim \mathcal{O}(10^{-2}). \tag{2.43}$$

Hence, $\Delta\Gamma_{B_d} \ll \Gamma_{B_d}$ is a rather safe and model independent assumption [45].

The value of Δm_d, on the other hand, is known with high precision [33]. It's common to give the result in terms of

$$x_d \equiv \Delta m_d/\Gamma = 0.73 \pm 0.05. \tag{2.44}$$

From (2.43) and (2.44) one concludes that

$$\Delta\Gamma \ll \Delta m_d \,, \tag{2.45}$$

that is, the two eigenstates of the Hamiltonian have very similar lifetimes but different masses. By using relations (2.43) and (2.45), one can simplify relations (2.35),(2.36), and (2.42) as

$$\Delta m_d = 2|M_{12}|, \quad \Delta\Gamma 2\mathcal{R}e(M_{12}\Gamma_{12}^*)/|M_{12}|, \tag{2.46}$$

$$q/p = -|M_{12}|/M_{12}. \tag{2.47}$$

The time evolution of the generic state $|\Psi\rangle$ in (2.30) can now be derived from relations (2.37) and (2.38), by expressing B^0 and $\overline{B}^0$ states as

$$|B^0\rangle = \frac{1}{2p}(|B_L\rangle + |B_H\rangle) \tag{2.48}$$

$$|\overline{B}^0\rangle = \frac{1}{2q}(|B_L\rangle - |B_H\rangle) \tag{2.49}$$

with the time evolution of mass eigenstates given by (2.28) and (2.29). In particular, one is interested in states that at $t = 0$ are a pure B^0 or $\overline{B}^0$ state, denoted by $|B^0_{\rm phys}\rangle$ and $|\overline{B}^0_{\rm phys}\rangle$, respectively. The time evolution of these states is given by

$$|B^0_{\rm phys}(t)\rangle = g_+(t)|B^0\rangle + (q/p)g_-(t)|\overline{B}^0\rangle, \tag{2.50}$$

$$|\bar{B}^0_{\rm phys}(t)\rangle = (p/q)g_-(t)|B^0\rangle + g_+(t)|\overline{B}^0\rangle, \tag{2.51}$$

where

$$g_+(t) = e^{-iMt}e^{-\Gamma t/2}\cos(\Delta m_d\, t/2), \tag{2.52}$$

$$g_-(t) = e^{-iMt}e^{-\Gamma t/2} i \sin(\Delta m_d\, t/2), \tag{2.53}$$

with $\Gamma = 1/\tau_{B^0}$, $M = \frac{1}{2}(M_H + M_L)$, and $\Delta m_d = M_H - M_L$. Relations (2.50) and (2.51) show explicitly that the probability of a B^0 to become a $\overline{B}^0$ oscillates as a function of time.

2.4.2 Significance of $\arg(q/p)$ and $|q/p|$

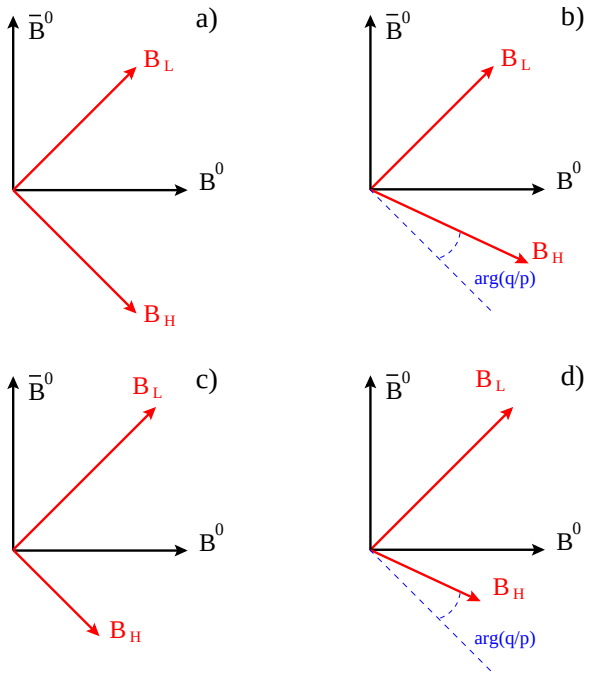

Figure 2.5: Graphical representation of the ratio q/p in the basis of flavor eigenstates.

The magnitude $|q/p|$ is better understood by defining

$$\delta \equiv \langle B_L|B_H\rangle \equiv |p|^2 - |q|^2 = \frac{2\mathcal{I}m(M_{12}^*\Gamma_{12})}{(\Delta m_d)^2 + |\Gamma_{12}|^2}. \tag{2.54}$$

The values of δ indicates the amount of B^0 and $\overline{B}^0$ in the mass eigenstates. For $\delta = 0$, the mass eigenstates $|B_L\rangle$ and $|B_H\rangle$ are also eigenstates of *CP*, with opposite eigenvalues, and there is no *CP* violation. However, whether $|B_H\rangle = |B_{CP=1}\rangle$ or $|B_H\rangle = |B_{CP=-1}\rangle$ should be determined experimentally.

The meaning of δ and $\arg(q/p)$ can be further clarified if one considers the graphical representation of a two-state system in the complex plane. The flavor eigenstates B^0 and $\overline{B}^0$ are shown as an orthonormal basis in Figure 2.5. The possible scenarios can be summarized as

- $\delta = 0$ and $\arg(q/p) = 0$: B_L and B_H are simply another orthonormal basis as shown in Figure 2.5a. They coincide with the *CP* eigenstate, meaning that *CP* is a symmetry of the Hamiltonian and therefore is conserved.
- $\delta = 0$ and $\arg(q/p) \neq 0$: B_L and B_H are still a normal basis but they are not orthogonal. Figure 2.5b shows an example with $\arg(q/p) = 20^o$. In this case *CP* is violated.
- $\delta \neq 0$: there is *CP* violation regardless of the phase $\arg(q/p)$ (Figures 2.5c and 2.5d). This is generally referred to as "*CP* violation in mixing". The magnitude of this effect is expected to be small in the Standard Model.

2.4.3 Decay of the $\Upsilon(4S)$ resonance

In *BABAR*, B mesons are produced in decays of the $\Upsilon(4S)$, which is a $b\bar{b}$ bound state similar to the positronium state. Its mass of $10.58\,\mathrm{GeV}/c^2$ is slightly above the energy threshold for production of two B mesons. About equal amounts of $B^+\ B^-$ and $B^0\ \overline{B}^0$ pair are produced in the $\Upsilon(4S)$ decay. The time evolution of the $B^0\ \overline{B}^0$ pair represents an example of the quantum coherence.

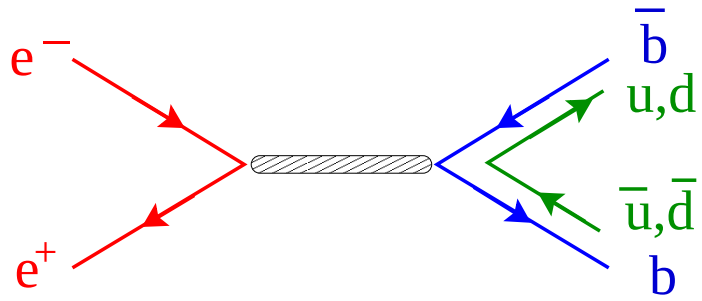

Figure 2.6: Production of $B\bar{B}$ pairs in the decay of the $\Upsilon(4S)$.

The initial state $|\Upsilon(4S)\rangle$ has spin $S = 1$, and therefore total angular momentum $J = S + L = 1$, and *CP* eigenvalue $\eta_{CP} = +1$. The decay proceeds through strong interactions and therefore the

angular momentum, the beauty quantum number ($b + \bar{b} = 1 - 1 = 0$), and CP must be conserved. The final state is given by the pair of pseudoscalar B mesons

$$|B^0_{\rm phys}\overline{B}^0_{\rm phys}\rangle = \frac{a}{\sqrt{2}}\,|B_L B_H\rangle + \frac{b}{\sqrt{2}}\,|B_H B_L\rangle\ . \tag{2.55}$$

with the usual normalization condition $|a|^2 + |b|^2 = 1$. Since the time evolution of the mass eigenstates B_L and B_H proceeds according to relations (2.28) and (2.29), The time evolution of $|B^0_{\rm phys}\overline{B}^0_{\rm phys}\rangle$ is given by

$$|B^0_{\rm phys}\overline{B}^0_{\rm phys}; t_1, t_2\rangle = a\ {\rm e}^{i\lambda_+ t_1}{\rm e}^{i\lambda_- t_2}|B_L B_H\rangle + b\ {\rm e}^{i\lambda_- t_1}{\rm e}^{i\lambda_+ t_2}|B_H B_L\rangle\ , \tag{2.56}$$

where t_1 and t_2 are the "proper" times of the B mesons. sentence here).

The Bose–Einstein statistics requires the total wave function $|\Psi\rangle = |\Psi_{\rm flavor}\rangle|\Psi_{\rm space}\rangle$ for this state to be symmetric at all times. Since the B mesons are spin–0 particles, the total spin S is zero, and the total angular momentum J is given by the orbital angular momentum L of the two mesons. Conservation of J requires $L = 1$, and therefore the B mesons are produced in a P-wave, and $|\Psi_{\rm space}\rangle$ is antisymmetric. For the total wave function $|\Psi\rangle$ to be symmetric, it is then necessary to have $a = -b = 1$.

In a thought experiment, and if the lifetime τ_{B^0} was long enough, one could separate the two B mesons and place them at two space-time points separated by a space-like distance so that events in one point could not influence those in the other. Nevertheless, due to the quantum coherence the decay of one of the two mesons as a B^0 would force the other meson to be necessarily a $\overline{B}^0$. This represents an example of the Einstein-Podolsky-Rosen paradox.

2.4.4 Time evolution of B mesons at the $\Upsilon(4S)$

The time evolution (2.56) of the $B\bar{B}$ state produced in the $\Upsilon(4S)$ decay is derived from relations (2.50) and (2.51), by taking into account the coherence discussed in the previous Section. Figure 2.7 shows a schematic view of the $\Upsilon(4S)$ decay in a $B^0\ \overline{B}^0$ pair. Two types of events are useful for the time-dependent studies in B decays.

1. One B meson is fully reconstructed in a flavor eigenstate ($B_{\rm rec}$) and the flavor of the other meson ($B_{\rm tag}$) is determined inclusively from its decay products. These events can be used to measure the frequency of $B^0\ \overline{B}^0$ oscillation.

2. One B meson is fully reconstructed in a CP eigenstate accessible to both B^0 and $\overline{B}^0$ mesons. The flavor of $B_{\rm rec}$ is determined by the flavor of the other meson ($B_{\rm tag}$). These events are used to measure CP violating effects.

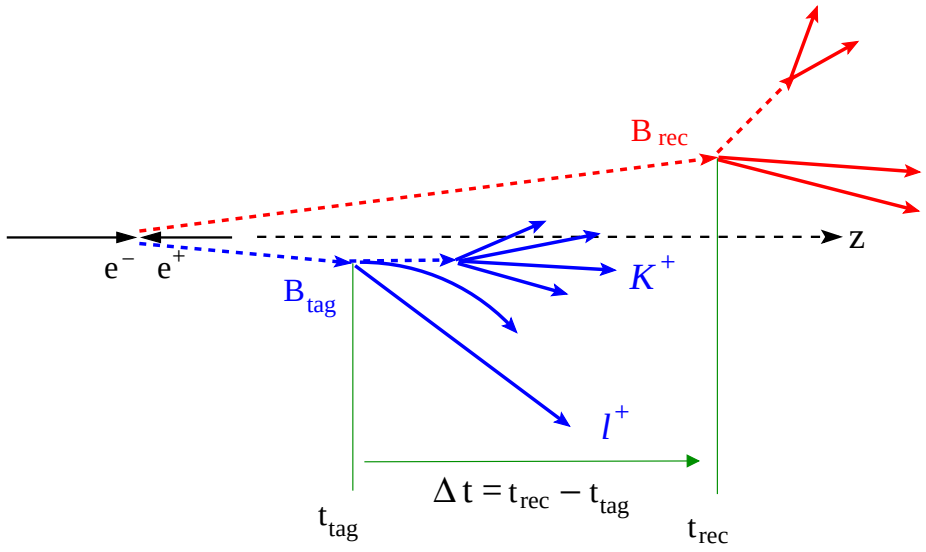

Figure 2.7: Topology of a typical $\Upsilon(4S) \rightarrow B\bar{B}$ decay, when the $\Upsilon(4S)$ is boosted in the laboratory frame.

The derivation of the rates for these two kinds of events is explained in detail in Section 1.2.4 of Reference [46] or in Chapter 7 of Reference [22].

Decays to flavor eigenstates

Events in which $B_{\rm rec}$ decays to flavor eigenstates, and the flavor of $B_{\rm tag}$ is determined from its decays products, can be divided in two categories:

- **Mixed events**: $B_{\rm rec}$ and $B_{\rm tag}$ mesons have the same flavor, that is a B^0 B^0 or a $\overline{B}^0$ $\overline{B}^0$ pair.
- **Unmixed events**: the two mesons have different flavors, that is one B^0 and one $\overline{B}^0$.

The number of events in each category depends on the time interval $\Delta t \equiv t_{\rm rec} - t_{\rm tag}$ between the decay of $B_{\rm rec}$ to a flavor eigenstate at time $t_{\rm rec}$, and the decay of $B_{\rm tag}$ at time $t_{\rm tag}$, as explained in Section 7.1. The time-dependent rates for mixed and unmixed events are given by

$$f_{\rm unmix}(\Delta t) \propto e^{-\Gamma|\Delta t|}\,(1+\cos\Delta m_d \Delta t) \tag{2.57}$$

$$f_{\rm mix}(\Delta t) \propto e^{-\Gamma|\Delta t|}\,(1-\cos\Delta m_d \Delta t) \tag{2.58}$$

and are illustrated in Figure 2.8. The oscillation frequency Δm_d is the difference between the masses M_H and M_L of mass eigenstates and was introduced in relations (2.50) and (2.51).

As explained earlier, at $\Delta t = 0$ all events are unmixed. The value of $\Delta m_d = 0.489 \pm 0.008\,{\rm ps}^{-1}$ [33] and is small compared to the B^0 lifetime $\tau_{B^0} = 1.542 \pm 0.016$, and allows the

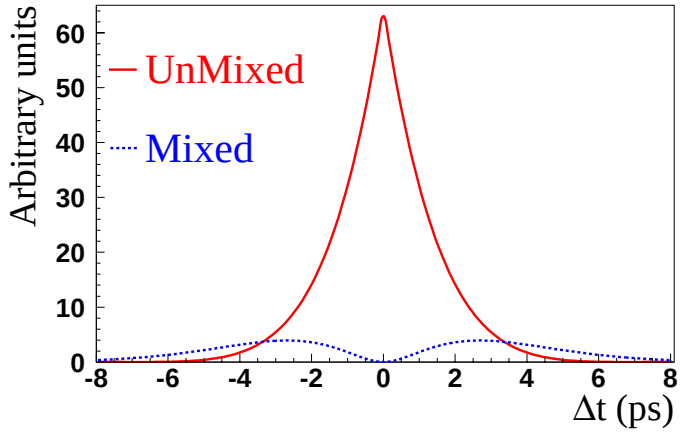

Figure 2.8: Rates of mixed and unmixed events as a function of $\Delta t \equiv t_{\rm rec} - t_{\rm tag}$.

experimental observation of the oscillation. The period of oscillation $T = 2\pi/\Delta m_d = 13\,\mathrm{ps}$ to be measured accurately.

The probability of B^0 $\overline{B}^0$ oscillation is given by the asymmetry

$$\mathcal{A}_{\rm mix}(\Delta t) = \frac{f_{\rm unmix} - f_{\rm mix}}{f_{\rm unmix} + f_{\rm mix}} \tag{2.59}$$

illustrated in Figure 2.9.

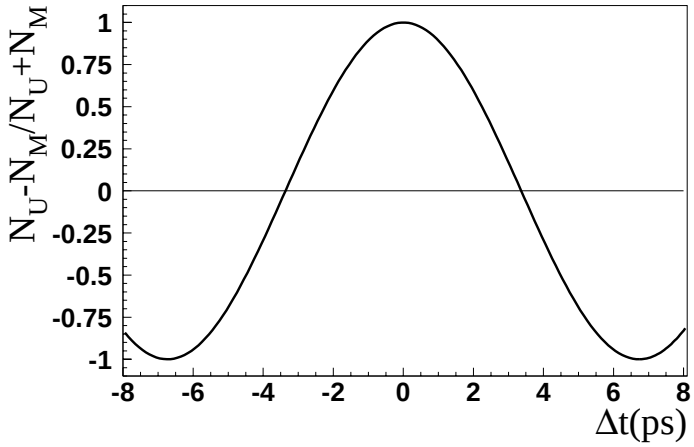

Figure 2.9: Asymmetry between numbers of mixed and unmixed events as a function of Δt.

As a comparison, the lifetime of the B_s^0 meson is $1.461 \pm 0.057\,\mathrm{ps}$ while the oscillation frequency $\delta \mathrm{m}_s$ for $B_s^0 \to \overline{B}_s^0$ oscillation is greater than $13.1\,\mathrm{ps}^{-1}$ at 95% CL [33]. The oscillation period is $T = 2\pi/\delta \mathrm{m}_s = 0.5\,\mathrm{ps}$. Measurement of such a small time interval, with good preci-

sion, is difficult from an experimental point of view, and represents one of the main obstacles in the measurement of the $B_s^0\overline{B}_s^0$ oscillation frequency.

Decays to CP eigenstates

Events where $B_{\rm rec}$ decays to a CP eigenstate f_{CP} can be used to study CP violating effects that occur in the B decays. State f_{CP} is accessible to both B^0 and $\overline{B}^0$ mesons. One can not know the flavor of $B_{\rm rec}$ at its decay time $t_{\rm rec}$. This is why the quantum coherence of the $B_{\rm rec}B_{\rm tag}$ pair is necessary. If $B_{\rm tag}$ is a B^0 ($\overline{B}^0$) at time $t_{\rm tag}$, the quantum coherence implies that $B_{\rm rec}$ must be a $\overline{B}^0$ (B^0) at that same time. When $B_{\rm tag}$ decays, the flavor of both mesons is known and $B_{\rm rec}$ evolve according to (2.50) if a B^0 (or (2.51) if a $\overline{B}^0$) until its decay at $t_{\rm rec}$. Note that this argument is valid regardless of the order of $t_{\rm tag}$ and $t_{\rm rec}$. In events where $B_{\rm rec}$ decays before $B_{\rm tag}$, that is $t_{\rm rec} < t_{\rm tag}$, its flavor is not determined until the decay of $B_{\rm tag}$ at a later time! This is the beauty of quantum mechanics.

The probability of observing the final state $|f_{CP}\ f_{\rm tag}\rangle$ depends on

- decay times $t_{\rm rec}$ and $t_{\rm tag}$,
- decay amplitudes

$$A_{f_{CP}} = \langle f_{CP}|H|B^0\rangle,\ \ \bar{A}_{f_{CP}} = \langle f_{CP}|H|\overline{B}^0\rangle, \tag{2.60}$$

- oscillation parameter q/p defined in 2.42, and
- flavor of $B_{\rm tag}$ whether $B_{\rm tag} = B^0$ or $B_{\rm tag} = \overline{B}^0$.

The time-dependent probabilities are given by

$$\begin{aligned} f_{B_{\rm tag}=B^0}(t_{\rm tag}, t_{f_{CP}}) \ &\propto\ e^{-\Gamma(t_{f_{CP}}-t_{\rm tag})}\Big\{1 + \frac{1-|\lambda_{f_{CP}}|^2}{1+|\lambda_{f_{CP}}|^2}\cos[\Delta m_d(t_{f_{CP}}-t_{\rm tag})] \\ &- \ \frac{2\mathcal{I}m\lambda_{f_{CP}}}{1+|\lambda_{f_{CP}}|^2}\sin[\Delta m_d(t_{f_{CP}}-t_{\rm tag})]\Big\} \end{aligned} \tag{2.61}$$

$$\begin{aligned} f_{B_{\rm tag}=\overline{B}^0}(t_{\rm tag}, t_{f_{CP}}) \ &\propto\ e^{-\Gamma(t_{f_{CP}}-t_{\rm tag})}\Big\{1 - \frac{1-|\lambda_{f_{CP}}|^2}{1+|\lambda_{f_{CP}}|^2}\cos[\Delta m_d(t_{f_{CP}}-t_{\rm tag})] \\ &+ \ \frac{2\mathcal{I}m\lambda_{f_{CP}}}{1+|\lambda_{f_{CP}}|^2}\sin[\Delta m_d(t_{f_{CP}}-t_{\rm tag})]\Big\} \end{aligned} \tag{2.62}$$

where

$$\lambda_{f_{CP}} \equiv \frac{q}{p}\frac{\bar{A}_{f_{CP}}}{A_{f_{CP}}} = \eta_{f_{CP}}\frac{q}{p}\frac{\bar{A}_{\bar{f}_{CP}}}{A_{f_{CP}}}\ . \tag{2.63}$$

The second form for $\lambda_{f_{CP}}$ uses the property

$$\bar{A}_{f_{CP}} = \eta_{f_{CP}} \bar{A}_{\bar{f}_{CP}}, \tag{2.64}$$

where $\eta_{f_{CP}}$ is the CP eigenvalue of the state f_{CP} and $\bar{A}_{\bar{f}_{CP}} = \langle \bar{f}_{CP}|H|\overline{B}^0\rangle$. As for the oscillation rates (2.57) and (2.58), these rates depend only on the difference $\Delta t = t_{\rm rec} - t_{\rm tag}$. Measurement of Δt from the distance between the B mesons decay vertices is discussed in Chapter 7.

Relations (2.61) and (2.62) are illustrated in Figure 2.10 and are visibly different for events in which $B_{\rm tag}$ is a B^0 and those where $B_{\rm tag}$ is a $\overline{B}^0$.

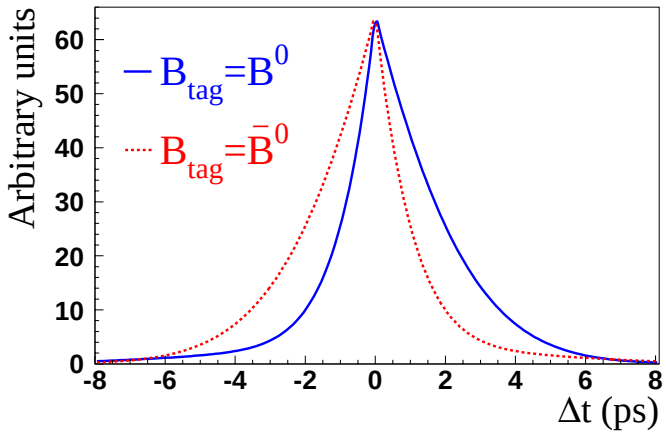

Figure 2.10: Time-dependent rates $f_{B_{\rm tag}=B^0}$ and $f_{B_{\rm tag}=\overline{B}^0}$.

An observable time-dependent CP asymmetry [47] can be defined as

$$a_{f_{CP}}(\Delta t) = \frac{f_{B_{\rm tag}=B^0} - f_{B_{\rm tag}=\overline{B}^0}}{f_{B_{\rm tag}=B^0} + f_{B_{\rm tag}=\overline{B}^0}} = \frac{1-|\lambda_{f_{CP}}|^2}{1+|\lambda_{f_{CP}}|^2}\cos\Delta m_d\Delta t - \frac{2\mathcal{I}m\lambda_{f_{CP}}}{1+|\lambda_{f_{CP}}|^2}\sin\Delta m_d\Delta t, \tag{2.65}$$

and is illustrated in Figure 2.11.

The amplitudes of the sine and cosine terms can be measured experimentally, and are related to different types of CP violation, discussed in Section 2.4.5. In the Standard Model, $|\lambda|$ is expected to be very close to 1, leaving only the sine term in $a_{f_{CP}}$. Since sine is an odd function of Δt, $\int_{-\infty}^{+\infty} a_{f_{CP}} {\rm d}\Delta t = 0$. Therefore, its amplitude $2\mathcal{I}m\lambda/(1+|\lambda|^2)$ can only be determined with a time-dependent analysis of the Δt distributions. This is the reason why the measurement of this amplitude could not be performed in previous experiments at symmetric e^+e^-, such as DORIS II at DESY and CESR at Cornell.

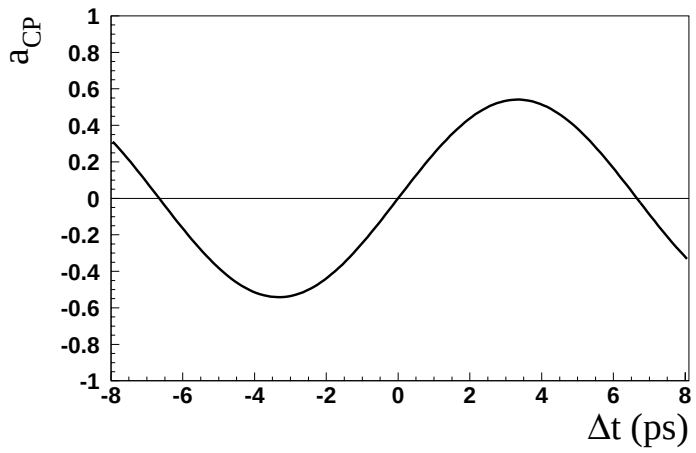

Figure 2.11: Time-dependent CP asymmetry a_{CP} with $|\lambda| = 1$ and $\mathcal{I}m\lambda/|\lambda| = 0.6$.

2.4.5 Types of CP violation

The manifestation of CP violation can be classified in three categories.

1. CP violation in decay
2. CP violation in mixing
3. CP violation in the interference between decay and mixing

A general discussion of all types of CP violation is beyond the scope of this thesis. The reader is referred to excellent discussions of the subject in References [22, 23]. The first two types are briefly introduced here, while the third type is the subject of the next Section.

Parameter $\lambda_{f_{CP}}$, defined in (2.63), is particularly useful for the study of CP violation and to classify the different types of it. Its relevant property is the invariance under arbitrary phase redefinition. This is shown easily with an explicit example [48].

The B^0 and $\overline{B}^0$ states are related through the CP operation

$$CP|B^0\rangle = e^{2i\xi_B}|\overline{B}^0\rangle, \quad CP|\overline{B}^0\rangle = e^{-2i\xi_B}|B^0\rangle \,, \tag{2.66}$$

where the phase ξ_B is arbitrary and does not have physical significance. This is because flavor is conserved in the strong interactions, and therefore a phase transformation of states (2.66) has no physical effect. Consider now the following phase redefinition

$$|B^0_\zeta\rangle = e^{-i\zeta}|B^0\rangle, \quad |\overline{B}^0_\zeta\rangle = e^{+i\zeta}|\overline{B}^0\rangle, \tag{2.67}$$

which results in a new CP phase

$$(CP)_\zeta|B^0_\zeta\rangle = e^{2i(\xi_B-\zeta)}|\overline{B}^0\zeta\rangle, \quad (CP)_\zeta|\overline{B}^0\zeta\rangle = e^{-2i(\xi_B-\zeta)}|B^0_\zeta\rangle \,. \tag{2.68}$$

As a consequence of (2.68), the phase of q/p, A_f, and $\bar{A}_f$ change according to

$$(q/p)_\zeta = e^{-2i\zeta}(q/p), \quad (A_f)_\zeta = e^{-i\zeta}A_f, \quad (\bar{A}_f)_\zeta = e^{+i\zeta}\bar{A}_f \; . \tag{2.69}$$

The combinations of these transformations, however, leaves $\lambda_{f_{CP}}$ invariant. Therefore, the measurement of $\mathcal{I}m\lambda_{CP}$ is physically meaningful.

CP violation in decay

This first type of CP violation can occur in both neutral and charged B mesons as illustrated in Figure 2.12. The violation is in the difference between decay rates of two self-conjugate pro-

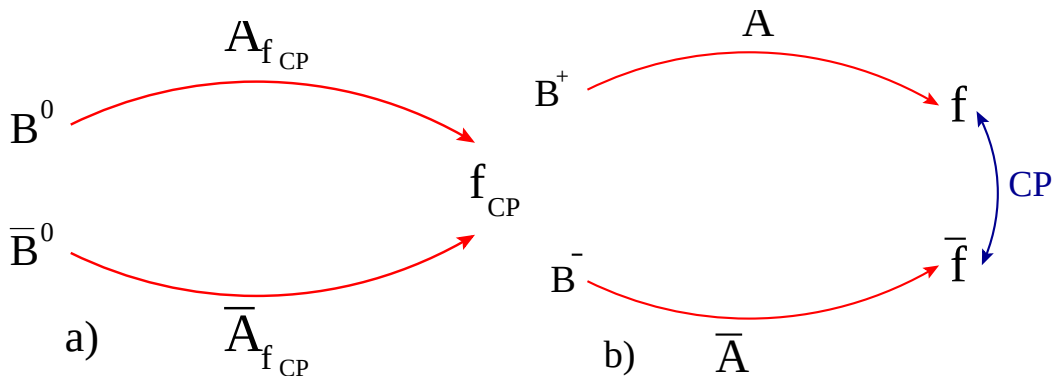

Figure 2.12: CP violation in decay in a) neutral B mesons when $|A_{f_{CP}}| \neq |\bar{A}_{f_{CP}}|$, and b) charged B mesons when $|A(B^+ \to f)| \neq |\bar{A}(B^- \to \bar{f})|$.

cesses. In terms of parameter $\lambda_{f_{CP}}$ (2.63), this type of CP violation requires $|\lambda_{CP}| \neq 1$. Therefore asymmetry (2.65) is non-vanishing and is a good observable to measure CP violation.

Any CP violation in charged B mesons is due to violation in decay. The observable asymmetry is given by

$$a_f = \frac{\Gamma(B^+ \to f) - \Gamma(B^- \to \bar{f})}{\Gamma(B^+ \to f) + \Gamma(B^- \to \bar{f})} = \frac{1 - |\bar{A}/A|^2}{1 + |\bar{A}/A|^2} \tag{2.70}$$

In neutral B mesons, CP violation occurs when the decays of B^0 and $\overline{B}^0$ mesons to a common state f_{CP} have different rates. However, this type of violation competes with the other two possible sources of violation in neutral B mesons.

The interpretation of the experimental results in terms of CKM matrix elements is not straightforward. The calculation of the decay amplitudes involves strong interactions and is dominated by theoretical uncertainties.

CP violation in mixing

The CP violation in mixing was discussed in Section 2.4.2. It occurs when $|q/p| \neq 1$ implying that the eigenstates of the Hamiltonian (mass eigenstates) are not eigenstates of CP. In other words, CP is not a symmetry of the theory. In terms of $\lambda_{f_{CP}}$, CP violation in mixing implies $|\lambda_{CP}| \neq 1$ and therefore the cosine term in Equation (2.65) is non-vanishing.

Violation in mixing can be studied in the semileptonic decays of neutral B mesons by measuring the asymmetry

$$a_{\mathrm{SL}} = \frac{\Gamma(\overline{B}^0_{\mathrm{phys}}(t) \to \ell^+ \nu_\ell X) - \Gamma(B^0_{\mathrm{phys}}(t) \to \ell^- \overline{\nu}_\ell X)}{\Gamma(\overline{B}^0_{\mathrm{phys}}(t) \to \ell^+ \nu_\ell X) - \Gamma(B^0_{\mathrm{phys}}(t) \to \ell^- \overline{\nu}_\ell X)} = \frac{1 - |q/p|^4}{1 + |q/p|^4} \tag{2.71}$$

The CP violating effects are expected to be small, at the order of $\mathcal{O}(10^{-2})$. The interpretation of the experimental results is complicated by the theoretical uncertainties involved in the calculation of $|q/p|$ [44].

2.4.6 CP violation in interference between decay and mixing

A third type of CP violation occurs due to quantum-mechanical interference between two possible amplitudes for a same physical process.

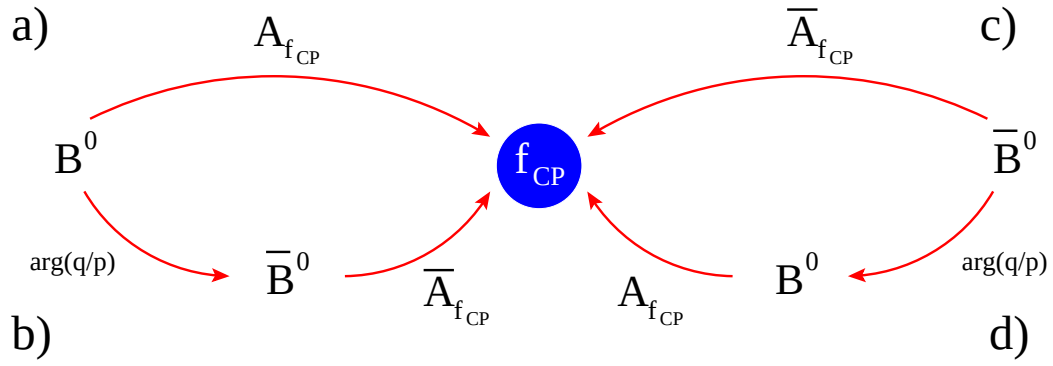

Figure 2.13: The B^0 meson can decay a) directly to CP eigenstate f_{CP}, or b) first oscillate to a $\overline{B}^0$ which then decays to the same final state f_{CP}. The analog amplitudes for the $\overline{B}^0$ mesons are shown in c) and d).

Consider a CP eigenstate f_{CP}, accessible to both B^0 and $\overline{B}^0$ mesons. A B^0 meson can decay to f_{CP} via two different amplitudes (or quantum-mechanical paths):

- decay directly to f_{CP} [49–51] (Figure 2.13a), or

- undergo oscillation to a $\overline{B}^0$ state which then decays to the same final state f_{CP} (Figure 2.13b).

Similar paths are possible for a $\overline{B}^0$ mesons and are shown in Figures 2.13c and 2.13d. In absence of violation in decay and in mixing

$$|A_f/\bar{A}_f| = 1, \quad |q/p| = 1, \tag{2.72}$$

and $\lambda_{f_{CP}}$ can be written as a pure phase

$$\lambda_{f_{CP}} = \eta_{f_{CP}} \mathrm{e}^{-2i\Phi} \ . \tag{2.73}$$

In this case, the asymmetry $a_{f_{CP}}$ (2.65) is reduced to

$$a_{f_{CP}}(\Delta t) = -\mathcal{I}m\lambda_{f_{CP}} \sin \Delta m_d \Delta t = \eta_{f_{CP}} \sin 2\Phi \sin \Delta m_d \Delta t \ . \tag{2.74}$$

Relation (2.74) implies that CP violation is observed simply as the consequence of a difference in phase between the two complex quantities q/p and $A_f/\bar{A}_f$.

This can be shown explicitly by writing amplitudes A_f and $\bar{A}_f$ as

$$A_f = A\mathrm{e}^{i(\Phi_W+\delta)} \tag{2.75}$$

$$\bar{A}_f = \eta_{f_{CP}} A\mathrm{e}^{i(-\Phi_W+\delta)} \ , \tag{2.76}$$

where amplitude A is real, the phase Φ_w is due to weak interactions and therefore changes sign under CP, and δ is the strong phase, invariant under CP. This can be done, for example, in the $B^0 \to J/\psi\, K^0_S$ decays (Section 2.5.2). Also, since $|q/p| = 1$, one can write $q/p = \mathrm{e}^{-2i\Phi_M}$. These definitions satisfy the conditions (2.72), and $\lambda_{f_{CP}}$ is now given by

$$\lambda_{f_{CP}} = \eta_{f_{CP}} \mathrm{e}^{-2i(\Phi_W - \Phi_M)} \ , \tag{2.77}$$

demonstrating that the phase Φ in (2.74) is from the difference $\Phi_W - \Phi_M$. As explained in Sections 2.5.2, 2.5.3, and 2.5.4.

In general, CP violation is established when $\lambda_{f_{CP}} \neq 1$, which can happen if $|\lambda_{f_{CP}}| \neq 1$, or $\mathcal{I}m\lambda_{CP} \neq 0$, or both simultaneously. The condition $|\lambda_{f_{CP}}| \neq 1$ corresponds to a difference between $N^{\mathrm{obs}}_{B^0}$, the number of observed B^0 mesons, and $N^{\mathrm{obs}}_{\overline{B}^0}$, the number of observed $\overline{B}^0$ mesons. These numbers can be computed by integrating the decay rates (2.61) and (2.62) for all values of Δt

$$N^{\mathrm{obs}}_{B^0} = \int_{-\infty}^{+\infty} d\Delta t \ f_{B_{\mathrm{tag}}=\overline{B}^0} \tag{2.78}$$

$$N^{\mathrm{obs}}_{\overline{B}^0} = \int_{-\infty}^{+\infty} d\Delta t \ f_{B_{\mathrm{tag}}=B^0} \tag{2.79}$$

with an integrated asymmetry

$$\int_{-\infty}^{+\infty} d\Delta t \; a_{f_{CP}} = \frac{1-|\lambda_{f_{CP}}|^2}{1+|\lambda_{f_{CP}}|^2} \frac{1}{1+(\tau_{B^0}\Delta m_d)^2} \; . \tag{2.80}$$

Deviation of $|\lambda_{f_{CP}}|$ from 1 is commonly called "direct CP violation". In the Standard Model such a deviation is expected to be small, considering that $|\lambda_{f_{CP}}| = |q/p||A_f/\bar{A}_f|$ and $|q/p$ is of the order of $\mathcal{O}(10^{-2})$.

2.5 Measurement of the Unitarity-Triangle parameters in B decays

The rich variety of decay modes for B mesons allows the determination of angles α, β, and γ of the Unitarity Triangle defined in (2.27), through the measurement CP asymmetries.Each angle can be measured with different classes of decays, and the consistency of the results thus obtained offers an important test of the Kobayashi-Maskawa mechanism of CP violation in the Standard Model. The ultimate goal is to provide independent measurements of angles and sides of the Unitarity Triangle.

A general discussion of the determination of these quantities and their related decay modes, although interesting, is beyond the realm of this discussion. A systematic and complete discussion of this subject is given in Chapter 28 of Reference [22]. This Section covers mainly the decay modes used in this analysis for the measurement of $\sin 2\beta$. Measurements of α and γ are more challenging, and are briefly discussed in Sections 2.5.3 and 2.5.4.

2.5.1 Parameter $\lambda_{f_{CP}}$ and angles α, β, and γ

The CP violating parameter $\lambda_{f_{CP}}$ is related to the angles α, β, and γ through the ratio q/p, and the decay amplitudes A_f and $\bar{A}_f$. In Section 2.4.6 it was shown that if

$$A_f = A\mathrm{e}^{i(\Phi_W+\delta)} \quad , \quad \bar{A}_f = \eta_{f_{CP}} A\mathrm{e}^{i(-\Phi_W+\delta)} \; ,$$
$$|q/p| = 1 \quad , \quad q/p = \mathrm{e}^{-2i\Phi_M} \; ,$$

the time-dependent asymmetry (2.65) can be rewritten as

$$a_{f_{CP}}(\Delta t) = -\mathcal{I}m\lambda_{f_{CP}} \sin \Delta m_d \Delta t = \eta_{f_{CP}} \sin 2(\Phi_W - \Phi_M) \sin(\Delta m_d \Delta t) \; .$$

Relation (2.76) is valid, for example, when the decay amplitude is dominated by a tree-level diagram. Figure 2.14a shows the tree-level diagram for the b quark, involving two CKM matrix

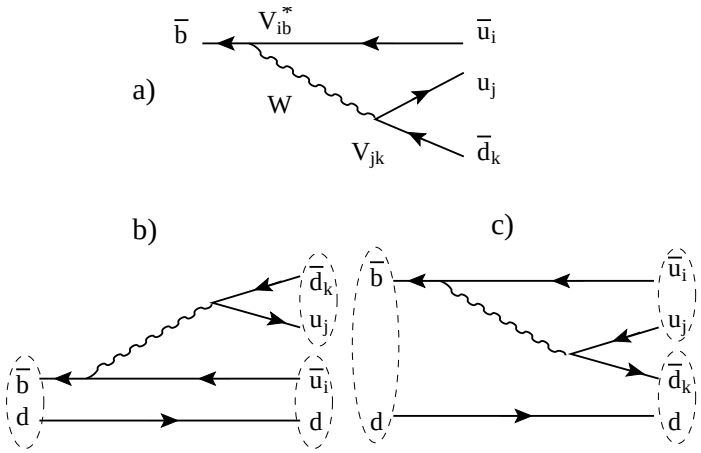

Figure 2.14: a) Quark-level tree diagram, b) color-favored meson diagram, and c) color-suppressed meson diagram for decays of B^0.

elements. This corresponds to two tree diagrams for the B^0 meson, Figures 2.14b and 2.14c, which have the same phase. In these Figures, $\bar{u}_i$ and u_j indicate either a c or a u quark, while d_k can be either an s or a d quark. The phase $\Phi_W - \Phi_M$ is directly related to the phase of $V_{ib}^* V_{jk}$.

Unfortunately, there are at least two diagrams contributing to the total amplitude in most of the B decay channels [52]. Before getting in the details of these additional contributions, it is useful to see their effect on the asymmetry $a_{f_{CP}}$. In presence of a second diagram, the decay amplitudes can be written as

$$A_f = A_1 \mathrm{e}^{i(\Phi_{W1}+\delta_1)} + A_2 \mathrm{e}^{i(\Phi_{W2}+\delta_2)}, \tag{2.81}$$

$$\bar{A}_f = \eta_{f_{CP}} \Big[A_1 \, \mathrm{e}^{i(-\Phi_{W1}+\delta_1)} + A_2 \, \mathrm{e}^{i(-\Phi_{W2}+\delta_2)} \Big], \tag{2.82}$$

Parameter $\lambda_{f_{CP}}$ is now given by

$$\lambda_{f_{CP}} = -\eta_{f_{CP}} \mathrm{e}^{-2i\phi_1} \frac{1 + re^{i(\Delta-\phi_2+\phi_1)}}{1 + re^{i(\Delta+\phi_2-\phi_1)}} \tag{2.83}$$

where $\Delta = \delta_2 - \delta_1$, $\phi_1 = \Phi_{W1} - \Phi_M$ and $\phi_2 = \Phi_{W2} - \Phi_M$ are the new observable phase differences, and $r = A_2/A_1$ is the ratio between the magnitude of the two diagrams. The coefficients S and C of the sine and cosine terms, respectively, in the time-dependent asymmetry $a_{f_{CP}}$ (2.74) are no longer related to any single weak phase ϕ_1 or ϕ_2. Therefore, the experimental results can not be interpreted cleanly in terms of CKM angles and require additional theoretical assumptions.

In general, the additional contributions to decay amplitudes come from one-loop flavor-changing neutral-current diagrams, commonly referred to as "penguin" diagrams [53]. The three types of penguins, gluonic and electroweak [54] with a photon or a Z^0 boson are shown in Figure 2.15. Using

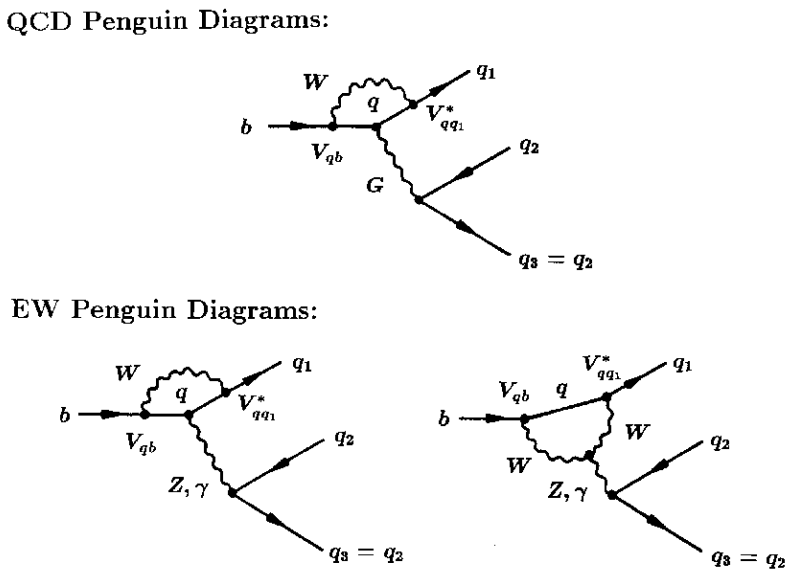

Figure 2.15: Quark-level diagrams for gluonic penguin in a) and electro-weak penguins with a photon or a Z^0 boson in b) and c).

the notation $b \to q[\bar{q}q']$ (Figure 2.14) with $[\bar{q}q']$ from the emitted W, the decay amplitude $A(q\bar{q}q')$ in presence of tree and penguin diagrams can be written as

$$A(q\bar{q}q') = V_{tb}V^*_{tq'}P^t_{q'} + V_{cb}V^*_{cq'}(T_{c\bar{c}q'}\delta_{qc} + P^c_{q'}) + V_{ub}V^*_{uq'}(T_{u\bar{u}q'}\delta_{qu} + P^u_{q'}) \; . \tag{2.84}$$

In this expression $T_{q\bar{q}q'}$ is the contribution of the tree diagrams (Figure 2.14) excluding the CKM elements. Similarly, $P^Q_{q'}$ are the penguin contributions, excluding the CKM elements, when the intermediate quark in the loop is a Q quark. The gluonic and electroweak penguins have the same phase structure. In addition, the electroweak penguin contribution is typically small of the order of $10\ \%$ of the gluonic contributions [54].

One problem with this expression is that the contributions $P^Q_{q'}$ are divergent. However, $A(q\bar{q}q')$ can be rewritten by using the unitarity conditions (2.17), (2.18), and (2.19)

$$V_{ud}V^*_{us} + V_{cd}V^*_{cs} + V_{td}V^*_{ts} = 0,$$
$$V_{us}V^*_{ub} + V_{cs}V^*_{cb} + V_{ts}V^*_{tb} = 0,$$
$$V_{ud}V^*_{ub} + V_{cd}V^*_{cb} + V_{td}V^*_{tb} = 0,$$

to remove one of the CKM factors and derive the following expressions for $q\bar{q}$ and $q\bar{q}d$ decays

$$A(c\bar{c}s) = V_{cb}V_{cs}^*(T_{c\bar{c}s} + P_s^c - P_s^t) + V_{ub}V_{us}^*(P_s^u - P_s^t), \quad (2.85)$$

$$A(s\bar{s}s) = V_{cb}V_{cs}^*(P_s^c - P_s^t) + V_{ub}V_{us}^*(P_s^u - P_s^t), \quad (2.86)$$

$$A(u\bar{u}s) = V_{cb}V_{cs}^*(P_s^c - P_s^t) + V_{ub}V_{us}^*(T_{u\bar{u}s} + P_s^u - P_s^t), \quad (2.87)$$

$$A(c\bar{c}d) = V_{tb}V_{td}^*(P_d^t - P_d^u) + V_{cb}V_{cd}^*(T_{c\bar{c}d} + P_d^c - P_d^u), \quad (2.88)$$

$$A(u\bar{u}d) = V_{tb}V_{td}^*(P_d^t - P_d^c) + V_{ub}V_{ud}^*(T_{u\bar{u}d} + P_d^u - P_d^c), \quad (2.89)$$

$$A(s\bar{s}d) = V_{tb}V_{td}^*(P_d^t - P_d^u) + V_{cb}V_{cd}^*(P_d^c - P_d^u), \quad (2.90)$$

where the convention is to retain $V_{tb}V_{td}^*$, which appears in the expression of q/p. One notices that the penguin contributions appear always in the form $P_q^{Q_1} - P_q^{Q_2}$, which is finite and hence the amplitudes are well defined.

These quark-level amplitudes can not be used directly to compute amplitudes of B decays involving hadrons, due hadronic interactions between quarks resulting in physical final states (final state interactions and rescattering). However, they are useful to classify groups of decays that allow the measurement of one particular CKM angle.

All amplitudes in (2.85)–(2.90) exhibit the common pattern

$$A = f_1(T + \Delta P_1) + f_2 \Delta P_2 \quad (2.91)$$

where f_1 and f_2 are CKM elements and T and $\Delta P_i \equiv P_{q_i}^{Q1} - P_{q_i}^{Q2}$ are contributions from tree and penguin diagrams. The best modes are those in which one contribution dominates, and thus has a simple relation with a CKM angle. The dominant contribution is determined by two factors

- ratio f_1/f_2 between the CKM elements: the best decay modes are those in which $|f_1/f_2| \approx 0$ or $|f_1/f_2| \approx 1$

- ratio $\Delta P_q/T$: the difference $P_q^c - P_q^u$ is suppressed compared to T by the GIM mechanism [55], while the combination $P_q^t - P_q^{c,u}$ is evaluated to be

$$r_{\rm T} \equiv \left| \frac{P_q^t - P_q^{c,u}}{T} \right| \sim \frac{\alpha_s(m_b)}{12\pi} \ln \frac{m_t^2}{m_b^2} \sim 0.04 \sim \lambda^2 \quad (2.92)$$

  where $\alpha_s(m_b) = 0.2$ is the strong running-coupling constant at the b-mass scale, λ is one of the Wolfenstein parameters in (2.20), and the ratio of hadronic matrix elements are assumed to be close to unity [56].

2.5.2 Measurement of $\sin 2\beta$

Decay amplitudes (2.85), (2.86), and (2.88) of modes $b \to c\bar{c}s$, $b \to s\bar{s}s$, and $b \to c\bar{c}d$ are related to angle β. Table 2.3 summarizes the contributions to these decay amplitudes.

$b \to c\bar{c}s$ decays

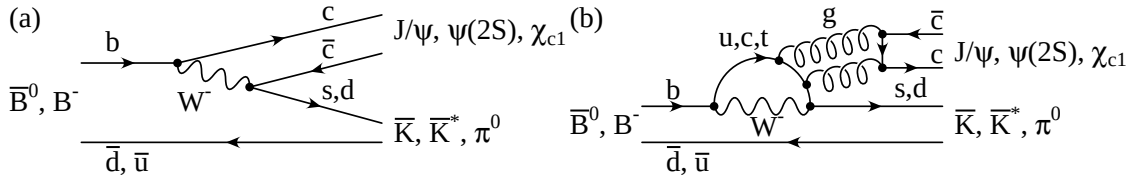

Figure 2.16: a) Tree and b) penguin diagrams in the leading term of decay amplitude $A(c\bar{c}s)$.

These decays provide the cleanest measurement of angle β and are commonly called golden modes. The secondary term in $A(c\bar{c}s)$ is suppressed by a factor $r_{\rm T}^2\lambda^2 \approx 10^{-3}$ with respect to the leading term (Table 2.3). The leading term has contributions from tree and penguin diagrams shown in Figure 2.16, which happen to have the same weak phase. Hence, $A(c\bar{c}s)$ has only one weak phase up to the order $\mathcal{O}(10^{-3})$. This is the ideal case discussed in Section (2.4.6), when the CP asymmetry amplitude measures the weak phase of the decay amplitudes. For decay modes $J/\psi\ K_S^0$, $\psi(2S)\ K_S^0$, $\chi_{c1}\ K_S^0$, $\eta_c\ K_S^0$, and $J/\psi\ K_L^0$ parameter $\lambda_{f_{CP}}$ is given by

$$\lambda = \frac{q}{p}\frac{\bar{A}(c\bar{c}s)}{A(\bar{c}c\bar{s})}\left(\frac{q}{p}\right)_K . \tag{2.93}$$

Here, the ratio

$$\left(\frac{q}{p}\right)_K = \frac{V_{cs}V_{cd}^*}{V_{cs}^*V_{cd}}\mathrm{e}^{-2i\zeta_K} \tag{2.94}$$

is due to flavor oscillation in kaons. The ratio q/p defined in (2.42), to good approximation, is given by [44]

$$\frac{q}{p} = -\frac{M_{12}^*}{|M_{12}|} = \frac{V_{tb}^*V_{td}}{V_{tb}V_{td}^*}\mathrm{e}^{2i\xi_B} . \tag{2.95}$$

By using the expression of $A(c\bar{c}s)$ in (2.85)

$$\frac{\bar{A}_{\psi K^0}}{A_{\psi K^0}} = \eta_{\psi K^0}\left(\frac{V_{cb}V_{cs}^*}{V_{cb}^*V_{cs}}\right)\left(\frac{V_{cs}V_{cd}^*}{V_{cs}^*V_{cd}}\right)e^{-2i\xi_B} , \tag{2.96}$$

with $\eta_f = +1$ for $J/\psi\ K^0_L$ and $\eta_f = -1$ for the other modes with a K^0_S. ξ_K is the arbitrary phase for the neutral kaons and has no physical significance. The phase ξ_B of q/p and $\bar{A}/A$ cancel each other as already shown in (2.69). Finally, using the expression of CKM matrix elements in the Wolfenstein parameterization (2.20), one obtains

$$\lambda_{f_{CP}} = \eta_f \mathrm{e}^{-2i\beta} \Rightarrow \quad |\lambda_{f_{CP}}| = 1, \quad \mathcal{I}m\lambda_{f_{CP}} = -\eta_f \sin 2\beta \tag{2.97}$$

and the time-dependent asymmetry

$$a_{CP} = -\eta_f \sin 2\beta \sin \Delta m_d \Delta t \tag{2.98}$$

Relation (2.97) holds up to the order $\mathcal{O}(10^{-3})$ and represents the cleanest measurement of a CKM parameter. It also implies that there is almost no direct *CP* violation in these modes. As explained earlier, direct *CP* violation requires at least two contributions to the decay amplitude A. Any experimental evidence of direct *CP* violation is a hint of New Physics beyond the Standard Model.

The measurement of $\sin 2\beta$ with a large sample of $J/\psi\ K^0_S$, $\psi(2S)\ K^0_S$, $\chi_{c1}\ K^0_S$, and $\eta_c\ K^0_S$ is discussed in this dissertation and the results are presented in Chapter 9. These modes have a cleaner experimental signature compared to the $J/\psi\ K^0_L$ mode and dominate the experimental sensitivity on $\sin 2\beta$. The decay mode $B^0 \to J/\psi K^{*0}$ is a pseudoscalar to vector-vector decay and can also be used to measure $\sin 2\beta$. However, this final state is a mixture of *CP* eigenstates with angular momenta $L = 0, 1, 2$, and an angular analysis is required to separate the contribution of each component. The results of the measurement with $J/\psi\ K^0_L$ and $J/\psi\ K^{*0}$ are discussed in Sections 9.5.1 and 9.5.2.

$b \to s\bar{s}s$ decays

The phenomenology of these decays, for example in the $Bz \to \phi K^0_S$ mode, is the same as for the $c\bar{c}s$ decays, and provides a very clean measurement of $\sin 2\beta$. The difference consists in the absence of tree-level contributions. As shown in Table 2.3, the leading order has only a penguin contribution and is therefore suppressed, in the Standard Model, compared to the $J/\psi\ K^0_S$ mode. An independent measurement of $\sin 2\beta$ with this mode represent a very important and significant test of the Standard Model. A preliminary measurement has been recently performed by the *BABAR* collaboration [57].

$b \to c\bar{c}d$ decays

The decay modes $b \to c\bar{c}d$ suffer from the presence of a secondary term, that has a different weak phase from the leading term, and is not suppressed (Table 2.3). Theoretical assumptions are

required to estimate the penguin contribution [58] and interpret the experimental results. In absence of the secondary term, the $D^+ D^-$ mode could provide a measurement of $\sin 2\beta$ similar to the $c\bar{c}s$ modes.

The $D^{*+} D^{*-}$ is another decay mode of interest but angular analysis is necessary (as for $J/\psi K^{*0}$) to separate the mixture of CP eigenstates in the final state. A preliminary measurement of time-dependent asymmetries in this mode can be found in Reference [59].

2.5.3 Measurement of α

Measurement of angle α is more problematic compared to $\sin 2\beta$. The difficulties are twofold: theoretical and experimental. Table 2.4 shows the contributions to decay amplitudes related to α. The penguin contribution in the secondary term has the same magnitude, but a different weak phase from the leading tree contribution. Measurements of branching fractions for $B \to K\pi$ and $B \to \pi\pi$ decay modes by *BABAR* [60] and BELLE [61] collaborations suggest that the penguin contribution can be large and non-negligible.

The time-dependent CP asymmetries in these modes, although related to $\sin 2\alpha$, require theoretical assumptions for their interpretation. A promising technique is the so-called "isospin analysis" that using the branching fractions for $B^0 \to \pi^+\pi^-, \pi^0\pi^0$ and $B^+ \to \pi^0\pi^+$, can measured α [63]. The branching fraction for $B^0 \to \pi^0\pi^0$ is expected to be of the order of $\mathcal{O}(10^{-7})$ and its measurement challenging. A preliminary results is available from the *BABAR* collaboration [64]. Time-dependent CP asymmetries have recently been measured by *BABAR* [60] and BELLE [62] collaborations.

2.5.4 Measurement of γ

Two examples of decay modes for the measurement of γ are listed in Table 2.5.

The good news with the decay modes $D^0 K^0_S$ and $D^0\pi^0$ is the absence of secondary, or penguin contributions. The value of γ can be measured through the interference of two tree-level contributions. This means that experimental results offer clean theoretical interpretation. However, the decay amplitudes for these decay modes are color suppressed and/or CKM suppressed. Therefore the branching fractions of these decays are very small.

The $D^0\ \pi^0$ mode has very large backgrounds from other B decay modes. For example, a $B^+ \to \overline{D}^0\pi^0\pi^+$ candidate, when the π^+ is not included, can be mis-reconstructed as a $\overline{D}^0\ \pi^0$ final state. Therefore, the selection of the small number of candidates on top of the large amount

of background can be a problem. Another potential problem is the large difference, order of λ^2, between the two decay amplitudes.

The D^0 K^0_S mode is experimentally very clean, and the difference between the two contributions is smaller, order of λ. This decay mode has not been observed yet but has the potential of providing a very clean measurement of γ.

2.6 Effects of New Physics

A general discussion of sources of CP violation beyond the Standard Model is beyond the scope of this thesis. An extensive treatment of this topic is given in Reference [65]. However, one can intuitively see how new theories can modify the CKM picture of CP violation.

As explained in Section 2.5.2, $\sin 2\beta$ is the phase of CP-violating parameter $\lambda_{f_{CP}}$ defined in (2.63) as

$$\lambda_{f_{CP}} \equiv \frac{q}{p}\frac{\bar{A}_{f_{CP}}}{A_{f_{CP}}} = \eta_{f_{CP}}\frac{q}{p}\frac{\bar{A}_{\bar{f}_{CP}}}{A_{f_{CP}}} \tag{2.99}$$

in the limit of $|\lambda|$=1 in the Standard Model. In terms of diagrams, $\sin 2\beta$ is the phase difference between the two diagrams in Figure 2.17. New Physics can modify the predicted CP asymmetry in

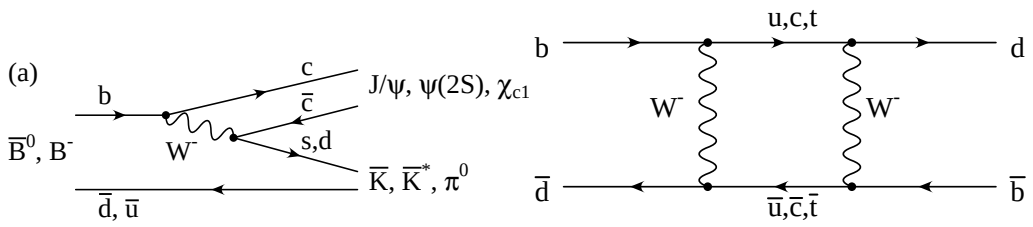

Figure 2.17: B^0 $\overline{B}^0$ oscillation diagram in a), and the decay diagram in b).

the Standard Model with new contributions to either diagram.

Contributions to amplitude A (Figure 2.17a) are unlikely in decay modes where A is dominated by a tree-level diagram in the Standard Model, e.g. J/ψ K^0_S. In this case, New Physics can contribute in two ways [66]:

1. with significant contribution to the box diagram (Figure 2.17a); or when
2. unitarity of the CKM matrix does not hold, for example when there are four or more generations of quarks.

The current level of agreement between the Standard Model prediction and the measured $\sin 2\beta$, excludes theories with contributions to the box diagram larger by 20% or more [146].

In theories with four quark generations, the measured amplitude $\sin 2\beta$ does not correspond to a simple phase of the CKM matrix. The quark-mass matrix, in this case, is a 4×4 unitary matrix of $SU(4)$, with 6 real angles and 3 complex phases [31]. The corresponding unitarity conditions are represented by *quadrangles* in the complex plane (Figure 2.18), and the relation between the observed CP asymmetry and the complex phases is not trivial.

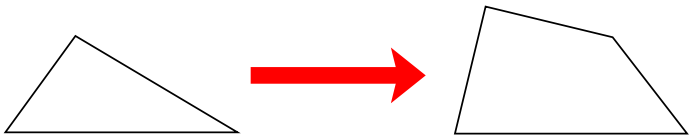

Figure 2.18: The unitarity conditions for theories with 3 and 4 quark generations.

Quark process	Leading term	Secondary term	B^0 decay modes
$b \to c\bar{c}s$	$V_{cb}V_{cs}^* = A\lambda^2$	$V_{ub}V_{us}^* = A\lambda^4(\rho - i\eta)$	$J/\psi\ K_S^0$, $\psi(2S)\ K_S^0$, $\chi_{c1}\ K_S^0$,
	$T + (P^c - P^t)$	$P^u - P^t$	$\eta_c\ K_S^0$, $J/\psi\ K_L^0$, $J/\psi\ K^{*0}$
$b \to s\bar{s}s$	$V_{cb}V_{cs}^* = A\lambda^2$	$V_{ub}V_{us}^* = A\lambda^4(\rho - i\eta)$	ϕK_S^0
	$P^c - P^t$	$P^u - P^t$	
$b \to c\bar{c}d$	$V_{cb}V_{cd}^* = -\lambda^3$	$V_{tb}V_{td}^* = A\lambda^3(1 - \rho + i\eta)$	$D^{*+}D^{*-}$
	$T + (P^c - P^u)$	$P^t - P^u$	$D^{*+}\ D^-$, $D^+\ D^-$

Table 2.3: Contributions to decay amplitudes related to angle β.

Quark process	Leading term	Secondary term	B^0 decay modes
$b \to u\bar{u}d$	$V_{ub}V_{ud}^* = A\lambda^3(\rho - i\eta)$	$V_{tb}V_{td}^* = A\lambda^3(1 - \rho + i\eta)$	$\pi^+\,\pi^-$, $\pi^0\,\pi^0$, $\pi\rho$
$b \to d\bar{d}d$	$T + (P^u - P^c)$	$P^t - P^c$	πa_1

Table 2.4: Contributions to decay amplitudes related to angle α.

Quark process	Leading term	Secondary term	B^0 decay modes
$b \to c\bar{u}s$	$V_{cb}V_{us}^* = A\lambda^3$	—	D^0K, $\overline{D}^0K$
$b \to u\bar{c}s$	$V_{ub}V_{cs}^* = -A\lambda^4(\rho - i\eta)$	—	common modes
$b \to c\bar{u}d$	$V_{cb}V_{ud}^* = A\lambda^2$	—	$D^0\pi^0$, $\overline{D}^0\pi^0$
$b \to u\bar{c}d$	$V_{ub}V_{cd}^* = -A\lambda^4(\rho - i\eta)$	—	common modes

Table 2.5: The decay modes, and their amplitudes, that can be used to measure the angle γ.

Chapter 3

Overview of analysis technique

Measurement of $\sin 2\beta$ requires several experimental ingredients that are described in Chapters 4–8. This Chapter provides a concise description of the analysis strategy, aimed at facilitating then reader through the more detailed discussion that follows.

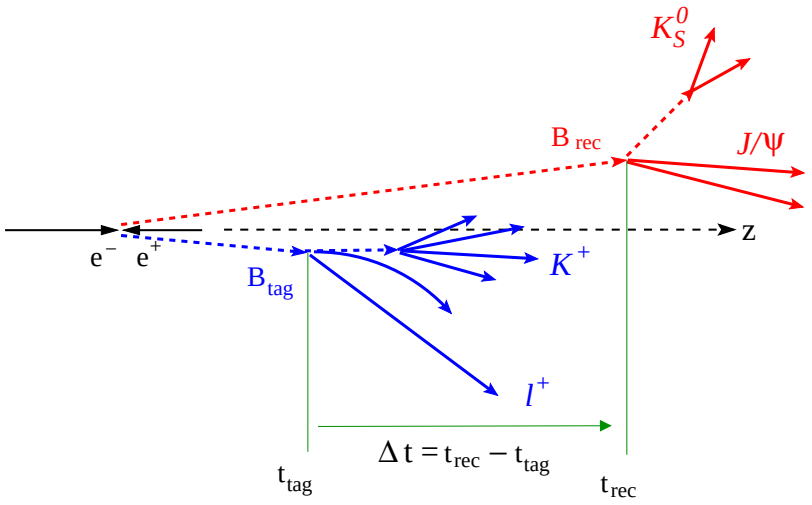

Figure 3.1: The decay $\Upsilon(4S) \rightarrow B^0\overline{B}^0$ where one B decays to a CP eigenstate, $B_{\rm CP}$, and the other B in a flavor eigenstate, $B_{\rm tag}$.

The theoretical framework of CP violation was discussed in Chapter 2 and it was pointed out that the decays of the B mesons provide an excellent experimental tool to study CP-violating effects. In particular the amplitude $\sin 2\beta$ of the time-dependent CP asymmetry (2.98)

$$a_{CP}(\Delta t) = -\eta_f \sin 2\beta \sin \Delta m_d \Delta t$$

can be measured with good precision in the decays $B^0 \to J/\psi\, K^0_S, \psi(2S) K^0_S, \chi_{c1} K^0_S$, and $\eta_c K^0_S$, with almost no theoretical assumption. Unfortunately, these decays occur in about 10^{-4} of all B decays and therefore it is necessary to produce a large number of B mesons, in order to have sufficient statistics for the CP analysis.

B mesons are, for example, produced in the decays of the $\Upsilon(4S)$ meson, which decays exclusively to a $B^0\ \overline{B}^0$ or a $B^+\ B^-$ pair. The PEP-II collider is a high luminosity e^+e^- storage ring operating at the $\Upsilon(4S)$ resonance energy, and has produced about 200 million B mesons between 1999 and 2002. About 2000 of these mesons have been reconstructed in the $B^0 \to J/\psi\, K^0_S, \psi(2S) K^0_S, \chi_{c1} K^0_S$, and $\eta_c K^0_S$ decay modes.

Measurement of $\sin 2\beta$ requires knowledge of the time difference Δt that appears in a_{CP}. This is the time interval between the decays of the two B mesons, and provides the **clock** for the time-dependent measurements in the $\Upsilon(4S)$ decays. The value of Δt can be computed from the spatial separation between the decay vertices of the B mesons.

In the $\Upsilon(4S)$ rest frame, the B mesons are separated in average by $30\,\mu\mathrm{m}$. Measurement of such a small distance with good precision is technologically challenging. This problem is solved at PEP-II by using asymmetric beam energies. The $\Upsilon(4S)$ is produced by colliding a $9\,\mathrm{GeV}$ electron beam with a $3.1\,\mathrm{GeV}$ positron beam, and has a Lorentz boost $\beta\gamma = 0.55$. As a consequence, the average separation between the two B mesons is about $250\,\mu\mathrm{m}$ along the collision axis in the laboratory frame and can be measured with a precision sufficient for a time-dependent analysis.

Figure 3.1 illustrates schematically the topology of a $\Upsilon(4S)$ decay at PEP-II used for the time-dependent CP analysis. One B meson (B_{rec}) is fully reconstructed in CP eigenstates, e.g. $J/\psi\, K^0_S$. The decay vertex of this meson is computed from its decay products and is known with a precision of about $50\,\mu\mathrm{m}$.

The remaining particles in the event belong to the other B meson (B_{tag}), and are utilized to determine its decay vertex. Since the efficiency for fully reconstructing B mesons is of the order $\mathcal{O}(10^{-3})$, an inclusive method is used to compute the second decay vertex, with a precision of about $110\,\mu\mathrm{m}$. The distance between the two vertices is then computed with a resolution of about $190\,\mu\mathrm{m}$.

The next step toward the measurement of asymmetry $a_{CP}(\Delta t)$ is to determine whether B_{rec} is a B^0 or a $\overline{B}^0$. Clearly this can not be deduced from a CP eigenstates, such as $J/\psi\ K^0_S$, accessible to both B^0 and $\overline{B}^0$ mesons. Instead, the quantum coherence in the decay of the $\Upsilon(4S)$, described in Section 2.4.3, requires B_{rec} to be a B^0 ($\overline{B}^0$) if B_{tag} is a $\overline{B}^0$ (B^0) at the time of its decay.

The flavor of B_{tag} is correlated with the charge of leptons and kaons produced in its decay chain. It can be determined by analyzing the kinematic properties and particle identification information

of reconstructed particles in the final state. The procedure of separating B^0 and $\overline{B}^0$ mesons, on the basis of their decay products, is commonly called b-flavor tagging, or simply flavor tagging. If determined, the flavor of $B_{\rm tag}$ allows to separate B^0 and $\overline{B}^0$ mesons that decay to CP eigenstates.

In a fraction w of events, the flavor-tagging procedure, being an inclusive method, assigns the wrong flavor tag to $B_{\rm tag}$. This fraction can be estimated with simulated events. However, it is always better not to rely on Monte Carlo and use data, if possible. Fortunately, decays of B mesons to flavor eigenstates can be used to measure w in data.

When $B_{\rm rec}$ is reconstructed in a flavor eigenstate, for example $D^{*-}\ \pi^+$, its flavor is known: $D^{*-}\ \pi^+$ indicates a B^0, and $D^{*+}\ \pi^-$ a $\overline{B}^0$. The flavor of $B_{\rm tag}$ is also known, from the flavor-tagging method. Therefore, events in which $B_{\rm rec}$ is fully reconstructed in flavor eigenstates can be divided in **mixed**, when there is a $B^0\ B^0$ or a $\overline{B}^0\ \overline{B}^0$ pair, and **unmixed** when there is one B^0 and one $\overline{B}^0$.

The number of mixed and unmixed events can be computed as a function of Δt from Equations (2.57) and (2.58). When $B_{\rm tag}$ is assigned the wrong flavor, a mixed event is wrongly classified as unmixed, and vice versa. The comparison between the estimated and observed numbers of mixed and unmixed events allows the measurement of w in data.

The branching fractions of flavor eigenstates are about an order of magnitude larger than those for the CP eigenstates. The large sample of events with one fully reconstructed flavor eigenstate allows a good measurement of the performance of the flavor-tagging algorithm. Furthermore, it is used to measure the detector resolution on Δt.

The CP asymmetry amplitude $\sin 2\beta$ is measured with a simultaneous maximum-likelihood fit to the Δt distributions of selected events in CP and flavor eigenstates. The value of $\sin 2\beta$ is constrained by the CP eigenstates, while the flavor eigenstates dominate the measurement of detector resolution and flavor-tagging parameters.

The ingredients of the $\sin 2\beta$ measurement, briefly summarized in this Chapter, are described in more detail in the remainder of this thesis. Particular attention is paid to those areas where the author has actively participated.

The main characteristics of the PEP-II collider are described in Chapter 4 followed by a brief description of the *BABAR* detector.

At the $\Upsilon(4S)$ energy, about 1/4 of produced events are $\Upsilon(4S)$ decays while the rest are continuum $q\bar{q}$ and QED events. Selection of $B\bar{B}$ events based on characteristic properties of each category of events is described in Section 5.1.

The variety of flavor and CP eigenstates utilized in this analysis are summarized in Section 5.2, followed by the selection of their decay products in Section 5.3, and the exclusive B reconstruction

technique in Section 5.4.

The B-flavor tagging algorithm is described in Chapter 6, where the characteristic signatures in B decays that allow the separation between B^0 and $\overline{B}^0$ mesons are discussed.

Reconstruction of B decay vertices, measurement of Δt and the Δt resolution function used to model the detector response are described in Chapter 7.

Finally, Chapter 8 describes the maximum-likelihood fit to the Δt distributions and the modeling of signal and background.

Chapter 4

The *BABAR* experiment

The primary goal in the design of the *BABAR* experiment is the study of CP violation in the decays of neutral B mesons. Decays of the $\Upsilon(4S)$ resonance exclusively to $B^0\ \overline{B}^0$ and $B^+\ B^-$ pairs provide a clean source of B mesons [67].

Measurement of time-dependent CP asymmetries requires the knowledge of the difference Δt between the times of decay of the two B mesons, which can be computed from the distance between their decay vertices.

Due to the $\Upsilon(4S)$ mass of $10.58\,\mathrm{GeV}/c^2$, these decays result in the production of two B mesons almost at rest in the $\Upsilon(4S)$ rest frame, illustrated schematically in Figure 4.1. At e^+e^- colliders with symmetric energies, such as CESR and DORIS II, the $\Upsilon(4S)$ rest frame coincides with the laboratory frame. The small momentum of the B mesons results in a small separation between them, which can not be measured with the necessary precision. This prevented experiments at these colliders from performing time-dependent measurements.

This problem is solved at PEP-II by colliding e^- and e^+ beams with unequal energies, so as to produce the $\Upsilon(4S)$ meson, and therefore the B mesons, with significant momenta in the laboratory frame, as shown in Figure 4.2. The Lorentz boost of the B mesons results in a displacement between their decay vertices, and thus allows the measurement of the distance between them.

The small branching fractions of B^0 decays to final CP eigenstates, of the order of 10^{-4} or smaller, require an e^+e^- collider with very high luminosity, and a detector with high efficiency of reconstructing these final states.

The main characteristics of the PEP-II collider that impact the study of the CP asymmetries are summarized in Section 4.1. A detailed description of the PEP-II collider can be found in References [68, 69]. A brief overview of the components of the *BABAR* detector and their performance is

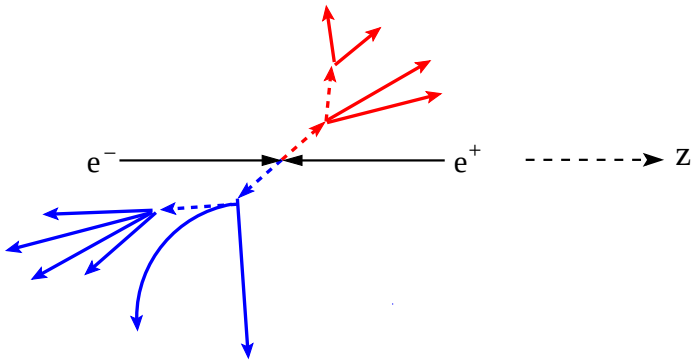

Figure 4.1: The $\Upsilon(4S) \rightarrow B\bar{B}$ decay in the $\Upsilon(4S)$ rest frame.

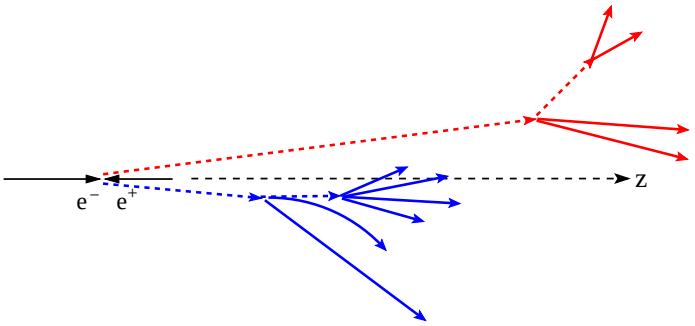

Figure 4.2: The $\Upsilon(4S) \rightarrow B\bar{B}$ decay in the laboratory frame.

given in Section 4.3, while a detailed description of *BABAR* can be found in Reference [70].

4.1 The asymmetric e^+e^- collider PEP-II

PEP-II is an asymmetric e^+e^- storage ring located at the Stanford Linear Accelerator Center (SLAC) and operating at a center-of-mass energy of 10.580 GeV, the mass of the $\Upsilon(4S)$ resonance. The structure of the Υ resonances are shown in Figure 4.3 [71]. $\Upsilon(4S)$ mesons are produced boosted in the laboratory frame, with $\beta\gamma = 0.55$, by colliding an electron beam of $9.0\,\mathrm{GeV}$ with a positron beam of $3.1\,\mathrm{GeV}$.

Most of the data are recorded near the peak of the $\Upsilon(4S)$ resonance (*on-resonance* data). Figure 4.4 shows the production cross section near the $\Upsilon(4S)$ resonance. The cross section for the main physics processes at the $\Upsilon(4S)$ energy are listed in Table 4.1 [46].

Events with production of $B\bar{B}$ pairs are of interest for the study of CP violation. Events with the production of a $q\bar{q}$ pair, with $q = u, d, s, c$, are commonly referred to as *continuum* events, and

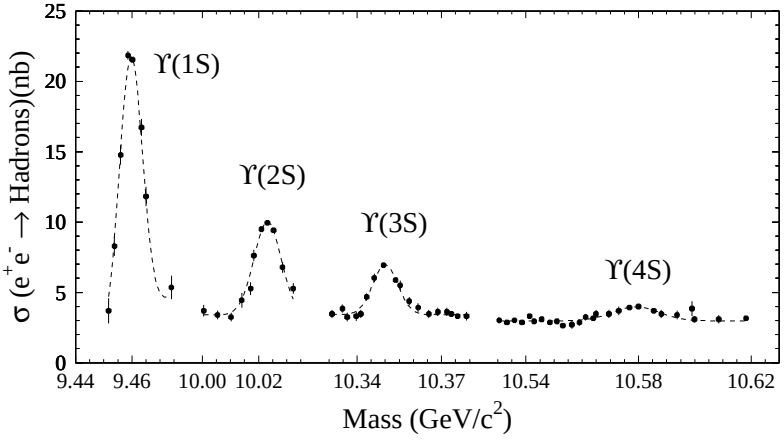

Figure 4.3: Structure of the Υ resonances. The mass of the $\Upsilon(4S)$ is above the threshold of $B\bar{B}$ production.

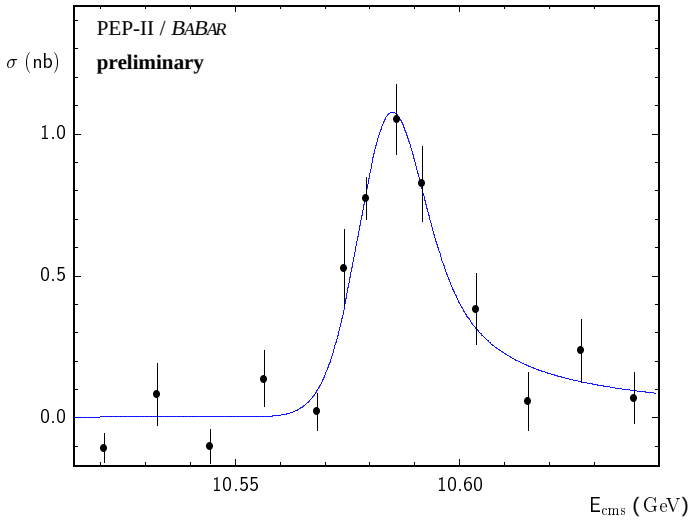

Figure 4.4: Cross section of $B\bar{B}$ production near the $\Upsilon(4S)$ energy.

represent the majority of combinatorial background for the charmless two-body decays of the B meson, such as $B^0 \to \pi^+\pi^-$. In order to study the properties of these events almost 12% of data are taken at a center-of-mass energy $40\,\mathrm{MeV}$ below the $\Upsilon(4S)$ peak (*off-resonance* data), below the energy threshold of $B\bar{B}$ production.

The QED processes $e^+e^- \to e^+e^-, \mu^+\mu^-, \tau^+\tau^-$ are mostly used to study and calibrate the detector subsystems. Therefore only a small fraction of these events is selected by the trigger system, designed to maximize the number of hadronic events ($B\bar{B}$ and continuum $q\bar{q}$).

$e^+e^- \to X$	Cross-section (nb)
$b\bar{b}$	1.05
$c\bar{c}$	1.30
$s\bar{s}$	0.35
$u\bar{u}$	1.39
$d\bar{d}$	0.35
$\tau^+\tau^-$	0.94
$\mu^+\mu^-$	1.16
e^+e^-	~ 40

Table 4.1: Production cross-sections at $\sqrt{s} = 10.58$ GeV. The e^+e^- cross section includes the detector acceptance.

The parameters of the storage rings, including the energy and the current, the number of bunches and their separation, the vertical and horizontal RMS size of the luminous region, and the luminosity are listed in Table 4.2 [70]. PEP-II has surpassed its design goals in terms of both the instantaneous and integrated daily luminosity, with significantly fewer bunches than anticipated.

At PEP-II, the bunches collide head-on and are separated magnetically in the horizontal plane by a pair of dipole magnets (B1), followed by a series of offset quadrupoles. The collision axis is offset from the z-axis of the *BABAR* detector by about $20\,\mathrm{mrad}$ in the horizontal plane to minimize the perturbation of the beams by the solenoid field [72].

The PEP-II beam parameters directly impact the physics performance of *BABAR*. The high luminosity of PEP-II is necessary to compensate the small branching fractions of the decay modes used in the analysis of CP violation. The relative luminosity is monitored by PEP-II through the measurement of the radiative Bhabha scattering. The absolute luminosity is measured by *BABAR*, offline, from other QED processes, primarily e^+e^- and $\mu^+\mu^-$ production. For a data sample of 1 fb, the relative luminosity is known with a statistical uncertainty of less than $1\,\%$ and a systematic uncertainty of $0.5\,\%$. The absolute luminosity has an estimated systematic error of about $1.5\,\%$.

Knowledge of the beam energies is necessary to compute two important kinematic variables, used to select B meson candidates and reject combinatorial background. The mean energies of the two beams are computed from the total magnetic bending strength, and the average deviations of the accelerating frequencies from their central values. While the systematic uncertainty in the PEP-II calculation of the absolute beam energies is estimated to be 5–10 MeV, the relative energy setting

Parameters	Design	Typical
Energy HER/LER (GeV)	9.0/3.1	9.0/3.1
Current HER/LER (A)	0.75/2.15	0.7/1.3
# of bunches	1658	553–829
Bunch spacing (ns)	4.2	6.3–10.5
σ_{Lx} (μm)	110	120
σ_{Ly} (μm)	3.3	5.6
σ_{Lz} (mm)	9	9
Luminosity ($10^{33}\,\mathrm{cm}^{-2}\mathrm{s}^{-1}$)	3	2.5
Luminosity (pb^{-1}/d)	135	120

Table 4.2: The design and typical values of the PEP-II beam parameters, during the period of 1999–2000. HER and LER refer to the high energy e^- and low energy e^+ ring, respectively. σ_{Lx}, σ_{Ly}, and σ_{Lz} are the horizontal, vertical, and longitudinal RMS size of the luminous region.

for each beam is accurate and stable to about $1\,\mathrm{MeV}$. The RMS energy spreads of the LER and HER beams are $2.3\,\mathrm{MeV}$ and $5.5\,\mathrm{MeV}$, respectively.

Finally, the parameters of the luminous region impact the measurement of the distance between the B-meson decay vertices. Events with two tracks such as $e^+e^- \to \mu^+\mu^-$ are used to determine these parameters relative to the *BABAR* coordinate system.

The transverse position, size, and angles of the luminous region are determined from the distribution of the distance of closest approach to the z-axis of the two tracks in these events.

The longitudinal parameters are derived from the longitudinal distribution of the the common vertex of the two tracks. The uncertainties in the average beam position are of the order of a few μm in the transverse plane and $100\,\mu\mathrm{m}$ along the collision axis. Since the vertical size is too small to be measured directly, it is inferred from the measured luminosity, the horizontal size, and the beam currents an is typically around 1–2 μm.

4.2 Total integrated luminosity

The integrated luminosity delivered by PEP-II and recorded with *BABAR* between October 1999 and June 2002 is shown in Figure 4.5. The total luminosity recorded by *BABAR* is about $99\,\mathrm{fb}^{-1}$, including $9.93\,\mathrm{fb}^{-1}$ of off-peak data [73]. About $82\,\mathrm{fb}^{-1}$ of on-resonance data, corresponding to 88 million $B\bar{B}$ pairs, are used in the analysis presented in this thesis.

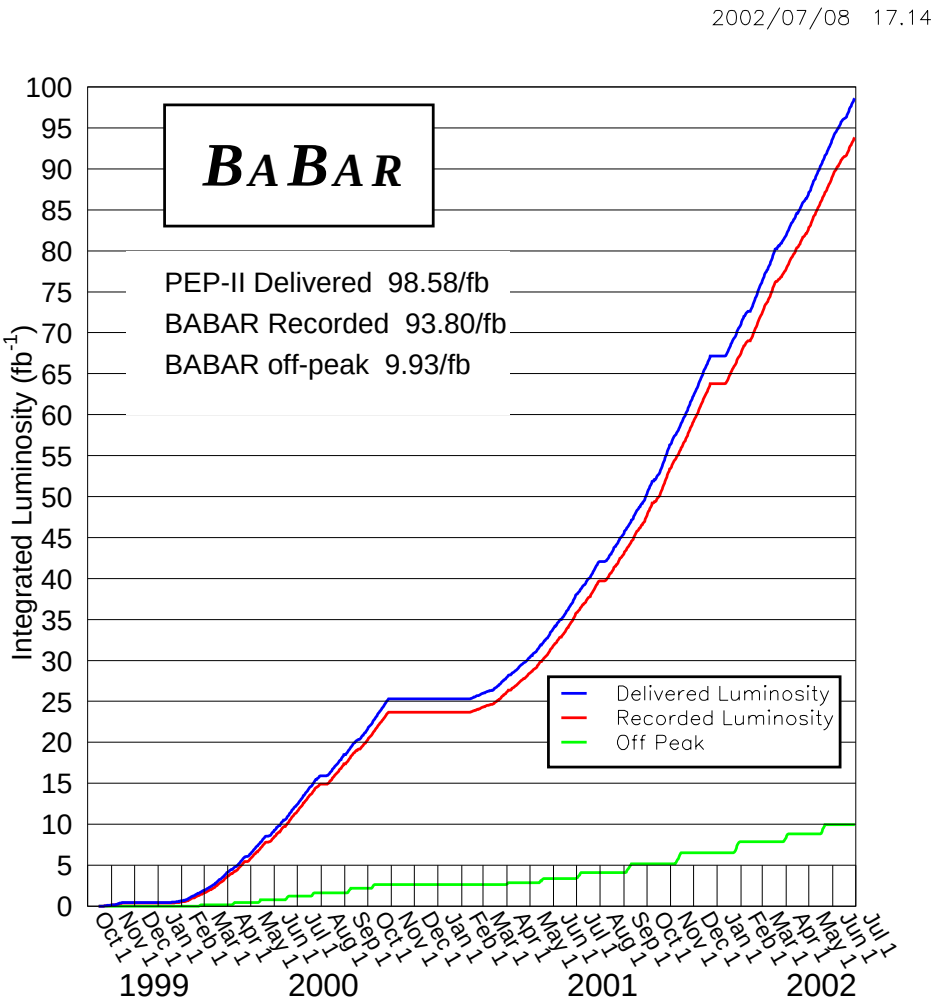

Figure 4.5: The integrated luminosity delivered by PEP-II and recorded by *BABAR* between October 1999 and June 2002.

4.3 The *BABAR* detector

The time-dependent study of CP violation in the B decays places stringent requirements on the *BABAR* detector. High reconstruction efficiency and good momentum resolution for charged particles, together with reconstruction of the neutral particles, are important ingredients to fully reconstruct the final CP eigenstates, and to separate signal events from background.

The measurement of the decay-time distributions relies on good vertex reconstruction along the collision axis and in the transverse plane.

The determination of the flavor of the B mesons requires efficient particle identification for muons, electrons, and kaons with low misidentification probability. Kaon identification also provides an additional tool to further reduce the amount of backgrounds in the decays of the B to hadronic final states.

A detailed description of the *BABAR* detector is given in Reference [70]. In this section the main characteristics of each subsystem are briefly described, with special attention for the subsystems relevant for this analysis.

Figure 4.6 shows a longitudinal section of *BABAR* through the detector center. The detector

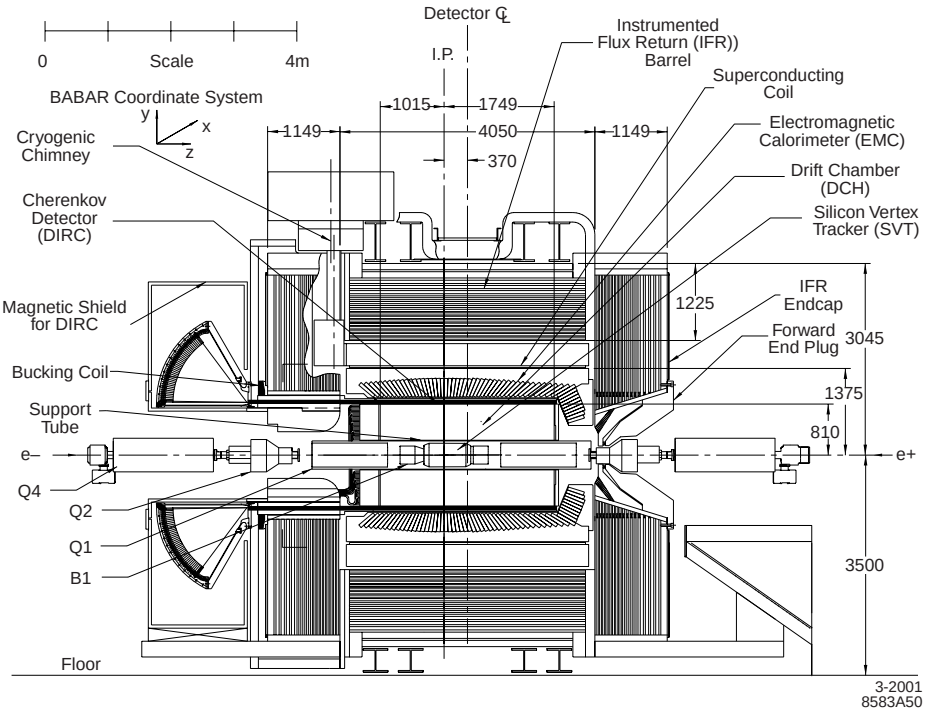

Figure 4.6: Longitudinal section of the *BABAR* detector.

surrounds the PEP-II interaction region and is offset relative to the interaction point by 0.37m to

maximize the geometric acceptance of particles in the final states, which, due to the $\Upsilon(4S)$ boost, are mostly in the forward region.

The inner detector consists of a silicon vertex tracker, a drift chamber, a ring-imaging Cerenkov detector, and a CsI calorimeter. These detector systems are surrounded by a superconducting solenoid that is designed for a field of 1.5 T. The steel flux return is instrumented for muon and neutral hadron detection. The polar angle coverage extends to $350\,\mathrm{mrad}$ in the forward direction and $400\,\mathrm{mrad}$ in the backward direction, defined relative to the high energy beam.

The right handed coordinate system is anchored on the main tracking system, the drift chamber, with the z-axis coinciding with its principal axis [74]. This axis is offset relative to the beam axis by about $20\,\mathrm{mrad}$. The positive y-axis points upward and the positive x-axis points away from the center of the PEP-II storage rings.

4.3.1 Silicon vertex tracker (SVT)

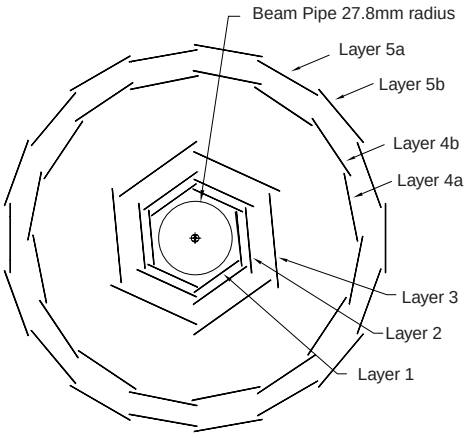

Figure 4.7: Schematic view of the transverse section of the silicon vertex tracker.

The silicon vertex tracker (SVT) has been designed to measure angles and positions of charged particles just outside the beam pipe. The SVT is composed of five layers of double-sided silicon strip detectors (Figure 4.7) that are assembled from modules with readout at each end, thus reducing the inactive material in the acceptance volume.

The inner three layers primarily provide position and angle information for the measurement of the vertex position. They are mounted as close to the water-cooled beryllium beam pipe as practical (radius of $3.2\,\mathrm{cm}$), thus minimizing the impact of multiple scattering in the beam pipe on the extrapolation to the vertex.

The outer two layers are at much larger radii ($9.1\,\mathrm{cm}$), providing the coordinate and angle measurements needed for linking tracks reconstructed in the SVT with those in the drift chamber.

4.3.2 Drift chamber (DCH)

The principal purpose of the drift chamber (DCH) is the momentum measurement for charged particles. It also provides information for the charged-particle trigger, and a measurement of energy loss $\mathrm{d}E/\mathrm{d}x$ for particle identification.

The DCH is of compact design. It consists of 7104 small and approximately hexagonal cells (Figure 4.8) arranged in 40 cylindrical layers.

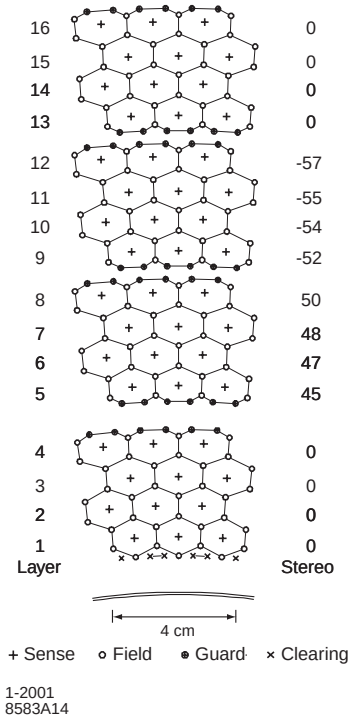

Figure 4.8: Schematic layout of drift cells for the four innermost superlayers. Lines have been added between field wires to aid in visualization of the cell boundaries. The numbers on the right side give the stereo angles (mrad) of sense wires in each layer. The $1\,\mathrm{mm}$-thick beryllium inner wall is shown inside of the first layer.

Each cell consists of one tungsten-rhenium sense wire, surrounded by six aluminum field wires. The field wires are at ground potential, while a positive high voltage ($1960\mathrm{V}$ and $1900\mathrm{V}$ in the period 1999–2002, and $1930\mathrm{V}$ in year 2002) is applied to the sense wires.

The sense wires parallel to the principal axis (*axial* layers) provide curvature information which is used to determine the momentum of the particles.

Longitudinal information about the trajectory of the charged particles is derived from layers in which the sense wires are placed at a small *stereo* angle relative to the principal axis (*stereo* layers).

The DCH is filled with a 80:20 mixture of helium and isobutane. The choice of gas mixture and wire material holds the multiple scattering in the chamber to a minimum, less than 0.2% of material radiation length X_0 [75].

The readout electronics are mounted on the backward endplate of the chamber, minimizing the amount of material in front of the calorimeter endcap.

4.3.3 Detector of internally reflected Cerenkov light (DIRC)

The DIRC, the detector of internally reflected Cerenkov light, is a novel device providing separation of pions and kaons from about $500\,\mathrm{MeV}/c$ to the kinematic limit of $4.5\,\mathrm{GeV}/c$. Cerenkov light is produced in $4.9\,\mathrm{m}$ long bars of synthetic fused silica of rectangular cross section, $1.7\,\mathrm{cm} \times 3.5\,\mathrm{cm}$. It is transported by total internal reflection, preserving the angle of emission, to an array of photomultiplier tubes (Figure 4.9). This array forms the backward wall of a toroidal water

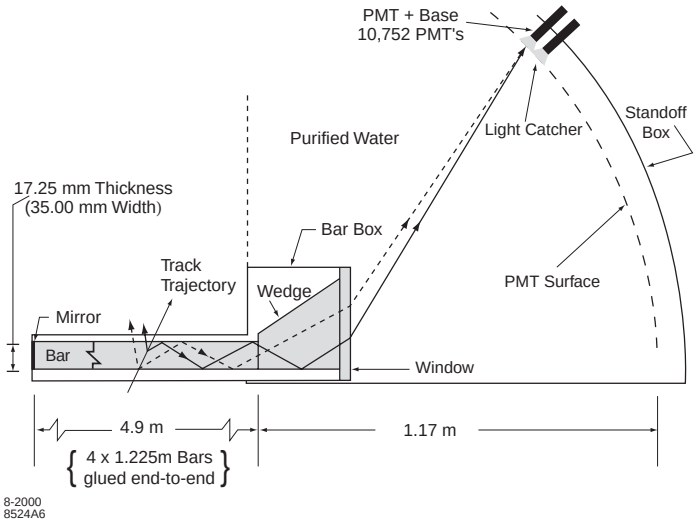

Figure 4.9: Schematics of the DIRC fused silica radiator bar and imaging region.

tank that is located beyond the backward end of the magnet. Images of the Cerenkov rings are reconstructed from the position and time of arrival of the signals in the photomultiplier tubes.

4.3.4 Electromagnetic calorimeter (EMC)

The electromagnetic calorimeter (EMC) is designed to detect electromagnetic showers with excellent energy and angular resolution, for energies between $20\,\mathrm{MeV}$ to $4\,\mathrm{GeV}$.

This coverage allows the detection of low energy π^0s and η^0s from B decays, and higher energy photons and electrons from electromagnetic, weak, and radiative processes.

The EMC is a finely segmented array of projective geometry, made of thallium doped cesium iodide (CsI(Tl)) crystals. The crystals are arranged in modules that are supported individually from an external support structure. This structure is built in two sections, a barrel and a forward endcap. To obtain the desired resolution, the amount of material in front of and in-between the crystals is held to a minimum.

The individual crystals are read out by pairs of silicon PIN diodes. Low noise analog circuits, and frequent precise calibration of the electronics and energy response over the full dynamic range, are crucial for maintaining the desired performance.

4.3.5 Instrumented flux return (IFR)

The instrumented flux return (IFR) is designed to identify muons and to detect neutral hadrons.

For this purpose, the magnet flux return steel in the barrel and the two end doors is segmented into layers, increasing in thickness from $2\,\mathrm{cm}$ on the inside to $10\,\mathrm{cm}$ at the outside. Between these steel absorbers, single gap resistive plate chambers (RPCs) are inserted which detect streamers from ionizing particles via external capacitive readout strips.

There are 19 layers of RPCs in the barrel sectors and 18 layers in the end doors. Two additional cylindrical layers of RPCs with four readout planes are placed just in front of the magnet cryostat to detect particles exiting the EMC.

4.3.6 Trigger

The trigger system is designed to select events of interest with a high, stable, and well-understood efficiency, while rejecting background events and keeping the total event rate under 120 Hz. Interesting events include $B\bar{B}$ and other $q\bar{q}$ events, as well as QED events needed for diagnostic and calibration purposes.

The production rates of these events for a luminosity of $3 \times 10^{33}\ \mathrm{cm}^{-2}\ \mathrm{s}^{-1}$ at the $\Upsilon(4S)$ resonance are shown in Table 4.3. Background events are due to interactions of beams with the residual gas or the beam pipe with typical rates up to 20 kHz.

Event type	Cross section (nb)	Production Rate (Hz)	Level 1 Trigger Rate (Hz)
$B\bar{B}$	1.1	3.2	3.2
$u\overline{u}$ +$d\overline{d}$ +$c\overline{c}$ +$s\overline{s}$	3.4	10.2	10.1
e^+e^-	$\sim$53	159	156
$\mu^+\mu^-$	1.2	3.5	3.1
$\tau^+\tau^-$	0.9	2.8	2.4

Table 4.3: Cross sections, production and trigger rates for the principal physics processes at 10.58 GeV for a luminosity of $3 \times 10^{33}\,\mathrm{cm}^{-2}\mathrm{s}^{-1}$. The e^+e^- cross section refers to events with either the e^+, e^-, or both inside the EMC detection volume.

The trigger is implemented as a two-level hierarchy, the *Level 1* (L1) in hardware, followed by the *Level 3* (L3) in software. It is designed to accommodate up to ten times the expected PEP-II background rates at design luminosity, and to degrade slowly for backgrounds above that level. Provision is made for an intermediate *Level 2* trigger should severe conditions require additional sophistication.

The L1 trigger is responsible for interpreting incoming detector signals, recognizing and removing beam-induced background to a level acceptable for the L3 software trigger, which runs on a farm of commercial processors. The L1 trigger decision is based on charged tracks in the DCH above a preset transverse momentum, showers in the EMC, and tracks detected in the IFR. During normal operation, the L1 is configured to have an output rate of typically 1 kHz.

The L3 receives the output from L1, performs a second stage rate reduction for the main physics sources, and identifies and flags the special categories of events needed for luminosity determination, diagnostic, and calibration purposes. At design luminosity, the L3 filter acceptance for physics is $\sim$ 90Hz, while $\sim$ 30Hz contain the other special event categories, with an average event size of $\sim$ 28 kbytes. Events selected by the L3 trigger are then stored for online processing.

Both L1 and L3 trigger systems have met the design requirement of 99% selection efficiency for $B\bar{B}$ events at a luminosity of $3 \times 10^{33}\ \mathrm{cm}^{-2}\ \mathrm{s}^{-1}$. They also provide solid foundation for an upgrade path to luminosities of $10^{34}\ \mathrm{cm}^{-2}\ \mathrm{s}^{-1}$.

4.4 Data acquisition system

The data acquisition system (DAQ) is responsible for the transport of the event data from the front-end electronics (FEE) of the detector, to the online event processing, through the trigger system. The components of the DAQ are schematically shown in Figure 4.10.

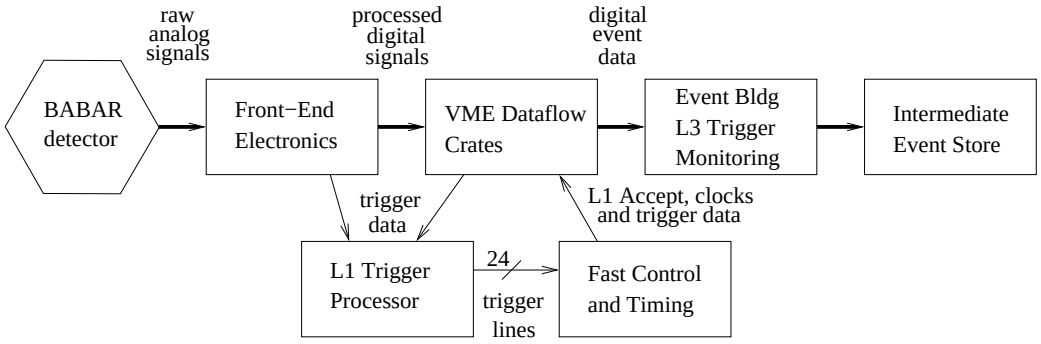

Figure 4.10: Schematic diagram of the data acquisition system.

All *BABAR* subsystems share a common electronics architecture. Event data flows through the FEE chain, which consists of signal processing, digitization, readout electronics, and a trigger latency buffer to store data during L1 trigger processing.

The FEE systems are mounted on the detector to optimize performance, and to minimize the cable plan, thereby avoiding noise pickup and ground loops in long signal cables.

At PEP-II, bunch crossings are nearly continuous at a 4.2 ns spacing. Dedicated L1 processors receive data continuously from the DCH, EMC, and IFR subsystems. These processors produce clocked outputs to the *fast control and timing system* (FCTS) [79] at a rate of 30 MHz, which is the granularity of the *L1 Accept* signal.

Upon the arrival of an *L1 Accept* signal, a portion of each system L1 latency buffer is read out, ranging from about $500\,\mathrm{ns}$ or the SVT, to $4-6\mu$s for the EMC. The processed digital signal is transfered via optical fiber links [76] from the FEE to a set of 133 specialized VME *readout modules* (ROMs).

These ROMs are grouped by detector subsystem and housed in 23 data acquisition VME crates, which contain between one and ten such ROMs. Each ROM consists of a processor [77] running the VxWorks [78] realtime operating system, and event buffers.

The online data flow (ODF) [80] connects, controls, and manages the flow of data in the acquisition hardware with little dead time, and is also in charge of building complete events from data transfered to the ROMs. Part of the ODF code is embedded in the processor of each ROM and is

used to process the data transfered from the FEE. ODF builds complete events by first collecting the data in each crate into an additional dedicated ROM, and then collecting the data from the 23 of these, and transferring them to the online farm, across an Ethernet network.

The online farm consists of 32 Sun workstations running the Solaris operating system. Each node runs the the online event processing (OEP) software [81], which provides a real-time framework within which complete events delivered from the ODF event builder are processed by the L3 trigger algorithms.

OEP performs also fast monitoring algorithms to provide real-time quality assurance of the data. Events selected by the L3 trigger algorithms in OEP are retained for subsequent full reconstruction, after merging the output of all OEP nodes, which is written to an intermediate storage.

The last step in the collection and processing of data is represented by the online prompt reconstruction (OPR), which bridges the online and offline systems [82, 83].

This system reads the raw data recorded on disk by OEP and, operating on a farm of 150 Unix processors, selects physics events and collects extensive monitoring data for quality assurance, and writes the output of the *BABAR* reconstruction program into an object oriented *event store* [84].

One important feature of OPR is the *rolling calibration*. This consists in the generation of reconstruction constants during event processing, which are then applied to the processing of subsequent data.

These constants are stored in a conditions database [85], also an object oriented database, and accessed by the analysis programs when reading the processed events from the event store.

4.4.1 Online detector control and run control

The online detector control (ODC) system controls and extensively monitors the electronics, the environment, and assures the safety of the detector. Its implementation is based on EPICS [86], providing detector-wide standardization for control and monitoring, diagnostics, and alarm handling. ODC also provides communication with PEP-II and the magnet control system.

The operator interacts with this part of the control system trough screens controlled by the EPICS display manager. Dedicated control and display panels are developed for each subsystem using common color codes to show the status of devices. A top-level panel summarizes the status of all subsystems. The operator is also provided with audible and color-coded alarms, and warnings for all detector components.

The online run control (ORC) system ties together the various components of the online system, and provides the user with a single graphical interface [88] to control the DAQ operations,

implemented as an application of SMI++ [87].

The DAQ system is modeled as a collection of objects behaving as a finite state machine. These objects represent both real entities, such as the ODF subsystem or the drift chamber, and abstract components, such as the *calibrator*, a supervisor program used during the detector calibration.

4.5 Reconstruction of charged particles

The charged particle tracking system is made of two components, the silicon vertex tracker and the drift chamber , and provides efficient detection of charged particles, and the measurement of their momentum with high precision.

Since the average momentum of charged particles produced in B decays is less than $1\,\mathrm{GeV}/c$, multiple scattering is a significant limitation on the track parameter resolution. Therefore, special care has been taken to reduce the volume and the amount of material in the tracking system as described in Section 4.3.2.

The SVT, with a typical single-hit resolution of 10 $\mu\mathrm{m}$, provides precise reconstruction of charged particle trajectory and decay vertices of B and D mesons near the interaction region. It also provides standalone tracking capability for charged particles with a transverse momentum p_t between 60 MeV/c and 120 MeV/c. The lower limit is due to the multiple scattering in the beam-pipe material, while the higher limit is the minimum that can be reconstructed reliably in the DCH alone.

The DCH contributes primarily to the p_t measurement and is also used to reconstruct decay and interaction vertices outside the SVT volume, for instance K^0_S decay.

The trajectory of charged particles is defined by five parameters [74] listed in Table 4.4.

Parameter	Description
ω	Curvature of the track defined as $\omega = 1/p_t$
d_0	Distance in the x–y plane between POCA and the origin
z_0	Distance along the z axis between POCA and the origin
ϕ_0	Azimuth angle of POCA
$\tan\lambda$	Dip angle of the track relative to the transverse plane

Table 4.4: Parameters defining the trajectory of a charged track. *POCA* is the point of closest approach of the trajectory from the z axis.

Charged track finding starts with pattern recognition in the DCH, based on three different algorithms [89]. The first uses the same fast algorithm employed by the L3 trigger, for finding and linking superlayer-based track segments from moderate-to-high p_T tracks, originating from the interaction point.

Two subsequent track finders then work on superlayer segments not already attached to a reconstructed track. They are designed to find tracks with lower p_T, passing through fewer than the full ten superlayers of the chamber, or originating away from the interaction point.

At the end of this process, all tracks are refit with a Kalman-filter fitter [90] that takes into account the detailed distribution of material in the detector, and the non-uniformities in the detector magnetic field.

These tracks are then projected into the SVT, and silicon-strip hits are added, if they are consistent within the extrapolation errors, through the intervening material and field. A search is performed for tracks that are reconstructed with the remaining unused silicon clusters, again with two different algorithms.

At the end of the SVT-only track finding, an attempt is made to match SVT- and DCH-only track segments, which may result when a hard scatter occurs in the support tube material between the two devices.

The resolution on the track parameters are determined with two different methods from cosmic rays and hadronic events [91, 92]. The two methods give similar results and are in agreement with the expectations. The measured resolutions depend on the transverse momentum p_t of the tracks.

Using cosmic ray tracks with $p_t = 3\,\mathrm{GeV}/c$, the resolutions on d_0 and z_0 are measured to be

$$\sigma_{d_0} = 23\,\mu\mathrm{m} \qquad \sigma_{\phi_0} = 0.43\,\mathrm{mrad}$$
$$\sigma_{z_0} = 29\,\mu\mathrm{m} \qquad \sigma_{\tan\lambda} = 0.53 \cdot 10^{-3}$$

Figure 4.11 shows the the dependence of d_0 and z_0 resolutions on the transverse momentum p_t, measured with tracks from hadronic events.

Figure 4.12 shows the resolution on the transverse momentum p_t measured with cosmic muons. The data are well represented by a linear function,

$$\sigma_{p_t}/p_t = (0.13 \pm 0.01)\% \cdot p_t + (0.45 \pm 0.03)\%,$$

with p_t is measured in GeV/c.

For a track with p_t of 1 GeV/c the resolution is about 5 MeV/c. These values for the resolution parameters are very close to the design expectations.

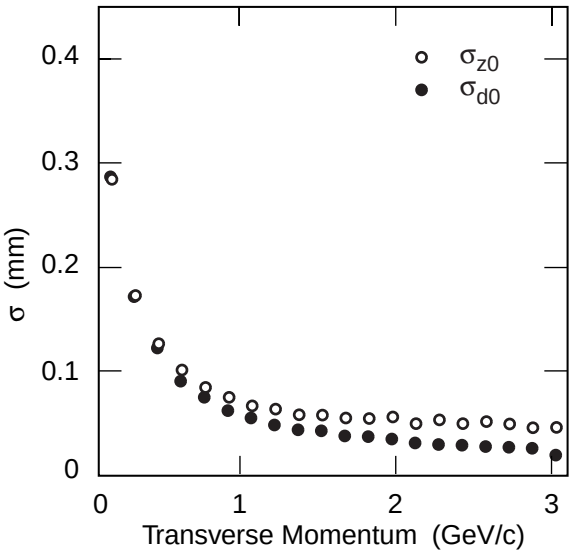

Figure 4.11: Resolution on impact parameters d_0 and z_0 for tracks in hadronic events, as a function of the transverse momentum p_t.

4.5.1 Selection of charged tracks

Several quality requirements are applied to the charged tracks reconstructed in the tracking system to define *lists* of tracks for analysis purposes [93]. The lists are hierarchical: starting from a list including all reconstructed charged tracks, tighter requirements are applied to define good quality tracks.

1. **`ChargedTracks`**: All tracks reconstructed in the drift chamber and/or the silicon vertex tracker with the pion hypothesis.

2. **`GoodTracksVeryLoose`**: Subset of `ChargedTracks` with additional requirements:

   - center-of-mass momentum p^* less than $10\,\mathrm{GeV}/c$, and
   - distance from the nominal beamspot less than $1.5\,\mathrm{cm}$ in the transverse x-y plane, and less than $10\,\mathrm{cm}$ along the z axis.

3. **`GoodTracksLoose`**: Subset of `GoodTracksVeryLoose` that satisfy the following requirements:

   - transverse momentum p_t greater than $100\,\mathrm{MeV}/c$, and
   - at least 12 hits in the drift chamber.

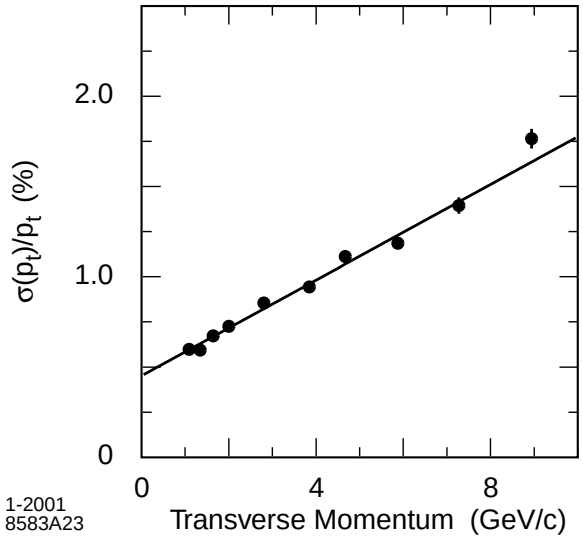

Figure 4.12: Resolution on the transverse momentum p_T, measured with cosmic muons traversing the DCH and the SVT.

4. **`GoodTracksAccLoose`**: Subset of `GoodTrackLoose` tracks within the *fiducial volume* of the tracking system defined as $0.41 < \theta_{\rm LAB} < 2.54\,{\rm rad}$, where $\theta_{\rm LAB}$ is the polar angle in the laboratory frame.

5. **`GoodTracksTight`**: Subset of `GoodTracksLoose` with:

   - at least 20 hits in the drift chamber, and
   - distance from the nominal beamspot less than $1\,{\rm cm}$ in the transverse x-y plane, and less than $3\,{\rm cm}$ along the z axis.

4.6 Reconstruction of neutral particles

The electromagnetic calorimeter (EMC) is used to measure electromagnetic showers produced from π^0 and η decays, and from electrons and photons in QED and radiative processes.

A typical electromagnetic shower spreads over many adjacent crystals, forming a *cluster* of energy deposits. Pattern recognition algorithms have been developed to efficiently identify these clusters, and to differentiate single clusters, with one energy maximum, from merged clusters, with more than one local energy maximum, referred to as *bumps*. Local maxima occur, for example, when photons from high-energy π^0 decays are unresolved, resulting in several showers are in close

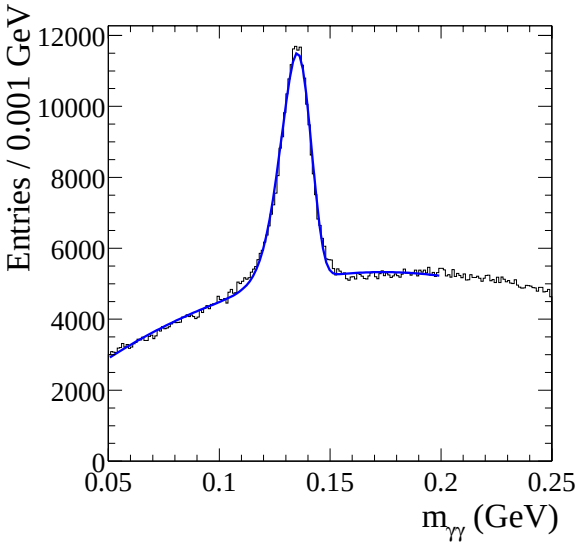

Figure 4.13: Invariant mass of two photons in $B\bar{B}$ events. The energies of the photons and the π^0 are required to exceed 30 MeV and 300 MeV, respectively. The solid line is a fit to the data. The signal Gaussian component has a width of 7 MeV.

proximity. Furthermore, the algorithms determine whether a bump is generated by a charged or a neutral particle.

Clusters are formed around initial seed crystals, containing at least 10 MeV of deposited energy. Neighboring crystals are added to the cluster, if their energy exceeds 1 MeV. If the newly added crystal has energy greater than 3 MeV, its contiguous neighbors (including corners) are also considered for inclusion in the cluster.

Local maxima within a cluster are defined as candidate crystals that have an energy exceeding each of its neighbors, by a fraction that depends on the number of crystals in the local neighborhood. Clusters are then divided into as many bumps as there are local maxima.

The division is based on a two-dimensional weighting scheme that assumes electromagnetic shower shapes to divide up the cluster energy. The position of each bump is calculated with a center-of-gravity method, with logarithmic weighting of crystal energies [94].

A bump is associated with a charged particle by projecting a track to the inner face of the calorimeter. The distance between the track impact point and the bump centroid is calculated, and compared to the Monte Carlo expectation for different particle species, based on the measured track parameters. If the distance is consistent with the expectation, the bump is associated with this charged particle. Otherwise, it is assumed to originate from a photon.

The energy resolution of the calorimeter is measured at low energies directly with a radioactive

source under ideal low-background conditions, while at high energies, it is derived from Bhabha scattering.

For energies below 2 GeV, the mass resolution of π^0 and η mesons (Figure 4.13), decaying into two photons of approximately equal energies, is used to determine the energy resolution [95].

A fit to the energy dependence yields

$$\frac{\sigma_E}{E} = \frac{(2.32 \pm 0.30)\%}{\sqrt[4]{E(\,\mathrm{GeV})}} \oplus (1.85 \pm 0.12)\%. \tag{4.1}$$

The energy-dependent term arises primarily from the fluctuations in photon statistics. The constant term, dominant at energy greater than 1 GeV, is due to non-uniformity in light collection, leakage or absorption in the material between and in front of the crystals, and uncertainties in the calibrations.

4.6.1 Selection of neutral particles

The neutral particles reconstructed in the electromagnetic calorimeter are organized in hierarchical lists, similar to charged tracks, on the basis of the following quality requirements:

1. **`CalorNeutral`**: All energy bumps in the electromagnetic calorimeter not associated with any charged track.

2. **`GoodNeutralLooseAcc`**: Subset of `CalorNeutral` with additional requirements:

   - energy E greater than $30\,\mathrm{MeV}/c$,
   - lateral shaper parameter λ_{LAT} [96] less than 1.1, and
   - within the *fiducial volume* of the EMC defined as $0.41 < \theta_{\mathrm{LAB}} < 2.409\,\mathrm{rad}$, where θ_{LAB} is the polar angle in the laboratory frame.

3. **`GoodPhotonLoose`**: Subset of `CalorNeutral` with additional requirements:

   - energy E greater than $30\,\mathrm{MeV}/c$, and
   - lateral shaper parameter λ_{LAT} [96] less than 0.8.

4. **`GoodPhotonDefault`**: Subset of `GoodPhotonDefault` with minimum energy of $100\,\mathrm{MeV}/c$.

4.7 Particle identification

Identification of electrons, muons and kaons is an essential ingredient in the determination of the flavor of B mesons as described in Chapter 6.

The charge of energetic leptons from semileptonic decays is correlated to the quark content of the decaying B meson.

The number and charge of kaons in the final state are used to determine the B flavor, through the decay chain $b \to c \to s$.

Kaon identification is also used to reduce combinatorial background in the reconstruction of B meson candidates, that decay to final states with many charged particles.

4.7.1 Kaon identification

Kaons are distinguished from pions and protons on the basis of specific energy-loss measurements $\mathrm{d}E/\mathrm{d}x$ in SVT and DCH, and the number of Cerenkov photons and the Cerenkov angle in the DIRC [97, 98].

The momenta of the kaons used for flavor tagging extend up to about $2\,\mathrm{GeV}/c$, with most of them below $1\,\mathrm{GeV}/c$, since they are produced in the secondary decays of charm mesons. Kaons and pions originated in the rare two-body decays of the B have momenta between 1.7 and $4.2\,\mathrm{GeV}/c$.

The difference between the measured truncated-mean $\mathrm{d}E/\mathrm{d}x$ in the DCH, and the expected mean for the pion, kaon, and proton hypotheses, with typical resolution of 7.5%, is used to compute likelihoods $\mathcal{L}_\pi$, $\mathcal{L}_K$ and $\mathcal{L}_p$, assuming Gaussian distributions. The distribution of the measured $\mathrm{d}E/\mathrm{d}x$ in the DCH for selected control samples, as a function of momentum, is shown in Figure 4.14.

The difference between the measured 60% truncated-mean $\mathrm{d}E/\mathrm{d}x$ in the SVT and the expected $\mathrm{d}E/\mathrm{d}x$ is described by an asymmetric Gaussian distribution. For minimum-ionizing particles, the resolution on the SVT truncated mean is about 14% which allows a 2σ separation between pions and kaons up to momentum of $500\,\mathrm{GeV}/c$, and between kaons and protons beyond $1\,\mathrm{GeV}/c$.

The DIRC provides π/K separation of $\sim 4\sigma$ or greater, for all tracks from B-meson decays, with momenta from the pion Cerenkov threshold, up to $4.2\,\mathrm{GeV}/c$.

In the DIRC, a likelihood is obtained for each particle hypothesis from the product of two components: the expected number N_γ of Cerenkov photons, with a Poisson distribution, and the difference between the measured average Cerenkov angle θ_c (Figure 4.15) and the expected angle θ_c^0, for a given mass hypothesis, assuming a Gaussian distribution.

Loose kaon identification is used in exclusive B reconstruction, while the b-flavor tagging is based on tighter criteria.

The `NotAPion` kaon selection is defined by combining individual likelihoods from SVT and DCH for momenta below $0.5\,\mathrm{GeV}/c$, from DCH only for momenta between 0.5 and $0.6\,\mathrm{GeV}/c$,

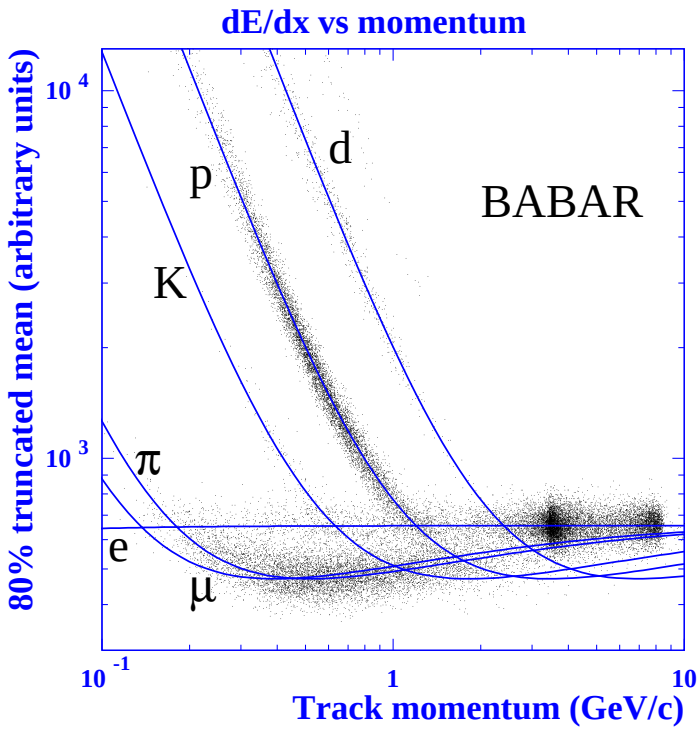

Figure 4.14: Measurement of $\mathrm{d}E/\mathrm{d}x$ in the DCH as a function of track momenta. The data include large samples of beam background triggers, evident from the high rate of protons. The curves show the Bethe-Bloch predictions derived from selected control samples of particles of different masses.

and from DIRC only for momenta above $0.6\,\mathrm{GeV}/c$. Kaon candidates are rejected if the likelihood ratios satisfy $\mathcal{L}_K/\mathcal{L}_\pi < r$ and $\mathcal{L}_K/\mathcal{L}_p < r$, where $r = 0.1$ for $p < 0.5\,\mathrm{GeV}/c$ and $r = 1$ for $p \geq 0.5\,\mathrm{GeV}/c$. Tracks with no particle information are assumed to be kaons.

The `NotAPion` kaon requirement has a nearly constant kaon-identification efficiency of about 96%, and a pion-misidentification probability of not larger than 30%, for tracks in the transverse momentum between 1 and $2.5\,\mathrm{GeV}/c$.

Tighter kaon selections require $\mathcal{L}_K/\mathcal{L}_\pi > r$, with r typically greater than one. For loose pion selection, candidates are rejected if they satisfy tighter kaon or lepton criteria.

4.7.2 Electron identification

The most important variable for the discrimination of hadrons is the ratio of the shower energy to the track momentum (E/p). Electrons are separated from charged hadrons primarily on the basis of their deposited energy, lateral and azimuthal shape of the shower in the EMC [96, 99], and track

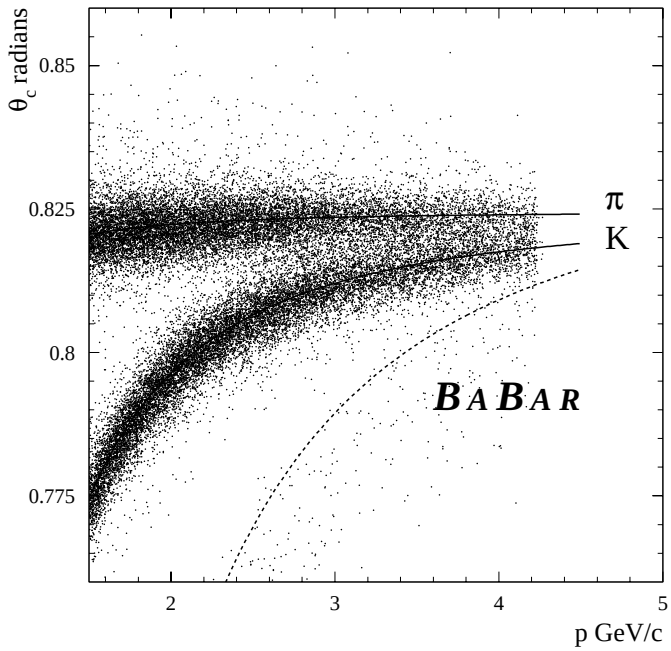

Figure 4.15: Distribution of the measured Cerenkov angle $\theta_{\rm c}$ in a control sample of $D^0 \to K^-\pi^+$ decays.

momentum. In addition, the $\mathrm{d}E/\mathrm{d}x$ energy loss in the DCH, and the Cerenkov angle in the DIRC, are required to be consistent with the electron hypothesis [100].

Four different categories of electron candidates (`VeryLoose`, `Loose`, `Tight`, and `VeryTight`) are defined with the criteria listed in Table 4.5. For each category the difference between the measured mean $\mathrm{d}E/\mathrm{d}x$ and the expectation for an electron must lie within an interval defined in terms of the expected $\mathrm{d}E/\mathrm{d}x$ resolution σ. Candidates that are not matched to an EMC bump are retained as `noCal` electron candidates if their measured $\mathrm{d}E/\mathrm{d}x$ satisfies the same requirements as the `VeryTight` selection.

Electron identification efficiencies in the momentum range $0.5 < p < 3.0\,\mathrm{GeV}/c$ vary between 88% and 98% for the criteria in Table 4.5. The pion misidentification rates are below 0.3% for the `VeryTight` selection.

4.7.3 Muon Identification

Muon candidates are primarily identified by the measured number of hadronic interaction lengths n_λ, traversed from the outside radius of the DCH through the IFR iron, and the difference Δn_λ, be-

Category	$\mathrm{d}E/\mathrm{d}x$ Interval	E/p	Additional requirements
`VeryLoose`	$[-3\sigma, 7\sigma]$	> 0.50	–
`Loose`	$[-3\sigma, 7\sigma]$	> 0.65	–
`Tight`	$[-3\sigma, 7\sigma]$	$[0.75, 1.3]$	Lateral shower shape
`VeryTight`	$[-2.2\sigma, 4\sigma]$	$[0.89, 1.2]$	Azimuthal shower shape; consistency of DIRC Cerenkov angle (3σ)

Table 4.5: Electron identification criteria.

tween n_λ and the predicted penetration depth for a muon of the same momentum and angle [101].

Contamination from hadronic showers is rejected by a combination of the average number $\overline{n}_{hits}$ and the variance $\sigma_{n_{hits}}$ of hits per RPC layer, the χ^2 for the geometric match between the track extrapolation into the IFR and the RPC hits, χ^2_{trk}, and the χ^2 of a polynomial fit to the RPC hits, χ^2_{fit}. In addition, for those muons within the acceptance of the EMC, the the energy E of the bump in the calorimeter must be consistent with a minimum ionizing particle.

In the forward region, which suffers from some machine background, additional requirements are made on the fraction of RPC layers with hits.

Four different categories of muon candidates (`VeryLoose`, `Loose`, `Tight`, and `VeryTight`) are selected with the criteria listed in Table 4.6.

Muon identification efficiencies in the momentum range $1.1 < p < 3.0\,\mathrm{GeV}/c$ vary between 60% to 92% for the criteria in Table 4.6, while pion-misidentification rates are about 3% for the `Tight` selection.

Category	n_λ	Δn_λ	$\overline{n}_{hits}$	$\sigma_{n_{hits}}$	χ^2_{trk}/n_{layers}	χ^2_{fit}/n_{layers}	E_{EMC} [GeV]
`VeryLoose`	> 2.0	< 2.5	< 10	< 6	–	–	< 0.5
`Loose`	> 2.0	< 2.0	< 10	< 6	< 7	< 4	< 0.5
`Tight`	> 2.2	< 1.0	< 8	< 4	< 5	< 3	[0.05, 0.4]
`VeryTight`	> 2.2	< 0.8	< 8	< 4	< 5	< 3	[0.05, 0.4]

Table 4.6: Muon identification criteria. The variables are defined in the text.

Chapter 5

Exclusive reconstruction of B mesons

The measurement of CP violation requires a large sample of fully reconstructed B mesons in CP and flavor eigenstates. Due to their heavy mass, B mesons decay to many channels with branching fractions of the order $\mathcal{O}(10^{-2})$ or smaller. It is, therefore, necessary to reconstruct B mesons in a relatively large number of final states containing charmed, light, and charmonium mesons.

The first step in the reconstruction process is the selection of $B\bar{B}$ events, which is described in Section 5.1. The CP and flavor eigenstates utilized in this analysis are summarized in Section 5.2. The selection criteria for the intermediate states in the decay chains are described in Section 5.3.

Exclusive reconstruction of B mesons is described in Section 5.4, where the two important kinematic variables, energy difference Δt and the energy-constrained mass $m_{\rm ES}$ are introduced.

The selection criteria for the CP and flavor eigenstates are summarized in Sections 5.5 and 5.6, respectively.

Reconstructed B^+ mesons represent a large and valuable control sample for time-dependent studies, as well for flavor-tagging validation. The selection criteria for this control sample are discussed in Section 5.7.

5.1 Event Selection

Production cross sections for the physics processes at the $\Upsilon(4S)$ energy were listed in Table 4.1. In addition to the $\Upsilon(4S) \rightarrow B\bar{B}$ decay, these processes include continuum $q\bar{q}$ and QED events such as $e^+e^- \rightarrow e^+e^-, \mu^+\mu^-, \tau^+\tau^-$, and $\gamma\gamma$.

The event topology is significantly different for each type of processes. Table 5.1 summarizes

the main characteristics of each process.

Event type	Main characteristics
$e^+e^- \to e^+e^-$	Two high-momentum back-to-back tracks, and associated energy deposit in the EMC
$e^+e^- \to \mu^+\mu^-$	Two high-momentum back-to-back tracks
$e^+e^- \to \tau^+\tau^-$	Back-to-back topology with large missing energy, due neutrinos from semileptonic τ decays
$e^+e^- \to \gamma\gamma$	Large missing energy, and small number of tracks due to preferential production of particles along the beam direction
$e^+e^- \to q\bar{q}$ with $q = u, d, s, c$	Large number of hadrons and jet-like topology, due to the hadronization of the quarks which are produced back-to-back.
$e^+e^- \to \Upsilon(4S) \to B\bar{B}$	Large number of hadrons and isotropic topology due to the B decays.

Table 5.1: Main characteristics of the physics processes at the $\Upsilon(4S)$ energy, in the center-of-mass frame.

The QED events are discriminated by selecting events with three **GoodTracksAccLoose** tracks (see Section 4.5.1) and a total visible energy greater than 4.5 GeV.

The visible energy $\mathcal{W}$ is defined as the sum over the energy of all **GoodTracksAccLoose** tracks and **GoodNeutralLooseAcc** neutral particles (see Section 4.6.1)

$$\mathcal{W} = \sum_{i}^{\texttt{GoodTracksAccLoose}} \sqrt{m_\pi^2 + p_i^2} + \sum_{j}^{\texttt{GoodNeutralLooseAcc}} E_j \qquad (5.1)$$

The distribution of the number of **GoodTracksAccLoose** tracks and the visible energy $\mathcal{W}$ are shown in Figures 5.1 and 5.2, respectively. The distributions are normalized to the same area,

hence only the shapes are meaningful. The above requirements remove, almost entirely, the QED events and select the hadronic $B\bar{B}$ and continuum $q\bar{q}$ events.

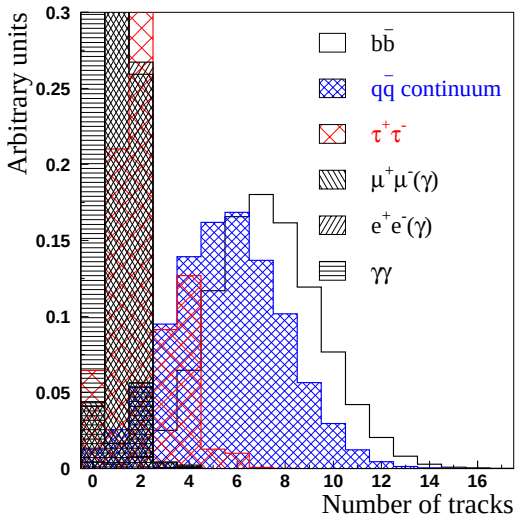

Figure 5.1: Distribution of the number of **`GoodTracksAccLoose`** tracks in the main physics processes at the $\Upsilon(4S)$ energy. The distributions are normalized to the same area.

For the the time-dependent CP analysis, only the $B\bar{B}$ events are needed. The normalized second Fox-Wolfram moment [102] R_2 is used to reduce background from continuum $u\bar{u}$, $d\bar{d}$, $s\bar{s}$, and $c\bar{c}$ events.

The $\ell^{\rm th}$ Fox-Wolfram moment $\mathcal{H}_\ell$ is the momentum-weighted sum of Legendre polynomial of $\ell^{\rm th}$ order, computed from the cosine of the angle between all pairs of tracks. Each $\mathcal{H}_\ell$ is basically a multipole moment of the momentum distribution in an event. The $\mathcal{H}_0$ moment is the analog of the electric charge distribution. The first moment $\mathcal{H}_1$ is zero because the momentum is not a signed quantity (unlike the electric charge) and therefore can not have a dipole moment. The quadrupole moment $\mathcal{H}_2$ can instead discriminate events with a jet-like structure of momentum ($q\bar{q}$ events) from those with a more spherically symmetric topology ($B\bar{B}$ events).

The normalized ratio $R_2 = \mathcal{H}_2/\mathcal{H}_0$ is therefore very close to unity for events with back-to-back tracks such as QED events, and approaches 0 for isotropic events like $B\bar{B}$ events. The distribution of R_2 for the physics processes at the $\Upsilon(4S)$ energy is shown in Figure 5.3. The value of R_2 is computed with the **`GoodTracksAccLoose`** charged tracks and the **`GoodNeutralLooseAcc`** neutral particles.

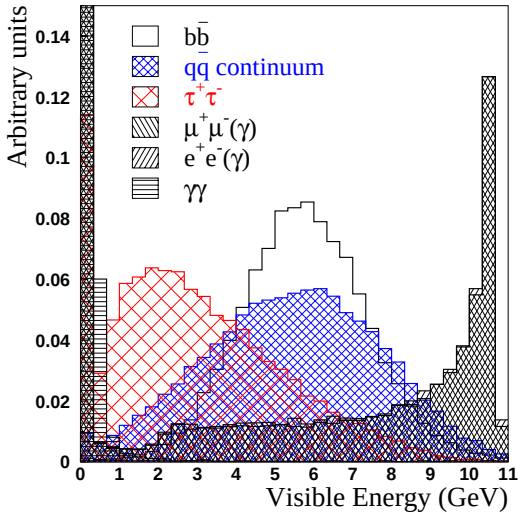

Figure 5.2: Distribution of the visible energy $\mathcal{W}$ in the main physics processes at the $\Upsilon(4S)$ energy. The distributions are normalized to the same area.

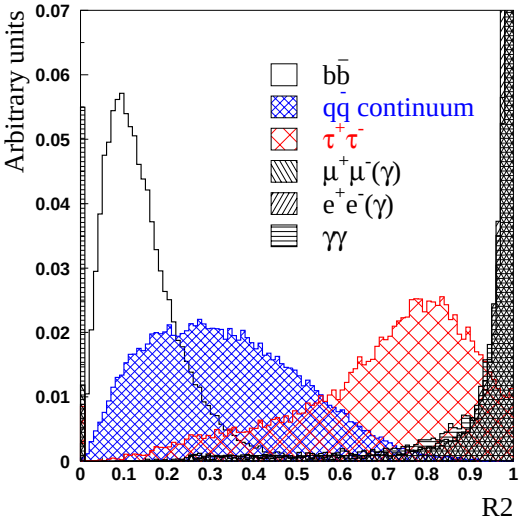

Figure 5.3: Distribution of R_2 for the main physics processes at the $\Upsilon(4S)$ energy. The distributions are normalized to the same area.

5.2 Reconstructed B decay modes

The CP and flavor eigenstates of the B meson which are fully reconstructed for this analysis are summarized in Table 5.2. The branching fractions for these modes [33] are also included in the same Table.

Decay mode	Branching fraction (%)
CP eigenstates ($B_{\rm CP}$ sample)	
$B^0 \to J/\psi\ K^0$	$(8.7 \pm 0.05) \times 10^{-2}$
$B^0 \to \psi(2S)\ K^0$	$(5.7 \pm 1.0) \times 10^{-2}$
$B^0 \to \chi_{c1}\ K^0$	$(4.0^{+1.2}_{-1.0}) \times 10^{-2}$
$B^0 \to \eta_c\ K^0$	$0.11^{+0.06}_{-0.05}$
Flavor eigenstates ($B_{\rm flav}$ sample)	
$B^0 \to D^{*-}\ \pi^+$	0.28 ± 0.02
$B^0 \to D^{*-}\ \rho^+$	0.73 ± 0.15
$B^0 \to D^{*-}\ a_1^+$	1.30 ± 0.27
$B^0 \to D^-\ \pi^+$	0.30 ± 0.04
$B^0 \to D^-\ \rho^+$	0.78 ± 0.14
$B^0 \to D^-\ a_1^+$	0.60 ± 0.33
$B^0 \to J/\psi\ K^{*0}$	0.13 ± 0.01
B^+ control sample	
$B^+ \to \overline{D}^{*0}\ \pi^+$	0.46 ± 0.04
$B^+ \to \overline{D}^0\ \pi^+$	0.53 ± 0.05

Table 5.2: Fully reconstructed CP and flavor eigenstates, and their branching fractions. The CP eigenstates are color suppressed, hence their branching fractions are smaller by at least an order of magnitude.

Figure 5.4 shows the full decay chain for the $B^0 \to D^{*-}\pi^+$ mode. The B reconstruction proceeds in the reverse order: first, charged tracks are combined to select $\overline{D}^0$ candidates; these candidates are then combined with the remaining charged tracks to identify the D^{*-} candidates; finally, B candidates are formed from combinations of D^{*-} candidates and remaining charged particles in the event. The next Section describes the selection criteria for the intermediate states. Charge conjugation is implied throughout this Section unless explicitly specified.

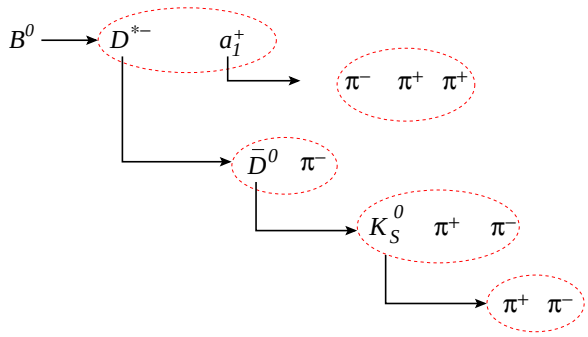

Figure 5.4: The full decay chain $B^0 \rightarrow D^{*-}a_1^+$, followed by $D^{*-} \rightarrow \overline{D}^0\pi^-$, $\overline{D}^0 \rightarrow K_S^0\pi^+\pi^-$ and $a_1^+ \rightarrow \pi^+\pi^-\pi^+$.

5.3 Reconstruction of decay daughters

Intermediate states in the decays of B mesons are selected from combinations of charged tracks and neutral particles, which are selected according to the criteria described in Sections 4.5.1 and 4.6.1.

Vertex and kinematic fitting techniques are applied to improve the resolution on the measured momentum of reconstructed mesons and further reduce contributions from combinatorial background. A general description of these techniques and their benefits is beyond the scope of this thesis. A comprehensive discussion of the kinematic- and vertex-fitting techniques can be found in a series of lectures by Paul Avery [103].

5.3.1 $\pi^0 \rightarrow \gamma\gamma$

The π^0 meson decays to a pair of photons in 98.8% of the time. Two **`GoodPhotonLoose`** photon candidates (see Section 4.6.1) are combined to form π^0 candidates.

Photon pairs with invariant mass within $\pm 20\,\mathrm{MeV}/c^2$ of the nominal π^0 mass ($135\,\mathrm{MeV}/c^2$ [33]), and a minimum energy of $200\,\mathrm{MeV}$ are selected. The invariant mass $m(\gamma\gamma)$ for these candidates is shown in Figure 5.5.

Selected candidates are subjected to a kinematic fit, with the the $\gamma\gamma$ invariant mass constrained to be the nominal π^0 mass (mass constraint). The mass constraint improves the energy resolution of the selected π^0 candidates.

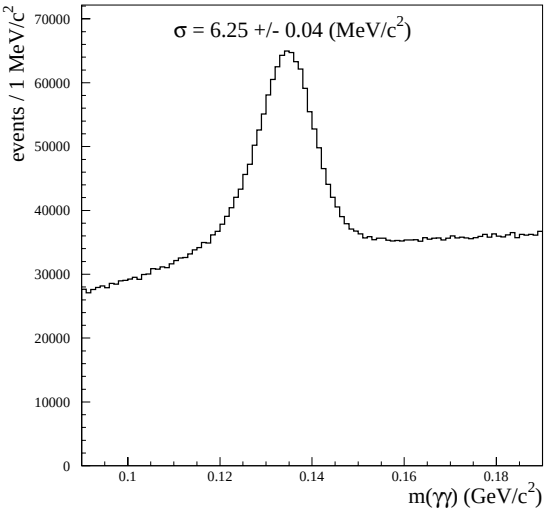

Figure 5.5: Invariant mass $m(\gamma\gamma)$ for selected π^0 candidates with $E_{\pi^0} > 200\,\mathrm{MeV}$.

5.3.2 $K^0_S \to \pi^+\pi^-$, $\pi^0\pi^0$

The K^0_S candidates are reconstructed in decay modes $\pi^+\,\pi^-$ and $\pi^0\,\pi^0$, which have a branching fraction of, respectively, 68.6% and 31.4% [33].

Candidates in the $\pi^0\,\pi^0$ mode are only used in the selection of *CP* eigenstates ($B_{\rm CP}$ sample) while the candidates in the $\pi^+\,\pi^-$ mode are used for both *CP* and flavor eigenstates ($B_{\rm flav}$ sample). The selection criteria are slightly different for $B_{\rm CP}$ and $B_{\rm flav}$ samples.

In the $\pi^+\pi^-$ mode, a pair of oppositely-charged **`GoodTracksLoose`** tracks (see Section 4.5.1) are required to originate from a common point (vertex fit). The invariant mass $m(\pi^+\pi^-)$ for these candidates is shown in Figure 5.6. Candidates with invariant mass $m(\pi^+\pi^-)$ between 462 and $534\,\mathrm{MeV}/c^2$ are selected. In addition, the probability for the tracks to have a common vertex (vertex χ^2 probability) must be greater than 0.1%. The distribution of the probability $P(\chi^2)$ for the selected candidates is shown in Figure 5.7. Candidates satisfying these requirements are used to reconstruct flavor eigenstates.

Additional requirements aimed at increasing the precision on $\sin 2\beta$ are applied for those candidates used in the $B_{\rm CP}$ sample [104]:

- angle α between the flight direction and the momentum vector of the K^0_S candidate (see Figure 5.8) is required to be smaller than $200\,\mathrm{mrad}$;

- the transverse flight distance ℓ_{xy} from the primary vertex in the event must be greater than

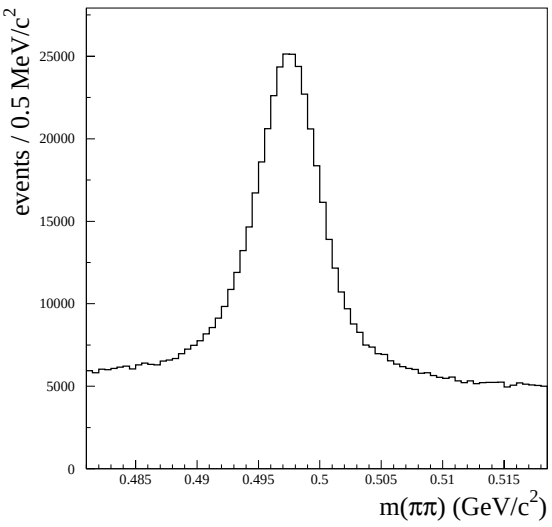

Figure 5.6: Invariant mass $m(\pi^+\pi^-)$ for selected $K^0_S \to \pi^+\pi^-$ candidates.

$2\,\mathrm{mm}$, while the three-dimensional distance $r_{3\mathrm{D}}$ from the vertex of the charmonium meson is required to be greater than $1\,\mathrm{mm}$; and

- the invariant mass must lie between 489 and $507\,\mathrm{MeV}/c^2$.

Pairs of π^0 candidates, each in the mass range 100–155 MeV/c^2, corresponding to -5σ and $+3\sigma$ of π^0 mass resolution, are combined to construct $K^0_S \to \pi^0\pi^0$ candidates. The π^0 candidates are assumed to originate at the interaction point. The K^0_S candidate must have energy greater than $800\,\mathrm{MeV}$ and invariant mass between 300 and 700 MeV/c^2.

The most probable K^0_S decay point is determined along the path defined by the initial K^0_S momentum vector and the charmonium meson vertex by maximizing the product of probabilities for the daughter π^0 mass-constrained fits (see Figure 5.9). The K^0_S invariant mass is re-evaluated at the measured decay point and must lie between 470 and 536 MeV/c^2.

5.3.3 ρ^+, a_1^+, and K^* mesons

The ρ^+ meson has a mass of 767 MeV/c^2 and a Breit-Wigner width of 150 MeV/c^2 [33]. The ρ^+ candidates are formed from combinations of one **`GoodTrackLoose`** track and a π^0 candidate with energy E_{π^0} greater than 300 MeV/c^2. Candidates with invariant mass within $\pm 150\,\mathrm{MeV}/c^2$ of the nominal ρ^+ mass are selected.

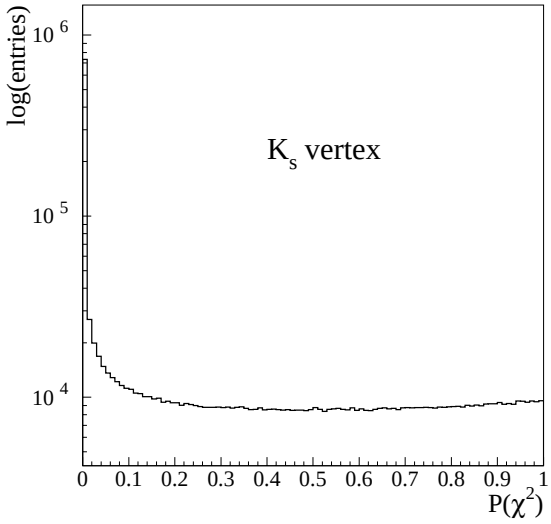

Figure 5.7: Distribution of the vertex probability $P(\chi^2)$ for selected $K^0_S \to \pi^+\pi^-$ candidates.

Candidates in the $a_1^+ \to \pi^+\pi^-\pi^+$ decay are selected from combinations of three **GoodTracksLoose** tracks with invariant mass in the range of 1.0 to 1.6 GeV/c^2. The mass of the a_1^+ meson is 1230 MeV/c^2 and the Breit-Wigner width is between 250 and 600 MeV/c^2 [33]. The combinatorial background for combinations of three charged tracks is relatively high. The random combinations are reduced by requiring the three tracks to have a common decay vertex with a probability greater than 0.1%.

K^{*0} mesons have a mass of 892 MeV/c^2 and a width of about 50 MeV/c^2, and decay almost entirely to final states $K^+\,\pi^-$ and $K^0_S\,\pi^0$ [33]. The K^{*+} has similar properties and is selected in the final states $K^0_S\,\pi^+$ and $K^+\,\pi^0$.

The **GoodTracksLoose** tracks are used as pion and kaon candidates in decay modes $K^+\,\pi^-$ and $K^+\,\pi^0$. Only the K^0_S candidates in the $\pi^+\,\pi^-$ mode are used in the final states $K^0_S\,\pi^0$ and $K^0_S\,\pi^+$. Combinations with invariant mass within 10 MeV/c^2 from the nominal K^* mass are selected.

Since the K^* is a vector meson with J=1, the conservation of angular momentum requires the particles in the final state to have orbital angular momentum L=1 and L_z=$\pm$1. As a consequence, angle θ_K, measured in the K^* rest frame, between the kaon momentum and the K^* direction, measured in the B frame, has a $\sin^2\theta$ distribution, while the background is distributed uniformly. The distribution of θ_K is therefore used to suppress combinatorial background in final states containing a π^0. The requirement $|\cos\theta_K| < 0.95$ rejects 5% of the random combinations.

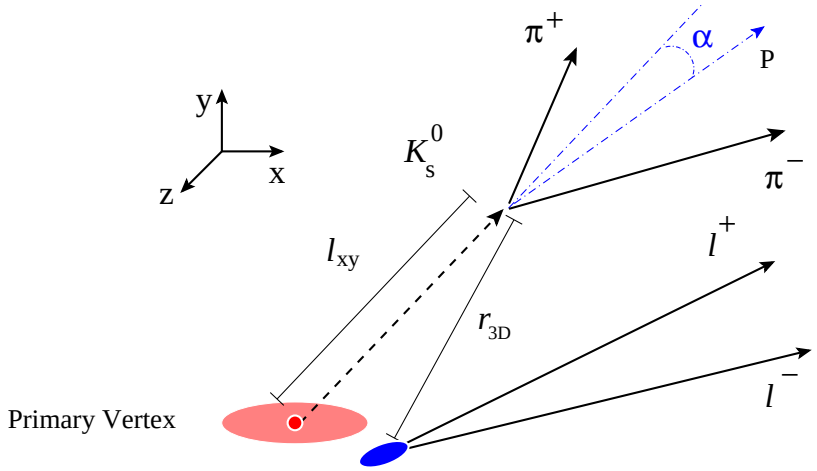

Figure 5.8: Flight length ℓ_{xy}, angle α between the flight direction and the momentum of the K^0_S candidates, and the three-dimensional distance r_{3D} between the K^0_S and the charmonium vertices.

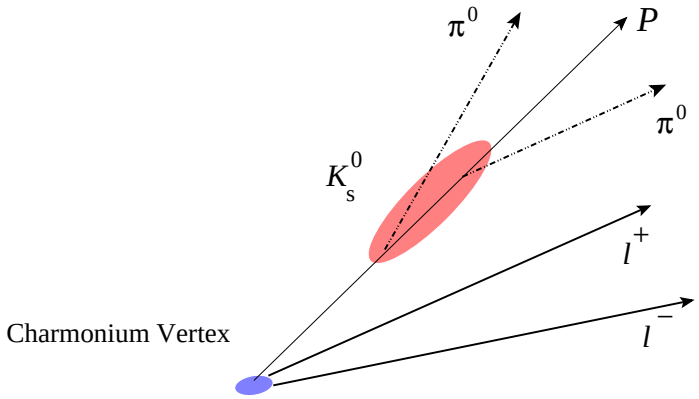

Figure 5.9: The decay vertex of $K^0_S \to \pi^0\pi^0$ candidates is constrained to be along the path defined by the K^0_S momentum P and the charmonium decay vertex.

5.3.4 Charmed mesons

$\overline{D}^0$ and D^-

The decay modes of the charmed $\overline{D}^0$ and D^- mesons, reconstructed in this analysis, are listed in Table 5.3. Candidates in these modes are formed by combining **`GoodTracksLoose`** tracks with π^0 and K^0_S candidates (only in the π^+ π^- mode). For each combination, the normalized mass variable $z \equiv (m_{\rm inv} - m_0)/\sigma_m$ must be less than 3. Here, m_0 is the nominal D mass, $m_{\rm inv}$ is the invariant mass of the candidate, and σ_m is its uncertainty computed from the measured error

Meson	Mass (MeV/c^2)	Decay mode	Branching fraction (%)
$\overline{D}^0$	1865	$K^+\,\pi^-$	3.80 ± 0.09
		$K^+\,\rho^-$	10.2 ± 0.9
		$K^+\,\pi^-\,\pi^+\,\pi^-$	7.5 ± 0.3
		$K^0_S\,\pi^+\,\pi^-$	3.0 ± 0.2
D^-	1869	$K^+\,\pi^-\,\pi^+$	9.1 ± 0.6
		$K^0_S\,\pi^-$	1.4 ± 0.1

Table 5.3: Selected decay modes of $\overline{D}^0$ and D^- mesons and their branching fractions.

matrices of the charged tracks. Kaon identification and the vertex probability are also used to reduce the combinatorial background. The required criteria vary for the different decay modes and are summarized later in Section 5.6. Figures 5.10 and 5.11 show the distributions of the invariant mass for the $\overline{D}^0 \to K^+\pi^-$ and $D^- \to K^+\pi^-\pi^-$ candidates, respectively, and the impact of kaon identification and vertex probability requirements. The distribution of the probability $P(\chi^2)$ for the vertex of the $\overline{D}^0 \to K^+\pi^-$ candidates is shown in Figure 5.12.

In the $\overline{D}^0 \to K^+\rho^-$ mode, the angular distribution of the ρ^- decay products is used to reduce combinatorial background. Conservation of angular momentum requires the ρ^- daughters to have L=1 and L_z=0. Therefore, angle $\theta_{D\pi}$ in Figure 5.13, between the directions of the π^- and the $\overline{D}^0$, computed in the ρ^- rest frame, has a $\cos^2\theta$ distribution, while the background is distributed uniformly. The requirement $|\cos\theta^*_{D\pi}| > 0.4$ rejects 40% of the random combinations.

Finally, momentum p^* of all $\overline{D}^0$ and D^- candidates in the $\Upsilon(4S)$ rest frame must lie between 1.3 and 2.5 GeV/c. The lower limit corresponds to the minimum momentum of D mesons produced in B decays, and reduces the combinatorial background. The higher limit is needed to reject high-momentum D mesons produced in continuum $c\bar{c}$ events.

$D^{*-} \to \overline{D}^0\pi^-$

The D^{*-} candidates are selected in the $D^{*-} \to \overline{D}^0\pi^-$ decay which has a branching fraction of 68% [33]. The π^- is commonly called the *soft pion* because of its low momentum. The origin of the low momentum is the small energy release in the decay, given by the difference $E_\pi = m_{D^{*-}} - m_{\overline{D}^0} = 146\,\mathrm{MeV}$.

A **GoodTracksVeryLoose** track (see Section 4.5.1) with a momentum greater than 70 MeV/c

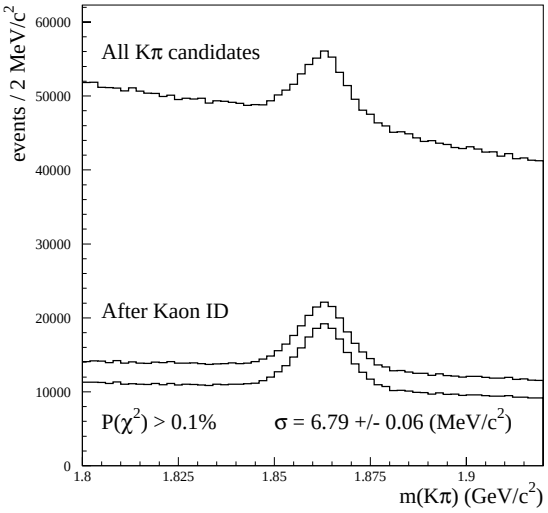

Figure 5.10: Distribution of the invariant mass $m(K^+\pi^-)$ for the $\overline{D}^0 \to K^+\pi^-$ candidates, and the impact of kaon identification and vertex probability requirements.

and less than 450 MeV/c is combined with a $\overline{D}^0$, to form D^{*-} candidates. The lower limit is the threshold for track reconstruction in the silicon vertex tracker, while the higher limit is the maximum possible momentum, in the laboratory frame, for the soft pion in this decay.

The mass difference $\delta m = m(\overline{D}^0\pi^-) - m(\overline{D}^0)$ between the $\overline{D}^0\pi^-$ invariant mass and the $\overline{D}^0$ mass is commonly used to select D^{*-} candidates. The resolution on δm is improved by constraining the $\overline{D}^0$ candidate mass to its nominal value, and by using the beamspot as an additional geometric constraint for the soft pion, when the D^{*-} decay vertex is computed (see Figure 5.14). The effective vertical size of the beamspot is increased to 40 $\mu\mathrm{m}$ (from a few microns) to account for the transverse flight of the B mesons, which have a transverse momentum of about 340 MeV/c.

The distribution of δm of selected candidates is shown in Figure 5.15. The D^{*-} candidates with a mass difference δm within 2.5 standard deviations $\sigma_{\delta m}$ of the expected value $\delta m_0 = 145.4\,\mathrm{MeV}/c^2$ [33] are selected. The value of $\sigma_{\delta m}$ varies within the $\overline{D}^0$ decay modes due to the multiplicity of the final state.

$\overline{D}^{*0} \to \overline{D}^0\pi^0$

The $\overline{D}^{*0} \to \overline{D}^0\pi^0$ candidates are selected from combinations of a $\overline{D}^0$ and a π^0 with center-of-mass momentum p^* less than 450 MeV/c in the $\Upsilon(4S)$ frame.

Since all π^0 mesons are subject to mass-constrained kinematic fits (see Section 5.3.1), the mass

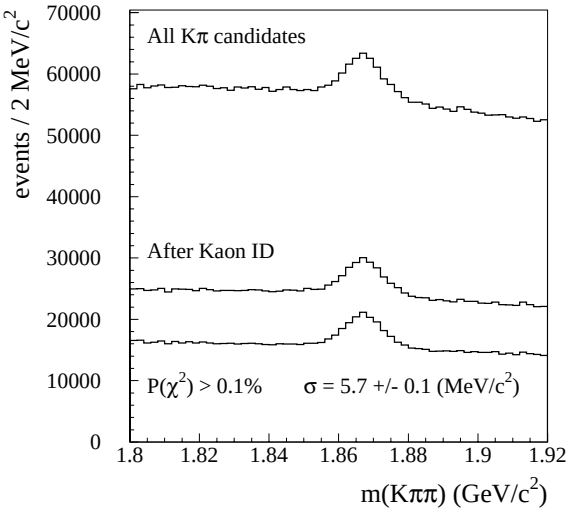

Figure 5.11: Distribution of the invariant mass $m(K^+\pi^-\pi^-)$ for the $D^- \to K^+\pi^-\pi^-$ candidates, and the impact of kaon identification and vertex probability requirements.

difference δm is computed from the reconstructed masses $m(\overline{D}^0\pi^0)$ and $m(\overline{D}^0)$, which in this case is not fixed to the nominal $\overline{D}^0$ mass.

Due to the worse energy resolution for π^0 s, compared to the momentum resolution for the charged tracks, the resolution $\sigma_{\delta m}$ is worse than for D^{*-}. The distributions of δm for the selected $\overline{D}^{*0}$ candidates are shown in Figure 5.16. The $\overline{D}^{*0}$ candidates with δm within $4\,\mathrm{MeV}/c^2$ of the nominal mass difference $\delta m_0 = 142.2\,\mathrm{MeV}/c^2$ [33] are selected.

5.3.5 Charmonium states

J/ψ, $\psi(2S)$, and χ_{c1}

The decay modes of the J/ψ, $\psi(2S)$, and χ_{c1} mesons reconstructed in this analysis, and their branching fractions, are listed in Table 5.4 [33].

The J/ψ and $\psi(2S)$ candidates are selected from pairs of oppositely-charged **`GoodTrackLoose`** tracks (see Section 4.5.1), on the basis of their invariant mass $m(\ell^+\ell^-)$ and particle identification criteria.

These criteria are different for each B decay mode, due to differing levels of background encountered, and have been optimized to provide the best sensitivity to $\sin 2\beta$. Tables 5.5 and 5.6 summarize the criteria for the e^+e^- and $\mu^+\mu^-$ modes, respectively. The particle-identification

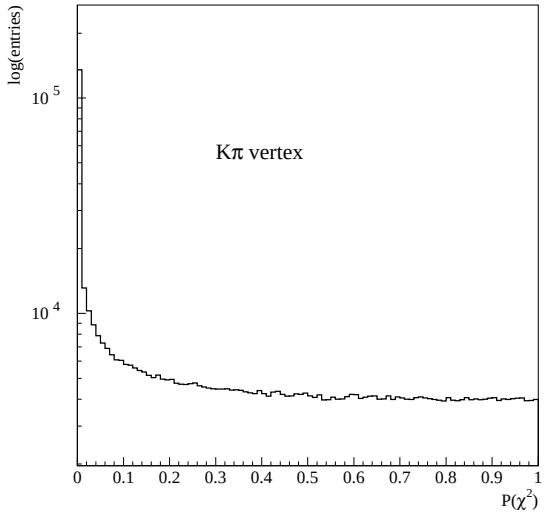

Figure 5.12: Distribution of the vertex probability $P(\chi^2)$ for selected $\overline{D}^0 \to K^+\pi^-$ candidates.

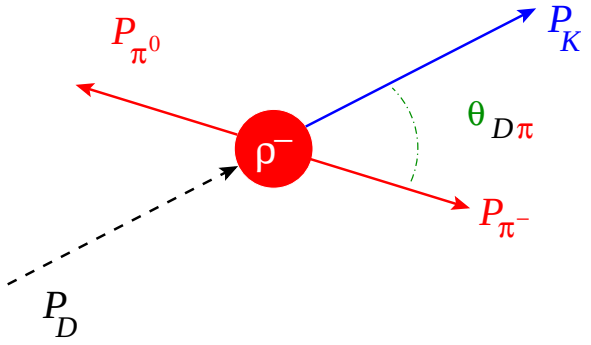

Figure 5.13: Definition of the helicity angle $\theta_{D\pi}$ in the $\overline{D}^0 \to K^+\rho^-$ decay.

criteria are described in Sections 4.7.2 for the electrons and in Section 4.7.3 for the muons.

The distributions of the invariant mass $m(\ell^+\ell^-)$ are shown in Figures 5.17 and 5.18 for J/ψ and $\psi(2S)$, respectively. The asymmetric tail to the left in the e^+e^- final state is due to Bremsstrahlung photons radiated by the electrons. The energy of these photons is recovered by identifying **`GoodPhotonLoose`** 4.6.1 photons within $35\,\mathrm{mrad}$ in polar angle and $50\,\mathrm{mrad}$ in azimuth, of the projected direction of the electrons.

For the $\psi(2S) \to J/\psi\,\pi^+\pi^-$ mode, $\ell^+\ell^-$ candidates are constrained to the nominal J/ψ mass and then combined with pairs of oppositely-charged **`GoodTracksLoose`** tracks. Candidates with $0.574 < m(\ell^+\ell^-\pi^+\pi^-) - m(J/\psi) < 0.604\,\mathrm{GeV}/c^2$ are selected. Distributions of the difference

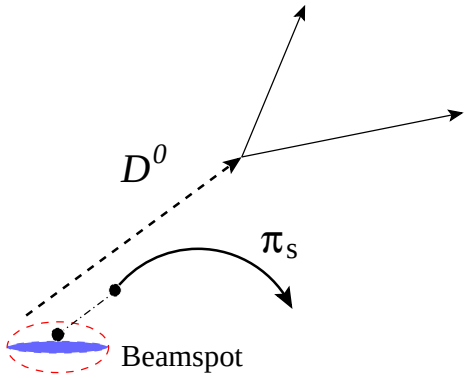

Figure 5.14: The blown up beamspot (dashed ellipse) is used as an additional constraint on the trajectory of the soft pion π_s.

Meson	Mass (MeV/c^2)	Decay mode	Branching fraction (%)
J/ψ	3097	e^+e^-	5.9 ± 0.1
		$\mu^+\mu^-$	5.9 ± 0.1
$\psi(2S)$	3686	$J/\psi\ \pi^+\ \pi^-$	30.5 ± 1.6
		e^+e^-	0.73 ± 0.04
		$\mu^+\mu^-$	0.70 ± 0.09
χ_{c1}	3511	$J/\psi\gamma$	31.6 ± 3.2

Table 5.4: Reconstructed decay modes of the J/ψ, $\psi(2S)$, and χ_{c1} mesons and their branching fractions.

$m(\ell^+\ell^-\pi^+\pi^-) - m(J/\psi)$ are shown in Figure 5.19.

The χ_{c1} candidates are formed from an $\ell^+\ell^-$ candidate constrained to the nominal J/ψ mass, and a **`GoodNeutralLooseAcc`** photon (see Section 4.6.1) with energy $E_\gamma > 150\,\mathrm{MeV}$. The photon candidate should not form, in combination with any other photon in the event having at least 70 MeV of energy, a π^0 candidate with mass between 120 and 150 MeV/c^2. Distributions of $m(J/\psi\gamma)$ for the χ_{c1} candidates are shown in Figure 5.20. The small bump on the right is from $\chi_{c2} \to J/\psi\gamma$ decays. The χ_{c2} has a mass of 3556 MeV/c^2 [33]. The current energy resolution in *BABAR* is not sufficient to resolve the two peaks. Candidates with invariant mass $m(J/\psi\gamma)$ between 3.476 and 3.546 GeV/c^2 are selected as χ_{c1} candidates.

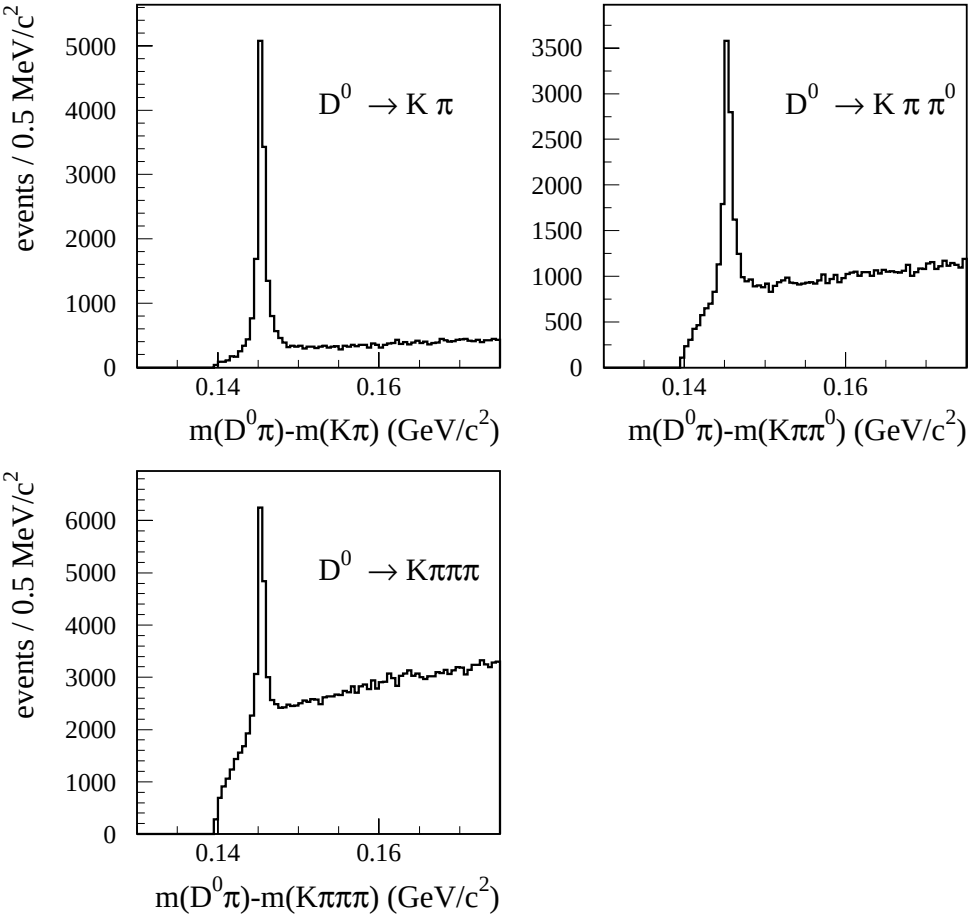

Figure 5.15: Distribution of the mass difference $\delta m = m(\overline{D}^0\pi^-) - m(\overline{D}^0)$ for selected D^{*-} candidates.

B channel	Particle ID	$m(e^+e^-)$ (MeV/c^2)
$J/\psi\, K^0_S$	None	2950–3140
$\psi(2S)K^0_S$ (e^+e^-)	`VeryLoose`	3436–3736
$\psi(2S)K^0_S$ ($J/\psi\pi^+\pi^-$)	`VeryLoose`	2950–3140
$\chi_{c1}K^0_S$ ($J/\psi\gamma$)	`Loose`	2950–3140

Table 5.5: Particle identification and invariant mass requirements for J/ψ and $\psi(2S) \to e^+e^-$ candidates. The minimal particle identification criteria are applied to both daughters, while only one daughter must pass the restrictive requirement.

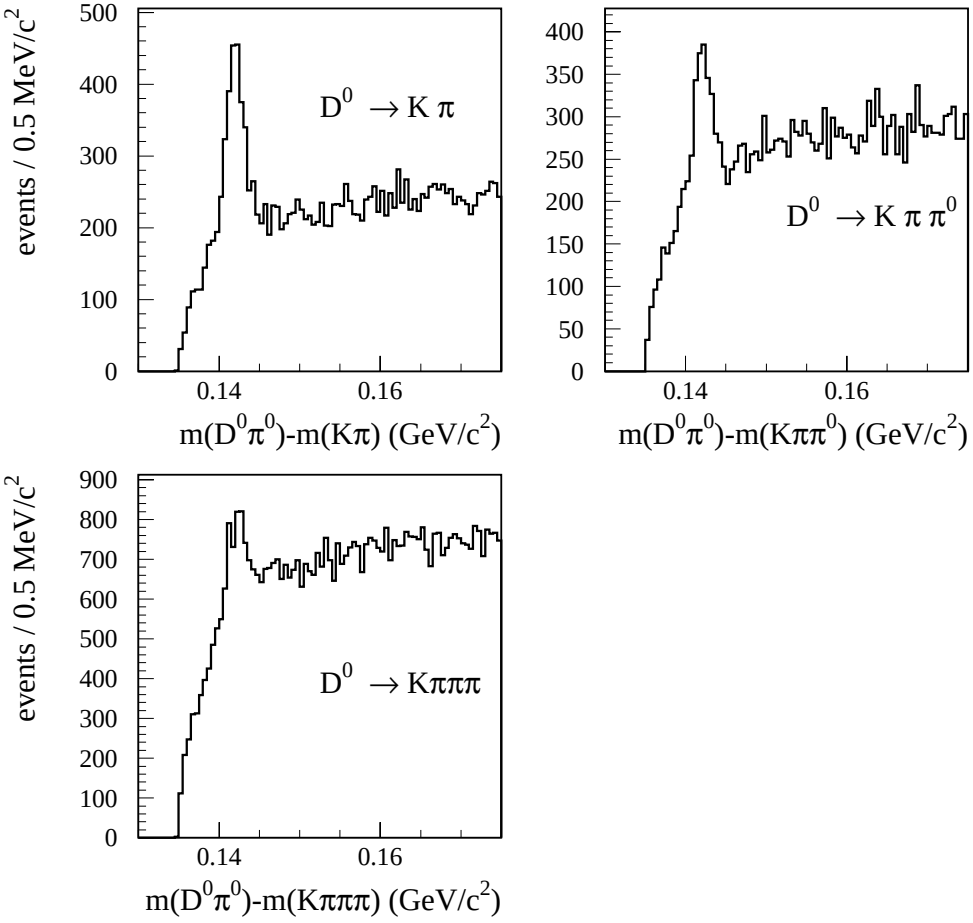

Figure 5.16: Distribution of the mass difference $\delta m = m(\overline{D}^0\pi^-) - m(\overline{D}^0)$ for selected $\overline{D}^{*0}$ candidates.

B channel	Particle ID	$m(\mu^+\mu^-)$ (MeV/c^2)
$J/\psi\, K_S^0$	`MIP`	3060–3140
$\psi(2S)K_S^0$ ($\mu^+\mu^-$)	`VeryLoose`	3636–3736
$\psi(2S)K_S^0$ ($J/\psi\,\pi^+\pi^-$)	`VeryLoose`	3060–3140
$\chi_{c1}K_S^0$ ($J/\psi\,\gamma$)	`VeryLoose`	3060–3140

Table 5.6: Particle identification and invariant mass requirements for J/ψ and $\psi(2S) \to \mu^+\mu^-$ candidates. The minimal particle identification criteria are applied to both daughters, while only one daughter must pass the restrictive requirement. Muon selection criteria are defined in Section 4.7.3. MIP refers to a minimum-ionizing particle.

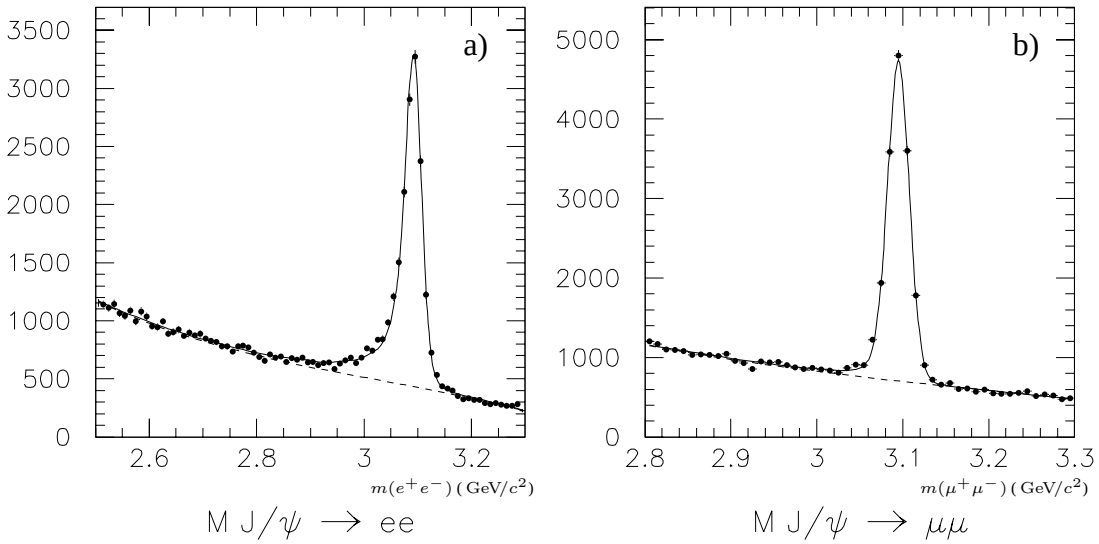

Figure 5.17: Distribution of the invariant mass $m(\ell^+\ell^-)$ for a) $J/\psi \rightarrow e^+e^-$ and b) $J/\psi \rightarrow \mu^+\mu^-$ final states.

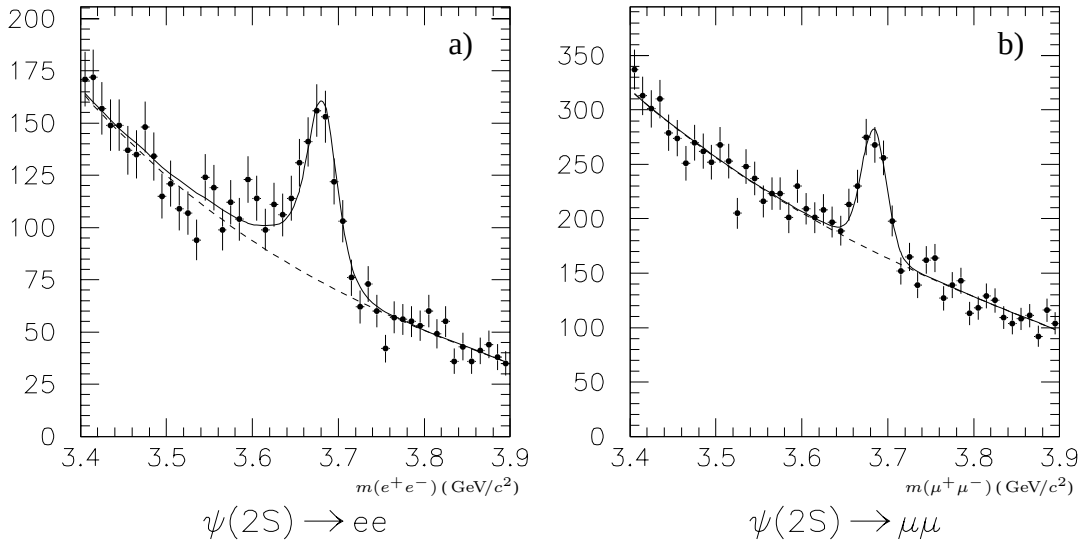

Figure 5.18: Distribution of the invariant mass $m(\ell^+\ell^-)$ for a) $\psi(2S) \rightarrow e^+e^-$ and b) $\psi(2S) \rightarrow \mu^+\mu^-$ final states.

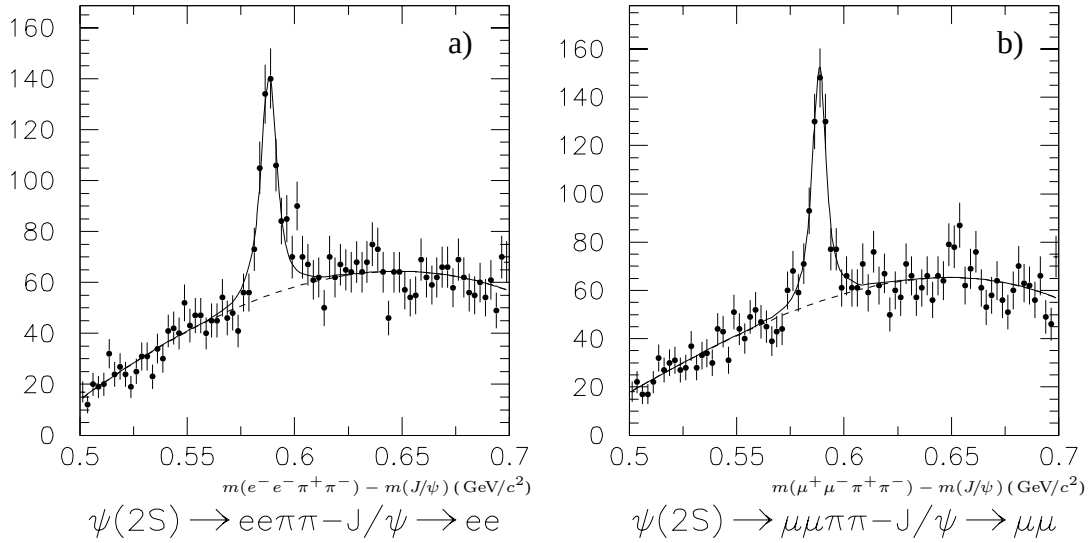

Figure 5.19: Distribution of $m(\ell^+\ell^-\pi^+\pi^-) - m(J/\psi)$, with a) $J/\psi \rightarrow e^+e^-$ and b) $J/\psi \rightarrow \mu^+\mu^-$.

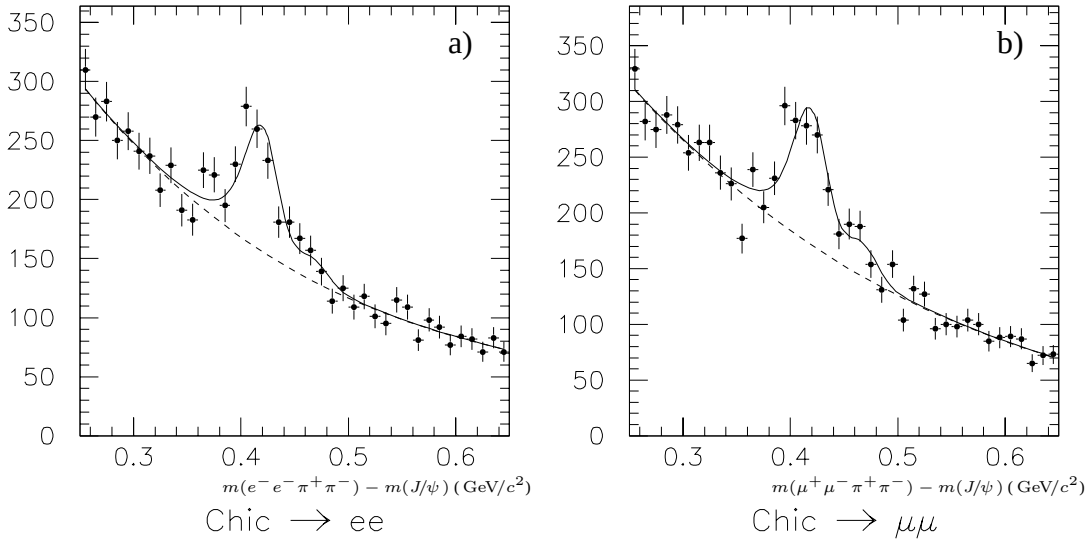

Figure 5.20: Distribution of $m(\ell^+\ell^-\pi^+\pi^-) - m(J/\psi)$, with a) $J/\psi \rightarrow e^+e^-$ and b) $J/\psi \rightarrow \mu^+\mu^-$.

$\eta_c \to K^0_S K^\pm \pi^\mp, K^+K^-\pi^0$

The η_c meson is reconstructed in the hadronic final states listed in Table 5.7 [33].

Meson	Mass (MeV/c^2)	Decay mode	Branching fraction (%)
η_c	2979.7 ± 1.5	$K\bar{K}\pi$	5.5 ± 1.7

Table 5.7: Reconstructed decay modes of the η_c meson and their branching fractions.

The discrimination of combinatorial background is an important issue in the selection of η_c candidates. The high multiplicity of the final state and the hadronic decays of the J/ψ represent the main contributions to the background. A dedicated selection aimed at maximizing the number of $B^0 \to \eta_c K^0_S$ candidates for the time-dependent CP violation studies is described in References [105–107].

Charged kaon candidates are **`GoodTracksVeryLoose`** tracks (see Section 4.5.1) with momentum greater than 250 MeV/c and polar angle θ between 0.35 rad and 2.54 rad, and must have particle identification information in the DIRC or in the drift chamber.

The $K^0_S \to \pi^+\pi^-$ candidates with reconstructed mass within 12.5 MeV/c^2 of their nominal mass are used in the $K^0_S K^\pm \pi^\mp$ final state. For these K^0_S candidates, the cosine of the angle between their flight direction and momentum (angle α in Figure 5.8) is required to be greater than 0.99.

In the $K^+K^-\pi^0$ mode, the $\pi^0 \to \gamma\gamma$ candidates are required to have a mass within 15 MeV/c the nominal π^0 mass. The energy of the lower energy photon must be greater than 130 MeV while the minimum value for the higher energy photon is 270 MeV. In addition, the opening angle between the two photons in the π^0 rest frame must be less than 0.82, in order to remove random combinations.

The $K\bar{K}\pi$ candidates with invariant mass $m(K\bar{K}\pi)$ between 2.90 and 3.15 GeV/c^2 are retained as η_c candidates. The distribution of $m(KK\pi)$ for the $K^0_S K^\pm \pi^\mp$ final state is shown Figure 5.21. This region include a $14.5 \pm 2.0\%$ contribution from hadronic decays of the J/ψ. Since the η_c and J/ψ mesons have the same CP eigenvalue $\eta_{CP} = -1$ it is not necessary to separate the J/ψ contribution in the time-dependent CP analysis.

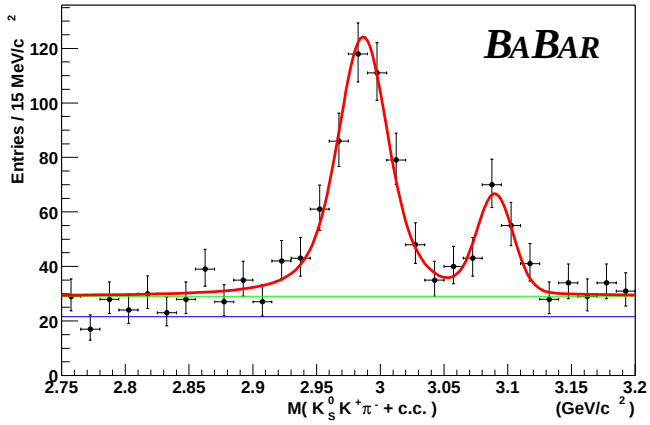

Figure 5.21: Distribution of the invariant mass $m(K^0_S K^{\pm}\pi^{\mp})$. The J/ψ peak overlaps with the η_c signal and contributes to the selected candidates with $2.9 < m(K^0_S K^{\pm}\pi^{\mp}) < 3.15\,\mathrm{GeV}/c^2$.

5.4 B reconstruction technique

Two kinematic variables are used to select B meson candidates [108]:

1. The difference ΔE, defined as

$$\Delta E = E^* - E_b^* \,, \tag{5.2}$$

is the difference between the energy E^* of the B candidate and the beam energy E_b^* in the $\Upsilon(4S)$ rest frame. In this frame, E_b^* is simply half the $\Upsilon(4S)$ energy and represents the best estimate for the true energy of the B meson. Hence, ΔE has an expected value of zero for signal candidates. The RMS spread $\sigma(\Delta E)$ is given by the uncertainty σ_E on the measured energy and by the spread σ_B of the true B meson energy

$$\sigma^2(\Delta E) = \sigma_B^2 + \sigma_E^2 \,. \tag{5.3}$$

The uncertainty σ_E depends on the specific final state and varies between 7 and 40 MeV. The measured spread in the beam energies result in variations of the $\Upsilon(4S)$ energy and are the main contribution to σ_B. The beam-energy spread is of the order of a few MeV (see Section 4.1) and therefore $\sigma(\Delta E)$ is dominated by σ_E.

2. The beam-energy–substituted mass m_{ES} is defined as

$$m_{\mathrm{ES}} = \sqrt{E_b^{*2} - p^{*2}} \tag{5.4}$$

where E_b^* is again the beam energy and p^* is the measured momentum of the B candidate in the $\Upsilon(4S)$ center-of-mass frame. The RMS spread of m_{ES} is given by [108]

$$\sigma^2(m_{\mathrm{ES}}) \approx \sigma_B^2 + \left(\frac{p}{M_B}\right)^2 \sigma_p^2 \tag{5.5}$$

where σ_p is the uncertainty on the measured momentum. Unlike $\sigma(\Delta E)$, since $p/M_B \approx [325\,\mathrm{MeV}/c]/[5279\,\mathrm{MeV}/c^2] \approx 0.06c$, the uncertainty $\sigma(m_{\mathrm{ES}})$ is dominated by the beam-energy spread σ_B.

These two variables are nearly uncorrelated. Figure 5.22 shows the distribution of m_{ES} versus ΔE for the decay mode $B^+ \to \overline{D}^0\pi^+$. Signal candidates accumulate around $m_{\mathrm{ES}} = m_B\,\mathrm{GeV}/c^2$ and $\Delta E = 0\,\mathrm{MeV}$. The signal region is defined below. There is a second satellite accumulation around $m_{\mathrm{ES}} = m_B$ and $\Delta E < -0.130\,\mathrm{GeV}$. This is due to final states with an additional low energy pion that has not been included. For example, a $B^+ \to \overline{D}^0\rho^+$ decay followed by $\rho^+ \to \pi^+\pi^0$, is selected in the $\overline{D}^0\pi^+$ final state when the π^0 is not included in the B candidate. Such a candidate can have the correct mass but shifted ΔE because of the missing energy of the π^0.

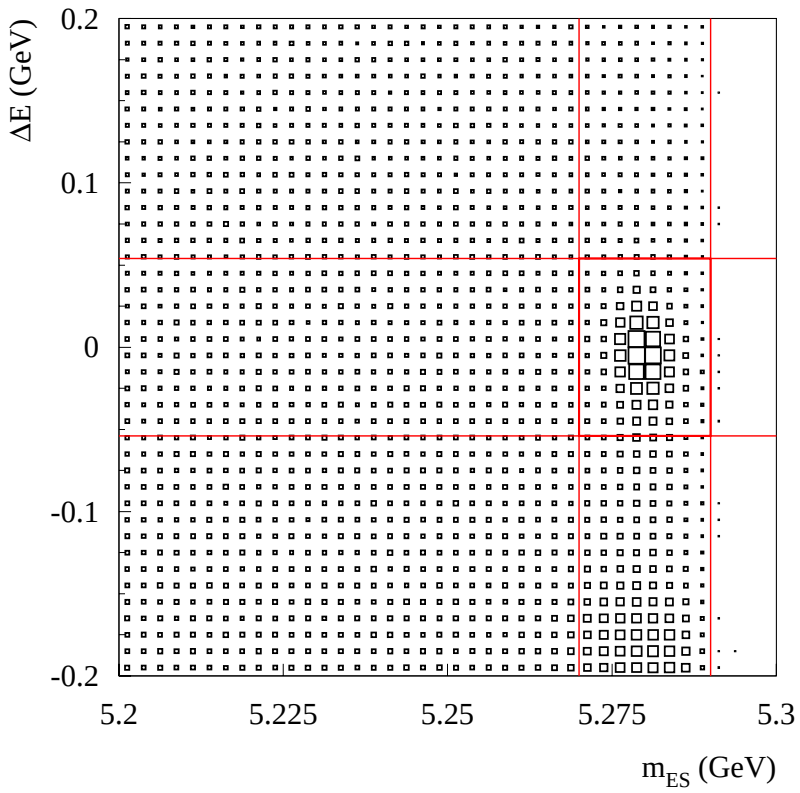

Figure 5.22: Distribution of $m_{\rm ES}$ and ΔE for selected $B^+ \to \overline{D}^0\pi^+$ candidates.

For the purpose of determining event yields and purities, four regions are defined in the ($m_{\rm ES}$, ΔE) plane. These regions are illustrated in Figure 5.23 and listed in Table 5.8. The composition of the candidates in the signal and $m_{\rm ES}$-sideband regions is illustrated in Figure 5.24. The signal component is parameterized with a Gaussian centered at the B meson mass. The background contribution is separated in *combinatorial* and *peaking* components.

The combinatorial background arises from random combinations of charged and neutral particles. The ΔE of these combinations is within the required window, while the $m_{\rm ES}$ is smoothly distributed and does not peak near the B mass. The $m_{\rm ES}$ distribution for these combinations is parameterized with a threshold function

$$\mathcal{A}(m_{\rm ES}; m_0, \xi) = N_B\, m_{\rm ES} \sqrt{1-(m_{\rm ES}/m_0)^2}\, {\rm e}^{\xi\left(1-(m_{\rm ES}/m_0)^2\right)}, \qquad (5.6)$$

commonly called the ARGUS function [109], where m_0 is the upper kinematic limit fixed at the beam energy E_b, N_B is the normalization factor, and ξ controls the slope of the function. The effect of variations in ξ is illustrated in Figure 5.25.

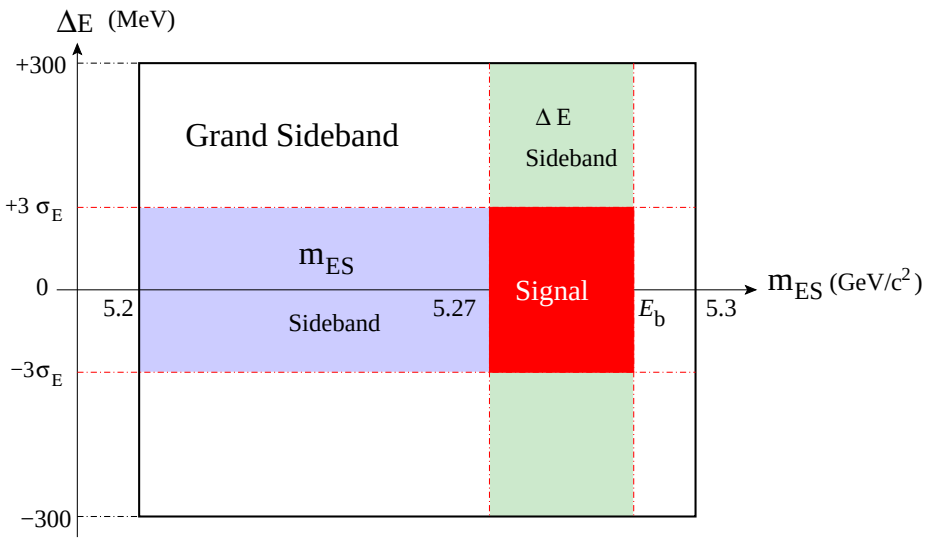

Figure 5.23: Definition of signal and sideband regions in the ($m_{\rm ES}$,ΔE) plane. The beam energy E_b is fixed at 5.291 GeV/c^2.

Region	$m_{\rm ES}$ window (GeV/c^2)	ΔE window (GeV)
Signal	$5.27 < m_{\rm ES} < E_b$	$\lvert\Delta E\rvert < 3\sigma_E$
$m_{\rm ES}$ sideband	$5.20 < m_{\rm ES} < 5.27$	$\lvert\Delta E\rvert < 3\sigma_E$
ΔE sideband	$5.27 < m_{\rm ES} < E_b$	$\lvert\Delta E\rvert > 3\sigma_E$
Grand sideband	$5.20 < m_{\rm ES} < 5.27$	$\lvert\Delta E\rvert > 3\sigma_E$

Table 5.8: Definition of signal and sideband regions in the ($m_{\rm ES}$,ΔE) plane. The beam energy E_b is fixed at 5.291 GeV/c^2. The energy resolution σ_E varies for different final states.

The peaking background is due to mis-reconstructed B candidates which have $m_{\rm ES}$ near the B mass. Figure 5.26 shows a true $B^+ \to \overline{D}^{*0} a_1^+$ candidate mis-reconstructed as a $B^0 \to D^{*-} a_1^+$ candidate. The soft pion from the $\overline{D}^{*0}$ candidate is replaced by a random charged track which has similar energy. The energy difference ΔE for this fake B candidate is close to zero. The $m_{\rm ES}$ of this candidate is near the B mass and is not accounted for by the ARGUS shape.

Signal yields and sample purities are determined from fits to the $m_{\rm ES}$ distributions of the $N_{\rm tot}$ candidates contained in the signal and $m_{\rm ES}$-sideband regions, with a sum of a Gaussian $\mathcal{G}$ for the signal and an ARGUS function $\mathcal{A}$ for the background

$$f(m_{\rm ES}) = N_{\rm sig}\,\mathcal{G}(m_{\rm ES}) + (N_{\rm tot} - N_{\rm sig})\,\mathcal{A}(m_{\rm ES})\ . \tag{5.7}$$

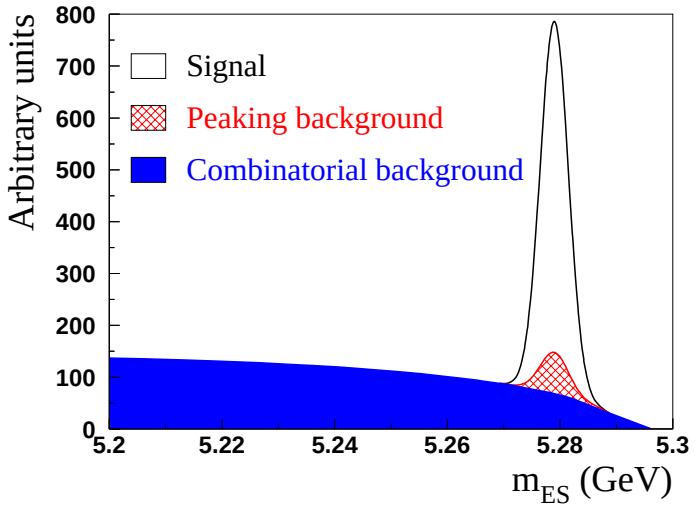

Figure 5.24: The composition of the $m_{\rm ES}$ distribution in the signal region.

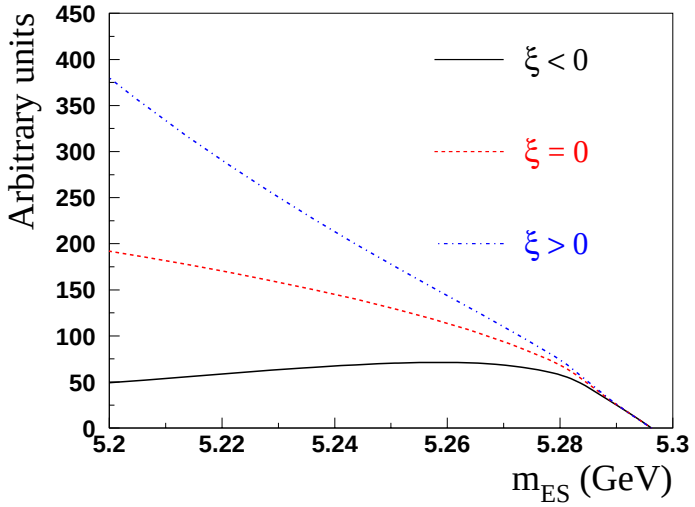

Figure 5.25: The shape of the ARGUS function for $\xi > 0$, $\xi = 0$, and $\xi < 0$.

The purity $\mathcal{P}$ for a selected sample candidates is defined as

$$\mathcal{P} = \frac{\int_{5.27}^{E_b} dm_{\rm ES}\, \mathcal{G}(m_{\rm ES})}{\int_{5.27}^{E_b} dm_{\rm ES}\, (\mathcal{G}(m_{\rm ES}) + \mathcal{A}(m_{\rm ES}))} \,. \tag{5.8}$$

Each candidate is assigned a per-event signal probability p, on the basis of the measured $m_{\rm ES}$, defined as

$$p(m_{\rm ES}) = \frac{\mathcal{G}(m_{\rm ES})}{\mathcal{G}(m_{\rm ES}) + \mathcal{A}(m_{\rm ES})} \,. \tag{5.9}$$

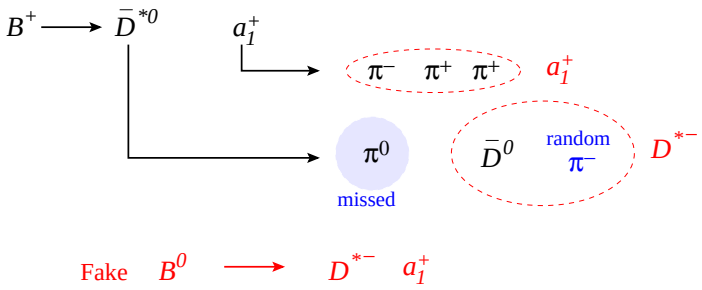

Figure 5.26: A true $B^+ \to \overline{D}^{*0} a_1^+$ mis-reconstructed as a $B^0 \to D^{*-} a_1^+$ candidate.

A fraction $f_{\rm pk}$ of the $N_{\rm sig}$ signal events is due to the peaking-background contribution. The determination of this fraction with simulated events is discussed separately for CP and flavor eigenstates in Sections 5.5 and 5.6.

In general, the fraction of peaking-background candidates is larger for final states with higher multiplicities. The Δt distribution of events with a fake B^0 is different from that of the signal, and therefore directly affects the measurement of the CP asymmetry $\sin 2\beta$. The impact of the peaking background on the measured CP asymmetry is taken into account in the systematic uncertainty, and is discussed in Section 9.4.8.

5.4.1 The B thrust axis and continuum suppression

The discrimination of continuum $q\bar{q}$ events on the basis of the normalized Fox-Wolfram variable R_2 was discussed in Section 5.1. Additional rejection of these events is provided by the *thrust axis* $\vec{A}_B$ of selected B candidates. Vector $\vec{A}_B$ for a B candidate is found by maximizing the ratio R_T

$$R_T = \frac{\sum_i^{1,N} |\vec{A}_B \cdot \vec{p}_i^*|}{\sum_i^{1,N} \sqrt{\vec{p}_i^* \cdot \vec{p}_i^*}}\,, \tag{5.10}$$

where the sum is over the charged and neutral particles in the event, not utilized to reconstruct the B candidate, and $\vec{p}_i^*$ is their three-momentum vector in the $\Upsilon(4S)$ rest frame. The cosine of the thrust angle θ_T between the three-momentum $\vec{p}_B^*$ of the B candidate and the thrust axis $\vec{A}_B$

$$\cos\theta_T = \frac{\vec{p}_B \cdot \vec{A}_B}{|\vec{p}_B||\vec{A}_B|} \tag{5.11}$$

peaks at ± 1 in the jet-like $q\bar{q}$ continuum events, but is uniformly distributed in the isotropic $B\bar{B}$ events. The requirements on $\cos\theta_T$ vary for different final states and are described in the next Sections.

5.5 B^0 decays to CP eigenstates

5.5.1 $B^0 \to J/\psi K^0_S$, $\psi(2S)K^0_S$, $\chi_{c1}K^0_S$

Candidates in the in the J/ψ K^0_S, $\psi(2S)$ K^0_S, and χ_{c1} K^0_S decay modes are formed by combining mass-constrained K^0_S candidates with J/ψ, $\psi(2S)$ or χ_{c1} candidates, also constrained to their nominal masses [110, 111].

These modes have generally high purities and do not require additional selection criteria. The background is reduced when $\psi(2S) \to J/\psi\,\pi^+\pi^-$ and χ_{c1} candidates are used in the final state, by requiring $|cos\theta_T| < 0.9$ for the thrust angle.

Signal yield $N_{\rm sig}$ and purity $\mathcal{P}$, and the resolution on $m_{\rm ES}$ and ΔE for all decays modes are summarized in Table 5.9. Figure 5.27 shows the $m_{\rm ES}$ distribution for B candidates in the signal and $m_{\rm ES}$-sideband regions.

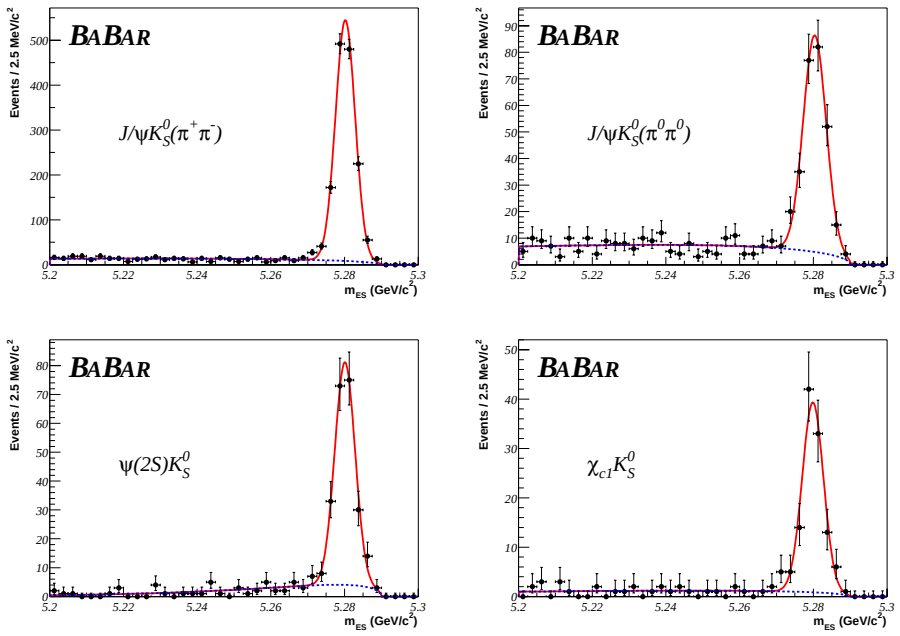

Figure 5.27: Distribution of $m_{\rm ES}$ for selected B^0 candidates in CP eigenstates in the signal and $m_{\rm ES}$-sideband regions.

Contribution of peaking background

The main source of peaking background for these modes are the decays $B^0 \to \psi K^0_S\,{\rm n}\pi$ (ψ=J/ψ,$\psi(2S)$,χ_{c1}) with n additional pion(s) in the final state. *Fake* candidates are selected when

Mode		$N_{\rm sig}$	$\mathcal{P}(\%)$	$\sigma_{\Delta E}(\,\mathrm{MeV})$	$\sigma_{m_{\rm ES}}(\,\mathrm{MeV}/c^2)$
$B^0 \to J/\psi\, K^0_S$	$e^+\, e^-$	683 ± 28	93	14.0 ± 0.3	2.69 ± 0.10
$(\pi^+\, \pi^-)$	$\mu^+\, \mu^-$	746 ± 28	98	11.0 ± 0.3	2.62 ± 0.08
$B^0 \to J/\psi\, K^0_S$	$e^+\, e^-$	112 ± 12	85	51.7 ± 2.3	3.44 ± 0.70
$(\pi^0\, \pi^0)$	$\mu^+\, \mu^-$	142 ± 13	91	49.3 ± 2.3	3.30 ± 0.26
$B^0 \to \psi(2S) K^0_S$	$e^+\, e^-$	106 ± 15	83	11.8 ± 0.7	2.88 ± 0.43
	$\mu^+\, \mu^-$	106 ± 11	93	9.2 ± 0.6	2.55 ± 0.22
$B^0 \to \chi_{c1} K^0_S$	$e^+\, e^-$	56 ± 8	96	11.1 ± 0.9	3.15 ± 0.39
	$\mu^+\, \mu^-$	55 ± 8	94	7.7 ± 0.6	2.61 ± 0.35

Table 5.9: Signal yield N_{sig}, purity $\mathcal{P}$, ΔE resolution $\sigma(\Delta E)$, and $m_{\rm ES}$ resolution $\sigma(m_{\rm ES})$ for reconstructed CP eigenstates.

the pion(s) have low energy and are not identified.

The fraction $f_{\rm pk}$ of mis-reconstructed candidates is estimated with a large sample of simulated $B \to J/\psi\, X$ events. In this sample, one B meson always decays to a final state containing a J/ψ, and the other B is free to decay to any channel. Hence, the sample also includes signal candidates in the decay modes under study.

For each decay mode, $f_{\rm pk}$ is determined from two fits to the $m_{\rm ES}$ distribution of selected candidates. In the first fit, the entire sample is used and the signal yield N_1 includes contributions from both signal and background. In the second fit, using the true Monte Carlo information, events with a B in the signal mode are removed, and the $m_{\rm ES}$ fit is performed to selected candidates in the remaining events. In this fit the shape of the combinatorial background is fixed to that from the first fit (same ARGUS function parameters). The yield N_2 from this fit has only contribution from background events and $f_{\rm pk}$ is given by the ratio $f_{\rm pk} = N_2/N_1$. The measured fractions are listed in Table 5.10.

5.5.2 $B^0 \to \eta_c K^0_S$

The selection of $\eta_c\, K^0_S$ candidates is described in Reference [105]. The K^0_S candidate is subject to tighter requirements compared to the other modes: its mass must be within $10\,\mathrm{MeV}/c^2$ of the nominal K^0_S mass, and the angle between its flight direction and momentum (angle α in Figure 5.8) must be greater than 0.9995. In addition, the distance ℓ between the K^0_S and the B decay vertices must be greater than $3\sigma_\ell$, where σ_ℓ is the uncertainty on ℓ.

Mode	$f_{\rm pk}$ (%)
$J/\psi\, K^0_S(\pi^+\pi^-)$	$0.28 \pm 0.11\%$
$J/\psi\, K^0_S(\pi^0\pi^0)$	$1.76 \pm 0.57\%$
$\psi(2S)K^0_S$	$1.17 \pm 3.10\%$
$\chi_{c1}K^0_S$	$3.54 \pm 1.44\%$

Table 5.10: Fraction of peaking background $f_{\rm pk}$ for reconstructed CP eigenstates. The uncertainties are statistical only, and are determined from the fits to the $m_{\rm ES}$ distributions.

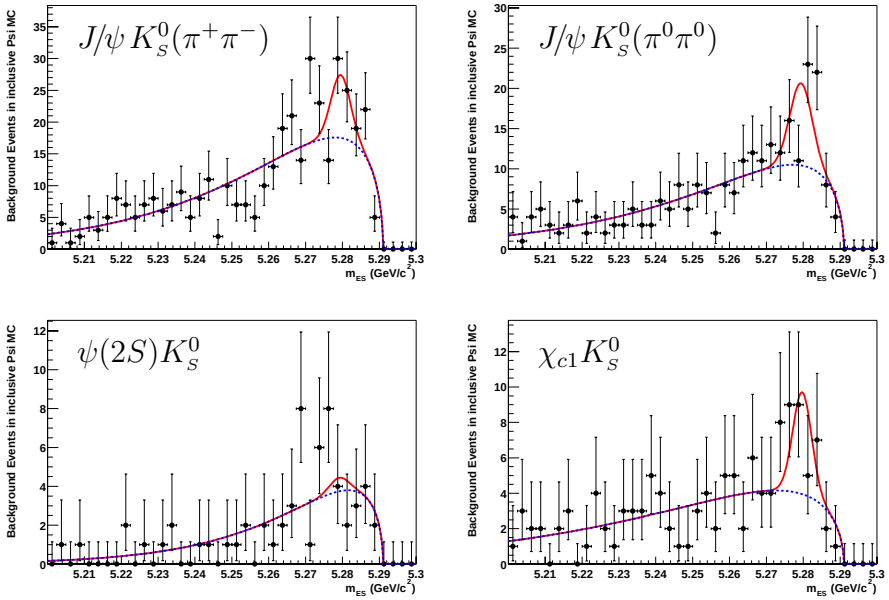

Figure 5.28: Fits to $m_{\rm ES}$ distributions of selected candidates for the in simulated $B \to J/\psi\, X$ events, after removing the signal events.

The ΔE distribution of these decay modes is not centered around zero and presents small shifts reported in Table 5.11. Instead of the usual 3σ requirement a ΔE window around the observed ΔE shift is used.

Signal yield $N_{\rm sig}$ and purity $\mathcal{P}$, the $m_{\rm ES}$ resolution, and the ΔE shift and window are summarized in Table 5.11. Figure 5.29 shows the $m_{\rm ES}$ distribution for the $\eta_c\, K^0_S$ candidates within the ΔE window.

Mode	$N_{\rm sig}$	$\mathcal{P}(\%)$	$\delta\Delta E$ (MeV)	ΔE window(MeV)	$\sigma_{m_{\rm ES}}$(MeV/c^2)
$K^0_S K^\pm \pi^\mp$	577 ± 29	74.3	-4.6	± 40	2.62 ± 0.13
$K^+ K^- \pi^0$	174 ± 17	69.7	-10.6	± 70	2.58 ± 0.25

Table 5.11: Signal yield N_{sig}, purity $\mathcal{P}$, ΔE shift $\delta\Delta E$, ΔE window, and $m_{\rm ES}$ resolution $\sigma(m_{\rm ES})$ for selected $B^0 \to \eta_c K^0_S$ candidates.

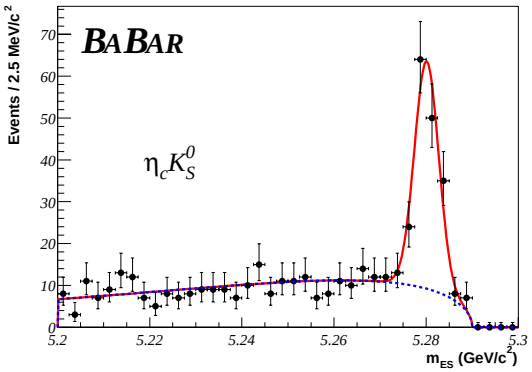

Figure 5.29: Distribution of $m_{\rm ES}$ for selected η_c K^0_S candidates within the required ΔE window.

Contribution of peaking background

The main source of peaking background for the η_c K^0_S mode are the B decays with the same particles in the final state, as for the signal candidate. For example the decay $B^0 \to K^0_S K^+ \pi^- K^0_S$ can fake the decay chain $B^0 \to \eta_c K^0_S$ followed by $\eta_c \to K^0_S K^+ \pi^-$.

Studies with large samples of simulated events show that the invariant mass $m(KK\pi)$ in these events has a uniform distribution, while peaks at the η_c mass for the signal. However, due to the poor precision on the measured branching fractions of such B decays, the determination of the fraction $f_{\rm pk}$ of peaking background can not rely only on Monte Carlo.

A method has been developed to estimate this fraction in data from the distributions of the $m_{\rm ES}$ and $m(KK\pi)$. This method is described in detail in Reference [105] and yields $f_{\rm pk} = (13.1 \pm 5.9)\%$ for the $B^0 \to \eta_c K^0_S$ decays.

5.6 B^0 decays to flavor eigenstates

Flavor eigenstates $D^{*-}\pi^+/\rho^+/a_1^+$, $D^-\pi^+/\rho^+/a_1^+$, and $J/\psi\, K^{*0}(K^+\pi^-)$ are reconstructed in this analysis. The branching fractions for these modes were summarized in Table 5.2.

The $J/\psi\ K^{*0}$ mode has very high purity (Table 5.14) and does not require additional selection requirements. For the remaining modes with a charmed meson, the background contribution is higher and additional requirements are applied.

Momentum requirements for charged tracks reduce combinatorial background, while the thrust-axis angle is used to reject continuum $q\bar{q}$ background, as described in Section 5.4.1. These additional requirements are listed in Table 5.12 for the modes with a $D^{*-} \to \overline{D}^0\pi^-$ in the final states, and in Table 5.13 for the modes with a D^- meson.

In general, the requirements are tighter for modes with higher multiplicity in the final state. The loose kaon identification **`NotAPion`** (see Section 4.7.1), with very high kaon selection efficiency and about 70% pion rejection, is applied to $K^\pm$ candidates in all decay modes, to further reduce the combinatorial background. The $\pi^0 \to \gamma\gamma$ candidates must have reconstructed mass between 120 and 150 GeV/c^2 and center-of-mass momentum $p^*_{\pi^0}$ greater than 400 MeV/c^2. The B candidates are formed from combinations of a charmed $D^{(*)}$ meson and a light $\pi^+/\rho^+/a_1^+$ meson constrained to their nominal mass (except π^+), and are used to compute the decay vertex of the B meson.

Signal yields and purities, and $m_{\rm ES}$ and ΔE resolutions for the selected candidates are listed in Table 5.14. The $m_{\rm ES}$ distribution of events with $|\Delta E| < 3\sigma_{\Delta E}$ is shown in Figure 5.30.

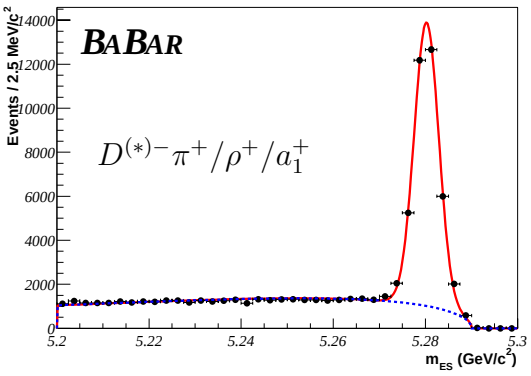

Figure 5.30: Distribution of $m_{\rm ES}$ for selected B^0 candidates in flavor eigenstates in the signal and $m_{\rm ES}$-sideband regions.

B Mode	D^0 mode	$\lvert\cos\theta_T\rvert$	Other
$D^{*-}\,\pi^+$	$K^+\,\pi^-$	—	$p_\pi, p_K > 200\,\mathrm{MeV}/c$
	$K^+\,\pi^-\,\pi^0$	—	$p_\pi, p_K > 200\,\mathrm{MeV}/c$
	$K^+\,\pi^-\,\pi^+\,\pi^-$	—	$p_\pi, p_K > 200\,\mathrm{MeV}/c$
	$K^0_S\,\pi^-\,\pi^+$	—	$p_\pi, p_{K^0_S} > 200\,\mathrm{MeV}/c$
$D^{*-}\,\rho^+$	$K^+\,\pi^-$	< 0.9	$p_\pi, p_K > 200\,\mathrm{MeV}/c$
	$K^+\,\pi^-\,\pi^0$	< 0.9	$p_\pi, p_K > 200\,\mathrm{MeV}/c$
	$K^+\,\pi^-\,\pi^+\,\pi^-$	< 0.8	$p_\pi, p_K > 200\,\mathrm{MeV}/c$
	$K^0_S\,\pi^-\,\pi^+$	< 0.8	$p_\pi, p_{K^0_S} > 200\,\mathrm{MeV}/c$
$D^{*-}\,a_1^+$	$K^+\,\pi^-$	< 0.8	$p_\pi, p_K > 150\,\mathrm{MeV}/c$
	$K^+\,\pi^-\,\pi^0$	< 0.8	$p_\pi, p_K > 150\,\mathrm{MeV}/c$
	$K^+\,\pi^-\,\pi^+\,\pi^-$	< 0.7	$p_\pi, p_K > 150\,\mathrm{MeV}/c$
	$K^0_S\,\pi^-\,\pi^+$	< 0.7	$p_\pi > 150\,\mathrm{MeV}/c$
			$p_{K^0_S} > 200\,\mathrm{MeV}/c$

Table 5.12: Selection criteria for $B^0 \to D^{*-}\pi^+/\rho^+/a_1^+$ decays.

Contribution of peaking background

Mis-reconstructed B^0 and B^+ decay modes contribute to the peaking background in flavor eigenstates. For the $J/\psi\ K^{*0}$ mode the B decay modes those discussed in Section 5.5.1 with a J/ψ in the final state.

In the modes with D^- or $\overline{D}^{*0}$ mesons, the B decays $B \to D^{(*)-}\,n\pi$, with n pions in the final state represent the main source of peaking background. Fake candidates are selected when a low momentum pion is not included in the reconstructed candidate, or is replaced with a random low momentum particle in the event.

Mis-reconstructed B^0 and B^+ candidates affect the number of signal candidates and are sources of background for measurements of branching fractions. However, for the time-dependent analysis, only mis-reconstructed B^+ candidates are cause of concern. The reason is that mis-reconstructed B^0 candidates undergo $B^0\ \overline{B}^0$ oscillation and have the same lifetime as signal. Therefore, as far as their time evolution is concerned, mis-reconstructed B^0 candidates behave exactly like signal. On the contrary, B^+ mesons do not oscillate and have a different lifetime. Hence, the time distribution

B Mode	D^- mode	$\lvert\cos\theta_T\rvert$	Other requirements
$D^-\,\pi^+$	$K^0_S\,\pi^-$	< 0.9	$p_\pi, p_K > 200\,\mathrm{MeV}/c$
	$K^+\,\pi^-\,\pi^+$	< 0.9	$p_\pi, p_{K^0_S} > 200\,\mathrm{MeV}/c$
$D^-\,\rho^+$	$K^0_S\,\pi^-$	< 0.8	$p_\pi, p_K > 200\,\mathrm{MeV}/c$
	$K^+\,\pi^-\,\pi^+$	< 0.8	$p_\pi, p_{K^0_S} > 200\,\mathrm{MeV}/c$
$D^-\,a_1^+$	$K^0_S\,\pi^-$	< 0.7	$p_\pi, p_K > 150\,\mathrm{MeV}/c$
	$K^+\,\pi^-\,\pi^+$	< 0.7	$p_\pi > 150\,\mathrm{MeV}/c$
			$p_{K^0_S} > 200\,\mathrm{MeV}/c$

Table 5.13: Selection criteria for $B^0 \to D^-\pi^+/\rho^+/a_1^+$ decays.

Mode	N_{sig}	$\mathcal{P}(\%)$	$\sigma_{m_{\rm ES}}(\mathrm{MeV}/c^2)$	$\sigma_{\Delta E}(\mathrm{MeV})$
$B^0 \to D^{*-}\pi^+$	7333 ± 143	92	2.69 ± 0.06	19.2 ± 0.3
$B^0 \to D^{*-}\rho^+$	4668 ± 199	85	3.11 ± 0.13	31.4 ± 1.2
$B^0 \to D^{*-}a_1^+$	3471 ± 150	79	2.69 ± 0.10	13.1 ± 0.4
$B^0 \to D^-\pi^+$	8222 ± 205	82	2.62 ± 0.06	18.2 ± 0.3
$B^0 \to D^-\rho^+$	4669 ± 201	77	3.00 ± 0.12	31.8 ± 1.1
$B^0 \to D^-a_1^+$	2634 ± 156	66	2.58 ± 0.14	12.6 ± 0.4
$B^0 \to J/\psi\,K^{*0}(K^+\pi^-)$	800 ± 54	96	2.61 ± 0.08	10.2 ± 0.4

Table 5.14: Signal yield N_{sig}, purity $\mathcal{P}$, ΔE resolution $\sigma_{\Delta E}$, and $m_{\rm ES}$ resolution $\sigma_{m_{\rm ES}}$ for all reconstructed B^0 flavor eigenstates.

of mis-reconstructed B^+ candidates is different from the signal distribution and must be modeled correctly in the time-dependent analysis.

Studies with large samples of simulated events [112] show that peaking background, in the flavor eigenstates, arises mainly from the decays $B^+ \to D^{(*)0}\pi^+/\rho^+/a_1^+$. The fraction $f_{\rm pk}$ of peaking background in the selected signal sample is estimated to be $(1.3 \pm 0.3^{+0.2}_{-0.5})\%$.

5.7 B^+ control samples

A large sample of B^+ candidates is used as a control sample for the time-dependent CP analysis, and for validation studies of the b-flavor tagging algorithm. The selected decay modes and their branching fractions [33] are summarized in Table 5.15. The selection of B^+ candidates is similar

Decay mode	Branching fraction (%)
$B^+ \to \overline{D}^0\,\pi^+$	0.53 ± 0.05
$B^+ \to \overline{D}^{*0}\,\pi^+$	0.46 ± 0.04
$B^0 \to J/\psi\ K^+$	$(1.01 \pm 0.05) \times 10^{-1}$
$B^0 \to J/\psi\ K^{*+}$	$(1.39 \pm 0.13) \times 10^{-1}$
$B^0 \to \psi(2S)\ K^+$	$(6.6 \pm 0.6) \times 10^{-2}$
$B^0 \to \chi_{c1}\ K^+$	$(6.5 \pm 1.1) \times 10^{-2}$

Table 5.15: Reconstructed B^+ decays and their branching fractions.

to the B^0 candidates, discussed in Sections 5.5 and 5.6.

In the decay modes with a charmonium meson, the K^+ candidate is a **`GoodTrackLoose`** track with polar angle θ within 0.35 and 2.5 rad and is combined with a mass-constrained J/ψ, $\psi(2S)$, χ_{c1}, or η_c meson.

The requirements for $\overline{D}^{*0}\pi^+$ and $\overline{D}^0\ \pi^+$ decay modes are listed in Table 5.16. The $\overline{D}^{*0}$ is selected in the $\overline{D}^0\pi^0$ channel as described in Section 5.3.4. For both B^+ decay modes, kaon identification on the K^+ from the $\overline{D}^0$ and the thrust angle θ_T are used to reduce combinatorial background. The K^+ candidate is **`GoodTrackLoose`** track with momentum greater than 200 MeV/c. The π^+ candidate, from the B^+, is also a **`GoodTrackLoose`** track but is required to have momentum greater than 150 MeV/c.

Signal yield and purity, as well as $m_{\rm ES}$ and ΔE resolutions for reconstructed B^+ decay modes are summarized in Table 5.17. Figure 5.31 shows the $m_{\rm ES}$ distribution for modes with a charmonium meson or a charmed meson separately.

B^+ mode	$\overline{D}^0$ mode	$\lvert\cos\theta_T\rvert$	kaon identification	Other
$\overline{D}^0\,\pi^+$	$K^+\,\pi^-$	< 0.9	`NotAPion`	
	$K^+\,\pi^-\,\pi^0$	< 0.8	`NotAPion`	
	$K^+\,\pi^-\,\pi^+\,\pi^-$	< 0.8	`NotAPion`	
	$K^0_S\,\pi^+\,\pi^-$	< 0.8	—	
$\overline{D}^{*0}\,\pi^+$	$K^+\,\pi^-$	< 0.8	`NotAPion`	
	$K^+\,\pi^-\,\pi^0$	< 0.7	`Tight`	
	$K^+\,\pi^-\,\pi^+\,\pi^-$	< 0.7	`Tight`	
	$K^0_S\,\pi^+\,\pi^-$	< 0.7	—	

Table 5.16: Selection criteria for $B^+ \to \overline{D}^{(*)0}\pi^+$ decay modes. The kaon identification is applied to the K^+ from the $\overline{D}^0$ decay.

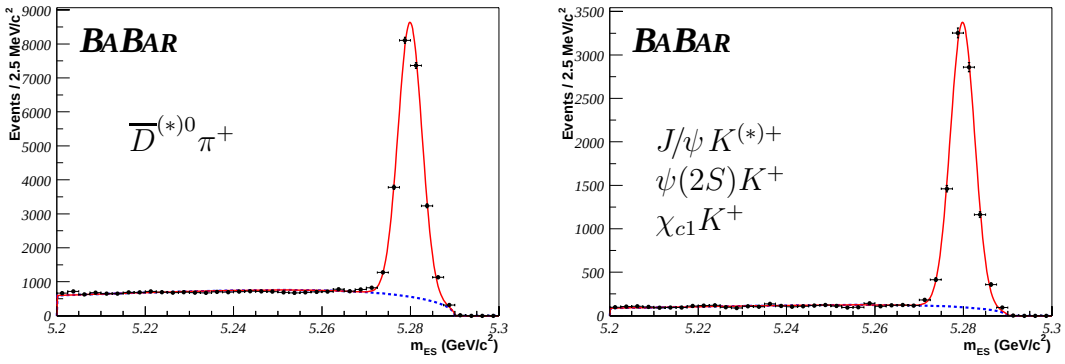

Figure 5.31: Distribution of $m_{\rm ES}$ for selected B^+ candidates in decay modes a) $\overline{D}^{*0}\,\pi^+$ and $\overline{D}^0\,\pi^+$ (left plot), and b) $J/\psi\;K^+/K^{*+}$, $\psi(2S)\;K^+$, and $\chi_{c1}\;K^+$ (right plot).

Mode	N_{sig}	$\mathcal{P}$(%)	$\sigma_{m_{\rm ES}}(\,{\rm MeV}/c^2)$	$\sigma_{\Delta E}(\,{\rm MeV})$
$B^+ \to \overline{D}^0\pi^+$	15647 ± 282	83	2.69 ± 0.05	17.4 ± 0.2
$B^+ \to \overline{D}^{*0}\pi^+$	6198 ± 183	89	3.10 ± 0.09	18.8 ± 0.4
$B^+ \to J/\psi\, K^+$	5666 ± 78	95	2.52 ± 0.04	15.1 ± 0.3
$B^+ \to J/\psi\, K^{*+}$	1942 ± 60	86	3.0 ± 0.3	18.5 ± 0.8
$B^+ \to \psi(2S)K^+$	865 ± 31	94	2.65 ± 0.16	10.2 ± 0.4
$B^+ \to \chi_{c1}K^+$	553 ± 25	95	2.81 ± 0.21	11.0 ± 0.7

Table 5.17: Signal yield N_{sig} and purity $\mathcal{P}$, $m_{\rm ES}$ resolution $\sigma_{m_{\rm ES}}$, and ΔE resolution $\sigma_{\Delta E}$ for all reconstructed B^+ decays.

Chapter 6

Determination of the flavor of neutral B mesons

The second ingredient of the time-dependent CP analysis is the separation between B^0 and $\overline{B}^0$ meson, by analyzing their decay products. This is referred to as b-flavor tagging.

As explained in Chapter 3, b-flavor tagging is necessary in order to distinguish B^0 and $\overline{B}^0$, mesons fully reconstructed in CP eigenstates ($B_{\rm CP}$). In fact, the flavor of the other B meson ($B_{\rm tag}$) determines the flavor of $B_{\rm CP}$, thanks to the coherence of the $B\bar{B}$ state in the $\Upsilon(4S)$ decay.

In principle, one could fully reconstruct $B_{\rm tag}$ in one of the flavor eigenstates discussed in Section 5.6, where the charge of decay products in the final state distinguish a B^0 from a $\overline{B}^0$ meson. This method could provide the cleanest sample of events with both neutral B mesons fully reconstructed. Unfortunately, this is a very inefficient approach, since the efficiency of fully reconstructing B mesons in flavor eigenstates is of the order of $\mathcal{O}(10^{-4})$, from the yields presented in Section 5.6.

The efficiency can be significantly improved by using an inclusive technique, that determines the flavor of neutral B mesons from the charge and kinematic properties of their decay products. The rich variety of B decays offers characteristic processes that can be recognized by an inclusive algorithm. Obviously such an algorithm has a non-zero probability of choosing the wrong flavor. In general, two quantities characterize a flavor-tagging algorithm

1. efficiency ϵ of providing a flavor tag, and

2. fraction w of candidates with the wrong flavor.

It is customary to define an "effective tagging power" $Q \equiv \epsilon(1-w)^2$ which takes into account

efficiency and mistag fraction, and affects directly the uncertainty on $\sin 2\beta$.

Characteristic B decays providing information about the flavor of the neutral B mesons are discussed in Section 6.1. In *BABAR*, B^0 and $\overline{B}^0$ are separated by an algorithm based on neural networks, which is described briefly in Section 6.2.

6.1 Sources of flavor-tag information

The flavor-tagging algorithm used in *BABAR*, is mainly based on the correlations between the flavor of neutral B mesons and the charge of leptons, kaons, and soft pions in the final state. These correlations are discussed in the following sections.

6.1.1 Leptons from semileptonic B decays

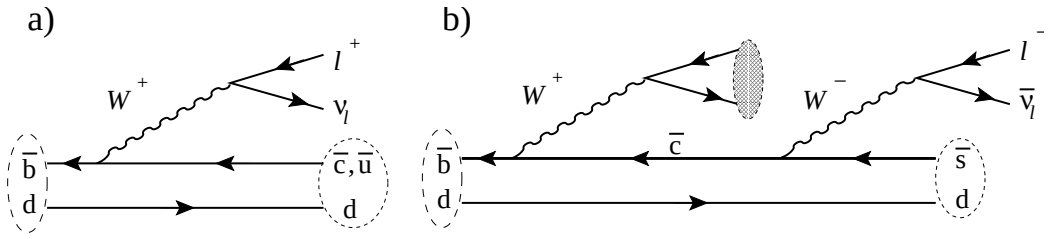

Figure 6.1: Primary leptons from B decays in a), and secondary leptons with the opposite charge in the cascade decays $b \to c \to s$.

The semileptonic decays $B \to X\ell\nu_\ell$ constitute 20% of all decay modes of the B mesons and represent the main source of leptons for flavor tagging. Figure 6.1a shows the quark-level tree diagram in the semileptonic B decays, where the lepton is generated from the W boson emitted by the b quark. A positive lepton ℓ^+ indicates a $\bar{b}$ quark, while a negative lepton ℓ^- is produced by a b quark. This charge correlation provides a clean distinction between B^0 and $\overline{B}^0$ mesons with low probability w of assigning the wrong flavor.

There are two sources of wrong flavor assignment

- hadrons mis-identified as leptons (fake leptons);
- leptons with opposite charge not originated from the b quark (**wrong-sign** leptons).

Tight requirements in the lepton-identification algorithm can reduce significantly contributions from fake leptons.

Figure 6.1b shows the origin of the wrong-sign leptons, at quark level, in the $b \to c \to s$ decays. The charmed mesons D^- and $\overline{D}^0$ produced in B decays, decay semileptonically in about 25% and 14% of the time [33], respectively, and produce wrong-sign leptons.

These leptons are called *secondary*, to distinguish them from the *primary* leptons produced by B mesons. Secondary leptons are discriminated on the basis of their kinematic properties. Figure 6.2 shows the center-of-mass momentum spectrum of leptons in data. Overlaid to data points are the expected contributions from primary leptons (open histogram), secondary leptons (cross-hatched histogram), and mis-identified leptons (diagonally-hatched histogram), all from simulated events.

One observes that secondary leptons have a much softer spectrum. For example, leptons with a momentum $p^* > 1.4\,\mathrm{GeV}/c$ are almost entirely primary leptons.

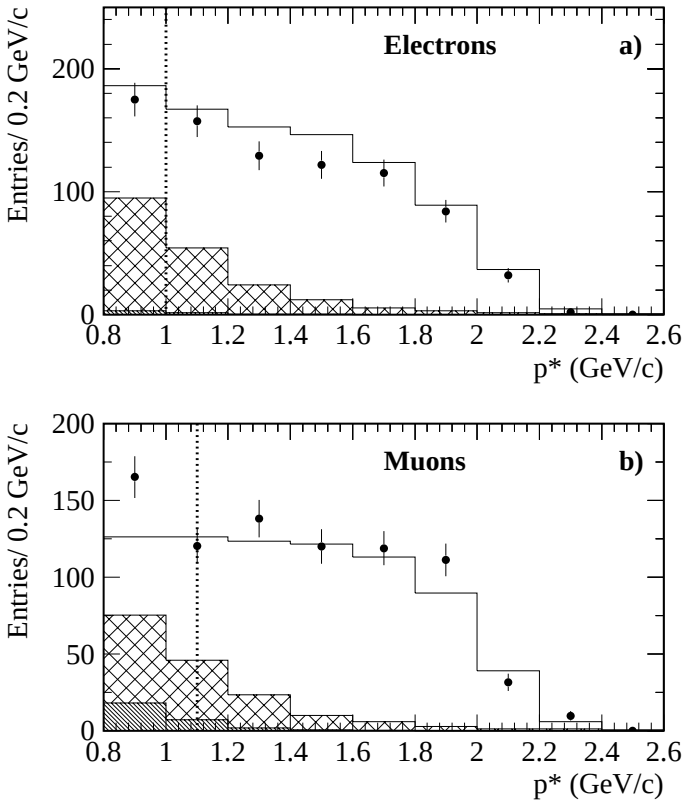

Figure 6.2: Center-of-mass momentum distribution for a) electrons and b) muons in data. Data are shown as points. The open histogram shows primary leptons, the cross-hatched histogram cascade leptons, and the diagonally-hatched histogram fake leptons, all from simulation.

6.1.2 Kaons from cascade $b \to c \to s$ decays

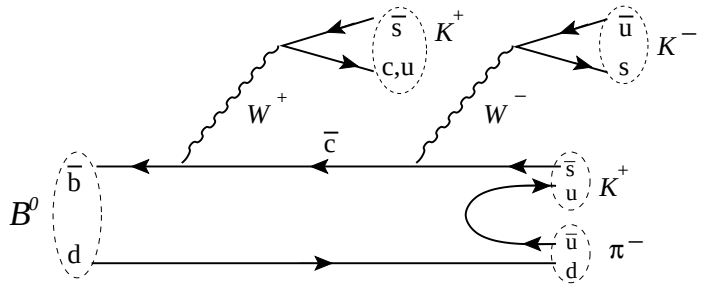

Figure 6.3: Sources of charged kaons in the decay of a B^0 meson.

The dominant source of kaons in B decays is the decay chain $b \to c \to s$. A maximum of three charged kaons can be produced in the decays of B^0 mesons, as shown in Figure 6.3.

1. The primary source is the hadronization of the $\bar{s}$ quark in the chain $\bar{b} \to \bar{c} \to \bar{s}$. The K^+ thus produced is called a **right-sign** kaon, and associated to an initial B^0 state.

2. The W^+ can hadronize to a $K^+ \equiv u\bar{s}$ meson and provide useful flavor tag information, although this process is Cabibbo-suppressed ($|V_{us}|^2 \sim 0.04$). It can also hadronized to a $D_s^+ \equiv c\bar{s}$ meson. An inclusive reconstruction of this meson could be used for flavor tagging. However, the production of a $u\bar{d}$ pair in the form of a light meson (π^+, ρ^+ etc) is Cabibbo-favored compared to $u\bar{s}$ pair and bears no flavor-tag information.

3. The W^- in the decay of the $\bar{c}$ quark can hadronize in a **wrong-sign** K^-. This process involves a $|V_{us}|^2$ factor and is Cabibbo-suppressed compared to the production of a π^+ meson, proportional to $|V_{ud}|^2$.

All these sources can also produce K_S^0 and K_L^0 mesons which are not helpful for flavor tagging through charge correlation, and contribute to the mistag probability.

The multiplicities for K^+ and K^- in B decays have been measured by the ARGUS [113] and CLEO collaborations:

$$\begin{aligned} n(B^0 \to K^+ X) &= 0.58 \pm 0.01 \pm 0.08 \\ n(B^0 \to K^- X) &= 0.13 \pm 0.01 \pm 0.05 \end{aligned} \tag{6.1}$$

The majority of kaons in the B decays have the right sign. Hence, the presence of an identified charged kaon provides a powerful flavor-tagging tool.

The main sources of wrong flavor tag using kaons is the presence of wrong-sign kaons and probability of mis-identifying pions as kaons.

6.1.3 Soft and hard pions from $D^{*\pm}$ decays

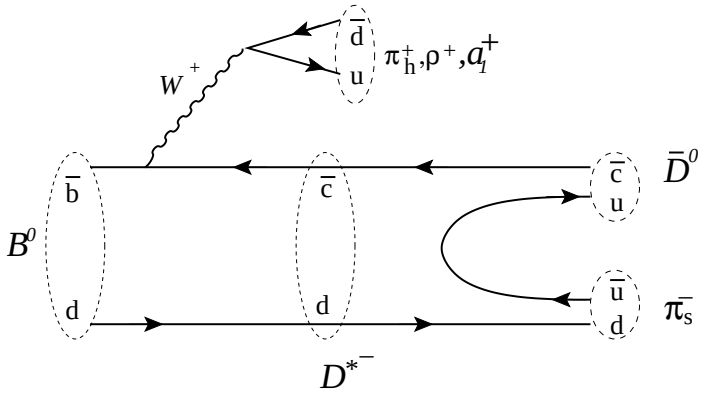

Figure 6.4: The $B^0 \to D^{*-}\pi^+, \rho^+, a_1^+$ decay. The charge of the soft pion $\pi_{\rm s}$ and that of the direct pion $\pi_{\rm h}$ are correlated with the flavor of the neutral B meson.

The decay $B^0 \to D^{*-}\pi^+, \rho^+, a_1^+$ in Figure 6.4 can be used to determine the flavor of neutral B mesons, from the charge of the π_s pion. The $\pi_{\rm s}$ meson has a very low momentum due to the small energy release $\Delta E \sim M(D^{*-}) - M(\overline{D}^0) \sim 146\,\mathrm{MeV}$ in the $D^{*-} \to \overline{D}^0\pi_s^-$ decay, and is called a soft pion. Therefore, its direction is very close to that of the $\overline{D}^0$ meson in the center of mass of the B meson (Figure 6.5). Soft pions can be identified with an inclusive algorithm based on the angular

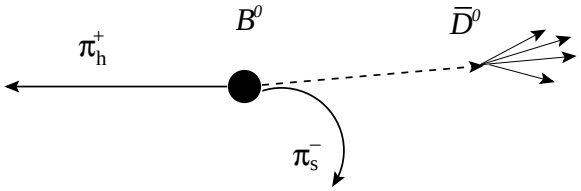

Figure 6.5: The $B^0 \to D^{*-}\pi^+$ decay in the B^0 center of mass.

correlation between low-momentum tracks and reconstructed $\overline{D}^0$ mesons.

Additional tagging information is available when the emitted W^+ hadronizes as a pion. The pion π_h has significant momentum in the decay $B^0 \to D^{*-}\pi^+$. The charge of π_h is opposite to that of the soft pion π_s and can be used to determine the B flavor.

6.2 The b-flavor–tagging algorithm

Several algorithms have been studied, in *BABAR*, to distinguish B^0 and $\overline{B}^0$ mesons in events with one fully reconstructed B meson ($B_{\rm rec}$ in Figure 6.6) in CP and flavor eigenstates.

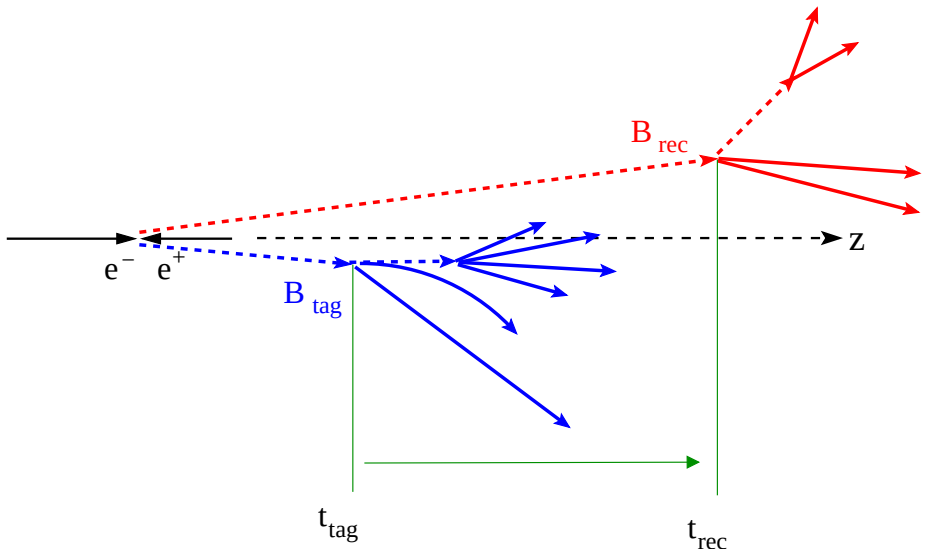

Figure 6.6: Topology of a $B\bar{B}$ event in which $B_{\rm rec}$ is fully reconstructed and the remaining particles are analyzed to determine the flavor of $B_{\rm tag}$.

Charged particles and neutral energy deposits utilized to reconstruct the $B_{\rm rec}$ candidate are removed, and the remaining particles are assigned to the other B meson, $B_{\rm tag}$. All algorithms attempt to determine the flavor of $B_{\rm tag}$ from its decay products by recognizing the processes described in the previous Section. Two algorithms use neural networks, whose inputs are the kinematic and angular properties of the $B_{\rm tag}$ decay products [114, 115]. These algorithms provide a probability for $B_{\rm tag}$ to be a B^0 or a $\overline{B}^0$ meson.

Another *cut-based* algorithm mainly selects clean samples of leptons and kaons, in order to determine the flavor of $B_{\rm tag}$ [116].

A fourth hybrid algorithm determines the flavor of $B_{\rm tag}$ with the cut-based algorithm, if leptons and kaons are positively identified, and utilizes neural networks otherwise [117].

The time-dependent analysis presented in this analysis is based on a new algorithm [118]. The structure of this algorithm is shown in Figure 6.7 and can be divided in two layers.

The first layer consists of several neural networks called subnets (blue rectangles). Each subnet is specialized in recognizing one of the characteristic signatures discussed in the previous Section. The input of subnets consists of kinematic properties of the $B_{\rm tag}$ decay products and particle-identification information. Each subnet provides a continuous output r_1^i between -1 and $+1$. Candidates with r_1 close to $+1(-1)$ are more likely to be a B^0 ($\overline{B}^0$).

A large sample of simulated events has been used to train the subnets. The training procedure also estimates the mistag probability p_w^i for each subnet. This is the probability of assigning the

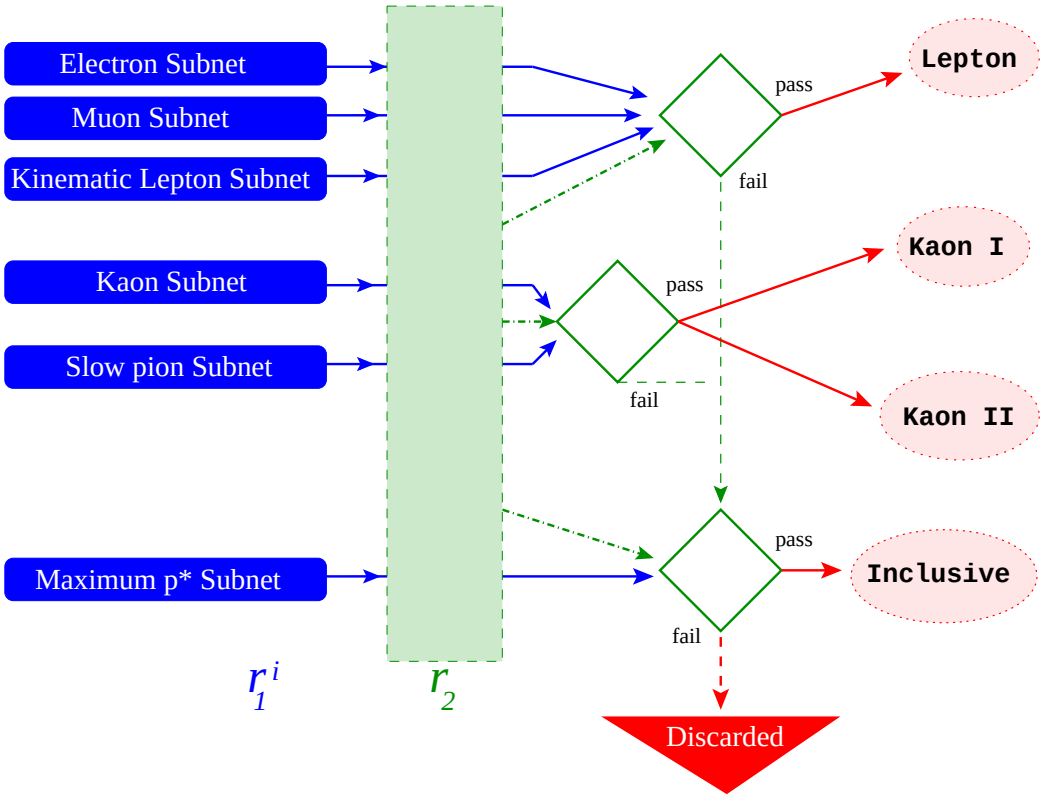

Figure 6.7: Structure of the b-flavor–tagging algorithm. The outputs r_1^i of each subnet are used by a neural network to produce a combined output r_2. Four tagging categories (red ellipses) are then defined based on the values of r_1^i and r_2.

wrong flavor tag to B_{tag}, on the basis of the subnet output r_1^i. The mistag probability depends on the physics processes used for flavor tagging, and varies within the subnets: an identified lepton, most likely, gives the correct flavor and has a low mistag probability. On the other hand, the selection of soft pions suffers from high background and has a large p_w.

The second layer is a neural network (green rectangle) that combines the output of the subnets. In the following discussion, this network is referred to as the *dispatch network*. The output of this network is another continuous variable r_2, similar to r_1, with values between -1 and $+1$.

The subnets with similar estimated mistag probabilities are grouped together, and B_{tag} candidates are assigned to four hierarchical mutually-exclusive categories `Lepton`, `Kaon I`, `Kaon II`, and `Inclusive`, on the basis of the values of r_1^i and r_2. The selection criteria for r_1^i and r_2 that define the tagging categories are discussed in detail in Reference [118], while a brief qualitative description is given in the next four subsections.

The motivation for having four categories is partly historical, and derives from the fact that

the hybrid tagging algorithm, previously used in this analysis, had four categories. However, the nature of the processes currently used for flavor tagging, the estimated mistag probabilities p_w for the subnets, and practical bookkeeping issues in the fit suggest that four categories are sufficient. Studies have been done with larger number of categories, including the limit of one category for each subnet, but no significant improvements in the precision of $\sin 2\beta$ have been observed.

The tagging efficiency ϵ and mistag fraction w of the four categories are measured in data, and are discussed in Section 9.2.2. The performance in simulated events is discussed in Section 6.3.

6.2.1 `Lepton` category

Electron and muons are treated separately because in general they have different detection efficiency and mis-identification probability. `Electron` and `Muon` subnets provide a flavor tag for events with an identified electron or muon. These subnets have the lowest mistag probability.

In absence of particle identification information, the `Kinematic Lepton` subnet selects candidate leptons on the basis of their kinematic variables, e.g. the center-of-mass momentum. This subnet suffers from higher backgrounds due to pions and kaons mis-identified as leptons.

Events are assigned to the `Lepton` category based on the values of $r_1^{\rm electron}$, $r_1^{\rm muon}$, and r_2. In presence of identified kaons, the value of $r_1^{\rm kaon}$ is also taken into account.

If the requirement criteria on r_1 and r_2 are not met, or the kaon and lepton outputs indicate opposite flavors, the events are retained for further analysis.

6.2.2 `Kaon I` and `Kaon II` categories

In events with only one identified kaon, the value of $r_1^{\rm kaon}$ is determined on the basis of the charge correlation between the sign of the kaon candidate and the B flavor. This approach suffers from the production of wrong-sign kaons which can not be discriminated from the right-sign, kaon based on their kinematic properties. For example, the the center-of-mass momentum of identified kaons in data is shown in Figure 6.8a, with overlaid the expected contributions from right-sign, wrong-sign, and mis-identified kaons. A large fraction of B decays have more than one charged kaon in the final state as shown in Figure 6.8b. In events with three identified kaon candidates, each candidate is analyzed under the hypothesis of being the only kaon in the event and is assigned a weight. The weighted-average of the charge of all three kaon candidates determines the value of $r_1^{\rm kaon}$.

The `Soft pion` subnet is, obviously, dedicated to the identification of slow pions, and although with a large mistag probability, contributes to flavor tagging.

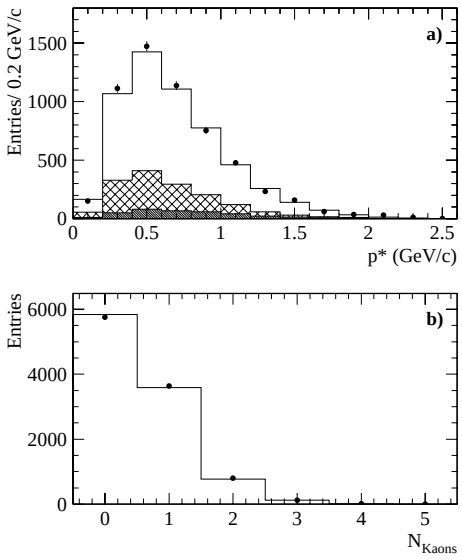

Figure 6.8: a) Center-of-mass momentum distribution for identified kaons in data (points), and contributions from right-sign (open histogram), wrong-sign (cross-hatched), and mis-identified (diagonally-hatched) kaons determined from simulation. b) kaon multiplicity in data.

Events are selected and assigned to the `Kaon I` and `Kaon II` categories by using $r_1^{\rm kaon}$, $r_1^{\rm slowpion}$ (if available), and r_2. When no soft pion is found, events are selected based on $r_1^{\rm kaon}$, and divided in `Kaon I` and `Kaon II` depending on r_2. The `Kaon I` category contains the events with higher $|r_2|$. When the output of the `Soft pion` subnet is available, it can either support the decision taken based on $r_1^{\rm kaon}$, or be in conflict with it, in which case events are retained for further analysis. Finally, in absence of kaons, events are assigned to the `Kaon II` category if the output of $r_1^{\rm slowpion}$ is above a required threshold. All other events are retained for further analysis.

6.2.3 `Inclusive` category

The last attempt to determine the flavor tag is through the `Maximum` p^* subnet, which uses the center-of-mass momentum of the charged tracks with an impact parameter smaller than $1{\rm mm}$, as its only discriminating variable. The purpose of this subnet is to identify fast tracks, e.g. fast pions from $B^0 \to D^{*-}\pi^+$ decays, and recover those primary leptons not assigned to the `Lepton` category. The output of this subnet determines whether events are assigned to the `Inclusive` category or discarded.

6.3 Performance of the b-flavor–tagging algorithm

The performance of the b-flavor–tagging algorithm in simulated events is reported in Table 6.1. These results are measured in a large sample of simulated $\Upsilon(4S) \rightarrow B\bar{B}$ events, with one B decaying to flavor eigenstates.

Category	$N_{\rm sig}$	ε(%)	$\langle w \rangle$(%)	Δw(%)	Q(%)
`Lepton`	11607 ± 108	10.3 ± 0.1	3.5 ± 0.3	-0.9 ± 0.5	8.9 ± 0.1
`KaonI`	19759 ± 141	17.5 ± 0.1	9.0 ± 0.3	-0.2 ± 0.5	11.8 ± 0.2
`KaonII`	22557 ± 150	20.0 ± 0.1	21.2 ± 0.4	-2.7 ± 0.6	6.6 ± 0.2
`Inclusive`	22330 ± 149	19.8 ± 0.1	30.9 ± 0.4	-3.2 ± 0.6	2.9 ± 0.1
Total	113050 ± 336	67.5 ± 0.2			30.2 ± 0.3

Table 6.1: The efficiency ε_i, average mistag fraction $\langle w_i \rangle$, mistag difference Δw_i, and tagging power $Q_i = \epsilon_i * (1 - 2\langle w_i \rangle)$ for each tagging category. $N_{\rm sig}$ is the number of simulated signal events.

The fraction w of wrongly tagged B^0 mesons can be different from the fraction $\overline{w}$ of mistagged $\overline{B}^0$ mesons. In order to account for such a difference the average mistag fraction $\langle w \rangle = (w + \overline{w})/2$ and the difference $\Delta w = w - \overline{w}$ are measured.

One observes that:

- About 2/3 of all selected B candidate are assigned a flavor tag;
- The `Lepton` category has the smallest mistag fraction, as expected;
- The `KaonI` and `KaonII` categories have the highest tagging efficiencies. As a consequence, although the mistag fractions are larger for these categories, compared to `Lepton`, they have a better effective tagging power Q;
- Categories `KaonII` and `Inclusive` show a significant difference in the mistag fractions for B^0 and $\overline{B}^0$ mesons. This is for example due to the different interaction cross sections of K^+ and K^- mesons with the i detector material, or different reconstruction efficiencies for negative and positive soft pions; and
- the total effective tagging power Q for all categories is about 30%. Intuitively, this is equivalent to a tagging efficiency with no mistag probability (perfect tagging).

Rather than using the above values in this analysis, the performance of the algorithm is measured directly in data with the sample of fully reconstructed flavor eigenstates. Two important reasons for not relying on Monte Carlo simulation are:

1. the reconstruction efficiency and pion mis-identification for both kaons and leptons are better in simulation than in data. Such a different can be caused by a non-completely realistic simulation of the detector response. The difference in particle identification can result in better tagging performance in simulation than in data;

2. only a small fraction of all B decays are today measured exclusively. The Monte Carlo generation of events uses the measured branching fractions for currently known B decay channels, and makes use of theoretical models to generate the remaining decay modes. This can result in different multiplicities of leptons and kaons in data and Monte Carlo, and therefore different mistag fractions.

In Chapter 8, the measurement of mistag fractions with the maximum-likelihood fit to Δt distributions in data is explained, and the results are discussed in Section 9.2.2.

Chapter 7

Time measurement at the $\Upsilon(4S)$

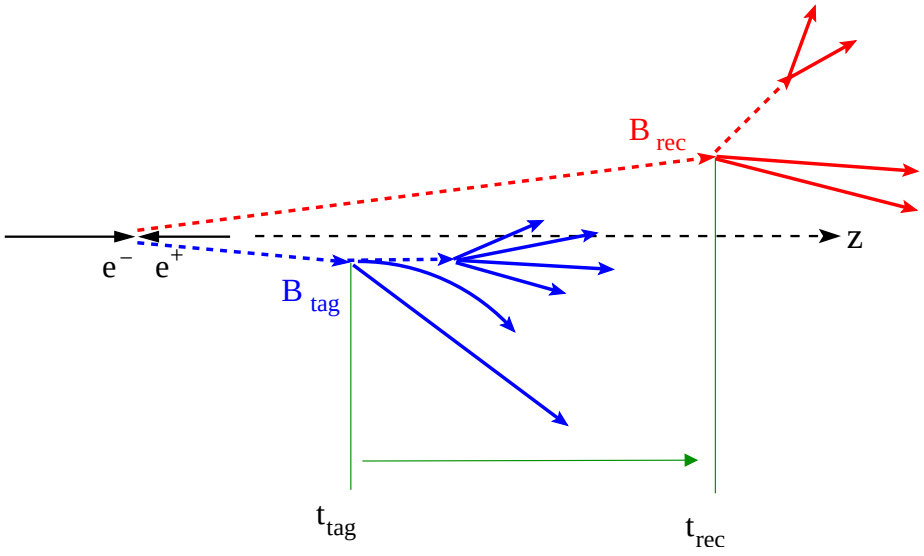

Figure 7.1: Schematic view of a $B\bar{B}$ events with one B meson fully reconstructed, $B_{\rm rec}$, and the other meson, $B_{\rm tag}$, used for flavor tagging.

The third ingredient of the time-dependent analysis of CP violation is the measurement of the time interval Δt between the decay of the fully reconstructed B meson, $B_{\rm rec}$, and the decay of the tagging B meson, $B_{\rm tag}$ (Figure 7.1). The value of Δt is computed from the spatial distance between the decay vertices of the two B mesons and the Lorentz boost factor $\beta\gamma$ of the $\Upsilon(4S)$.

The definition of Δt in *BABAR* is very different from previous experiments at the Tevatron, SLC, or LEP, due to the coherent production of $B\bar{B}$ pairs in the $\Upsilon(4S)$ decay, and is discussed in Section 7.1.

The vertex reconstruction techniques for $B_{\rm rec}$ and $B_{\rm tag}$ are described in Sections 7.2 and 7.3. A detailed discussion of their implementation can be found in Reference [119].

Due to the boost along the z axis, the measurement of Δt relies only on the Δz separation and is described in Section 7.4. However, the small momentum of the B mesons in the transverse plane results in small corrections when computing Δt from Δz. These corrections are discussed in Section 7.5.

Section 7.6 describes the resolution function model used to parameterize the detector resolution on Δt. This is dominated by the resolution on the $B_{\rm tag}$ vertex, and therefore a common resolution function is used for the samples of fully reconstructed B mesons in CP and flavor eigenstates. The comparison between the two samples is discussed in Section 7.7.

Finally, correlations between parameters of the resolution function and the flavor-tag mistag probabilities are discussed in in Section 7.8.

7.1 Definition of time difference Δt

The coherence of the $B\bar{B}$ state is a unique aspect of the PEP-II asymmetric e^+e^- collider at the $\Upsilon(4S)$ energy, and has important implications on the measurement of the B meson decay times.

As discussed in Section 2.4.3, the two neutral B mesons produced in the $\Upsilon(4S)$ decay are in a coherent state. If t_0 is the time when the $\Upsilon(4S)$ decays in two B mesons, there must be always one B^0 and one $\overline{B}^0$ for times $t > t_0$. This conditions holds until the decay of one of the two mesons, $B_{\rm tag}$, in a flavor eigenstate at time $t_{\rm tag} > t_0$. The flavor of the other B meson, $B_{\rm rec}$ which is fully reconstructed, must be opposite to the flavor of $B_{\rm tag}$, in order to satisfy the coherence condition.

Let's assume $B_{\rm tag} = \overline{B}^0$, and therefore $B_{\rm rec} = B^0$ at $t = t_{\rm tag}$. Two scenarios are possible for the decay of $B_{\rm rec}$:

1. $B_{\rm rec}$ decays after $B_{\rm tag}$, at time $t_{\rm rec} > t_{\rm tag}$ (Figure 7.2a). The time evolution of $B_{\rm rec}$ is described by Equation (2.50)

$$|B^0_{\rm rec}(t - t_{\rm tag})\rangle = g_+(t - t_{\rm tag})|B^0\rangle + (q/p)g_-(t - t_{\rm tag})|\overline{B}^0\rangle, \tag{7.1}$$

   with $|B^0_{\rm rec}(0)\rangle = |B^0\rangle$. At time $t_{\rm rec}$, $B_{\rm rec}$ decays to the final state f as a B^0 or a $\overline{B}^0$, depending on the time difference $\Delta t \equiv t_{\rm rec} - t_{\rm tag}$, which in this case is positive. The flavor of $B_{\rm rec}$ is known at $t_{\rm rec}$, if f is a flavor eigenstate. If $B_{\rm rec} = \overline{B}^0$ at $t_{\rm tag}$, then oscillation has occurred ($B^0 \to \overline{B}^0$) and the event is called **mixed**, otherwise $B_{\rm rec}$ is still a B^0, and the event is called **unmixed**.

When f is a CP eigenstate, the flavor of $B_{\rm rec}$ is not known at $t_{\rm rec}$. The event is called $\overline{B}^0$**-tagged**, since $B_{\rm tag}$=$\overline{B}^0$.

2. $B_{\rm rec}$ decays to the final state f at time $t_{\rm rec}$, with $t_{\rm tag} > t_{\rm rec} > t_0$ (Figure 7.2b), and $\Delta t < 0$. If f is a CP eigenstate, the flavor of $B_{\rm rec}$ is not known at $t_{\rm rec}$, but its time evolution is still described by Equation (7.1) with the constraint that when $B_{\rm tag}$ decays at $t_{\rm tag}$, it must be a B^0. In other words, the boundary condition is not specified at the initial time $t_{\rm rec}$ but at $t_{\rm tag}$.

   When f is a flavor eigenstate, the flavor of $B_{\rm rec}$ is known at $t_{\rm rec}$ from reconstructing the final state, and at $t_{\rm tag}$ from the flavor of $B_{\rm tag}$. On the other hand, once $B_{\rm rec}$ decays, its flavor can not change. Therefore, if $B_{\rm rec} = \overline{B}^0$, $B_{\rm tag}$ should be a B^0 at that same time and must undergo oscillation in order to decay as a $\overline{B}^0$ at $t_{\rm tag}$. Alternatively, when the flavor of $B_{\rm rec}$ is found to be the same at both times, one concludes that $B_{\rm tag}$ has not oscillated.

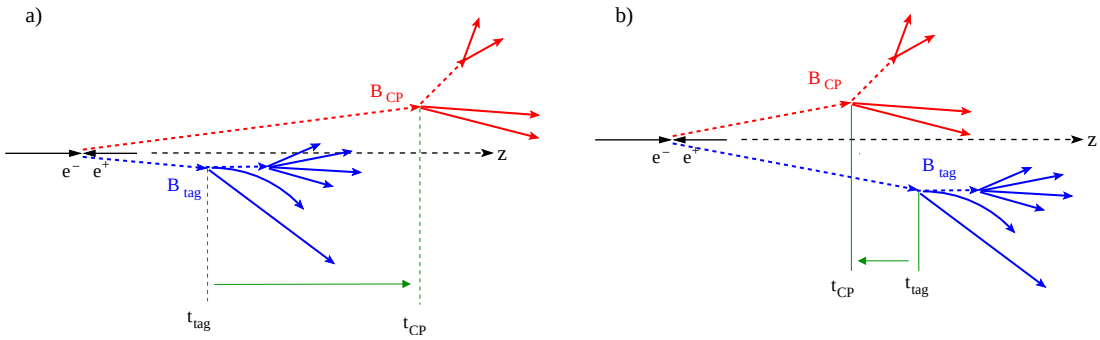

Figure 7.2: The sign of $\Delta t \equiv t_{\rm rec} - t_{\rm tag}$ can be a) positive or b) negative, depending on the decay order.

From the above scenarios for the decays of $B_{\rm rec}$ and $B_{\rm tag}$, one concludes that:

- the decay of $B_{\rm tag}$ in flavor eigenstates defines the start of the clock for time measurements; and

- the evolution of the B mesons is a function of the interval $\Delta t \equiv t_{\rm rec} - t_{\rm tag}$, and does not depend on the $\Upsilon(4S)$ decay time t_0.

The value of Δt can be measured by reconstructing the decay vertices of the B mesons, and by measuring the spatial separation between them, without reconstructing the $\Upsilon(4S)$ decay point.

The distance is then converted in Δt by using the boost factor $\beta\gamma$ that is known from the beam energies. The Δt distribution in the $\Upsilon(4S)$ decays is shown in Figure 7.3, and is described by a

two-sided exponential $\mathrm{e}^{-|\Delta t|\tau_{B^0}}/\tau_{B^0}$, reflecting the fact that the decay of B_{tag} can occur before ($\Delta t > 0$) or after ($\Delta t < 0$) the decay of B_{rec}.

At other colliders, operating at the Z^0 energy or in hadron colliders, B mesons are produced without any correlation between them (incoherent production) at the interaction point, which is known with good precision and provides the reference time t_0. The time interval is defined as $\Delta t \equiv t_{\mathrm{decay}} - t_0$ and is measured from the distance between the decay and interaction points. Since the decay happens after the production, Δt is always positive. The distribution of Δt in this case is a one-sided exponential described by $\mathrm{e}^{-\Delta t/\tau_{B^0}}/\tau_{B^0}$, and is shown in Figure 7.3.

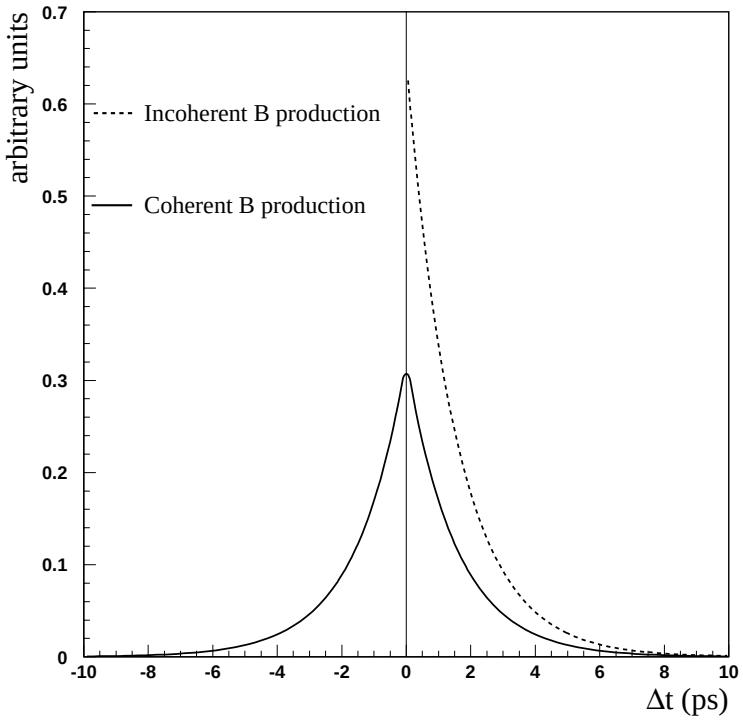

Figure 7.3: Distribution of Δt with for coherent and incoherent production of B mesons.

7.2 The B_{rec} vertex

The decay vertex of the B_{rec} candidate is reconstructed by using all its decay daughters in the final state. However, since neutral particles, like π^0s and photons, do not carry any spatial information, in practice only the charged daughter particles contribute.

As mentioned in Section 5.4, charged tracks originating from intermediate states, e.g. a D^0 or a K_S^0 are replaced by *virtual* composite candidates and appropriate spatial and kinematic constraints are used in the fit to the $B_{\rm rec}$ vertex.

The typical resolutions on the position of the vertex along the z axis and in the transverse plane are $\approx 45\,\mu{\rm m}$ and $\approx 65\,\mu{\rm m}$, for the $B_{\rm CP}$ and $B_{\rm flav}$ samples, respectively.

7.3 The $B_{\rm tag}$ vertex

The decay vertex of the $B_{\rm tag}$ candidate is reconstructed with an inclusive technique, using those charged tracks not utilized in the reconstruction of $B_{\rm rec}$.

Pairs of oppositely-charged tracks consistent with photon conversions ($\gamma \rightarrow e^+e^-$) are excluded. Charged tracks originating from long-lived particles, K_S^0s and Λ^0s, are removed and replaced by the reconstructed composite candidates in order to reduce potential biases. These composite candidates and the remaining charged tracks are used as input in a geometrical fit to determine a common decay vertex.

The estimated production point of the B^0 $\overline{B}^0$ pair and the three-momentum of the $B_{\rm tag}$ candidate are incorporated in the fit as kinematic and geometric constraints. This is illustrated in Figure 7.4. The three-momentum $\vec{p}_{\rm rec}$ and the decay vertex of the $B_{\rm rec}$ candidate are measured with good precision and the average interaction point (beamspot) is known as well. The intersection of $\vec{p}_{\rm rec}$ with the beamspot provides a good estimate of the production point of the B^0 $\overline{B}^0$ pair. The three-momentum $\vec{p}_{\Upsilon(4S)}$ of the $\Upsilon(4S)$ is measured from the beam energies. Momentum conservation yields $\vec{p}_{\rm tag} = \vec{p}_{\Upsilon(4S)} - \vec{p}_{\rm rec}$.

The common vertex is determined with an iterative procedure. After each iteration, tracks with a large contribution to the fit χ^2 ($\Delta\chi^2 > 6$) are removed, and the vertex is recomputed until no track fails the χ^2 requirement, or only two tracks are left. This procedure is aimed at reducing contributions from decay daughters of charmed mesons, which have a long decay length.

For example, the D^0 and D^+ mesons have a decay lengths $c\tau$ of about, $130\,\mu{\rm m}$ and $300\,\mu{\rm m}$, respectively, which result in a decay vertex detached from the B decay point. Figure 7.5a shows the correct $B_{\rm tag}$ vertex when the decay daughters of the charmed meson are excluded. The inclusion of a D^0 daughter in Figure 7.5b results in a biased position of the vertex. In fact, since all particles are boosted forward, $z_{\rm tag}^{\rm meas} = z_{\rm tag}^0 + \delta z$, where δz is the bias and is positive. Since Δz is defined as $z_{\rm rec} - z_{\rm tag}$, the measured distance is $\Delta z^{\rm meas} = \Delta z^0 - \delta z$, and the induced bias $-\delta z$ is always negative.

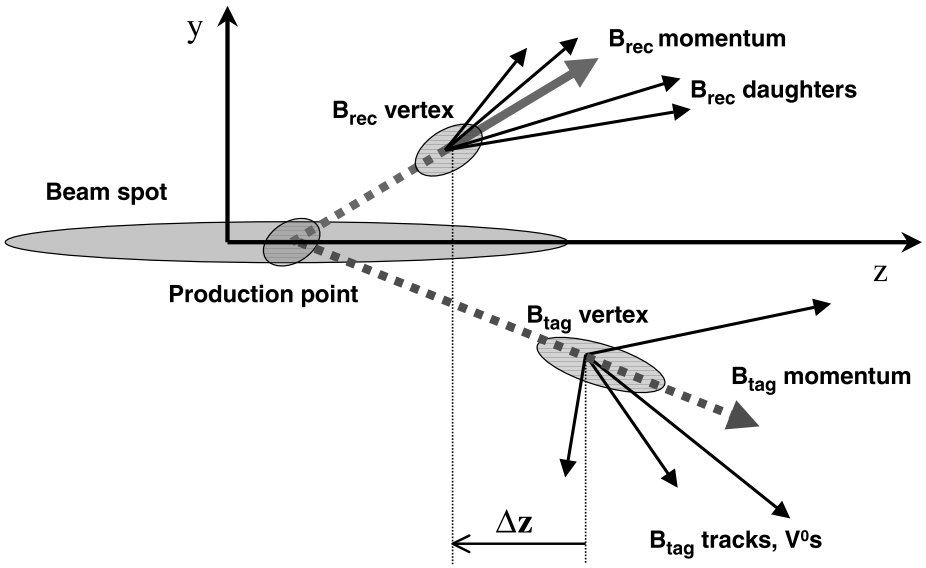

Figure 7.4: Schematic view of the $\Upsilon(4S) \to B\overline{B}$ decay in the y-z plane. Note that the scale in the y direction is substantially magnified compared to that in the z direction for illustration purposes.

7.4 Measurement of Δz between the B decay vertices

The spatial separation between the $B_{\rm rec}$ and $B_{\rm tag}$ decay points is computed from the reconstructed decay vertices. Although the decay points are known in three dimensions, because of the boost along the z axis, only Δz is significant.

In the $\Upsilon(4S)$ rest frame, B mesons are produced with an average momentum of $340\,{\rm MeV}/c$, which corresponds to a Lorentz boost of $\beta\gamma \sim 0.06$, and an average decay length $\beta\gamma\, c\tau \sim 17\,\mu{\rm m}$ along each axis. Since the two mesons are produced back-to-back in this frame, the average separation between them is about $30\,\mu{\rm m}$ along the z axis, and about $50\,\mu{\rm m}$ in the transverse x-y plane.

In the laboratory frame, the $\Upsilon(4S)$ meson is boosted along the z axis with $\beta\gamma = 0.55$. This results in an average separation $|\Delta z|$ of $260\,\mu{\rm m}$ while the separation $|\Delta\ell|$ in the transverse plane is unchanged. A precise measurement of $\Delta\ell$ is beyond the reach of the *BABAR* tracking system, while Δz can be measured with good precision. The value of Δz is determined directly in the $B_{\rm tag}$ vertex fit. The fit also provides a correct estimate of the uncertainty $\sigma_{\Delta z}$ by taking into account the correlation between the $B_{\rm tag}$ and $B_{\rm rec}$ vertices. The origin of this correlation is in the use of kinematic properties of $B_{\rm rec}$, as constraints in the $B_{\rm tag}$ vertex fit. The direction of $B_{\rm tag}$ is estimated by using the $B_{\rm rec}$ vertex and its measured three-momentum. Therefore, variations in the $B_{\rm rec}$ direction and decay vertex affect directly the position of the $B_{\rm tag}$ vertex.

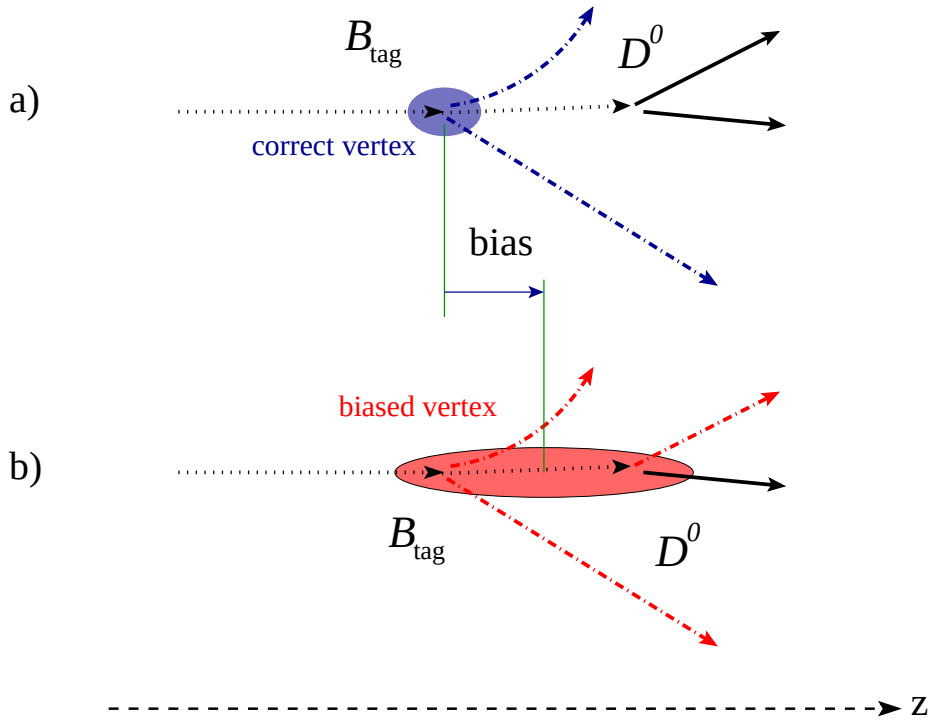

Figure 7.5: a) The correct $B_{\rm tag}$ vertex and b) the biased vertex position when the D^0 decay daughter is included. The ellipse represents the estimated uncertainty. The dash-dotted lines are the tracks used to compute the position of the vertex.

The resolution on Δz is measured in data and is discussed in Section 7.6. In simulated events, the distribution of the residual $\delta_z \equiv \Delta z_{\rm meas} - \Delta z_{\rm true}$ is fit with a sum of three Gaussian distributions. The RMS of the two narrow components (core and tail) is about 190 μm. The core component alone has an RMS of 100 μm and contains about 70% of the events, while the wide component (outliers) contains only 1% of the events.

7.5 Measurement of Δt

A naive estimate of the difference Δt is given by the relation

$$\Delta z = \beta\gamma c \Delta t \ , \tag{7.2}$$

where $\beta\gamma = 0.55$ is the $\Upsilon(4S)$ Lorentz boost factor, and is known with a precision of 0.1%. Its value is calculated from the beam energies which are monitored every 5 seconds. The spread of the beam energies results in an RMS spread of 6 MeV/c in the $\Upsilon(4S)$ momentum, but this has a negligible effect on $\beta\gamma$.

Relation (7.2) is an exact expression in the limit of B mesons being at rest in the $\Upsilon(4S)$ frame, and the boost being exactly along the z axis. In practice, the detector symmetry axis is rotated with respect to the beams, and therefore the boost axis, by $20\,\mathrm{mrad}$ as discussed in Section 4.1. Furthermore, the B mesons have a momentum of about $340\,\mathrm{MeV}/c$ in the $\Upsilon(4S)$ frame.

The rotation is incorporated through the Lorentz transformations, and the measured momentum of the B_{rec} candidate can be used to correct (7.2) and account for the B momentum. The relation between Δt and Δz, including these corrections, is given by [120]

$$\Delta z = \beta\gamma\gamma^*_{\mathrm{rec}} c\Delta t + \gamma\beta^*_{\mathrm{rec}}\gamma^*_{\mathrm{rec}}\cos\theta^*_{\mathrm{rec}}\, c\,\langle t_{\mathrm{rec}} + t_{\mathrm{tag}}\rangle \tag{7.3}$$

where θ^*_{rec}, β^*_{rec}, and γ^*_{rec} are the polar angle with respect to the beam direction, the velocity, and the boost factor of B_{rec} in the $\Upsilon(4S)$ frame, and $\langle t_{\mathrm{rec}} + t_{\mathrm{tag}}\rangle$ is the expected value for the sum of the decay times.

In order to compute $t_{\mathrm{rec}} + t_{\mathrm{tag}}$, one should know the $\Upsilon(4S)$ decay time, and hence its decay point. The precision of this point can not be better than the B_{tag} vertex since an inclusive method must be used in order to have reasonably high efficiencies. Instead of measuring the sum $t_{\mathrm{rec}} + t_{\mathrm{tag}}$, its expected value can be estimated by

$$\langle t_{\mathrm{rec}} + t_{\mathrm{tag}}\rangle = \tau_B + |\Delta t| \tag{7.4}$$

The variation in Δt when using (7.3) in place of (7.2) is small because $\gamma^*_{\mathrm{rec}} = 1.002$, and $\beta^*_{\mathrm{rec}} = 0.064$. This difference is computed for each event and has an RMS spread of 0.20 ps which is small compared to the B^0 lifetime of $1.542 \pm 0.016\,\mathrm{ps}$ [33]. Relation (7.3) improves the resolution on Δt by about 5%.

7.6 Δt resolution function

The measured and true values of Δt differ due to the finite resolution of the detector in the measurement of decay vertices. The detector response for Δt, called the Δt resolution function, is parameterized with a sum of three Gaussian distributions (core, tail, and outliers components) as a function of the residual $\delta_t \equiv \Delta t_{\mathrm{meas}} - \Delta t_{\mathrm{true}}$ as

$$\mathcal{R}(\delta_{\mathrm{t}};\hat{a}) \;=\; \sum_k^{\mathrm{core,tail}} \frac{f_k}{S_k\sigma_{\Delta t}\sqrt{2\pi}} \exp\left(-\frac{(\delta_{\mathrm{t}} - b_k\sigma_{\Delta t})^2}{2(S_k\sigma_{\Delta t})^2}\right) + \frac{f_{\mathrm{outl}}}{\sigma_{\mathrm{outl}}\sqrt{2\pi}} \exp\left(-\frac{\delta_{\mathrm{t}}^2}{2{\sigma_{\mathrm{outl}}}^2}\right) \tag{7.5}$$

where f_k is the fraction of events in each component, and the other parameters are described below. All parameters of the Δt resolution function are measured in data with a maximum-likelihood fit described in Chapter 8.

The width σ of the core and tail components can be written as

$$\sigma_{\rm core} = S_{\rm core}\ \sigma_{\Delta t} \quad , \quad \sigma_{\rm tail} = S_{\rm tail}\ \sigma_{\Delta t}$$

where $\sigma_{\Delta t}$ is the measured uncertainty on Δt, and $S_{\rm core}$ and $S_{\rm tail}$ are scale factor parameters. These factors account for an overall underestimate ($S_k > 1$) or overestimate ($S_k < 1$) of the uncertainty $\sigma_{\Delta t}$ for all events. Figure 7.6a shows the correlation between the RMS spread of Δt and $\sigma_{\Delta t}$ in simulated events.

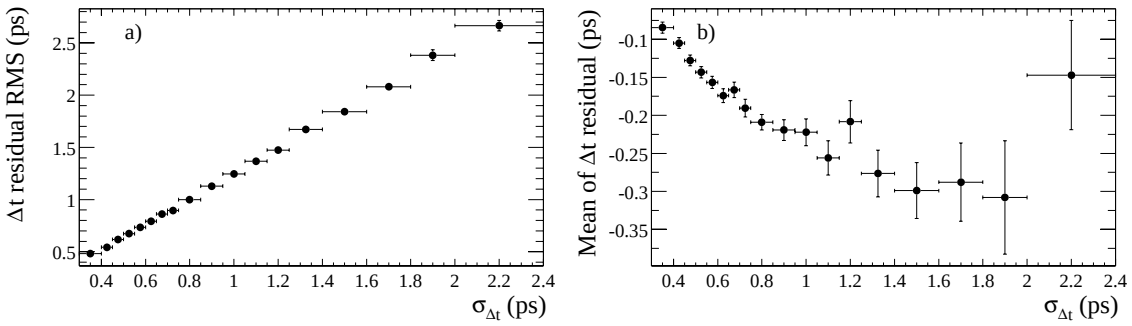

Figure 7.6: Correlation between $\sigma_{\Delta t}$ and a) the RMS spread and b) the mean of the residual $\delta_t = \Delta t_{\rm meas} - \Delta t_{\rm true}$, in simulated events.

The core and tail Gaussians are allowed to have a non-zero mean offset δ_0 to account for residual charm decay products included in the $B_{\rm tag}$ vertex. These offsets are proportional to the uncertainty $\sigma_{\Delta t}$ as shown in Figure 7.6b and are therefore parameterized as

$$\delta^0_{\rm core} = b_{\rm core}\ \sigma_{\Delta t} \quad , \quad \delta^0_{\rm tail} = b_{\rm tail}\ \sigma_{\Delta t}\ .$$

The origin of this correlation is illustrated in Figure 7.7, where the ellipse represents the uncertainty on the position of the $B_{\rm tag}$ vertex. The main contribution of the D^0 decay daughters to the vertex uncertainty is along the D^0 flight direction. The D^0 flight length along the z axis also is correlated to the D^0 flight direction, and contributes to the bias on the $B_{\rm tag}$ vertex. Therefore the bias and the uncertainty of the $B_{\rm tag}$ vertex are correlated, due to their correlation with the D^0 flight direction.

The D mesons with flight direction perpendicular to the z axis in the laboratory frame have the best z resolution, and introduce the smallest bias in the measured z position of the $B_{\rm tag}$ vertex. On the contrary, D mesons that travel forward in the laboratory have poorer z resolution, and introduce a larger bias in the position of the $B_{\rm tag}$ vertex.

The outliers component has a fixed width of $8\,{\rm ps}$ and no offset and accounts for 0.3% of selected events, which have mis-reconstructed vertices.

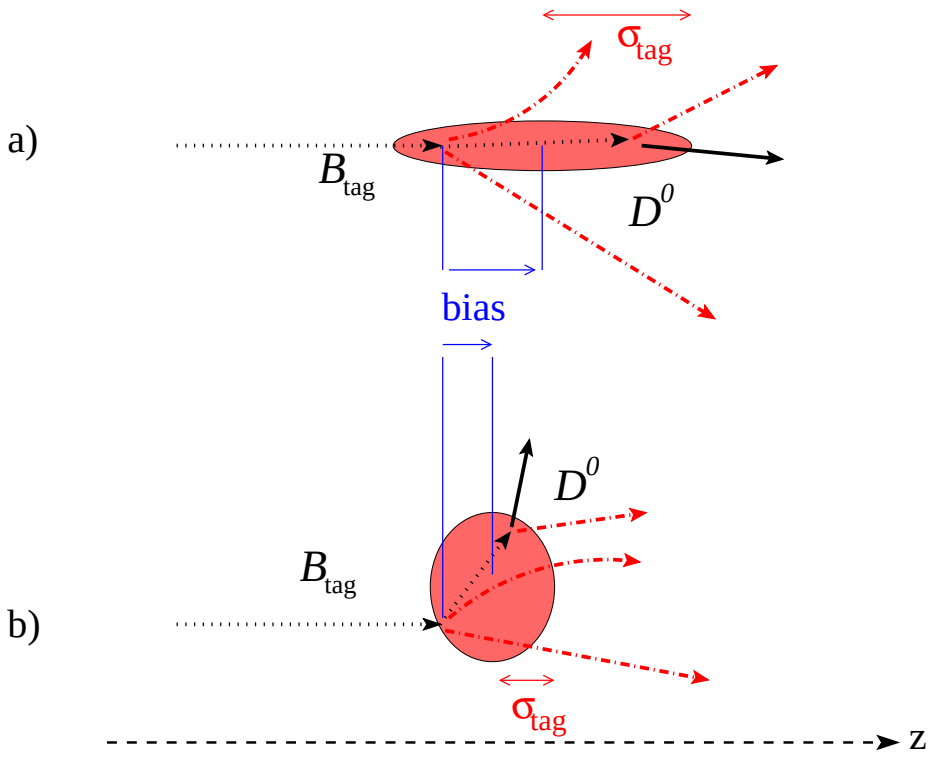

Figure 7.7: Correlation between the bias of the $B_{\rm tag}$ vertex and its uncertainty $\sigma_{\rm tag}$ when a) the D^0 flies in the direction of $B_{\rm tag}$, or b) the D^0 is perpendicular to the direction of $B_{\rm tag}$.

7.7 Comparison of Δt in CP and flavor eigenstates

There are two important assumptions in this analysis:

- the event-by-event uncertainty from the vertex fit provides a good measure of $\sigma_{\Delta t}$; and
- a common Δt resolution function can be used for events with fully reconstructed B mesons in CP and flavor eigenstates.

Several studies with data and simulated events are performed to validate these assumptions and are described in detail in Reference [121].

In Section 7.2, it was reported that the uncertainty on the reconstructed $B_{\rm rec}$ vertex varies between 45 and 65 μm for the $B_{\rm CP}$ and $B_{\rm flav}$ samples. However, since the resolution on the $B_{\rm tag}$ vertex is around 190 μm (Section 7.3), the two samples are expected to have similar Δz resolutions, and therefore a common Δt resolution function is used for both samples.

Note that, this assumption does not require the distribution of $\sigma_{\Delta t}$ to be identical for the two samples. In fact, the topology of the $B_{\rm rec}$ vertex is different for CP and flavor eigenstates. For ex-

ample, the flavor eigenstates have generally higher multiplicities. Figure 7.8 shows the distribution of the uncertainty $\sigma_{\Delta t}$, separately for CP and flavor eigenstates. The expected distributions from simulated events are also shown (open histogram) and the agreement with data is satisfactory for both samples.

Events in the $B_{\rm CP}$ sample have a slightly better Δt resolution. In simulated events the most probable value for $\sigma_{\Delta t}$ is about 3% worse for the $B_{\rm flav}$ sample. The effect of this difference in the time-dependent CP analysis is negligible and is accounted for in the systematic uncertainty (Section 9.4.2).

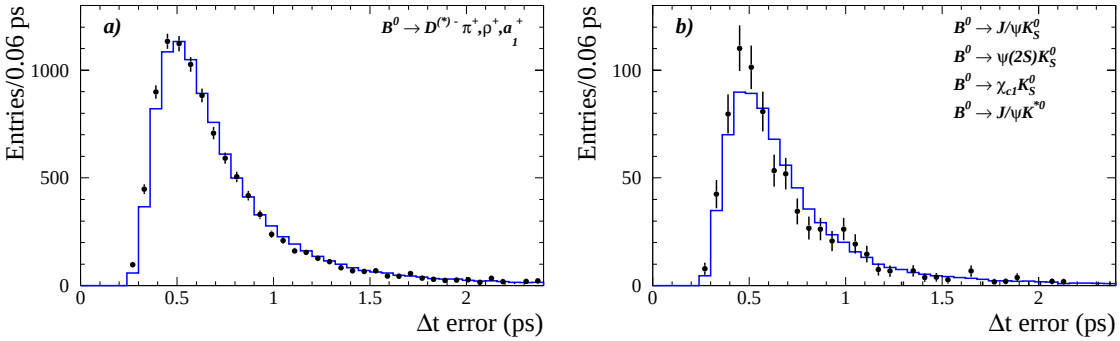

Figure 7.8: Distribution of $\sigma_{\Delta t}$ for a) the $B_{\rm flav}$ sample excluding the $J/\psi\, K^{*0}(K^+\pi^-)$ mode and b) the $B_{\rm CP}$ sample together with the $J/\psi\, K^{*0}$ mode. Points are from data and the open histogram is the expected distribution from Monte Carlo simulation.

7.8 Correlations between mistag fraction w and $\sigma_{\Delta t}$

A correlation is observed between the measured $\sigma_{\Delta t}$ and the mistag fractions w_i of the tagging categories [122, 123], as shown in Figure 7.9. The correlation is stronger for the categories using kaons for flavor tagging, and is, almost entirely, due to the dependence of both w and $\sigma_{\Delta t}$ on the transverse momentum p_t of the particles used for flavor tagging, and in the $B_{\rm tag}$ vertex [124].

The value of $\sigma_{\Delta t}$ is computed from $\sigma_{\Delta z}$, which is dominated by the uncertainty $\sigma_{z_{\rm tag}}$ on the position of the $B_{\rm tag}$ vertex. The contribution σ_{z_i} of each charged track to $\sigma_{z_{\rm tag}}$ is of the form

$$\sigma^2_{z_i} \propto \frac{1}{p^2_{t_i}} \tag{7.6}$$

and therefore

$$\frac{1}{\sigma^2_{z_{\rm tag}}} = \sum_i \frac{1}{\sigma^2_{z_i}} \propto \sum_i p^2_{t_i}\,. \tag{7.7}$$

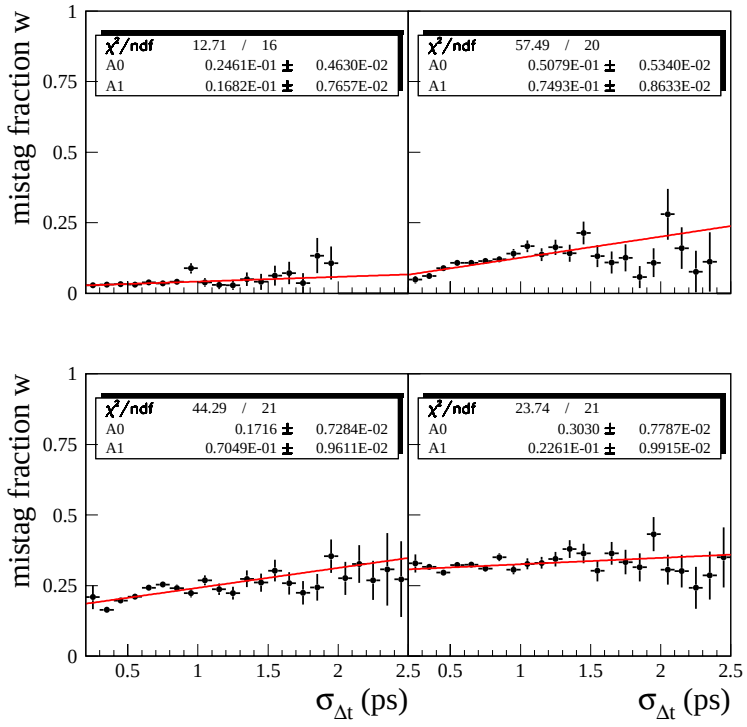

Figure 7.9: Correlation between the mistag fractions w_i and the measured $\sigma_{\Delta t}$.

In other words, the position of the vertices composed of high-momentum tracks is known with smaller uncertainty. Figure 7.10 shows the correlation between $\sigma_{\Delta t}$ and $\alpha \equiv 1/\sum_i \sqrt{p_{t_i}^2}$ in simulated events.

The mistag fractions w_i depend on α as well, as illustrated in Figure 7.11. A study of the B decays in Monte Carlo simulation [123] shows that, the momentum spectrum of the particles in the final state is softer in events with a wrong flavor tag. This is illustrated in Figure 7.12, where the distribution of $1/\alpha$ is shown separately for the correctly- and wrongly-tagged events in the four categories.

The correlation is stronger for the `KaonI` and `KaonII` categories, which rely mainly on identified kaons in the final state for flavor tagging. In Section 6.1.2, it was shown that a K^+ (correct sign), or a total positive charge of all kaons, is associated to a B^0 meson, while a K^- (wrong-sign), or a total negative charge for all kaons, indicates a $\overline{B}^0$. The probability of assigning the wrong flavor tag, based on the charge of the kaons, is higher because of the presence of wrong-sign kaons in many B decays. It is found that usually the wrong-sign kaons are present in events with higher multiplicity of particles in the final state, which results in a softer momentum spectrum.

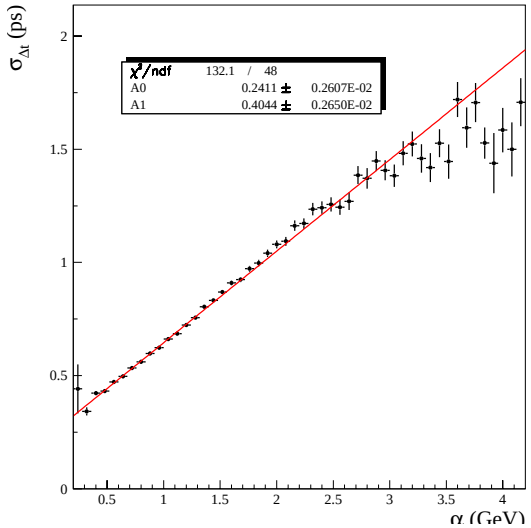

Figure 7.10: Correlation between $\sigma_{\Delta t}$ and α in simulated events.

For example the decays $B \to DDK$ can produce many kaons, and have a higher probability of being mistagged. Since the charmed D mesons are heavy, the presence of two of them in the final state results in a softer momentum for all their decay products.

Events with only one $\overline{D}^0$ or one D^- can be mistagged if the D meson produces a wrong-sign kaon. The D mesons mostly produce correct-sign kaons, e.g. $D^-, \overline{D}^0 \to K^+ X$, but can also produce a wrong-sign kaon K^-, at the cost of additional particles, in order to conserve the total charge. For example, the decay $D^- \to K^+\pi^-\pi^-$ has only three tracks and one correct-sign kaon, while $D^- \to K^-K^+\pi^-\pi^0$ has two oppositely charged kaons and four particles. The latter decay produces lower momentum particles, and increases the probability of the event being assigned the wrong flavor tag. The branching fractions for such decays are different for $\overline{D}^0$ and D^- and are studied in Reference [123].

The effect of the correlation between w_i and $\sigma_{\Delta t}$ on the measured CP asymmetry is small, and is discussed in Section 8.4.4.

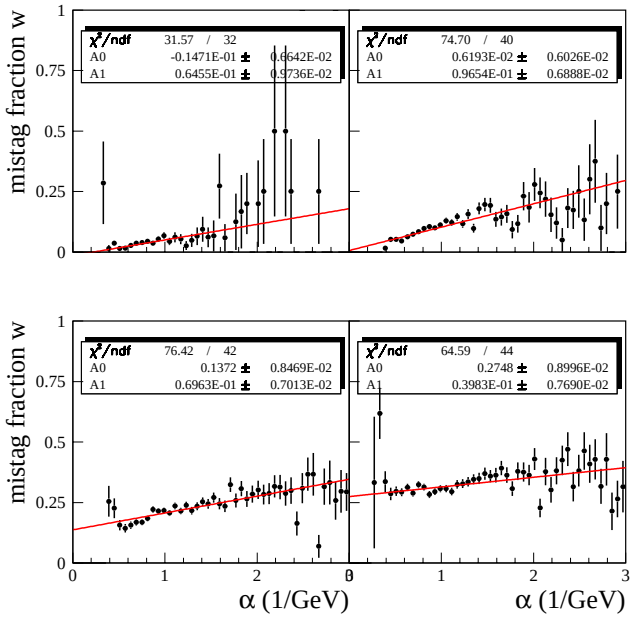

Figure 7.11: Correlation between $\alpha \equiv 1/\sum_i \sqrt{p_{t_i}^2}$ and the mistag fractions w_i for the four tagging categories.

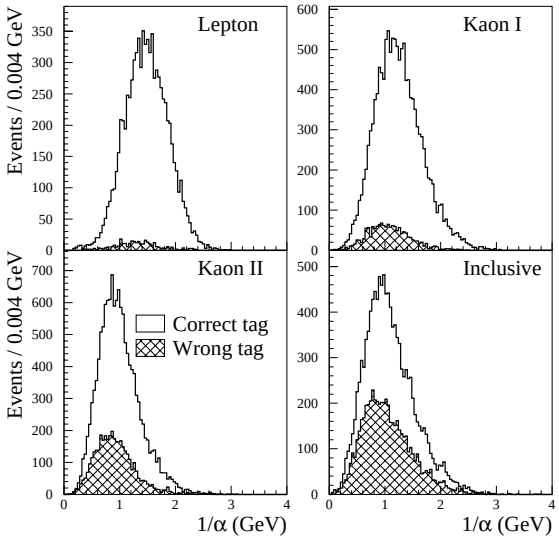

Figure 7.12: Distribution of α in simulated events. Events with the wrong flavor tag have generally a softer momentum spectrum resulting in a higher average α.

Chapter 8

Likelihood fit method

The CP asymmetry amplitude $\sin 2\beta$ is measured with a maximum-likelihood fit to the Δt distributions of events with one fully reconstructed B meson in CP eigenstates ($B_{\rm CP}$ sample) discussed in Section 5.5. The B flavor of these mesons is determined with the inclusive flavor-tagging algorithm described in Section 6.2. The theoretical Δt distributions for these events were introduced in Section 2.4.4. Those expressions are valid for a perfect detector and do not take into account the finite detector resolution on Δt (Section 7.6) and the probability of assigning the wrong flavor tag (mistag fractions) to a reconstructed B meson. Mistag fractions can not be determined with the $B_{\rm CP}$ sample and must be provided as input to the fit. The fully reconstructed B mesons in flavor eigenstates ($B_{\rm flav}$ sample) can be used to measure the mistag fractions in data.

In principle, one can measure the detector parameters with the $B_{\rm flav}$ sample and fix them in the analysis of the $B_{\rm CP}$ sample. But this approach has the disadvantage that correlations between $\sin 2\beta$ and the detector parameters can result in complicated systematic uncertainties. A better approach, which is used in this analysis, is to perform a maximum-likelihood fit to the Δt distributions of the $B_{\rm flav}$ and $B_{\rm CP}$ samples. The former are used to measure the detector parameters, while the latter constrain the value of $\sin 2\beta$. The advantage of this approach is that correlations among all parameters are properly taken into account and are part of the statistical uncertainty, which does not increase significantly, because of the weak correlation between $\sin 2\beta$ and the other parameters.

The maximum-likelihood fit used to measure $\sin 2\beta$ is described in this Chapter. Section 8.1 starts with the description of the likelihood functions for the events in the $B_{\rm CP}$ sample. The signal likelihood functions are derived from the theoretical distributions by incorporating the mistag fractions and the Δt resolution function. The $B_{\rm CP}$ sample includes a small fraction of background events for which an empirical approach is used to model the likelihood functions. Likelihood func-

tions for the signal and background components of the $B_{\rm flav}$ sample are described in Section 8.2. In the fit to the data, some of the parameters are fixed due to the limited statistics. The free parameters in the fit are summarized in Section 8.3.

Section 8.4 gives a summary of studies performed with simulated events to validate the fitting method. A small but significant bias on the value of $\sin 2\beta$ is observed and is discussed in Section 8.4.3. The expected statistical uncertainty on $\sin 2\beta$, and its dependence on the performance of the b-flavor–tagging algorithm and on the Δt resolution, are discussed in Section 8.5.

8.1 Likelihood function for CP eigenstates

The likelihood function for the events in the $B_{\rm CP}$ sample can be written as

$$\ln \mathcal{L}_{CP} = \sum_{i}^{N_c} \left[\sum_{B^0 \ {\rm tag}} \ln \mathcal{F}_{+,i} + \sum_{\overline{B}^0 \ {\rm tag}} \ln \mathcal{F}_{-,i} \right], \tag{8.1}$$

where $N_c = 4$ is the number of tagging categories, and $\mathcal{F}_{+,i}(\mathcal{F}_{-,i})$ is the likelihood function for events in the $i^{\rm th}$ tagging category with $B_{\rm tag} \equiv B^0$ and $\overline{B}^0 \to f_{CP}$ ($B_{\rm tag} \equiv \overline{B}^0$ and $B^0 \to f_{CP}$). It is customary to refer to the events based on the flavor of $B_{\rm tag}$. Therefore in the following, a B^0-*tagged* event is an event with $B_{\rm tag} \equiv B^0$ and $\overline{B}^0 \to f_{CP}$, while a $\overline{B}^0$-*tagged* has $B_{\rm tag} \equiv \overline{B}^0$ and $B^0 \to f_{CP}$. The four tagging categories are mutually exclusive which means that each event can only belong to one category, and can be tagged as either a B^0 or a $\overline{B}^0$. Therefore the two sums in Equation (8.1) are equivalent to a sum over all tagged $B_{\rm CP}$ events. Events without a flavor tag can not be used to measure $\sin 2\beta$, as explained below, and are excluded from the fit.

The likelihood functions $\mathcal{F}_{\pm,i}$ can be expressed as a sum of three contributions

$$\mathcal{F}_{\pm,i} = f^{CP}_{i,{\rm sig}} \mathcal{F}_{\pm} + f^{CP}_{i,{\rm pk}} \mathcal{B}^{CP}_{\pm,i,{\rm pk}} + f^{CP}_{i,{\rm comb}} \mathcal{B}^{CP}_{\pm,i,{\rm comb}} \, , \tag{8.2}$$

where $\mathcal{F}_{\pm}$ are the signal components, $\mathcal{B}^{CP}_{\pm,i,{\rm pk}}$ are the contributions of the peaking background, and $\mathcal{B}^{CP}_{\pm,i,{\rm comb}}$ are the combinatorial-background components. Sources of the peaking background for the CP eigenstates were discussed in Section 5.5.

The probabilities $f^{CP}_{i,{\rm sig}}$, $f^{CP}_{i,{\rm pk}}$, and $f^{CP}_{i,{\rm comb}}$ for an event to be signal or background are estimated from fits to $m_{\rm ES}$ distributions as described in Section 5.4. Fits are performed separately for each tagging category and the probabilities must satisfy the constraint $f^{CP}_{i,{\rm sig}} + f^{CP}_{i,{\rm pk}} + f^{CP}_{i,{\rm comb}} = 1$.

8.1.1 Probability density function of signal events

The Δt distributions for tagged events in the $B_{\rm CP}$ sample with perfect flavor-tagging and Δt resolution were introduced in Equations (2.61) and (2.62). Assuming $|\lambda_{f_{CP}}| = 1$, those relations can be written as

$$f\big(B_{\rm tag} \equiv B^0, \Delta t\big) = \frac{\Gamma}{4} e^{-\Gamma \Delta t}\big(1 - \eta_{CP} \sin 2\beta \sin \Delta m_d \Delta t\big) \tag{8.3}$$

$$f\big(B_{\rm tag} \equiv \overline{B}^0, \Delta t\big) = \frac{\Gamma}{4} e^{-\Gamma \Delta t}\big(1 + \eta_{CP} \sin 2\beta \sin \Delta m_d \Delta t\big) \tag{8.4}$$

where η_{CP} is the CP eigenvalue of the final state f_{CP}, $\tau_{B^0} = 1/\Gamma$ is the B^0 lifetime, and Δm_d is the B^0 $\overline{B}^0$ oscillation frequency. These distributions are shown in Figure 8.1a.

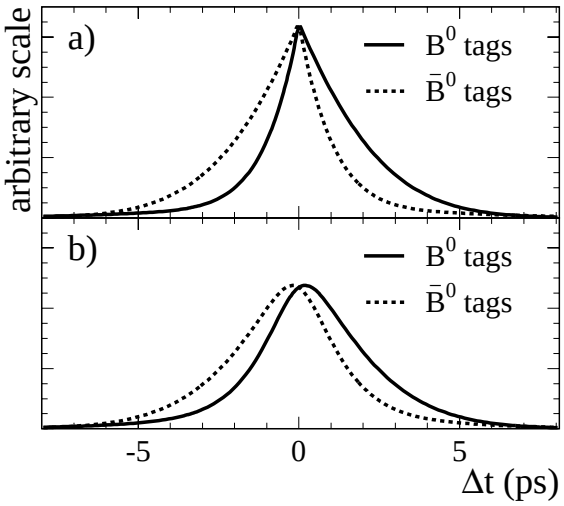

Figure 8.1: Expected Δt distribution for B^0- and $\overline{B}^0$-tagged CP events with a) perfect tagging and Δt resolution, and b) typical mistag fractions and finite Δt resolution. The scale is arbitrary but is the same for the two plots.

The mistag fractions for each category are defined separately for B^0 and $\overline{B}^0$ as

$$\begin{aligned} w_i &: \text{Fraction of true } B^0\text{s tagged as } \overline{B}^0\text{s} \\ \overline{w}_i &: \text{Fraction of true } \overline{B}^0\text{s tagged as } B^0\text{s} . \end{aligned} \tag{8.5}$$

The fractions w_i and $\overline{w}_i$ are expected to be very nearly, but not exactly, equal. For example, the response of the detector to positive pions and kaons differs from its response to negative pions and kaons, due to differences in the total and charge-exchange cross sections. Such a difference is accounted for by using two separate mistag fractions.

The observed Δt distributions for B^0-tagged and $\overline{B}^0$-tagged events are derived from distributions (8.3) and (8.4) by including for the fractions w_i and $\overline{w}_i$, and are given by

$$f'_+(\Delta t;\Gamma,\Delta m_d,w_i,\overline{w}_i) = (1-w)\,f\big(B_{\rm tag}\equiv B^0,\Delta t\big)+\overline{w}\,f\big(B_{\rm tag}\equiv \overline{B}^0,\Delta t\big) \quad (8.6)$$

$$f'_-(\Delta t;\Gamma,\Delta m_d,w_i,\overline{w}_i) = w\,f\big(B_{\rm tag}\equiv B^0,\Delta t\big)+(1-\overline{w})\,f\big(B_{\rm tag}\equiv \overline{B}^0,\Delta t\big) \quad (8.7)$$

In order to keep the expression of these distributions simple, it is convenient to use two new parameters in place of w and $\overline{w}$. The average dilution $\langle\mathcal{D}\rangle$ and the difference $\Delta\mathcal{D}$ between the dilutions for B^0 and $\overline{B}^0$ are linear functions of w and $\overline{w}$ and are defined as

$$\begin{aligned} \langle w\rangle &= \frac{1}{2}(w+\overline{w}), & \Delta w &= (w-\overline{w}) \\ \mathcal{D} &= 1-2w, & \overline{\mathcal{D}} &= 1-2\overline{w} \\ \langle\mathcal{D}\rangle &= \frac{1}{2}(\mathcal{D}+\overline{\mathcal{D}}), & \Delta\mathcal{D} &= (\mathcal{D}-\overline{\mathcal{D}})\,. \end{aligned}$$

After some algebra, the distributions (8.6) and (8.7) can be written as

$$f'_+(\Delta t;\Gamma,\Delta m_d,\langle\mathcal{D}\rangle_i,\Delta\mathcal{D}_i) = \frac{\Gamma}{4}e^{-\Gamma|\Delta t|}\big(1+\frac{\Delta\mathcal{D}_i}{2}-\langle\mathcal{D}\rangle_i\eta_{CP}\sin2\beta\sin\Delta m_d\Delta t\big) \quad (8.9)$$

$$f'_-(\Delta t;\Gamma,\Delta m_d,\langle\mathcal{D}\rangle_i,\Delta\mathcal{D}_i) = \frac{\Gamma}{4}e^{-\Gamma|\Delta t|}\big(1-\frac{\Delta\mathcal{D}_i}{2}+\langle\mathcal{D}\rangle_i\eta_{CP}\sin2\beta\sin\Delta m_d\Delta t\big) \quad (8.10)$$

These expressions clarify why untagged events do not can not be used for the measurement of $\sin2\beta$. Untagged events can be regarded as events with equal probability of being tagged as B^0 or $\overline{B}^0$, that is $w=\overline{w}=0.5$ and therefore $\langle\mathcal{D}\rangle=\Delta\mathcal{D}=0$. The Δt distribution of these events is not sensitive to $\sin2\beta$ and contains only the exponential lifetime decay. Hence, untagged events can be used to measure the B^0 lifetime, but not $\sin2\beta$.

The finite Δt resolution is incorporated by convolving (8.9) and (8.10) with the Δt resolution function $\mathcal{R}(\delta_t;\hat{a})$

$$\mathcal{F}_+(\Delta t;\Gamma,\Delta m_d,\langle\mathcal{D}\rangle_i,\Delta\mathcal{D}_i,\hat{a}_i) = f'_+(\Delta t_{\rm true};\Gamma,\Delta m_d,\langle\mathcal{D}\rangle_i,\Delta\mathcal{D}_i)\otimes\mathcal{R}(\delta_t;\hat{a}_i) \quad (8.11)$$

$$\mathcal{F}_-(\Delta t;\Gamma,\Delta m_d,\langle\mathcal{D}\rangle_i,\Delta\mathcal{D}_i,\hat{a}_i) = f'_-(\Delta t_{\rm true};\Gamma,\Delta m_d,\langle\mathcal{D}\rangle_i,\Delta\mathcal{D}_i)\otimes\mathcal{R}(\delta_t;\hat{a}_i)\,, \quad (8.12)$$

where $\delta_t=\Delta t-\Delta t_{\rm true}$ is the difference between the measured and the true values of Δt, and $\hat{a}_i$ are the parameters of the resolution function. The Δt resolution function was described in Section 7.6 and is modeled with a sum of three Gaussian distributions. Figure 8.1b illustrates distributions (8.11) and (8.12) for realistic choice of mistag fractions and Δt resolution function. These distributions are used as the probability density functions (PDFs) for the signal component and are normalized such that

$$\int_{-\infty}^{+\infty}(\mathcal{F}_++\mathcal{F}_-)\,d\Delta t = 1 \quad (8.13)$$

8.1.2 Δt spectrum of background events

The $B_{\rm CP}$ sample although very pure, includes a small fraction of combinatorial and peaking background events as discussed in Section 5.5.

Each event is assigned a probability to be signal on the basis of its measured energy-constrained mass $m_{\rm ES}$, as described in Section 5.4. The $m_{\rm ES}$ distribution is described with a single Gaussian distribution $\mathcal{G}(m_{\rm ES})$ for the signal and an ARGUS parameterization $\mathcal{A}(m_{\rm ES})$ for the background. The fit is performed separately for each tagging category and the probabilities that appear in Equation (8.2) are defined as

$$\begin{aligned} f_{i,{\rm sig}}(m_{\rm ES}) &= \frac{(1-\delta_{\rm peak})\mathcal{G}(m_{\rm ES})}{\mathcal{G}(m_{\rm ES})+\mathcal{A}(m_{\rm ES})} \\ f_{i,{\rm peak}}(m_{\rm ES}) &= \frac{\delta_{\rm peak}\mathcal{G}(m_{\rm ES})}{\mathcal{G}(m_{\rm ES})+\mathcal{A}(m_{\rm ES})} \\ f_{i,{\rm comb}}(m_{\rm ES}) &= \frac{\mathcal{A}(m_{\rm ES})}{\mathcal{G}(m_{\rm ES})+\mathcal{A}(m_{\rm ES})} \end{aligned} \tag{8.14}$$

The fraction $\delta_{\rm peak}$ accounts for the peaking-background contribution and is evaluated in simulated events as described in Section 5.5.

Backgrounds arise from many different sources. Rather than describing the Δt distribution of each physics process that contributes, an empirical description is used in the fit which allows for different time dependencies.

The PDF for the peaking background is parameterized as

$$\mathcal{B}^{CP}_{\pm,i,{\rm peak}} = \frac{\Gamma^{CP}_{\rm peak}}{4}{\rm e}^{-\Gamma^{CP}_{\rm peak}|\Delta t_{\rm true}|}(1 \pm \langle\mathcal{D}\rangle_i \eta_{\rm pk}\sin\Delta m_d\Delta t_{\rm true}) \otimes \mathcal{R}(\delta_{\rm t};\hat{a}_i)\ , \tag{8.15}$$

where dilutions $\langle\mathcal{D}\rangle_i$ and resolution function parameters $\hat{a}_i$ are those used for the signal, $1/\Gamma^{CP}_{\rm peak}$ is an empirical lifetime, and $\eta_{\rm pk}$ is an effective CP eigenvalue.

The Δt spectrum of the combinatorial background is modeled with a sum of three distributions

$$\begin{aligned} \mathcal{B}^{CP}_{\pm,i,comb} &= f^{CP}_{i,1}\mathcal{B}_{\pm,i,1}(\Delta t;\hat{b}_i) \\ &+ (1-f^{CP}_{i,1})\Big((1-f^{CP}_{i,3})\mathcal{B}_{\pm,i,2}(\Delta t;\hat{b}_i) + f^{CP}_{i,3}\mathcal{B}_{\pm,i,3}(\Delta t;\hat{b}_i)\ ,\Big) \end{aligned} \tag{8.16}$$

where the three components are defined as

$$\mathcal{B}^{CP}_{\pm,i,1} = \frac{1}{2}\delta(\Delta t_{\rm true}) \otimes \mathcal{R}(\delta t;\hat{b}_i)\ , \tag{8.17}$$

$$\mathcal{B}^{CP}_{\pm,i,2} = \frac{1}{4}\Gamma^{CP}_2{\rm e}^{-\Gamma^{CP}_2|\Delta t_{\rm true}|} \otimes \mathcal{R}(\delta t;\hat{b}_i)\ , \tag{8.18}$$

$$\mathcal{B}^{CP}_{\pm,i,3} = \frac{1}{4}\Gamma^{CP}_3{\rm e}^{-\Gamma^{CP}_3|\Delta t_{\rm true}|}\big(1 \pm \eta^{\rm comb}_i\sin\Delta m_d\Delta t_{\rm true}\big) \otimes \mathcal{R}(\delta t;\hat{b}_i)\ . \tag{8.19}$$

Here, Γ_2^{CP} and Γ_3^{CP} are empirical lifetimes, $f_{i,1}^{CP}$ is the fraction of events in the prompt component, $f_{i,3}^{CP}$ is the fraction of events in the non-prompt components, $\eta_i^{\rm comb}$ are effective CP asymmetry amplitudes, and $\hat{b}_i$ are the resolution function parameters for the background events.

Note that distributions (8.17) and (8.18) for B^0-tagged and $\overline{B}^0$-tagged events are even functions of Δt and do not include CP-violating effects, which are instead allowed in the third component (8.19). The background PDFs are normalized similarly to signal by requiring

$$\int_{-\infty}^{+\infty} \left(\mathcal{B}_{+,i,j} + \mathcal{B}_{-,i,j}\right)\, d\Delta t = 1 \tag{8.20}$$

8.2 Likelihood function for flavor eigenstates

Events with a fully reconstructed B meson in flavor eigenstates can be used to measure the B^0 $\overline{B}^0$ oscillation. The flavor of the fully reconstructed B meson ($B_{\rm rec}$) is known from the reconstructed final state, and the flavor of the other B meson ($B_{\rm tag}$) is measured with an inclusive method. Since the flavor of both B mesons is known, events can be divided in two categories:

- **Unmixed events**: the B mesons have different flavors, that is $|B_{\rm rec}, B_{\rm tag}\rangle$ is either $|B^0, \overline{B}^0\rangle$ or $|\overline{B}^0, B^0\rangle$;
- **Mixed events**: the two B mesons have the same flavor, that is $|B_{\rm rec}, B_{\rm tag}\rangle$ is either $|B^0, B^0\rangle$ or $|\overline{B}^0, \overline{B}^0\rangle$.

The likelihood function for events in the $B_{\rm flav}$ sample is written, in analogy with (8.1) for the $B_{\rm CP}$ sample, as

$$\ln \mathcal{L}_{\rm flav} = \sum_i^{N_c} \left[\sum_{\rm unmixed} \ln \mathcal{H}_{+,i} + \sum_{\rm mixed} \ln \mathcal{H}_{-,i} \right], \tag{8.21}$$

where $\mathcal{H}_{+,i}$ and $\mathcal{H}_{-,i}$ are, respectively, the probability density functions for unmixed and mixed events in $i^{\rm th}$ tagging category. Since each event can be classified as either mixed or unmixed, and can only belong to one tagging category, the two sums in Equation (8.21) are equivalent to a sum over all tagged events in the $B_{\rm flav}$ sample. Events in which the flavor of $B_{\rm tag}$ is not determined can not be classified as mixed or unmixed and are therefore excluded from further analysis.

The likelihood functions $\mathcal{H}_{\pm,i}$ are defined as a sum of signal, peaking background, and combinatorial background components

$$\mathcal{H}_{\pm,i} = f_{i,\rm sig}^{\rm flav}\mathcal{H}_{\pm} + f_{i,\rm pk}^{\rm flav}\mathcal{B}_{\pm,i,\rm pk}^{\rm flav} + f_{i,\rm comb}^{\rm flav}\mathcal{B}_{\pm,i,\rm comb}^{\rm flav}\,. \tag{8.22}$$

As for the $B_{\rm CP}$ sample, the probabilities $f_{i,\rm sig}^{\rm flav}$, $f_{i,\rm pk}^{\rm flav}$, and $f_{i,\rm comb}^{\rm flav}$ are estimated from the $m_{\rm ES}$ distributions of the selected events and satisfy the constraint $f_{i,\rm sig}^{\rm flav} + f_{i,\rm pk}^{\rm flav} + f_{i,\rm comb}^{\rm flav} = 1$.

8.2.1 Probability density function of signal events

The Δt distributions of mixed and unmixed events with perfect flavor tagging and Δt resolution were discussed in Section 2.4.4 and are given by

$$h_{\rm unmix}(\Delta t) \equiv {\rm Prob}(B_{\rm rec}B_{\rm tag} \to B^0\overline{B}^0 \text{ or } \overline{B}^0B^0) = \frac{\Gamma}{4}{\rm e}^{-\Gamma|\Delta t|}\big(1+\cos\Delta m_d\Delta t\big) \quad (8.23)$$

$$h_{\rm mix}(\Delta t) \equiv {\rm Prob}(B_{\rm rec}B_{\rm tag} \to B^0B^0 \text{ or } \overline{B}^0\overline{B}^0) = \frac{\Gamma}{4}{\rm e}^{-\Gamma|\Delta t|}\big(1-\cos\Delta m_d\Delta t\big) \quad (8.24)$$

where Δm_d is the oscillation frequency and $1/\Gamma = \tau_{B^0}$ is the B^0 lifetime. These distributions are shown in Figure 8.2a. In practice, since the flavor-tagging algorithm is not perfect, a B^0 ($\overline{B}^0$) can

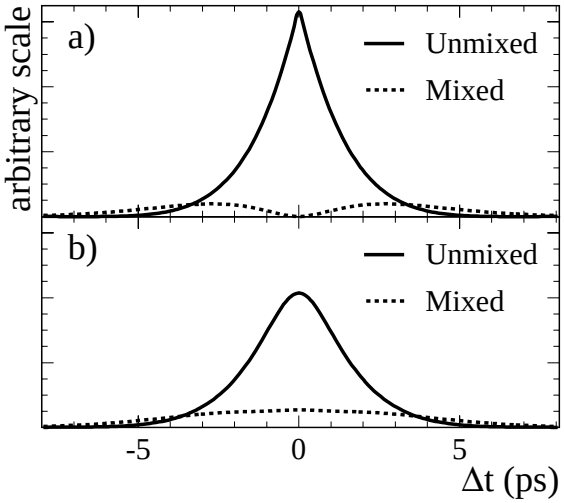

Figure 8.2: The Δt distribution for mixed and unmixed events with a) perfect tagging and Δt resolution, and b) typical mistag fractions and Δt resolution. The scale is arbitrary but is the same for the two plots.

be tagged as a $\overline{B}^0$ (B^0) due to mistag fraction w ($\overline{w}$) defined in (8.5). As a consequence, a *true* unmixed (mixed) event can be *observed* as mixed (unmixed).

The observed Δt distributions are computed from (8.23) and (8.24) by including the effect of w and $\overline{w}$ as

$$\begin{aligned} h'_+(B_{\rm rec}B_{\rm tag} \equiv \overline{B}^0B^0) &= (1-w)\, h_{unmix}(B_{\rm tag} \equiv B^0) + \overline{w}\, h_{\rm mix}(B_{\rm tag} \equiv \overline{B}^0) \\ h'_+(B_{\rm rec}B_{\rm tag} \equiv B^0\overline{B}^0) &= (1-\overline{w})\, h_{unmix}(B_{\rm tag} \equiv \overline{B}^0) + w\, h_{\rm mix}(B_{\rm tag} \equiv B^0) \end{aligned}$$

$$\begin{aligned} h'_-(B_{\rm rec}B_{\rm tag} \equiv B^0B^0) &= (1-w)\, h_{mix}(B_{\rm tag} \equiv B^0) + \overline{w}\, h_{\rm unmix}(B_{\rm tag} \equiv \overline{B}^0) \\ h'_-(B_{\rm rec}B_{\rm tag} \equiv \overline{B}^0\overline{B}^0) &= (1-\overline{w})\, h_{mix}(B_{\rm tag} \equiv \overline{B}^0) + w\, h_{\rm unmix}(B_{\rm tag} \equiv B^0)\ . \end{aligned}$$

There are now four distinct distributions although the underlying physics distributions were only two. This is different from the situation for the CP distributions discussed in Section 8.1.1. The reason is that in the $B_{\rm flav}$ sample events tagged with a B^0 or a $\overline{B}^0$ can be distinguished by the flavor of the fully reconstructed candidate. This is not possible when the fully reconstructed B is in a CP eigenstate. These distributions can be rearranged by using the average dilution $\langle\mathcal{D}\rangle$ and the difference $\Delta\mathcal{D}$ defined in (8.8)

$$h'_+\left(\Delta t;\Gamma,\Delta m_d,\langle\mathcal{D}\rangle_i,\Delta\mathcal{D}_i,B^0_{\rm tag}\right) = \frac{1}{4}\Gamma\, e^{-\Gamma|\Delta t|}\big(1+\frac{\Delta\mathcal{D}_i}{2}+\langle\mathcal{D}\rangle_i\cos\Delta m_d\Delta t\big) \quad (8.25)$$

$$h'_+\left(\Delta t;\Gamma,\Delta m_d,\langle\mathcal{D}\rangle_i,\Delta\mathcal{D}_i,\overline{B}^0_{\rm tag}\right) = \frac{1}{4}\Gamma\, e^{-\Gamma|\Delta t|}\big(1-\frac{\Delta\mathcal{D}_i}{2}+\langle\mathcal{D}\rangle_i\cos\Delta m_d\Delta t\big) \quad (8.26)$$

$$h'_-\left(\Delta t;\Gamma,\Delta m_d,\langle\mathcal{D}\rangle_i,\Delta\mathcal{D}_i,B^0_{\rm tag}\right) = \frac{1}{4}\Gamma\, e^{-\Gamma|\Delta t|}\big(1+\frac{\Delta\mathcal{D}_i}{2}-\langle\mathcal{D}\rangle_i\cos\Delta m_d\Delta t\big) \quad (8.27)$$

$$h'_-\left(\Delta t;\Gamma,\Delta m_d,\langle\mathcal{D}\rangle_i,\Delta\mathcal{D}_i,\overline{B}^0_{\rm tag}\right) = \frac{1}{4}\Gamma\, e^{-\Gamma|\Delta t|}\big(1-\frac{\Delta\mathcal{D}_i}{2}-\langle\mathcal{D}\rangle_i\cos\Delta m_d\Delta t\big) \quad (8.28)$$

The probability density functions (PDFs) for the signal component are given by the convolution of (8.25)-(8.28) with the resolution function $\mathcal{R}(\delta t;\hat{a}_i)$ (Section 7.6)

$$\mathcal{H}_+\left(\Delta t;\Gamma,\Delta m_d,\langle\mathcal{D}\rangle_i,\Delta\mathcal{D}_i,\hat{a}_i,B^0_{\rm tag}\right) = h'_+\left(\Delta t_{\rm true};B^0_{\rm tag}\right)\otimes\mathcal{R}(\delta_t;\hat{a}_i) \quad (8.29)$$

$$\mathcal{H}_+\left(\Delta t;\Gamma,\Delta m_d,\langle\mathcal{D}\rangle_i,\Delta\mathcal{D}_i,\hat{a}_i,\overline{B}^0_{\rm tag}\right) = h'_+\left(\Delta t_{\rm true};\overline{B}^0_{\rm tag}\right)\otimes\mathcal{R}(\delta_t;\hat{a}_i) \quad (8.30)$$

$$\mathcal{H}_-\left(\Delta t;\Gamma,\Delta m_d,\langle\mathcal{D}\rangle_i,\Delta\mathcal{D}_i,\hat{a}_i,B^0_{\rm tag}\right) = h'_-\left(\Delta t_{\rm true};B^0_{\rm tag}\right)\otimes\mathcal{R}(\delta_t;\hat{a}_i) \quad (8.31)$$

$$\mathcal{H}_-\left(\Delta t;\Gamma,\Delta m_d,\langle\mathcal{D}\rangle_i,\Delta\mathcal{D}_i,\hat{a}_i,\overline{B}^0_{\rm tag}\right) = h'_-\left(\Delta t_{\rm true};\overline{B}^0_{\rm tag}\right)\otimes\mathcal{R}(\delta_t;\hat{a}_i) \quad (8.32)$$

These Δt distributions are illustrated in Figure 8.2b. The normalization of these distributions is defined by the constraint

$$\int_{-\infty}^{+\infty}\left(\mathcal{H}_+(B^0_{\rm tag})+\mathcal{H}_+(\overline{B}^0_{\rm tag})+\mathcal{H}_-(B^0_{\rm tag})+\mathcal{H}_-(\overline{B}^0_{\rm tag})\right)d\Delta t = 1\ .$$

8.2.2 Δt spectrum of background events

The treatment of the Δt distribution of background events in the $B_{\rm flav}$ sample is similar to the method described in Section 8.1.2 for the $B_{\rm CP}$ sample. Empirical description is used to model the Δt distributions of the background events. The event-by-event signal and background probabilities $f^{\rm flav}_{i,{\rm sig}}$, $f^{\rm flav}_{i,{\rm peak}}$, and $f^{\rm flav}_{i,{\rm comb}}$ were defined in Section 5.4 and are measured with fits to the $m_{\rm ES}$ distributions of events in each tagging category as described in Section 8.1.2.

Peaking background in the $B_{\rm flav}$ sample is mainly due to mis-reconstructed B^+ and B^0 decays, as discussed in Section 5.6. Mis-reconstructed B^0 decays have a Δt distribution similar to the

signal: they have the correct lifetime and are also subject to B^0 $\overline{B}^0$ oscillation. Therefore they do not require a specific Δt distribution and are accounted for by the signal PDF. On the other hand, the B^+ mesons have a different lifetime and do not oscillate. Therefore their Δt distribution is very different from the signal and must be correctly modeled. Assuming that the peaking background contribution in the $B_{\rm flav}$ sample is only due to mis-reconstructed B^+ decays, its Δt distribution can be described as

$$\mathcal{B}_{\pm,i,\rm peak} = \frac{1}{4}\Gamma_{B^+}\mathrm{e}^{-\Gamma_{B^+}|\Delta t_{\rm true}|}\big(1 \pm \mathcal{D}_i^{B^+}\big) \otimes \mathcal{R}(\delta_{\rm t};\hat{a}_i), \tag{8.33}$$

where $1/\Gamma_{B^+} = \tau_{B^+}$ is the B^+ lifetime and $\hat{a}_i$ are the parameters of the signal Δt resolution function. Dilution factors $\mathcal{D}_i^{B^+}$ are measured with the large sample of fully reconstructed $B^\pm$ mesons (Section 5.7). The charge of the fully reconstructed $B^\pm$ determines its flavor, therefore $\mathcal{D}_i^{B^+}$ can be simply computed by counting the number of events with the wrong flavor tag.

For the combinatorial background, the Δt distribution is modeled with a sum of three components

$$\begin{aligned}\mathcal{B}^{\rm flav}_{\pm,i,comb} &= f^{\rm flav}_{i,1}\mathcal{B}_{\pm,i,1}(\Delta t;\hat{b}_i) \\ &+ (1-f^{\rm flav}_{i,1})\Big((1-f^{\rm flav}_{i,3})\mathcal{B}_{\pm,i,2}(\Delta t;\hat{b}_i) + f^{\rm flav}_{i,3}\mathcal{B}_{\pm,i,3}(\Delta t;\hat{b}_i)\ ,\Big)\end{aligned} \tag{8.34}$$

where the components are defined as

$$\mathcal{B}^{\rm flav}_{\pm,i,1} = \frac{1}{2}\big(1 \pm \mathcal{D}^{\rm flav}_{i,1}\big)\delta(\Delta t_{\rm true}) \otimes \mathcal{R}(\delta t;\hat{b}_i)\ , \tag{8.35}$$

$$\mathcal{B}^{\rm flav}_{\pm,i,2} = \frac{1}{4}\Gamma^{\rm flav}_2\big(1 \pm \mathcal{D}^{\rm flav}_{i,2}\big)\mathrm{e}^{-\Gamma^{\rm flav}_2|\Delta t_{\rm true}|} \otimes \mathcal{R}(\delta t;\hat{b}_i)\ , \tag{8.36}$$

$$\mathcal{B}^{\rm flav}_{\pm,i,3} = \frac{1}{4}\Gamma^{\rm flav}_3\big(1 \pm \mathcal{D}^{\rm flav}_{i,2}\big)\mathrm{e}^{-\Gamma^{\rm flav}_3|\Delta t_{\rm true}|}\big(1 \pm \mathcal{D}_i\cos\Delta m_d\Delta t_{\rm true}\big) \otimes \mathcal{R}(\delta t;\hat{b}_i)\ . \tag{8.37}$$

The empirical dilutions $\mathcal{D}^{\rm flav}_{i,1}$, $\mathcal{D}^{\rm flav}_{i,2}$, and $\mathcal{D}^{\rm flav}_{i,3}$ as well as the empirical lifetimes $1/\Gamma^{\rm flav}_{i,2}$ and $1/\Gamma^{\rm flav}_{i,3}$ are measured in data. A common resolution function is used for the background events in the $B_{\rm CP}$ and the $B_{\rm flav}$ samples, and hence $\hat{b}_i$ are the same parameters introduced in Section 8.1.2

8.3 Simultaneous fit to samples of flavor and CP eigenstates

The value of $\sin 2\beta$ is measured with an unbinned likelihood fit to the Δt distributions of events with a fully reconstructed B meson in flavor and CP eigenstates by maximizing

$$\ln\mathcal{L}_{\rm tot} = \ln\mathcal{L}_{CP} + \ln\mathcal{L}_{\rm flav}\ , \tag{8.38}$$

with $\ln \mathcal{L}_{CP}$ and $\ln \mathcal{L}_{\rm flav}$ defined in (8.1) and (8.21). There are a total of 35 free parameters, listed in Table 8.1, including $\sin 2\beta$, Δt resolution function parameters, mistag fractions, and the parameters of the empirical Δt spectrum of the background events. A number of other parameters, e.g. oscil-

Description	Number of parameters
CP asymmetry $\sin 2\beta$	1
Signal Δt resolution function	8
Signal dilutions	8
Background Δt resolution function	3
$B_{\rm flav}$ background composition	13
$B_{\rm CP}$ background composition	2
Total	35

Table 8.1: Summary of the free parameters in the maximum-likelihood fit.

lation frequency Δm_d and peaking background fractions, are used as input to the fit and their value is fixed. The signal and peaking-background parameters are determined from the Δt distribution of the events in the signal region, while the parameters of the background components are measured with the events in the $m_{\rm ES}$ sideband.

The determination of each parameter is dominated by a subset of events and is discussed in the following.

8.3.1 CP asymmetry amplitude $\sin 2\beta$

The amplitude $\sin 2\beta$ of the time-dependent asymmetry appears in Δt distributions (8.11) and (8.12) for the signal component. Events with a fully reconstructed B meson in CP eigenstates in the $m_{\rm ES}$ signal region (Section 5.4) dominate the measurement of $\sin 2\beta$.

8.3.2 Signal Δt resolution function

A common Δt resolution function is used for signal components of the the $B_{\rm flav}$ and $B_{\rm CP}$ samples. The value of these parameters is mainly dominated by events in the $B_{\rm flav}$ sample due to its larger number of events compared to the $B_{\rm CP}$ sample. The Δt resolution function model was

described in Section 7.6 as a sum of three Gaussians

$$\mathcal{R}^{\rm sig}(\delta_t,\hat{a}) = (1 - f^{\rm sig}_{\rm tail} - f^{\rm sig}_{\rm outl})\ \mathcal{G}^{\rm sig}_{\rm core} + f^{\rm sig}_{\rm tail}\ \mathcal{G}^{\rm sig}_{\rm tail} + f^{\rm sig}_{\rm outl}\ \mathcal{G}^{\rm sig}_{\rm outl}\ . \tag{8.39}$$

where $f_{\rm tail}$ and $f_{\rm outl}$ are, respectively, the fraction of events in the tail and outliers components. In addition to these two fractions, there are five parameters to describe the core Gaussian and one for the tail, for a total of eight free parameters $\hat{a}$.

The core Gaussian has one scale factor for the width and four bias scale factors. The width σ_c of the core is given by the product of a scale factor $S^{\rm sig}_{\rm core}$ and the event-by-event uncertainty $\sigma_{\Delta t}$

$$\sigma_c = S^{\rm sig}_{\rm core}\sigma_{\Delta t}\ .$$

Studies with simulated events show that the mean offset δ^0_c of the core Gaussian is different for the four tagging categories. For each category, the mean offset $\delta^0_{c,i}$ is given by the product of a bias scale factor $b^{\rm sig}_{i,{\rm core}}$ and the uncertainty $\sigma_{\Delta t}$

$$\delta^0_{c,i} = b^{\rm sig}_{i,{\rm core}}\sigma_{\Delta t}\ .$$

For the tail component the width σ_t and the mean offset δ^0_t are given by the products

$$\sigma_t = S^{\rm sig}_{\rm tail}\ \ \sigma_{\Delta t}$$
$$\delta^0_t = b^{\rm sig}_{\rm tail}\ \ \sigma_{\Delta t}$$

Note that unlike the core component, one common mean offset is used for all tagging categories. Monte Carlo studies indicate that $S^{\rm sig}_{\rm tail}$ is highly correlated with $b^{\rm sig}_{\rm tail}$ and the fraction $f^{\rm sig}_{\rm tail}$ of events in the tail component which is left free in the fit. When left floating, the measured value of $S^{\rm sig}_{\rm tail}$ has a large uncertainty. Moreover, the results of the fit are not sensitive to the value of $S^{\rm sig}_{\rm tail}$, and hence its value is fixed to 3 in the fit to data as indicated in simulated events. The systematic uncertainty due to this assumption is evaluated in Section 9.4.1 by varying the fixed value of $S^{\rm sig}_{\rm tail}$.

The outliers component accounts for a very small fraction of events, typically less then 0.5% of all events, with mis-reconstructed vertices. The width and the mean offset of this component are fixed, respectively, to $8\,{\rm ps}$ and $0\,{\rm ps}$, while the fraction $f^{\rm sig}_{\rm outl}$ is allowed to vary. The systematic uncertainty on $\sin 2\beta$ due to this choice of parameters is evaluated in Section 9.4.2.

As explained in Section 8.1.2 and 8.2.2, the peaking-background component utilizes the signal Δt resolution function and does not require any additional parameter.

8.3.3 Signal dilutions

Four average dilutions $\langle\mathcal{D}\rangle_i$ and four dilution differences $\Delta\mathcal{D}_i$ (one for each category) are used to describe the signal components of events in $B_{\rm flav}$ and $B_{\rm CP}$ samples. These parameters are determined by the $B_{\rm flav}$ sample where the flavor of the fully reconstructed B meson is known.

8.3.4 Background Δt resolution function

A common Δt resolution function with five free parameters is used for the combinatorial-background components in the $B_{\rm flav}$ and $B_{\rm CP}$ samples. The background Δt resolution function is modeled as a sum of a core Gaussian and a wide outliers component

$$\mathcal{R}^{\rm bkg}(\delta_t,\hat{a}) = (1-f^{\rm bkg}_{\rm outl})\ \mathcal{G}^{\rm bkg}_{\rm core} + f^{\rm bkg}_{\rm outl}\ \mathcal{G}^{\rm bkg}_{\rm outl}\,. \tag{8.40}$$

by fixing the fraction $f^{\rm bkg}_{\rm tail}$ of events in the tail to zero. The fraction $f^{\rm bkg}_{\rm outl}$ is left floating in the fit. Similarly to the signal resolution function, the $B_{\rm flav}$ sample dominates the determination of parameters $\hat{b}$.

All four tagging categories use the same width and mean offset given by the products

$$\sigma_c = S^{\rm bkg}_{\rm tail}\ \sigma_{\Delta t}$$
$$\delta^0_c = b^{\rm bkg}_{\rm tail}\ \sigma_{\Delta t}$$

with the scale factor $S^{\rm bkg}_{\rm tail}$ and $b^{\rm bkg}_{\rm tail}$ left free to vary in the fit.

The width and the offset of the outliers component are fixed, respectively, to $8\,{\rm ps}$ and $0\,{\rm ps}$ similar to the signal resolution function.

8.3.5 Δt spectrum of $B_{\rm flav}$ background

The Δt distribution of the peaking background is described by (8.33). Following the discussion in Section 8.2.2, the lifetime for this component is fixed to the B^+ lifetime $\tau_{B^+} = 1.674\,{\rm ps}$ [33]. The fraction $\delta^{\rm flav}_{\rm peak}$ of signal events due to the peaking background is estimated with simulated events to be $\delta^{\rm flav}_{\rm peak} = (1.3\pm0.3^{+0.2}_{-0.5})\%$ (Section 5.6). Dilutions $\mathcal{D}^{B^+}_i$ are measured with the sample of fully reconstructed B^+ mesons (Section 5.7) and are listed in Table 8.3.5.

Several assumptions are made to simplify the parameterization of the Δt spectrum of combinatorial background in (8.34). The mixing component $\mathcal{B}^{\rm flav}_{\pm,i,3}$ is removed by setting $f^{\rm flav}_{i,3} = 0$. A systematic uncertainty is assigned to this assumption and is evaluated in Section 9.4.12.

The effective dilutions $\mathcal{D}^{\rm flav}_{i,1}$ and $\mathcal{D}^{\rm flav}_{i,2}$ for the prompt and non-prompt components ($\mathcal{B}_{\pm,i,1}$ and $\mathcal{B}_{\pm,i,2}$) in each tagging category are allowed to vary, and are determined by the events in the $m_{\rm ES}$

Category	$N_{\rm signal}$	$\varepsilon(\%)$	$w^{B^+}(\%)$	$Q(\%)$
`Lepton`	2060 ± 48	9.9 ± 0.2	1.1 ± 0.3	9.5 ± 0.2
`Kaon I`	3710 ± 68	17.9 ± 0.3	7.7 ± 0.5	12.8 ± 0.4
`Kaon II`	4083 ± 73	19.7 ± 0.3	17.4 ± 0.6	8.3 ± 0.4
`Inclusive`	3870 ± 70	18.6 ± 0.3	27.7 ± 0.8	3.7 ± 0.3
Total	20771 ± 164	66.1 ± 0.6		34.3 ± 0.6

Table 8.2: Efficiency ε, mistag fraction w^{B^+}, and effective tagging efficiency Q in the sample of fully reconstructed B^+ candidates for each tagging category. Dilution $\mathcal{D}^{B^+}$ is defined as $\mathcal{D}^{B^+} = 1 - 2w$.

sideband of the selected $B_{\rm flav}$ candidates. The relative amount of these two components $f_{i,1}^{\rm flav}$ is allowed to vary independently for each tagging category, while $\Gamma_{i,2}^{\rm flav}$ is assumed to be the same for all categories, giving one more free parameter.

8.3.6 $B_{\rm CP}$ background composition

The number of events in the $m_{\rm ES}$-sideband region of the $B_{\rm CP}$ is relatively small due to the high purity of the sample. Since these events are used to measure the parameters of the empirical Δt spectrum of the background, it is necessary to reduce the number of free parameters.

The parameterization of the combinatorial background (8.16) is simplified by setting $f_{i,3}^{CP} = 0$. This means that no CP asymmetry is allowed in the background events. In addition, a common fraction $f_{i,1}^{CP}$ of the prompt component, and a common empirical lifetime $1/\Gamma_2^{CP}$ of the non-prompt component are used for all tagging categories. The fraction is left floating in the fit, while $1/\Gamma_2^{CP}$ is fixed to the B^0 lifetime τ_{B^0}. The systematic uncertainties due to the these assumptions are evaluated in Sections 9.4.9 and 9.4.10.

The fraction $\delta_{\rm peak}^{CP}$ of peaking-background in the signal events is evaluated separately for each decay mode (Section 5.5). The values of $\delta_{\rm peak}^{CP}$ for all decay modes are listed in Table 5.10. Signal dilutions and resolution function are used for the peaking-background component and no additional parameter is needed. Finally, the effective CP eigenvalue $\eta_{\rm pk}$ for the peaking background is fixed to zero. A systematic uncertainty is assigned to this assumption and is evaluated in Section 9.4.9.

External Parameters

The B^0 lifetime τ_{B^0} and the oscillation frequency Δm_d are fixed to the world average values [33]

$$\begin{aligned} \tau_{B^0} &= 1.548 \pm 0.016 \text{ ps} \\ \Delta m_d &= 0.489 \pm 0.008 \text{ ps}^{-1} \end{aligned}$$

The systematic uncertainty on $\sin 2\beta$ due to these fixed values is evaluated in Section 9.4.13.

8.4 Validation studies with simulated events

Very large samples of simulated events are used to validate the fit procedure. The size of the $B_{\rm CP}$ sample is about 130 times the observed number of signal in data, while the $B_{\rm flav}$ sample is about 10 times larger than in data. Due to the large number of events, fits to all events require typically a factor of 8 more CPU time than the fits to the data. In the following studies, unless otherwise specified, the Δt resolution function parameters and the dilution factors are measured in the $B_{\rm flav}$ sample, and are fixed in the fits to the $B_{\rm CP}$ sample. This assumption has no impact on the measured value of $\sin 2\beta$.

8.4.1 Fits to signal events

Signal events in all reconstructed decay modes are generated with a true value of $\sin 2\beta = 0.7033$. Fits are performed by using the true Δt resolution function parameters and dilutions, and by using the values measured in the $B_{\rm flav}$ sample. In these fits, events with $m_{\rm ES} > 5.27\,{\rm GeV}/c^2$ are assigned a signal probability of 1, while all other events are discarded.

The fit results are listed in Table 8.3. It is observed that measured values are always larger than the generated value which indicates a bias in the measurement of $\sin 2\beta$. The magnitude of this bias is evaluated below, in Section 8.4.3. The table includes also the fit result when using the $B_{\rm flav}$ as a control sample. The fitted asymmetry is consistent with zero, as expected.

8.4.2 Fits to inclusive $B \to J/\psi\, X$ events

The effect of background is studied with samples of events where one B always decays to a final state including a the charmonium meson. In addition to the signal decay modes, these samples include sources of combinatorial and peaking backgrounds.

Mode	$\sin 2\beta$	
	B_{flav} parameters	True parameters
$J/\psi\, K^0_S\, (\pi^+\pi^-)$	0.716 ± 0.007	0.719 ± 0.007
$J/\psi\, K^0_S\, (\pi^0\pi^0)$	0.718 ± 0.014	0.722 ± 0.014
$\psi(2S) K^0_S\, (\pi^+\pi^-)$	0.724 ± 0.015	0.727 ± 0.015
$\chi_{c1} K^0_S\, (\pi^+\pi^-)$	0.729 ± 0.021	0.734 ± 0.021
B_{flav}	-0.009 ± 0.011	-0.006 ± 0.011

Table 8.3: Results of fits to simulated signal events, with dilutions and resolution function parameters either from the B_{flav} sample, or from the true Δt and flavor tag.

The fit results are summarized in Table 8.4, and are in agreement with the generated value, although the statistical uncertainty is large.

Mode	$\sin 2\beta$
$J/\psi\, K^0_S\, (\pi^+\pi^-)$	0.685 ± 0.034
$J/\psi\, K^0_S\, (\pi^0\pi^0)$	0.778 ± 0.074
$\psi(2S) K^0_S\, (\pi^+\pi^-)$	0.406 ± 0.258
$\chi_{c1} K^0_S\, (\pi^+\pi^-)$	0.320 ± 0.193

Table 8.4: Fit results in Samples of simulated events $B \to J/\psi\, X$. All events are generated with $\sin 2\beta = 0.703$.

8.4.3 Evaluation of the bias in $\sin 2\beta$

The fit results in the Table 8.3 indicate the presence of a positive bias in the measured value of $\sin 2\beta$. In order to estimate the size of this bias, simulated signal events are divided in 130 samples equivalent to the full data sample. Each sample is fit twice: first using the true dilutions and Δt resolutions function parameters, and then using the parameters measured in the B_{flav} sample.

The mean of the distribution of the residual $\delta \sin 2\beta = \sin 2\beta - 0.7033$ for the two configurations is reported in Table 8.5. Figure 8.3 shows the distribution of residual $\delta \sin 2\beta$ when true dilutions and resolution function parameters are used. Since the bias is significantly different from zero, the fitted $\sin 2\beta$ in data is corrected by subtracting 0.014 from the measured value. A systematic uncertainty is assigned to this correction and is discussed in Section 9.4.17.

	true parameters	$B_{\rm flav}$ parameters
$\langle \delta \sin 2\beta \rangle$	0.0124 ± 0.005	0.0138 ± 0.005
RMS $\frac{\delta \sin 2\beta}{\sigma_{\sin 2\beta}}$	1.04 ± 0.07	1.05 ± 0.07

Table 8.5: Mean of $\delta \sin 2\beta$ distribution and the RMS spread of the pull $\delta \sin 2\beta / \sigma_{\sin 2\beta}$.

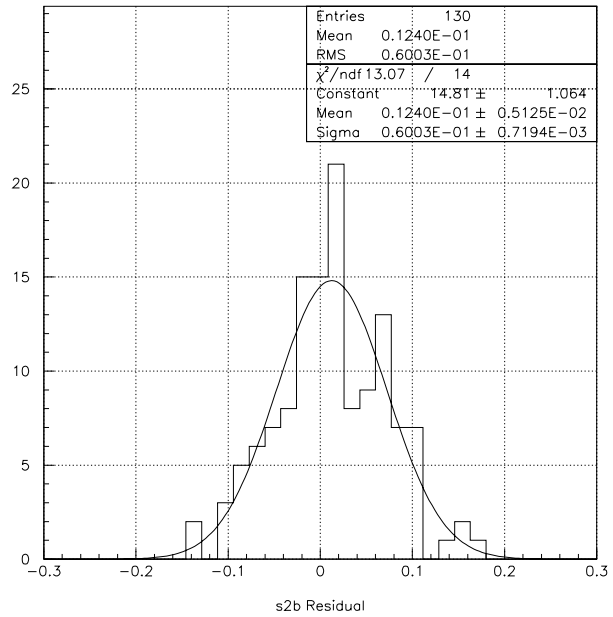

Figure 8.3: Distribution of the residual $\delta \sin 2\beta$ in fits with the true dilutions and resolution function parameters.

8.4.4 Correlation between dilution $\langle \mathcal{D} \rangle$ and $\sigma_{\Delta t}$

The origin of the correlation between the mistag fraction w and $\sigma_{\Delta t}$ was discussed in Section 7.8. Average dilution $\langle \mathcal{D} \rangle$ is a related to w by Equation (8.8), and hence exhibits the same correlation. In order to study the effect of this correlation on $\sin 2\beta$, the average dilution $\langle \mathcal{D} \rangle_i$ for each tagging category is parameterized as

$$\langle \mathcal{D} \rangle_i = \langle \mathcal{D} \rangle_i^0 + \mathcal{S}_i \, \sigma_{\Delta t} \tag{8.41}$$

in fits to data-size $B_{\rm CP}$ and $B_{\rm flav}$ samples of simulated events. The value of $\sin 2\beta_{\rm slope}$ measured in these fits is compared to $\sin 2\beta_0$, measured with $\mathcal{S}_i = 0$. Distribution of the difference $\delta =$

$\sin 2\beta_{\rm slope} - \sin 2\beta_0$ is shown in Figure 8.4, and has a mean of 0.004 and an RMS spread of 0.004. Similar study has been performed with fast parameterized simulated events (toy Monte Carlo) and has a larger mean of 0.006 and an RMS spread of 0.006. The distribution of δ for these fits is also shown in Figure 8.4.

Therefore, neglecting the correlation between mistag fractions and $\sigma_{\Delta t}$ results in a bias of +0.004 in $\sin 2\beta$. This bias is taken into account in the evaluation of the systematic uncertainty on $\sin 2\beta$ due to the total Monte Carlo bias, discussed in Section 9.4.17

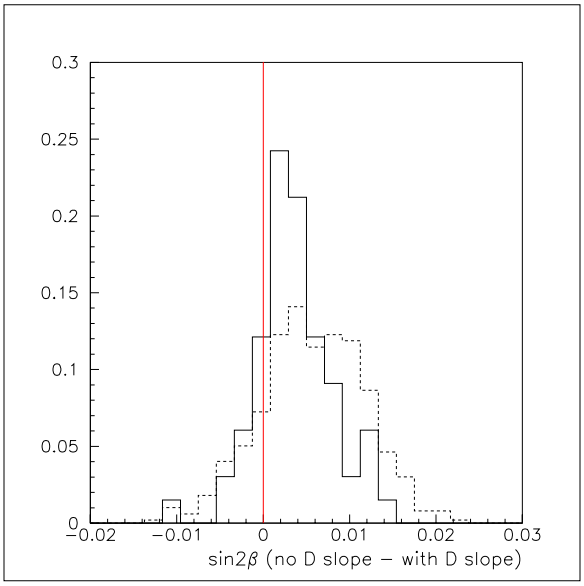

Figure 8.4: Variation in $\sin 2\beta$ due to the correlation between mistag fractions and $\sigma_{\Delta t}$.

8.5 Expected uncertainty on $\sin 2\beta$

The uncertainty on $\sin 2\beta$, including the Δt resolution, can be computed analytically from the likelihood function $\mathcal{L}$ to be [125]

$$\sigma_{\sin 2\beta} = \frac{\Sigma(\sin 2\beta, \tau_{B^0}\ \Delta m_d, \sigma_t)}{\sqrt{N_{\rm sig}}\sqrt{\sum_{i=1}^{4} \varepsilon_i (1-2w_i)^2}} \frac{\sqrt{1 + N_{\rm bkg}/N_{\rm sig}}}{1 + (A_{\rm sig}/A_{\rm bkg})(N_{\rm bkg}/N_{\rm sig})} \tag{8.42}$$

where

- $N_{\rm sig}$ is the number of fully reconstructed CP eigenstates with asymmetry amplitude $A_{\rm sig}$,
- $N_{\rm bkg}$ is the number of background events in the CP sample, with asymmetry amplitude $A_{\rm bkg}$,

- σ_t is the Δt resolution, and
- ε_i and w_i are, respectively, the efficiency and the mistag fraction of the ith tagging category.

In order to understand this expression, one can consider the limit of perfect flavor tagging with $w = 0$, and no background events, $N_{\rm bkg} = 0$. In this case, Σ is the estimate of the per-event uncertainty and depends on the Δt resolution, and $1/\sqrt{N_{\rm sig}}$ is from the Poisson statistics.

Since only the flavor-tagged events can be used to measure $\sin 2\beta$, the statistical power of the sample is reduced by the tagging efficiency ε.

The dependence on the mistag fraction w can be understood, if one recalls that the amplitude of the sine term in the likelihood function is given by the product $(1 - 2w)\sin 2\beta$. Since the fit is sensitive to the total amplitude, variations in w directly affect $\sin 2\beta$.

The value of Σ depends on the exact expression of the Δt resolution function. Tabulated values of Σ in the simple case of a single Gaussian resolution function, and no scale factors, can be found in Reference [125].

A better approach to estimate the $\sin 2\beta$ uncertainty with realistic resolution functions is to use toy Monte Carlo events. This approach is used in Section 9.2.1 to estimate the agreement between the measured and expected uncertainties.

Chapter 9

Measurement of $\sin 2\beta$

Results of the maximum-likelihood fit, described in Chapter 8, to the Δt distributions of events in CP eigenstates $J/\psi\ K^0_S$, $\psi(2S)\ K^0_S$, $\chi_{c1}\ K^0_S$, and $\eta_c\ K^0_S$ are presented in this Chapter. The sample of events used in the fit, after some loose vertex quality requirements, is described in Section 9.1. The results and the estimate of the goodness of fit are discussed in Section 9.2. The large sample of reconstructed B mesons allows various cross checks, including fits to subsamples of events, which are described in Section 9.3. Sources of systematic uncertainty on the measured value of $\sin 2\beta$, and the evaluation of their size are discussed in Section 9.4. In Section 2.5.2, it was pointed out that the decay modes $B \to J/\psi\, K^0_L$ and $J/\psi\, K^{*0}(K^0_S\pi^0)$ can also be used to measure $\sin 2\beta$. Measurement of $\sin 2\beta$ with those modes are discussed in Section 9.5. Finally, the combined result from a fit all decay modes, including $J/\psi\ K^0_L$ and $J/\psi\ K^{*0}$ $(K^0_S\ \pi^0)$ is discussed in Section 9.6.

9.1 Event Sample

Signal yields for the sample of selected CP eigenstates ($B_{\rm CP}$) and flavor eigenstates ($B_{\rm flav}$) were presented in Sections 5.5 and 5.6, and summarized in Tables 5.9 and 5.14. Additional vertex quality requirements are applied to select events with a well-measured interval Δt:

- the fits performed to compute the decay vertices of the fully reconstructed and the tagging B mesons must converge;
- the measured Δt must be in the interval $[-20, 20]\,{\rm ps}$. This is a very loose requirement considering the B^0 lifetime of $1.542\,{\rm ps}$; and
- the measured uncertainty $\sigma_{\Delta t}$ must be less than $2.5\,{\rm ps}$.

These requirements reject almost entirely all events with mis-reconstructed vertices, and are satisfied by about 95% of the events in data and simulation. Numbers of selected events in the $m_{\rm ES}$ signal region (Section 5.4) after these requirements are summarized in Table 9.1.

	CP eigenstates			Flavor eigenstates		
Tagging category	B^0 tag	$\overline{B}^0$ tag	All	B^0 tag	$\overline{B}^0$ tag	All
`Lepton`	80	83	163	1782	1688	3470
`KaonI`	132	145	277	5135	5059	10194
`KaonII`	141	175	316	7436	6730	14166
`Inclusive`	159	149	308	7332	6801	14133
No tag	550			29843		
Total	1614			71806		

Table 9.1: Number of selected events with $m_{\rm ES} > 5.27\,{\rm GeV}/c^2$ after vertex quality requirements.

Distributions of $m_{\rm ES}$ for events in each tagging category are shown in Figure 9.1 for the $B_{\rm CP}$ sample, and in Figure 9.2 for the $B_{\rm flav}$ sample. Overlaid is the result of the fit used to determine the event-by-event signal probability as well as the signal purity in the signal region, defined in Section 5.4. The amount of the background varies within the four tagging categories, and also slightly for each decay mode, therefore separate $m_{\rm ES}$ fits provide a better estimate of the signal probability.

Fits for the $B_{\rm CP}$ sample are performed in two steps. First, all selected events after vertex requirements, including untagged events, are fit to determine the mean m_B and the width σ_m of the Gaussian component for signal, as well as parameter ξ of the ARGUS component for background. These values are fixed in fits to $m_{\rm ES}$ distributions of each tagging category and only the normalizations of the signal and background components are left floating. Fixing the parameters is necessary because the amount of background and the number of events in each category are different. For example, the `Lepton` category has a very high purity, but also the smallest number of events which are not sufficient to determine correctly the shape of the ARGUS function. The results of all $m_{\rm ES}$ fits are summarized in Tables 9.2 through 9.6.

The $B_{\rm flav}$ sample is about ten times bigger than the $B_{\rm CP}$ sample and has large number of events in all tagging categories. Hence, all parameters are left floating in fits to the $m_{\rm ES}$ distribution of individual tagging categories. Results of these fits are summarized in Table 9.7.

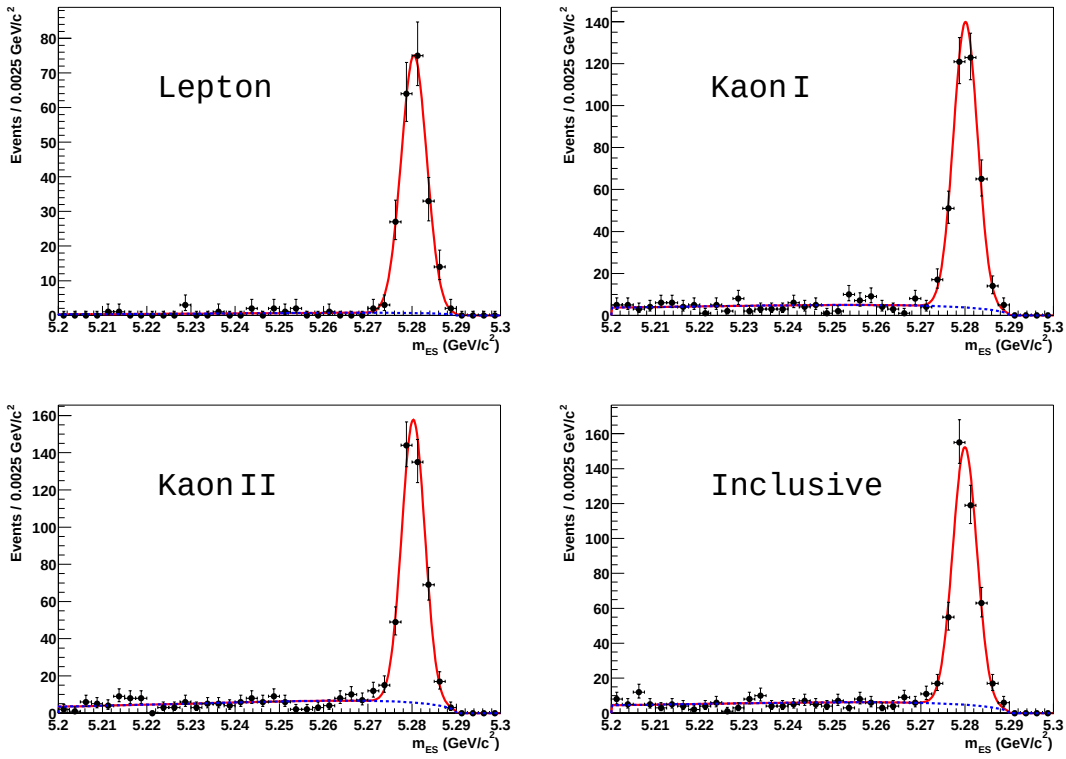

Figure 9.1: Distribution of $m_{\rm ES}$ for reconstructed CP eigenstates, after vertex quality requirements, in the four tagging categories.

Parameter	Lepton	Kaon I	Kaon II	Inclusive
Signal Yield	140 ± 12	251 ± 16	271 ± 17	275 ± 17
$m_B(\,\mathrm{MeV}/c^2)$		5280.2 ± 0.1 (fixed)		
$\sigma_m(\,\mathrm{MeV}/c^2)$		2.73 ± 0.06 (fixed)		
Background Events	5 ± 3	56 ± 16	54 ± 8	79 ± 10
$\mathcal{P}$(%)	99.3 ± 0.3	96.4 ± 0.6	96.7 ± 0.5	95.3 ± 0.6
ARGUS parameter ξ		-29 ± 6 (fixed)		

Table 9.2: Results of the $m_{\rm ES}$ fits to reconstructed $J/\psi\ K^0_S\ (\pi^+\pi^-)$ candidates.

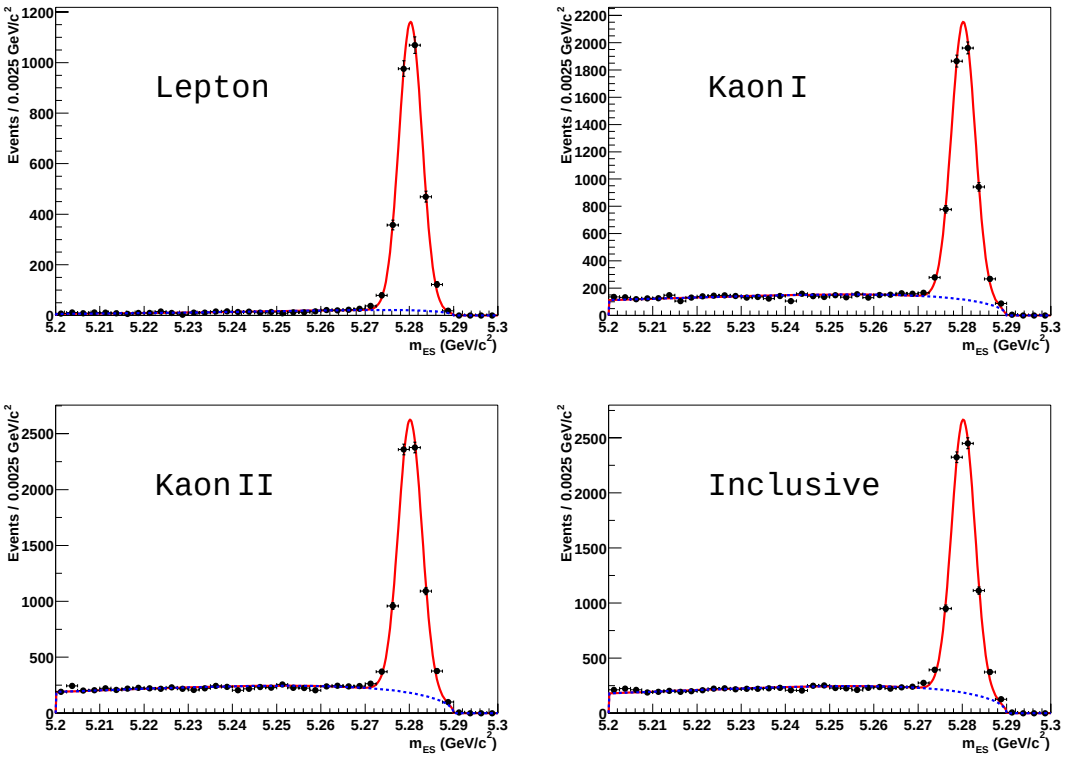

Figure 9.2: Distribution of $m_{\rm ES}$ for reconstructed flavor eigenstates, after vertex quality requirements, in the four tagging categories.

Parameter	Lepton	Kaon I	Kaon II	Inclusive
Signal Yield	23 ± 5	40 ± 7	47 ± 7	39 ± 7
m_B(MeV/c^2)	5280.2 ± 0.1 (fixed)			
σ_m(MeV/c^2)	2.73 ± 0.06 (fixed)			
Background Events	3 ± 5	31 ± 6	43 ± 7	34 ± 6
$\mathcal{P}$(%)	98 ± 1	88 ± 3	87 ± 3	87 ± 3
ARGUS parameter ξ	-29 ± 6 (fixed)			

Table 9.3: Results of the $m_{\rm ES}$ fits to reconstructed J/ψ K^0_S (π^0 π^0) candidates.

Parameter	Lepton	KaonI	KaonII	Inclusive
Signal Yield	30 ± 6	32 ± 6	46 ± 7	35 ± 6
$m_B(\mathrm{MeV}/c^2)$	5280.2 ± 0.1 (fixed)			
$\sigma_m(\mathrm{MeV}/c^2)$	2.73 ± 0.06 (fixed)			
Background Events	2 ± 6	4 ± 6	8 ± 3	16 ± 4
$\mathcal{P}$(%)	99 ± 1	98 ± 1	97 ± 1	93 ± 2
ARGUS parameter ξ	-29 ± 6 (fixed)			

Table 9.4: Results of the m_{ES} fits to reconstructed $\psi(2S)$ K^0_S candidates.

Parameter	Lepton	KaonI	KaonII	Inclusive
Signal Yield	9 ± 3	19 ± 5	20 ± 5	27 ± 5
$m_B(\mathrm{MeV}/c^2)$	5280.2 ± 0.1 (fixed)			
$\sigma_m(\mathrm{MeV}/c^2)$	2.73 ± 0.06 (fixed)			
Background Events	1 ± 1	8 ± 3	7 ± 3	6 ± 5
$\mathcal{P}$(%)	98 ± 2	94 ± 3	94 ± 3	96 ± 2
ARGUS parameter ξ	-29 ± 6 (fixed)			

Table 9.5: Results of the m_{ES} fits to reconstructed χ_{c1} K^0_S candidates.

Parameter	Lepton	KaonI	KaonII	Inclusive
Signal Yield	14 ± 4	28 ± 6	23 ± 6	29 ± 6
$m_B(\mathrm{MeV}/c^2)$	5280.2 ± 0.1 (fixed)			
$\sigma_m(\mathrm{MeV}/c^2)$	2.73 ± 0.06 (fixed)			
Background Events	7 ± 3	56 ± 8	68 ± 9	54 ± 8
$\mathcal{P}$(%)	92 ± 4	72 ± 6	64 ± 7	74 ± 5
ARGUS parameter ξ	-36 (fixed)			

Table 9.6: Results of the m_{ES} fits to reconstructed η_c K^0_S candidates.

Parameter	Lepton	KaonI	KaonII	Inclusive
Signal Yield	2979 ± 57	5450 ± 83	6489 ± 92	6535 ± 94
m_B(MeV/c^2)	5280.30 ± 0.05	5280.20 ± 0.04	5280.20 ± 0.04	5280.20 ± 0.04
σ_m (MeV/c^2)	2.60 ± 0.04	2.64 ± 0.04	2.62 ± 0.03	2.60 ± 0.04
Background Yield	491 ± 28	4745 ± 78	7677 ± 99	7599 ± 99
$\mathcal{P}$(%)	95.6 ± 0.5	86.2 ± 0.5	82.6 ± 0.5	82.3 ± 0.5
ARGUS parameter ξ	-72 ± 7	-35 ± 2	-32 ± 2	-35 ± 2

Table 9.7: Results of the m_{ES} fits to the B_{flav} sample.

9.2 Fit results

The fit to the Δt distributions of events in the $B_{\rm CP}$ and $B_{\rm flav}$ samples yields

$$\sin 2\beta = 0.755 \pm 0.074 \ . \tag{9.1}$$

This value includes the –0.014 correction to account for the bias observed in simulated events and discussed in Section 8.4.3. Table 9.8 summarizes the measured value of all free parameters in the fit and their correlation with $\sin 2\beta$. The largest correlation between $\sin 2\beta$ and any linear combination of the other free parameters is 13%.

The Δt distributions of events in the $B_{\rm CP}$ sample are shown in Figure 9.3a, where the asymmetry between events with a B^0 tag and those with a $\overline{B}^0$ tag is apparent. Figure 9.3b illustrates the raw asymmetry defined by

$$\mathcal{A}_{CP}(\Delta t) = \frac{N(\Delta t; B^0_{\rm tag}) - N(\Delta t; \overline{B}^0_{\rm tag})}{N(\Delta t; B^0_{\rm tag}) + N(\Delta t; \overline{B}^0_{\rm tag})} \ , \tag{9.2}$$

where $N(\Delta t; \overline{B}^0_{\rm tag})$ and $N(\Delta t; B^0_{\rm tag})$ are, respectively, the observed number of $\overline{B}^0$-tagged and B^0-tagged events in intervals of Δt.

9.2.1 Goodness of fit and expected statistical uncertainty

The goodness of fit is evaluated with 1000 samples of fast parameterized simulated events (toy Monte Carlo). In each sample, the number of generated events is equal to the observed number of events in data for each tagging category, and for both $B_{\rm CP}$ and $B_{\rm flav}$ samples. The total number of signal and background is equal to those in Tables 9.2–9.6 and 9.7.

The value of $m_{\rm ES}$ for each event is generated from a distribution that has the parameters measured in data and listed in the above tables. Each event is then assigned a signal probability from a fit to the generated distribution of $m_{\rm ES}$ for all events.

The value of Δt for each event is also generated by taking into account the measured resolution function in data. For signal events, the true value of Δt (Δt_0) is extracted from the Δt distributions (8.3) for B^0-tagged, (8.4) for $\overline{B}^0$-tagged, (8.23) for unmixed, and (8.24) for mixed events in absence of detector effects. The measured Δt is computed as $\Delta t_{\rm meas} = \Delta t_0 + \delta t$, where δt is drawn from a distribution corresponding to a sum of three Gaussians, whose parameters are fixed to the values measured in data (Table 9.8) for the signal resolution function.

Finally, the measured dilutions $\langle \mathcal{D} \rangle$ and dilution differences $\Delta \mathcal{D}$ in Table 9.8 are used to assign the wrong flavor-tag to a fraction of events and simulate the effect of mistag fraction.

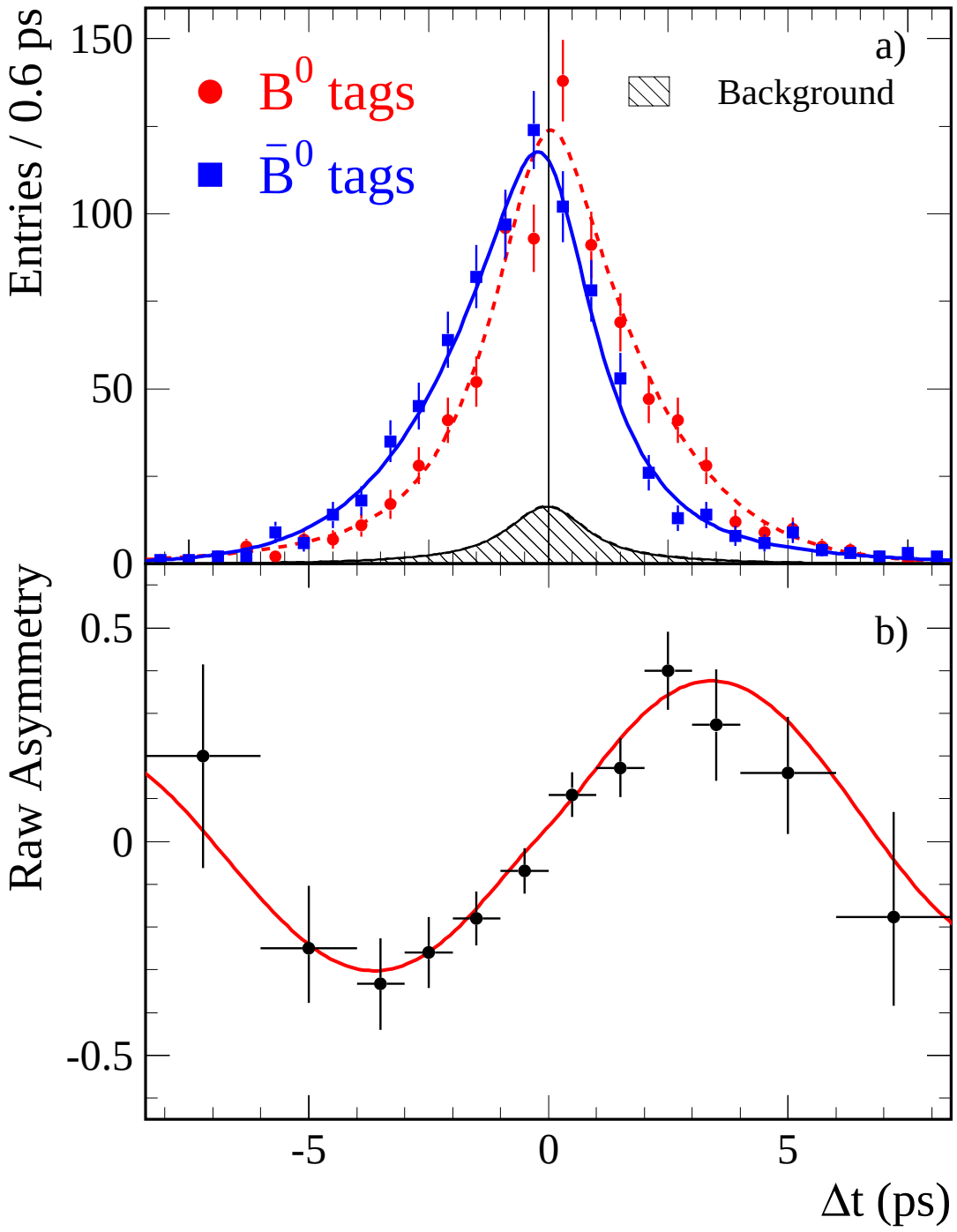

Figure 9.3: a) The Δt distributions of flavor-tagged events after vertex requirements in the $B_{\rm CP}$ sample, and b) the raw asymmetry $\mathcal{A}_{CP}$. The lines are the result of the likelihood fit and the shaded area is the contribution of the background.

The goodness of fit is estimated by comparing the value of the likelihood function $\ln \mathcal{L}$ from the fit to data, to values from the fits to simulated samples. Figure 9.4 shows the distributions of $\ln \mathcal{L}_{\rm MC}$ in the simulated samples with the arrow indicating the value in data. The value in data is in good agreement with the expected values. The fraction of samples with $\ln \mathcal{L}_{\rm MC} < \ln \mathcal{L}_{\rm data}$ is given in Table 9.9.

Figure 9.5 shows the comparison between the measured uncertainty $\sigma_{\sin 2\beta}$ (indicated with the arrow) and the distributions of $\sigma_{\sin 2\beta_{\rm MC}}$ in simulated samples. The expected uncertainty and the value measured in data are listed in in Table 9.9 and are in good agreement.

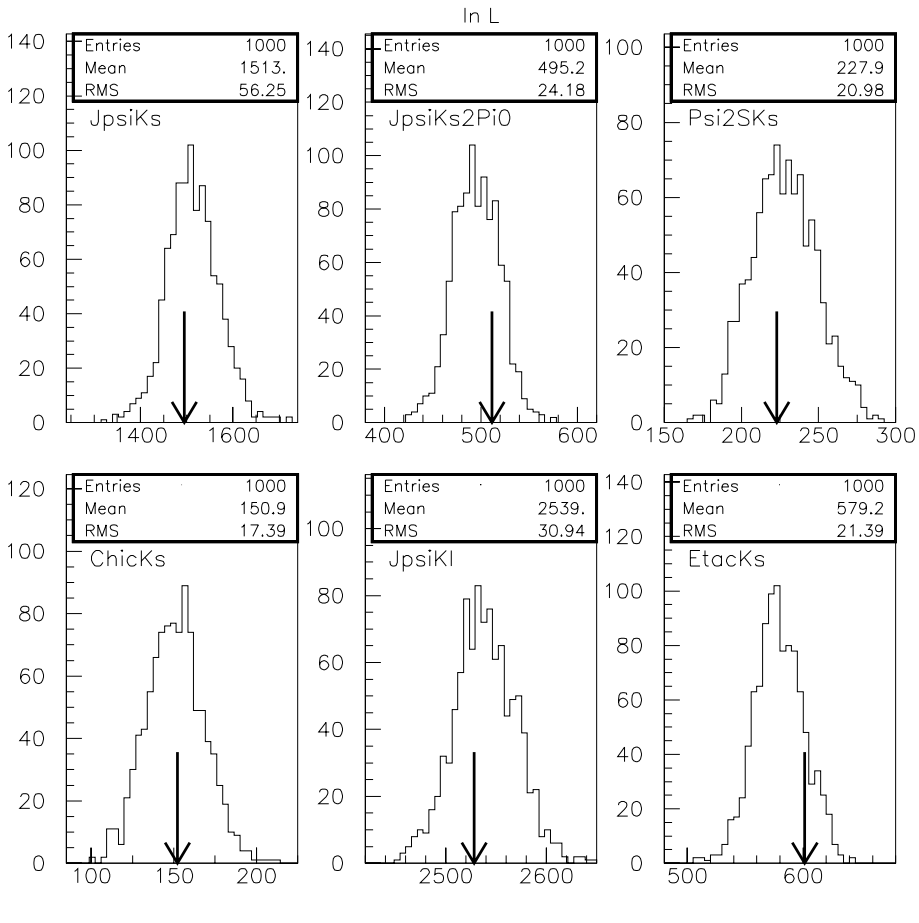

Figure 9.4: Distribution of $\ln \mathcal{L}$ in 1000 samples of toy Monte Carlo events. The arrow indicates the value from the fit to data.

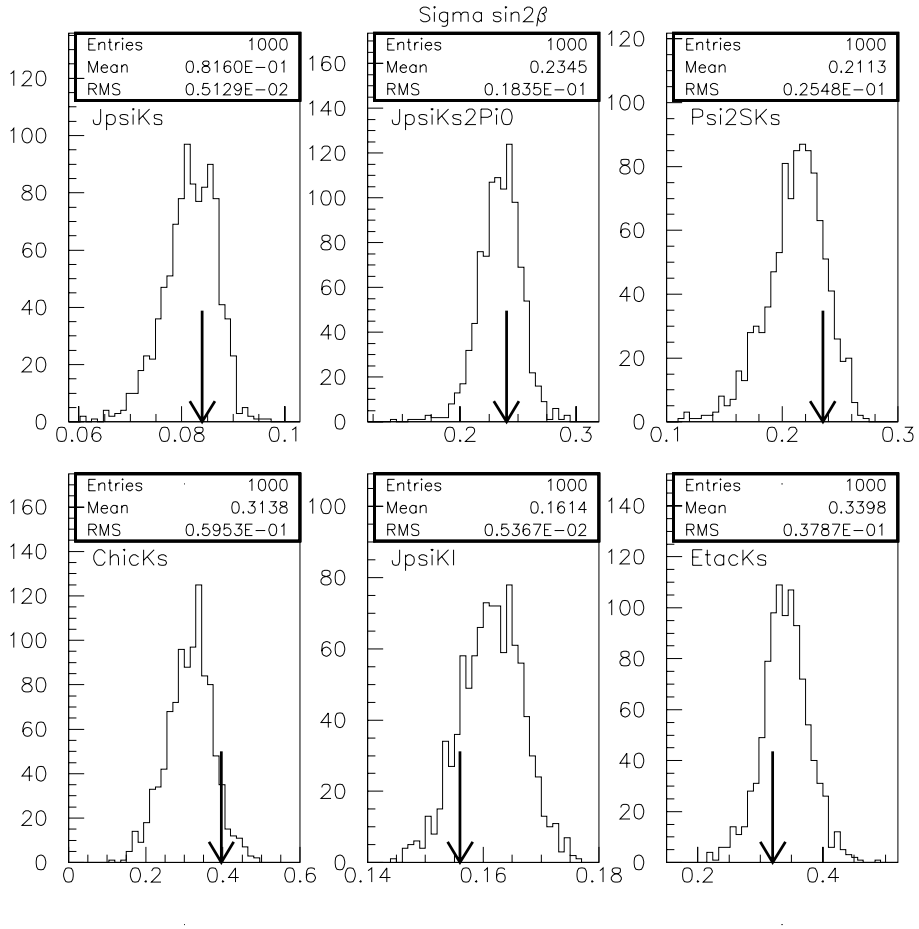

Figure 9.5: Distribution of measured $\sigma_{\sin 2\beta}$ in 1000 samples of toy Monte Carlo events. The arrow indicates the value measured in data.

Parameter	Result	Correlation with $\sin 2\beta$
$\sin 2\beta$	0.755 ± 0.074	1.000
Signal Resolution Function		
$S_{\rm core}$	1.094 ± 0.048	0.020
$S_{\rm tail}$	3.0 (fixed)	
$b_{\rm core}$ `Lepton`	0.039 ± 0.061	0.010
$b_{\rm core}$ `Kaon I`	-0.234 ± 0.050	0.011
$b_{\rm core}$ `Kaon II`	-0.232 ± 0.044	0.012
$b_{\rm core}$ `Inclusive`	-0.219 ± 0.045	0.007
$b_{\rm tail}$	-1.020 ± 0.293	-0.007
$f_{\rm tail}$	0.106 ± 0.020	0.017
$f_{\rm outl}$	0.003 ± 0.001	-0.010
Signal dilutions		
$\langle\mathcal{D}\rangle$, `Lepton`	0.934 ± 0.013	-0.046
$\langle\mathcal{D}\rangle$, `Kaon I`	0.801 ± 0.014	-0.066
$\langle\mathcal{D}\rangle$, `Kaon II`	0.582 ± 0.016	-0.056
$\langle\mathcal{D}\rangle$, `Inclusive`	0.367 ± 0.017	-0.048
$\Delta\mathcal{D}$, `Lepton`	0.029 ± 0.022	0.003
$\Delta\mathcal{D}$, `Kaon I`	0.021 ± 0.022	0.004
$\Delta\mathcal{D}$, `Kaon II`	0.078 ± 0.023	-0.007
$\Delta\mathcal{D}$, `Inclusive`	0.051 ± 0.025	0.006
Background properties		
$1/\Gamma_2^{\rm flav}$ (ps)	1.325 ± 0.062	-0.001
f_2^{CP}	0.639 ± 0.050	-0.024
$f_2^{\rm flav}$, `Lepton`	0.289 ± 0.163	0.000
$f_2^{\rm flav}$, `Kaon I`	0.630 ± 0.026	0.000
$f_2^{\rm flav}$, `Kaon II`	0.657 ± 0.024	0.000
$f_2^{\rm flav}$, `Inclusive`	0.683 ± 0.022	0.000
Background resolution function		
$S_{\rm core}$	1.398 ± 0.019	-0.003
$b_{\rm core}$	-0.045 ± 0.013	0.000
$f_{\rm outl}$	0.016 ± 0.002	-0.001
Background dilutions		
$\mathcal{D}_1^{\rm flav}$, `Lepton`	1.372 ± 0.630	0.002
$\mathcal{D}_1^{\rm flav}$, `Kaon I`	0.649 ± 0.030	0.006
$\mathcal{D}_1^{\rm flav}$, `Kaon II`	0.393 ± 0.024	0.006
$\mathcal{D}_1^{\rm flav}$, `Inclusive`	0.158 ± 0.024	0.005
$\mathcal{D}_2^{\rm flav}$, `Lepton`	0.170 ± 0.104	0.000
$\mathcal{D}_2^{\rm flav}$, `Kaon I`	0.251 ± 0.048	0.000
$\mathcal{D}_2^{\rm flav}$, `Kaon II`	0.279 ± 0.042	0.000
$\mathcal{D}_2^{\rm flav}$, `Inclusive`	0.032 ± 0.046	0.000

Table 9.8: Results of the likelihood fit. The parameters are defined in Chapter 8.

Sample	$\langle\sigma^{\rm MC}_{\sin2\beta}\rangle$	RMS $\sigma^{\rm MC}_{\sin2\beta}$	$\sigma^{\rm data}_{\sin2\beta}$	$\ln\mathcal{L}_{\rm MC}$	$\ln\mathcal{L}_{\rm data}$	f
$J/\psi\ K^0_S\ (\pi^+\ \pi^-)$	0.082	0.005	0.084	-1513.0 ± 1.7	-1494.9	0.623
$J/\psi\ K^0_S\ (\pi^0\ \pi^0)$	0.235	0.018	0.240	-495.1 ± 0.8	-511.5	0.263
$\psi(2S)\ K^0_S$	0.211	0.025	0.235	-227.6 ± 0.7	-222.9	0.576
$\chi_{c1}\ K^0_S$	0.314	0.060	0.396	-151.0 ± 0.6	-152.2	0.472
$\eta_c\ K^0_S$	0.340	0.038	0.320	-579.4 ± 0.7	-601.5	0.151

Table 9.9: Comparison between the expected uncertainty $\sigma^{\rm MC}_{\sin2\beta}$ and $\ln\mathcal{L}^{\rm MC}$, and the values measured in the fit to data, with f the fraction of samples with $\ln\mathcal{L}_{\rm MC} < \ln\mathcal{L}_{\rm data}$.

9.2.2 Performance of the b-flavor–tagging algorithm

Average mistag fraction $\langle w \rangle_i$ and difference Δw_i for B^0 and $\overline{B}^0$ tags in tagging category i are related to the measured $\langle \mathcal{D} \rangle_i$ and $\Delta \mathcal{D}_i$ in Table 9.8 through Equation (8.8). Values of $\langle w \rangle_i$ and Δw_i are listed in Table 9.10 for the four tagging categories. Included in the same Table is the tagging efficiency ε_i for the $i^{\rm th}$ category, defined as

$$\varepsilon_i = \frac{N_i^{\rm sig}}{N_{\rm untag}^{\rm sig} + \sum_{i=1}^{N_c} N_i^{\rm sig}} \, , \tag{9.3}$$

where $N_i^{\rm sig}$ is the number of signal events in category i, $N_c = 4$ is the number of tagging categories, and $N_{\rm untag}^{\rm sig}$ is the number of untagged events. The number of events $N_i^{\rm sig}$ and $N_{\rm untag}^{\rm sig}$ are measured in the $B_{\rm flav}$ sample and are listed in Table 9.7. The tagging algorithm assigns a flavor tag to about $2/3$ of all events. The effective tagging power $Q_i = \varepsilon_i \, (1 - \langle w \rangle_i)^2$ was defined in Chapter 6 and impacts directly the uncertainty on $\sin 2\beta$, as discussed in Section 8.5. The total tagging power $Q = \sum_{i=1}^{N_c} Q_i$ is smaller than the value obtained in simulated events in Section 6.3. As pointed out earlier, it is important to evaluate the performance of the tagging algorithm in data and not to rely on simulated events.

Category	$N_{\rm sig}$	ε(%)	$\langle w \rangle$(%)	Δw(%)	Q(%)
`Lepton`	2979 ± 57	9.1 ± 0.2	3.3 ± 0.6	-1.4 ± 1.1	7.9 ± 0.3
`KaonI`	5450 ± 83	16.7 ± 0.2	9.9 ± 0.7	-1.1 ± 1.1	10.7 ± 0.4
`KaonII`	6489 ± 92	19.8 ± 0.3	20.9 ± 0.8	-4.2 ± 1.1	6.7 ± 0.4
`Inclusive`	6535 ± 94	20.0 ± 0.3	31.6 ± 0.9	-2.9 ± 1.2	2.7 ± 0.3
Total	32700 ± 208	65.6 ± 0.5			28.1 ± 0.7

Table 9.10: The efficiency ε_i, average mistag fraction $\langle w_i \rangle$, mistag difference Δw_i, and tagging power $Q_i = \epsilon_i * (1 - 2\langle w_i \rangle)$ for each tagging category measured with the maximum-likelihood fit. Signal yields $N_{\rm sig}$ are those in Table 9.7.

9.3 Cross checks

The large $B_{\rm CP}$ sample allows a number of cross checks by measuring $\sin 2\beta$ in subsets of events. Data is divided on the basis of reconstructed B decay mode, tagging category, J/ψ decay mode, flavor tag, and data taking period. Unless specified, the fits are performed to the full $B_{\rm flav}$ sample and subsets of the $B_{\rm CP}$ sample.

9.3.1 B decay modes

Table 9.11 and Figure 9.6 summarize the results of the fits to exclusive CP eigenstates. In Section 5.5 it was shown that the amount of peaking background in signal events varies for the decay modes (Table 5.10) and could potentially impact the value of $\sin 2\beta$. Results in Table 9.11, however, are in good agreement with the value measured in the full sample. The value of the χ^2, computed as

$$\chi^2 = \sum_{i}^{CP \text{ modes}} \left(\frac{\sin 2\beta_i - \sin 2\beta_{\rm All}}{\sigma_i} \right)^2 , \tag{9.4}$$

is 3.7 with 4 degrees of freedom. The Δt distributions and raw asymmetries $\mathcal{A}_{CP}$ for each decay mode are shown, respectively, in Figure 9.7 and Figure 9.8.

Sample	$N_{\rm sig}$	$\mathcal{P}$	$\sin 2\beta$
CP sample	1399 ± 39	93.5	0.755 ± 0.074
$J/\psi\, K^0_S$ ($K^0_S \to \pi^+\pi^-$)	937 ± 31	96.5	0.820 ± 0.084
$J/\psi\, K^0_S$ ($K^0_S \to \pi^0\pi^0$)	150 ± 13	88.5	0.394 ± 0.241
$\psi(2S) K^0_S$ ($K^0_S \to \pi^+\pi^-$)	143 ± 12	96.9	0.691 ± 0.235
$\chi_{c1} K^0_S$	75 ± 9	94.5	1.014 ± 0.397
$\eta_c K^0_S$	95 ± 11	73.3	0.586 ± 0.320

Table 9.11: Measurement of $\sin 2\beta$ in exclusive B decay modes. $N_{\rm sig}$ is the signal yield and $\mathcal{P}$ the purity.

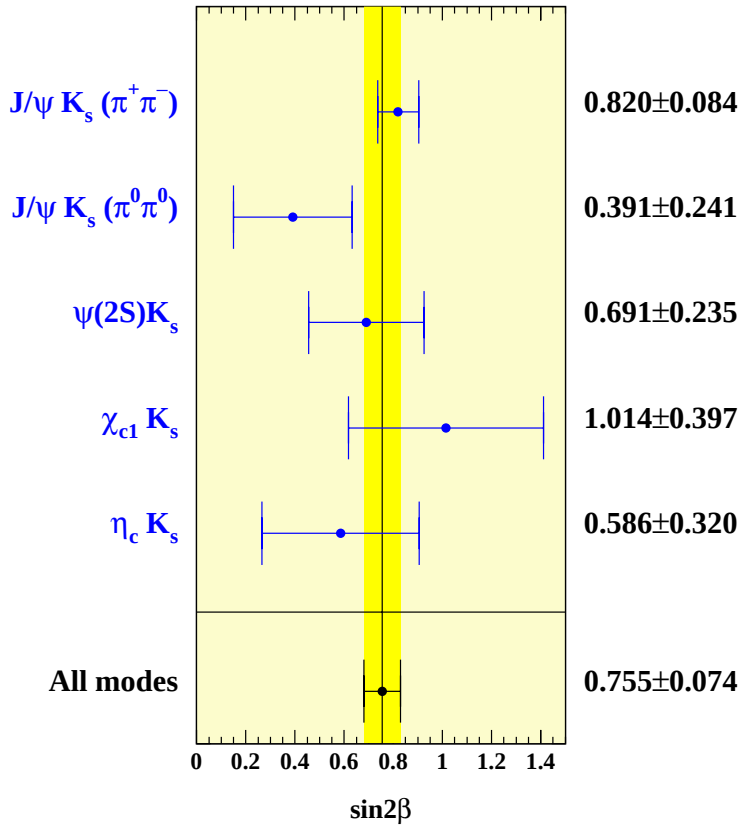

Figure 9.6: Measurement of $\sin 2\beta$ in exclusive B decay modes. The value of χ^2, defined in Equation 9.4, for the agreement between the decay modes is is 3.7 with 4 degrees of freedom.

9.3.2 Data subsamples

Fits to subsamples of data are discussed in the following. All results are summarized in Table 9.13 and compared to the value of $\sin 2\beta$ in the full sample in Figure 9.11.

Data-taking periods

The data sample used for this analysis was collected between October 1999 and June 2002. Fits are performed in subsets of data collected in four different periods of data taking defined in Table 9.12. Fit results are summarized in Table 9.13 and no significant variation in $\sin 2\beta$ is observed for different subsets of data.

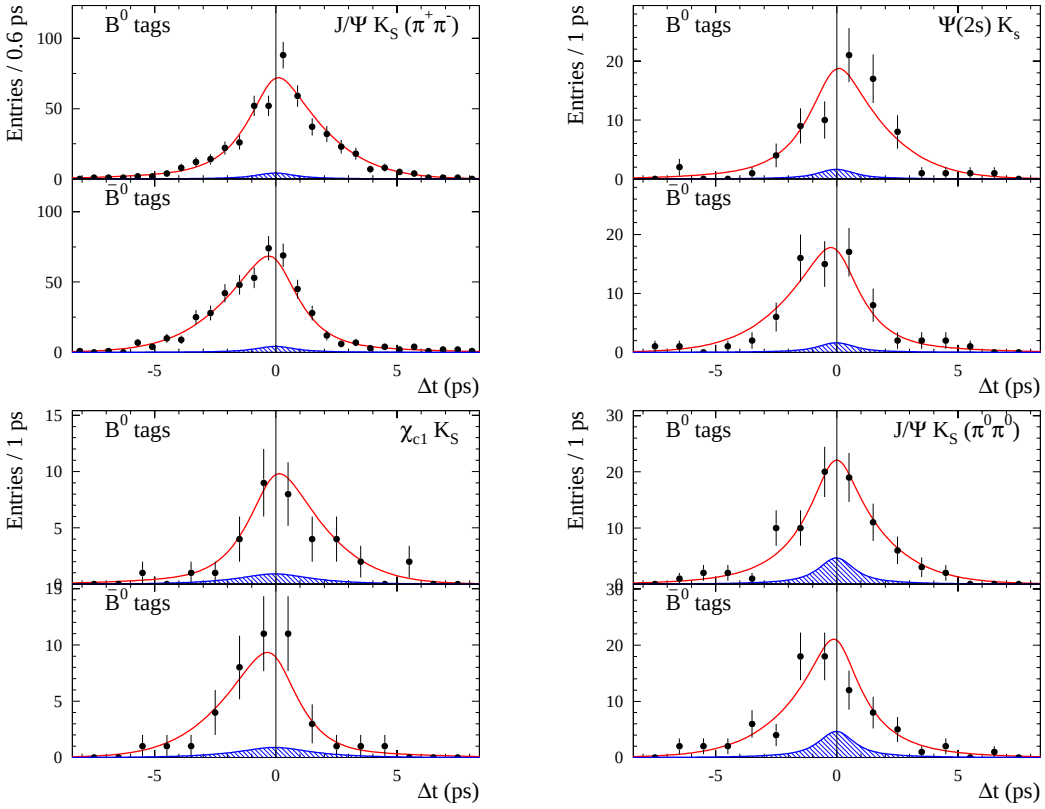

Figure 9.7: Distribution of Δt for $J/\psi K_s$, $\psi(2s)K_s$, $\chi_{c1}K_s$, and $J/\psi K_s(\pi^0\pi^0)$ decay modes. The solid line is the result of the fit. The shaded area is the contribution of background.

Tagging categories

Another useful cross check is fitting the events in individual tagging categories. The physics processes utilized to determine the flavor tag of B mesons in each tagging category are different, as discussed in Chapter 6, and result in different mistag fractions and sample purities. Hence, it is important to check that the value of $\sin 2\beta$ does not vary within the categories. Results of the fits are listed in Table 9.13 and do not show any significant variation. The Δt distributions for the events in each category, and the raw asymmetry are shown in Figures 9.9 and 9.10, respectively. The effect of the difference in the mistag fractions for the four categories is evident. The amplitude of the raw asymmetry in the `Lepton` category is the closest to the measured value of $\sin 2\beta$, while it is reduced significantly in the `Inclusive` category.

Subset	Period	Luminosity (fb^{-1})
`Run1`	October 1999 — December 2000	20.78
`Run2a`	January 2001 — June 2001	9.07
`Run2b`	July 2001 — December 2001	26.58
`Run2c+d`	January 2002 — June 2002	24.72

Table 9.12: Periods of data taking used for cross checks.

B^0 vs. $\overline{B}^0$ flavor tags

Measurement of $\sin 2\beta$ can be performed separately in events with B^0 flavor tags and those with $\overline{B}^0$ flavor tags. In fact, the Δt distributions (8.3) and (8.4) for these events are individually asymmetric with respect to $\Delta t = 0$, if $\sin 2\beta \neq 0$. Therefore, in absence of $\overline{B}^0$ (B^0) tags, $\sin 2\beta$ can still be measured with a fit to the Δt distribution of events with B^0 ($\overline{B}^0$) tags. In these fits the value of $\Delta\mathcal{D}$ for all tagging categories must be fixed to zero since there is only one flavor tag. The parameters of the resolution function are fixed to values obtained in the full fit. The results of the fits are summarized in Table 9.13 and Figure 9.13 and are in very good agreement with the combined fit as well as with each other.

$J/\psi \to e^+e^-$ and $J/\psi \to \mu^+\mu^-$ decay modes

One additional cross check is to separate events with J/ψ reconstructed in e^+e^- or $\mu^+\mu^-$ final states. These decay modes differ due to the Bremsstrahlung photons in the e^+e^- mode, which could affect the decay-vertex reconstruction. The fit results are shown in Table 9.13 and Figure 9.13, and no discrepancy is found.

9.3.3 Control samples

The sample of events with fully reconstructed B^+ mesons described in Section 5.7, and the B_{flav} sample of B^0 mesons in flavor eigenstates represent a large and valuable control sample for the measurement of $\sin 2\beta$. The B^+ mesons do not oscillate and their Δt distribution is simply an exponential decay with the B^+ lifetime. The Δt distribution of the B_{flav} sample has a $\cos \Delta m_d \Delta t$

Sample	$N_{\rm sig}$	$\mathcal{P}$(%)	$\sin 2\beta$
$B_{\rm CP}$ sample	1399 ± 39	93.5	0.755 ± 0.074
`Lepton`	217 ± 15	98.0	0.789 ± 0.113
`KaonI`	370 ± 20	93.2	0.778 ± 0.119
`KaonII`	407 ± 21	92.7	0.732 ± 0.171
`Inclusive`	406 ± 21	92.4	0.452 ± 0.282
B^0-Tag	688 ± 27	94.1	0.754 ± 0.105
$\bar{B}^0$-Tag	712 ± 28	93.3	0.739 ± 0.105
$J/\psi \to e^+e^-$	623 ± 26	93.7	0.799 ± 0.099
$J/\psi \to \mu^+\mu^-$	681 ± 26	97.1	0.696 ± 0.104
`Run 1`	357 ± 19	93.3	0.628 ± 0.149
`Run 2a`	190 ± 14	94.4	0.866 ± 0.206
`Run 2b`	445 ± 22	94.2	0.761 ± 0.135
`Run 2c+d`	408 ± 21	93.9	0.824 ± 0.127

Table 9.13: Results of the fits in subsets of the $B_{\rm CP}$ samples.

term but no *CP*-violating term. Therefore, no asymmetry is expected in these control samples and fits to their Δt distributions should yield a value of $\sin 2\beta$ consistent with zero. The results of the fits are summarized in Table 9.14 and Figure 9.12, and are consistent with no asymmetry. These results indicate that the fit procedure does not create a fake asymmetry where there is none.

Control sample	$N_{\rm sig}$	$\mathcal{P}$ (%)	$\sin 2\beta$
$B^+ \to D^{(*)0}\pi^+$	19764 ± 160	84.2	0.021 ± 0.022
$B^+ \to (c\bar{c})K^+$	6736 ± 87	93.8	0.021 ± 0.037
$B^+ \to J/\psi\, K^+$	5836 ± 81	93.8	0.047 ± 0.046
$B^+ \to \psi(2S)K^+$	555 ± 25	94.4	0.258 ± 0.121
$B^+ \to \chi_{c1}K^+$	345 ± 20	93.2	-0.194 ± 0.144
$B_{\rm flav}$ sample	21453 ± 166	85.0	0.017 ± 0.021
$B^0 \to D^{(*)-}\pi^+/\rho^+/a_1^+$	19612 ± 154	88.9	0.022 ± 0.021
$B^0 \to J/\psi\, K^{*0}(K^+\pi^-)$	1678 ± 43	95.8	-0.009 ± 0.073

Table 9.14: Fit results in control samples of fully reconstructed B^+ and B^0 mesons in flavor eigenstates.

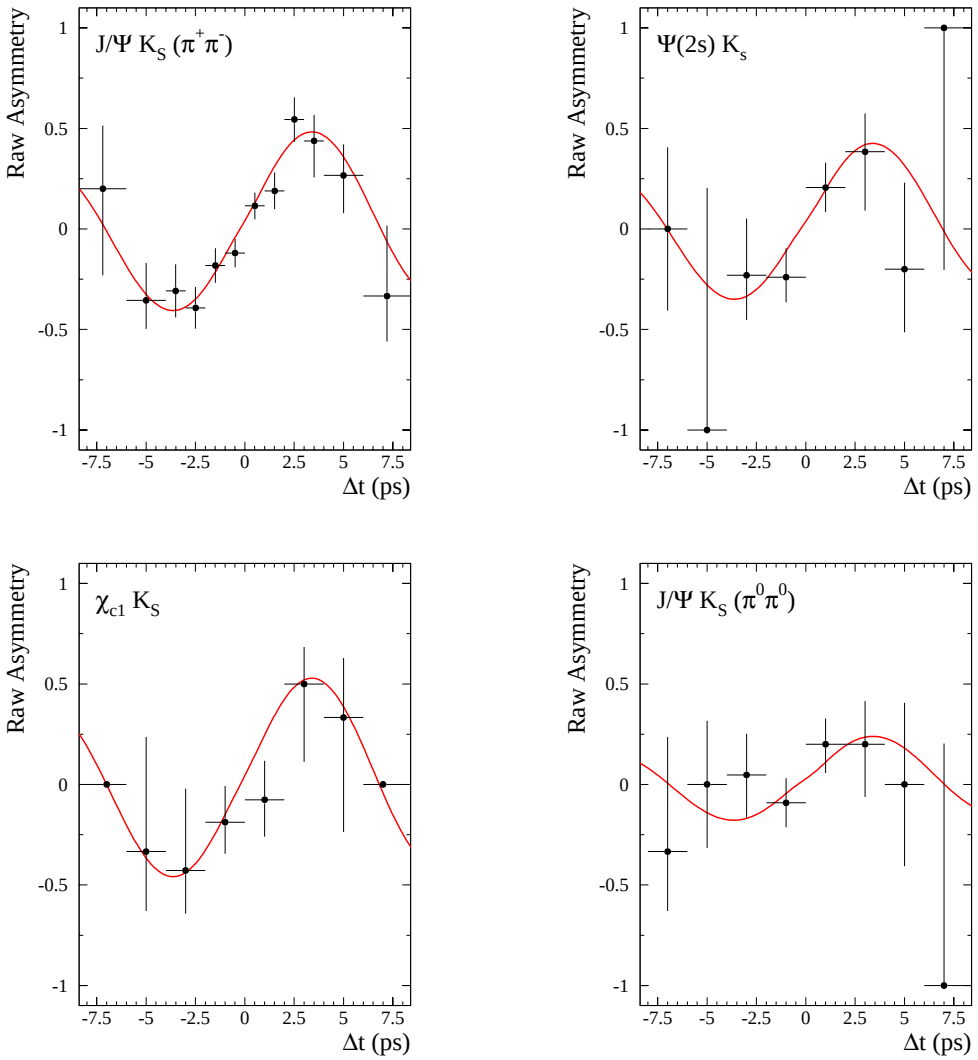

Figure 9.8: Raw asymmetry $\mathcal{A}_{CP}$ for decay modes $J/\psi K_s$, $\psi(2s)K_s$, $\chi_{c1}K_s$, and $J/\psi K_s(\pi^0\pi^0)$. The solid line is obtained from the result of the likelihood fit to Δt in Figure 9.7.

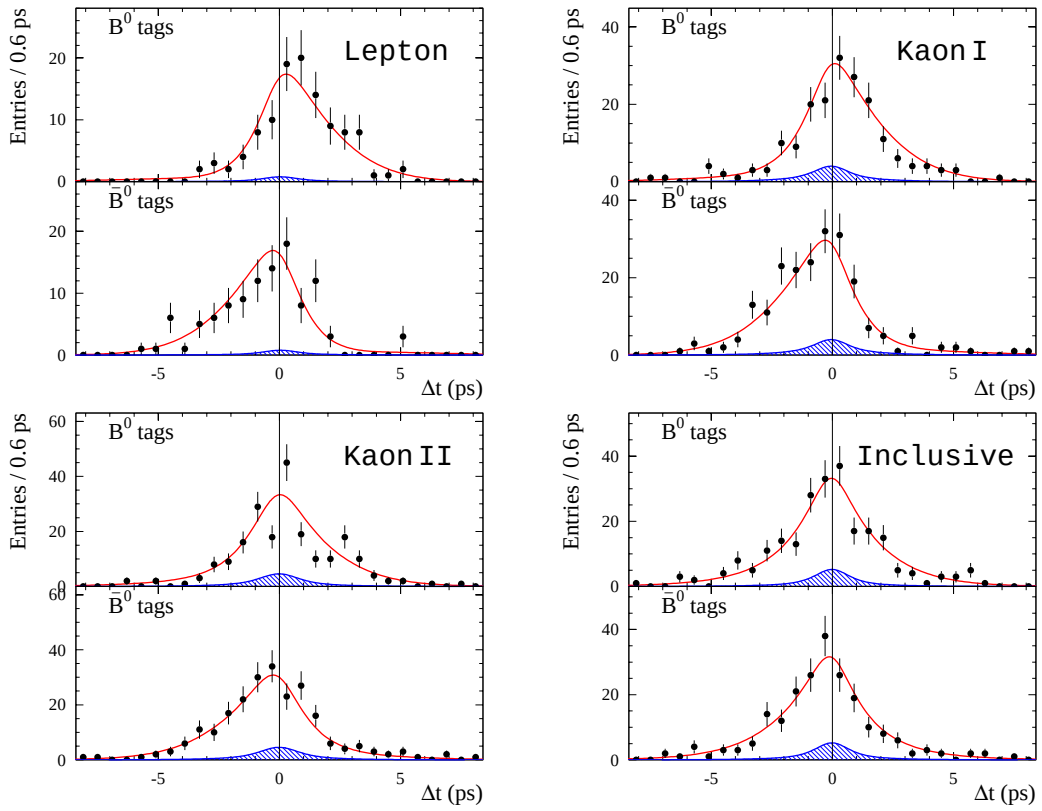

Figure 9.9: Distribution of Δt for the selected events in the four tagging categories. The solid line is the result of the fit. The shaded area is the contribution of background.

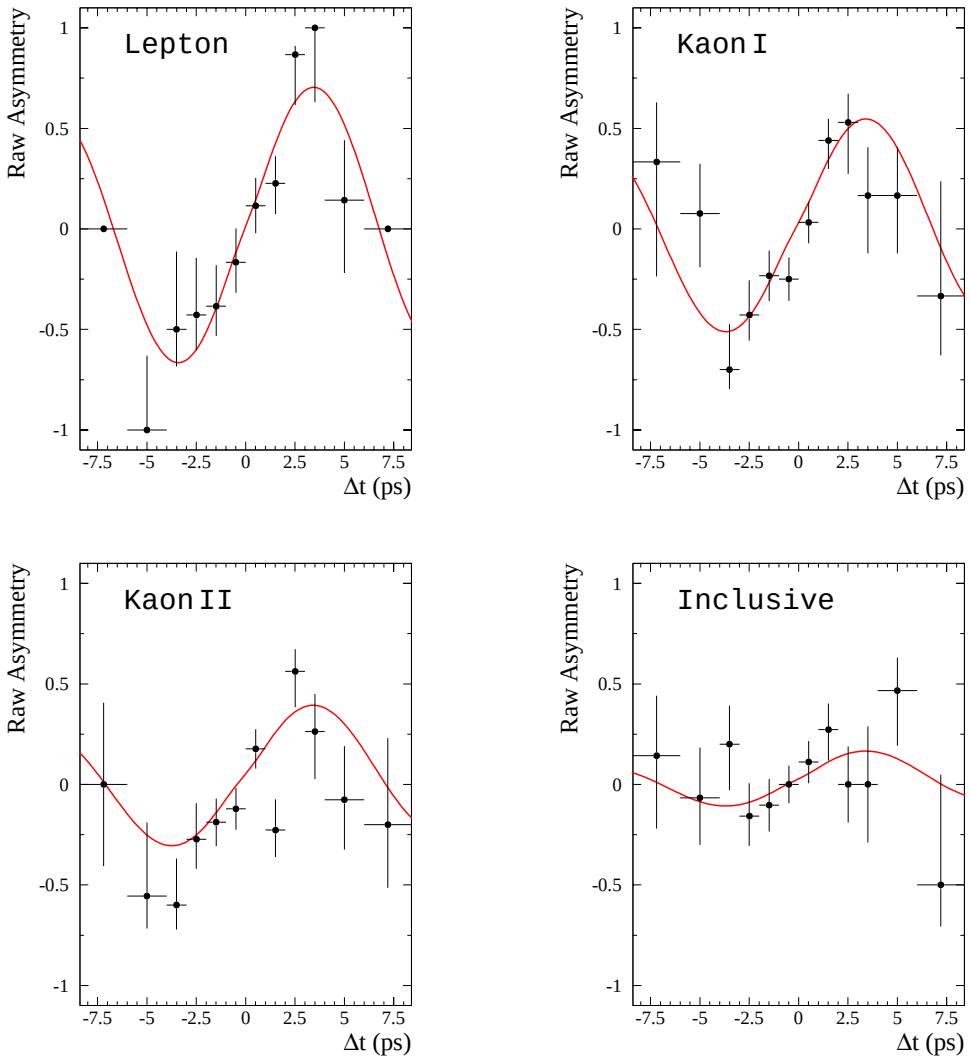

Figure 9.10: Raw asymmetry $\mathcal{A}_{CP}$ in the four tagging categories. The solid line is obtained from the result of the likelihood fit to Δt in Figure 9.9.

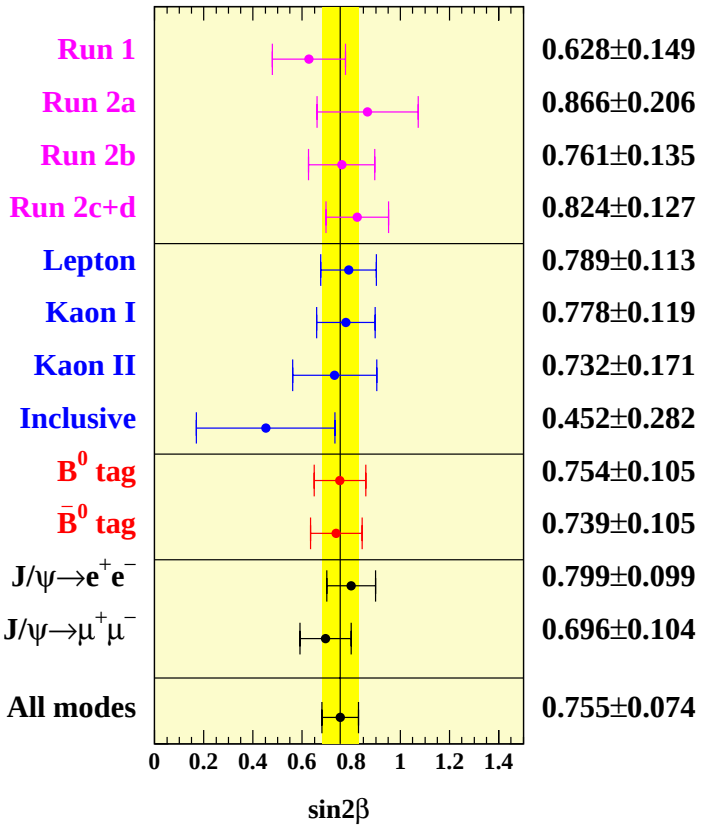

Figure 9.11: Measurement of $\sin 2\beta$ in subsamples of data.

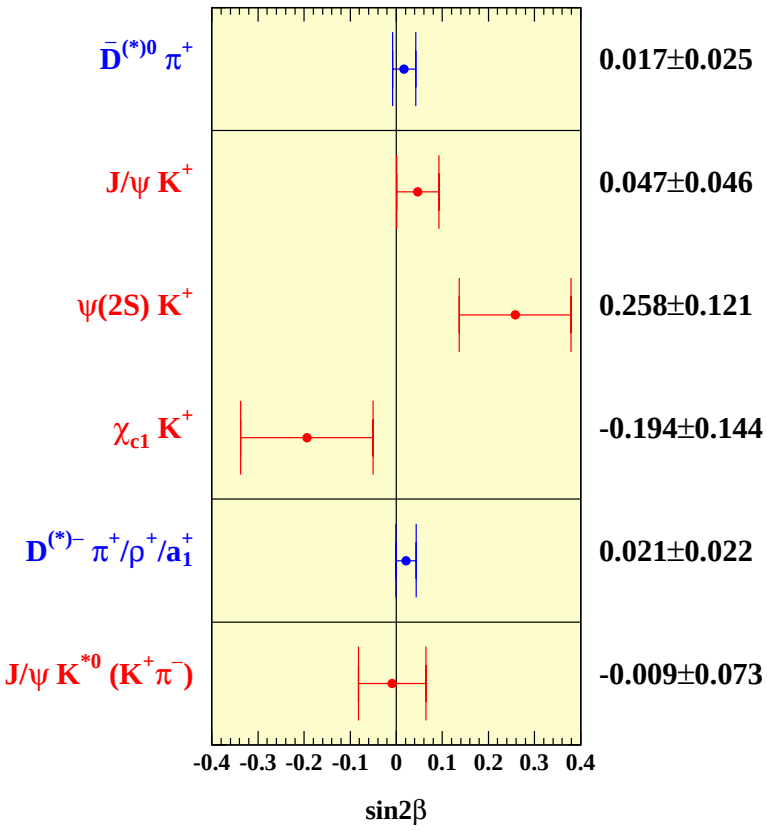

Figure 9.12: Fit results in control samples of fully reconstructed B^+ mesons and in the $B_{\rm flav}$ sample.

9.4 Evaluation of systematic uncertainty

Systematic uncertainties on $\sin 2\beta$ arise from systematic effects in the measurement of the time-difference Δt, assumptions in the analysis technique, and the parameterization of the Δt distributions for signal and background. These uncertainties are evaluated in data, where possible, or in samples of simulated events.

The value of Δt is computed from the spatial distance Δz between the decay vertices of the two B mesons in the event, and by using the measured boost factor for the $\Upsilon(4S)$. Hence, systematic effects in the reconstruction of decay vertices and measurement of the boost result in systematic uncertainties on Δt. Sources of systematic effects on Δt include:

- knowledge of the z-scale of the detector,
- knowledge of the $\Upsilon(4S)$ boost factor $\beta\gamma$,
- local alignment of the SVT that provides high precision reconstruction of decay vertices, and
- position of the beamspot used in the measurement of Δz.

The uncertainty on $\sin 2\beta$ due to these sources is evaluated in data. For example, the value of $\beta\gamma$ is varied within its measured uncertainty and the variation in $\sin 2\beta$ is taken as the systematic uncertainty.

Two assumptions in the analysis technique can cause systematic effects in the measurement of $\sin 2\beta$:

- common Δt resolution function for $B_{\rm CP}$ and $B_{\rm flav}$ samples, and
- similar performance for the flavor-tagging algorithm in $B_{\rm CP}$ and $B_{\rm flav}$ samples.

The impact of these assumptions is evaluated in simulated events, where the true values of Δt and the flavor tag are known and allow the comparison of the parameters of the Δt resolution functions and the mistag fractions between the the two samples.

The parameterization of the Δt distributions for signal and background in the fit, was discussed in Chapter 8. It was pointed out that assumptions in the empirical description of the background is a source of systematic effects. These effects are estimated in data from the change in $\sin 2\beta$ when the assumptions are varied.

In the remainder of this Section, individual sources of systematic uncertainty on $\sin 2\beta$ are described, and their contribution is evaluated. For simplicity, the fit to data is referred to as the nominal fit.

The order in which the various sources are discussed does not correspond to the size of their contribution. Given the relatively large number of effects considered, contributions of those sources with similar nature are discussed together. All contributions are summarized in Section 9.4.19 where the total systematic uncertainty is computed.

9.4.1 Common Δt resolution function

The assumption of a common Δt resolution function for the $B_{\rm CP}$ and $B_{\rm flav}$ samples is tested in simulated events. In these events, the resolution function parameters $\hat{a}_{CP} \pm \delta a_{CP}$ and $\hat{a}_{\rm flav} \pm \delta a_{\rm flav}$, respectively for the $B_{\rm CP}$ and the $B_{\rm flav}$samples, are measured from fits to the residual $\delta t = \Delta t_{\rm meas} - \Delta t_{\rm true}$ (see Section 7.6). The parameters $\hat{a}$ were described in Section 8.3.2 and consist of one width scale factor and four bias scale factors for the core component, one bias scale factor for the tail, the fraction of events in the tail, and the fraction of events in the outliers component. The other parameters are fixed and their contributions to the systematic uncertainty are estimated as described in the next section.

For the measured parameters $\hat{a}_{CP} \pm \delta a_{CP}$, $\sin 2\beta$ is measured in sixteen different configurations: each parameter a^i_{CP} is varied separately by $+\delta a^i_{CP}$ and $-\delta a^i_{CP}$ while keeping the other parameters fixed. The mistag fractions are fixed to zero and the true flavor tag for each event is used.

The mean $\langle \sin 2\beta \rangle_{CP}$ and the RMS spread $\delta \sin 2\beta_{CP}$ of measured values of $\sin 2\beta$ are reported in Table 9.15. Similar fits are performed by using the parameters $\hat{a}_{\rm flav} \pm \delta a_{\rm flav}$ of the $B_{\rm flav}$ sample, and their results are also reported in Table 9.15.

	$\langle \sin 2\beta \rangle$	$\delta \sin 2\beta$
$\hat{a}_{CP} \pm \delta a_{CP}$	0.70872	0.00021
$\hat{a}_{\rm flav} \pm \delta a_{\rm flav}$	0.70697	0.00040

Table 9.15: Mean and RMS spread of measured $\sin 2\beta$ with resolution function parameters $\hat{a}_{CP} \pm \delta a_{CP}$ and $\hat{a}_{\rm flav} \pm \delta a_{\rm flav}$ in simulated events. The $B_{\rm CP}$ sample is generated with $\sin 2\beta$ =0.7033.

The difference between the means is 0.00175 ± 0.00045. A systematic uncertainty of 0.002 is assigned to the assumption of a common Δt resolution function for the $B_{\rm CP}$ and the $B_{\rm flav}$ samples.

9.4.2 Signal Δt resolution function

Tail component

In the nominal fit the width scale factor $S^{\rm sig}_{\rm tail}$ is fixed to 3, as discussed in Section 8.3.2. The systematic uncertainty due to this assumption is estimated as the biggest variation in $\sin 2\beta$ when $S^{\rm sig}_{\rm tail}$ is instead fixed at 2 and 5. A systematic uncertainty of 0.002 is assigned.

Outlier Component

The mean offset and the width of the outlier component are fixed, respectively, to $0\,{\rm ps}$ and $8\,{\rm ps}$ in the nominal fit (see Section 8.3.2). The systematic uncertainty due to this assumption is evaluated by varying these parameters separately and repeating the fit. The width of the outlier Gaussian is varied between $4\,{\rm ps}$ and $12\,{\rm ps}$ and its mean offset is varied by $\pm 2\,{\rm ps}$ around the nominal value. Table 9.16 shows the variations in $\sin 2\beta$ for the four different sets of parameters for the outlier Gaussian.

The variations due to the mean offset and due to the width are assumed to be uncorrelated. The largest variations are added in quadrature to evaluate a total contribution of 0.005 to the systematic uncertainty.

width/bias (ps)	$\delta \sin 2\beta$
8/0	–
4/0	-0.004
12/0	-0.002
8/–2	-0.001
8/+2	-0.003
Total	0.005

Table 9.16: Systematic uncertainty on $\sin 2\beta$ due to fixed width and mean offset of the outliers component. The variations due to the width and due to the mean offset are assumed to be uncorrelated. The total uncertainty is computed as the sum in quadrature of the two largest contributions.

9.4.3 Signal Δt resolution function model

In this analysis the Δt resolution function is parameterized with a sum of three Gaussians (Section 7.6). The mean offsets of the core and tail components are allowed to vary in the fit. These offsets account for the negative bias in Δt due to charm-decay daughters included in the decay vertex of the tagging B meson (Section 7.4). The sensitivity of $\sin 2\beta$ to the resolution function model is estimated by using an alternative model, called `GExp` for brevity, and defined as

$$\begin{aligned} \texttt{GExp}(\delta_t;\sigma,\tau,f_t,f_o) &\equiv G(\mu\equiv 0,\sigma)\otimes\Big((1-f_t-f_o)\delta(\delta_t)+f_t\,\mathrm{e}^{\delta_t/\tau}\Big)+f_o\,G(0\,\mathrm{ps},8\,\mathrm{ps}) \quad (9.5)\\ &= (1-f_t-f_o)\,G(\mu\equiv 0,\sigma)+f_t\,G(\mu\equiv 0,\sigma)\otimes\mathrm{e}^{\delta_t/\tau}+f_o\,G(0\,\mathrm{ps},8\,\mathrm{ps}) \end{aligned}$$

where $\delta t \equiv \Delta t_{\rm meas} - \Delta t_{\rm true}$, and $G(\mu,\sigma)$ is a Gaussian with mean μ and width σ.

The first term corresponds to the core component with no mean offset and the third component is the same as the outliers component. The bias from the charm decays is accounted for with the one-sided exponential in the second term. One common effective lifetime τ is used but each tagging category has a different f_t to allow for different biases. The fitted value of $\sin 2\beta$ changes by 0.007 when the `GExp` model is used. This variation is taken as the systematic uncertainty.

9.4.4 Δt resolution function in events with wrong flavor tag

In this analysis, a common Δt resolution function is used for all signal events. In principle, events which are assigned a correct flavor tag and those with a wrong flavor tag could have different resolution functions. For example, if tracks from the tagging B meson ($B_{\rm tag}$) are included in the fully reconstructed B meson ($B_{\rm rec}$), the measured Δt can be smaller than its true value.

The effect of possible differences between the two subsets of events is estimated with simulated $B_{\rm CP}$ events. The method is similar to that used in in Section 9.4.1. The true flavor tag is used to separate events with the correct tag (sample $\mathcal{A}$) and those with the wrong tag (sample $\mathcal{B}$). Parameters $\hat{a}\pm\delta a$ of the resolution function are measured from fits to the residual $\delta t \equiv \Delta t_{\rm meas} - \Delta t_{\rm true}$ for all events ($\hat{a}_{\rm all}$), for sample $\mathcal{A}$ ($\hat{a}_A$), and for sample $\mathcal{B}$ ($\hat{a}_B$).

The value of $\sin 2\beta$ is measured separately for samples $\mathcal{A}$ and $\mathcal{B}$ with fits in which the resolution function parameters are fixed to $\hat{a}_{\rm all}$, and the true flavor tag is used. The mistag fractions are fixed to 0 in the fits to sample $\mathcal{A}$ (all events have the correct tag), and to 1 in the fits to sample $\mathcal{B}$. The value of $\sin 2\beta_{\rm all}$ for the entire sample is computed as the weighted average of $\sin 2\beta_A$ and $\sin 2\beta_B$. The fits are then repeated after changing each of the parameters a_i by $\pm\delta a_i$ while keeping all other parameters fixed (sixteen configurations). The mean and the RMS spread of the distribution of $\sin 2\beta_{\rm all}$ are reported in Table 9.17.

	$\langle \sin 2\beta_{\rm all} \rangle$	$\delta \sin 2\beta_{\rm all}$
$\hat{a}_{\rm all}$	0.69909	0.00031
$\hat{a}_A$ and $\hat{a}_B$	0.69926	0.00073

Table 9.17: Mean and RMS spread of measured $\sin 2\beta_{\rm all}$ with common resolution functions parameters $\hat{a}_{\rm all}$ and separate parameters $\hat{a}_A$ and $\hat{a}_B$.

A second set of fits are performed where each sample uses its own set of parameters: $\hat{a}_A$ for fits to sample $\mathcal{A}$ and $\hat{a}_B$ in fits to sample $\mathcal{B}$. The value of $\sin 2\beta_{\rm all}$ is then computed for the full sample as the weighted average of the two fitted values. The mean and the RMS spread of $\sin 2\beta_{\rm all}$ for these fits are also reported in Table 9.17.

The observed variation in $\langle \sin 2\beta_{\rm all} \rangle$ is 0.0002 ± 0.0008, and a systematic uncertainty of 0.0008 is assigned.

9.4.5 Common dilutions and dilutions differences

The systematic uncertainty due to possible differences in dilutions $\langle \mathcal{D} \rangle$ and dilution differences $\Delta\mathcal{D}$ between the $B_{\rm CP}$ and the $B_{\rm flav}$ samples is estimated with simulated events.

Resolution function parameters $\hat{a}_{CP}$ for the $B_{\rm CP}$ samples are measured with fits to the distribution of the Δt residual $\delta_t \equiv \Delta t_{\rm meas} - \Delta t_{\rm true}$. Dilutions $\langle \mathcal{D} \rangle \pm \delta\langle \mathcal{D} \rangle$ and dilution differences $\Delta\mathcal{D} \pm \delta\Delta\mathcal{D}$ for the $B_{\rm CP}$ and $B_{\rm flav}$ samples are measured by using the true flavor tag and by counting the number of wrongly tagged events.

Two sets of fits are performed to the $B_{\rm CP}$ sample, first using $\langle \mathcal{D} \rangle_{CP}$ and $\Delta\mathcal{D}_{CP}$ measured in the $B_{\rm CP}$ sample, and then using $\langle \mathcal{D} \rangle_{\rm flav}$ and $\Delta\mathcal{D}_{\rm flav}$ measured in the $B_{\rm flav}$ sample. In all fits, the resolution function parameters fixed to $\hat{a}_{CP}$. In the first sixteen fits, $\langle \mathcal{D} \rangle_{CP}$ are varied by $\pm\delta\langle \mathcal{D} \rangle_{CP}$ and $\Delta\mathcal{D}_{CP}$ by $\pm\delta\Delta\mathcal{D}_{CP}$, separately for each tagging category. The mean and the RMS spread of $\sin 2\beta$ measured in these fits are reported in Table 9.18. In the second set of fits $\langle \mathcal{D} \rangle_{\rm flav}$ and $\Delta\mathcal{D}_{\rm flav}$ are varied. The mean and RMS spread of $\sin 2\beta$ from these fits are also reported in Table 9.18. A systematic uncertainty of 0.012 is assigned to the difference in flavor tagging between the $B_{\rm flav}$ and the $B_{\rm CP}$ sample.

	$\langle \sin 2\beta \rangle$	$\delta \sin 2\beta$
$\langle \mathcal{D} \rangle_{CP}, \Delta\mathcal{D}_{CP}$	0.7109	0.0006
$\langle \mathcal{D} \rangle_{\rm flav}, \Delta\mathcal{D}_{\rm flav}$	0.7232	0.0010

Table 9.18: Mean and RMS spread of measured $\sin 2\beta$ using $\langle \mathcal{D} \rangle_{CP}, \Delta\mathcal{D}_{CP}$ and $\langle \mathcal{D} \rangle_{\rm flav}, \Delta\mathcal{D}_{\rm flav}$.

9.4.6 Signal probability

Each event in the $B_{\rm CP}$ sample is assigned a signal probability $f_{\rm sig}$ on the basis of the measured value of $m_{\rm ES}$ for the fully reconstructed B meson in the event. The amplitude of the sine term in the Δt distributions is $\sin 2\beta$ for the signal, but is fixed to zero for the background. Therefore, variations in $f_{\rm sig}$ can result in variations in the measured amplitude and therefore the fitted value of $\sin 2\beta$. The evaluation of the systematic uncertainty due to the uncertainty on the measured value of $f_{\rm sig}$ consists of two steps.

First, $\sin 2\beta$ is measured with fits in which $f_{\rm sig}$ is fixed to the sample purity $\mathcal{P}$ for events with $m_{\rm ES} > 5.27\,{\rm GeV}/c^2$, and to zero for events with $m_{\rm ES} < 5.270\,{\rm GeV}/c^2$. Purity $\mathcal{P} \pm \delta\mathcal{P}$ is measured from fits to the $m_{\rm ES}$ distributions for each tagging category as described in Section 5.4.

Then, the fits are repeated after varying $f_{\rm sig}$ by $\pm\delta\mathcal{P}$ simultaneously for all tagging categories but independently for the $B_{\rm CP}$ and $B_{\rm flav}$ samples.

Variations in $\sin 2\beta$ are listed in Table 9.19. The largest variations of 0.007 and 0.001 are taken as systematic uncertainties for the $B_{\rm CP}$ and the $B_{\rm flav}$ samples, respectively.

Variation	$\delta \sin 2\beta$
Δ(up) $f_{\rm Sig}^{CP}$	$+0.007$
Δ(down) $f_{\rm Sig}^{CP}$	-0.006
Δ(up) $f_{\rm Sig}^{\rm flav}$	-0.001
Δ(down) $f_{\rm Sig}^{\rm flav}$	$+0.001$

Table 9.19: Systematic uncertainty on $\sin 2\beta$ due to statistical uncertainty on the signal probability $f_{\rm sig}$.

9.4.7 Beam energy E_b in the $m_{\rm ES}$ fits

The beam energy E_b is fixed to $5.291\,\mathrm{GeV}/c^2$ in the $m_{\rm ES}$ fits performed to determine the signal probability $f_{\rm sig}$. Variations in E_b can change the signal probability and therefore change the value of $\sin 2\beta$.

The value of E_b is known with an uncertainty of $0.002\,\mathrm{GeV}/c^2$. The systematic uncertainty on $\sin 2\beta$ is estimated by repeating the $m_{\rm ES}$ fits with E_b varied by $\pm 0.002\,\mathrm{GeV}/c^2$. The largest variation of 0.001 is assigned as the systematic uncertainty on $\sin 2\beta$.

9.4.8 Fraction of peaking background

Fractions $f_{\rm pk}$ of peaking background for the $B_{\rm CP}$ and the $B_{\rm flav}$ samples are measured in simulated events (Sections 5.5 and 5.6). Variations in $f_{\rm pk}$, and therefore the signal probability, can change the value of $\sin 2\beta$, as explained in Section 9.4.6.

The systematic uncertainty due to the uncertainty on $f_{\rm pk}$ is evaluated by performing fits in which this fraction is varied by its uncertainties. The value of $\sin 2\beta$ does not change when $f_{\rm pk}^{\rm flav}$ for the $B_{\rm flav}$ sample is varied. For the $B_{\rm CP}$ sample, a conservative approach is used. The fractions for all decay modes are increased and decreased simultaneously in the fit, and result in a variation of 0.006 in $\sin 2\beta$. This variation is taken as the systematic uncertainty on $\sin 2\beta$.

9.4.9 Background composition in the $B_{\rm CP}$ sample

The empirical description of the Δt distribution for the background in the $B_{\rm CP}$ sample was discussed in Section 8.1.2. In the nominal fit, this description includes only a prompt and a non-prompt components, and no *CP*-violating term. Similarly, the peaking background is assigned an effective *CP* eigenvalue $\eta_{\rm pk} = 0$, and therefore does not include *CP* violation.

A conservative approach is used to evaluate the presence of potential asymmetries in the Δt distribution of the background. For the peaking background, the value of $\eta_{\rm pk}$ is varied between -1 and $+1$, corresponding to maximal *CP* violation in these events. For the combinatorial background, the fit is repeated by including the *CP*-violating term in Equation (8.19): fraction $f_{i,3}^{CP} = 0$ and effective *CP* amplitudes $\eta_i^{\rm comb}$ are left floating, while the effective lifetime $1/\Gamma_3^{CP}$ is fixed to the B^0 lifetime.

The largest variation in $\sin 2\beta$ with respect to the nominal fit is 0.012, and is assigned as the systematic uncertainty.

9.4.10 Background effective lifetime in the $B_{\rm CP}$ sample

The effective lifetime $1/\Gamma_2^{CP}$ of the non-prompt $B_{\rm CP}$ background in (8.18) is fixed to the B^0 lifetime in the nominal fit. The variation of $1/\Gamma_2^{CP}$ between 0.7 ps and 2 ps changes the value of $\sin 2\beta$ by 0.002, which is taken as the systematic uncertainty.

9.4.11 Background Δt resolution function

The background Δt resolution function in the fit was discussed in Section 8.3.4 and is modeled with a sum of a core and an outliers component, by fixing the fraction $f_{\rm tail}^{\rm bkg}$ of the tail to zero. The systematic uncertainty on $\sin 2\beta$ due to this assumption is estimated by floating the tail fraction $f_{\rm tail}^{\rm bkg}$ and the mean offset of the background resolution function. The width scale factor is fixed to 3 (as for signal). The variation in $\sin 2\beta$ with this configuration is 0.006, and is assigned as the systematic uncertainty.

9.4.12 Background composition in the $B_{\rm flav}$ sample

In the nominal fit, the Δt distribution (8.34) for the combinatorial background in the $B_{\rm flav}$ sample does not include any oscillatory term (Section 8.3.5), by fixing $f_{i,3}^{\rm flav}$ to zero in Equation (8.34).

The fit is repeated with $f_{i,3}^{\rm flav}$ free to vary, and $f_{i,2}^{\rm flav}$ fixed to zero instead. Thus, the background is described by a prompt term and a purely oscillatory term. The value of $\sin 2\beta$ from this fits differs by 0.003 with respect to the nominal fit. This variation is assigned as the systematic uncertainty.

9.4.13 Fixed B^0 lifetime and oscillation frequency Δm_d

In the nominal fit, the B^0 lifetime and the oscillation frequency Δm_d are fixed to the world average values 1.542 ± 0.016 ps and $0.489 \pm 0.008\,{\rm ps}^{-1}$ [33], respectively.

The dependency of $\sin 2\beta$ on τ_{B^0} and Δm_d is determined from fits where the fixed values of these parameters are varied. Figure 9.13 shows the measured $\sin 2\beta$ as a function of Δm_d and τ_{B^0}. The correlation coefficients (i.e. the slopes of the linear dependency) are listed in Table 9.20. The systematic uncertainty is estimated by the product of the correlation coefficient and the known uncertainty for each parameter.

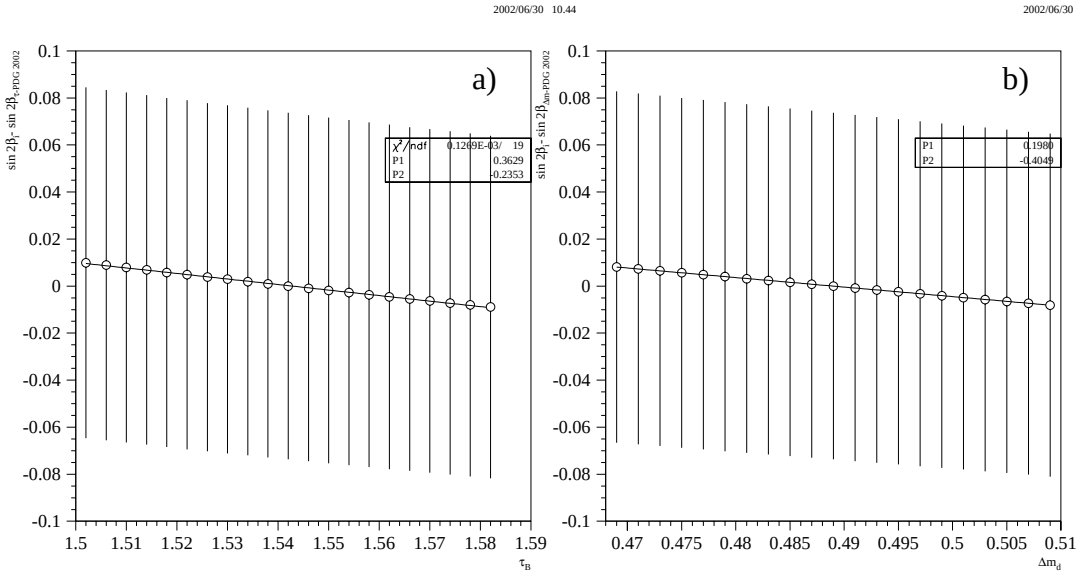

Figure 9.13: Correlation between $\sin 2\beta$ and τ_{B^0} in a) and between $\sin 2\beta$ and Δm_d in b).

$\delta \sin 2\beta / \delta \tau(B^0)$	-0.24 ps^{-1}
$\sigma_{syst}(\tau(B^0))$	0.004
$\delta \sin 2\beta / \delta \Delta m_d$	–0.40 ps
$\sigma_{syst}(\Delta m_d)$	0.003

Table 9.20: Variations in $\sin 2\beta$ due to uncertainties on τ_{B^0} and Δm_d.

9.4.14 Boost and z-scale uncertainty

In first approximation, the value of Δt and the measured Δz are related by $\Delta z = \beta\gamma\Delta t$. Hence, variations in $\beta\gamma$ or the z scale directly impact the value of Δt, which can result in variations of the fitted $\sin 2\beta$.

The z scale is measured by reconstructing interactions of electrons and positrons from the beam with the material of the beam pipe [126]. The measured relative uncertainty is 0.2% at the radius of the beampipe. Since the distance Δz is measured near the interaction region, and not at the beampipe radius, an uncertainty of 0.6% is used for the evaluation of the systematic uncertainty. The measured $\sin 2\beta$ varies by 0.001, when the measured Δt and $\sigma_{\Delta t}$ are scaled by $\pm 0.6\%$.

The boost factor $\beta\gamma$ is measured from the knowledge of the PEP-II beam energies with a relative

uncertainty of 0.1% [70]. Since this uncertainty is smaller than the uncertainty on the z scale, a conservative systematic uncertainty of 0.001 is assigned.

9.4.15 Beamspot position

The position of the beamspot is used as a constraint in the measurement of the distance Δz between the decay vertices of the two B mesons (Section 7.4). This position is computed for each run of data taking from $e^+e^- \to e^+e^-$ and $\mu^+\mu^-$ events (Section 4.1). The strongest constraint comes from the y position of the beamspot which is known with a precision of about $10\,\mu\mathrm{m}$.

Two types of systematic effects are studied to evaluate the sensitivity of $\sin 2\beta$ to the beamspot position: the y position of the beamspot is either shifted by a known amount, or convoluted with a Gaussian of fixed width. The value of $\sin 2\beta$ is measured after applying shifts of $20\,\mu\mathrm{m}$ and $40\,\mu\mathrm{m}$, and convolutions with Gaussians with a width of $30\,\mu\mathrm{m}$ and $60\,\mu\mathrm{m}$. The largest variation in $\sin 2\beta$ is 0.010 and occurs when the y position is shifted by $40\,\mu\mathrm{m}$. This variation is assigned as the systematic uncertainty.

9.4.16 SVT alignment

Reconstruction of decay vertices of B mesons relies on the high precision reconstruction of charged-particle trajectories. For particles originating from the interaction point, the measurement of the trajectory parameters is dominated by the silicon vertex tracker. The measured parameters are very sensitive to the relative positions of the silicon wafers and strips that are used to detect the interactions of the charged particles. The knowledge of actual positions of the wafers and strips with respect to their nominal positions is referred to as the SVT *local alignment.*

The local alignment of the SVT is measured with $e^+e^- \to \mu^+\mu^-$ events by studying the impact parameters d_0 and z_0 in the xy plane and along the z axis (see Table 4.4) as a function of azimuthal angle ϕ_0 [127]. The position of the wafers is expressed in terms of rotations $\mathfrak{R}$ and translations $\mathfrak{T}$ with respect to the **perfect** alignment, where all wafers are at their nominal positions.

The effect of systematic uncertainties associated to the alignment procedure is estimated with simulated events. The reconstruction of these events utilizes the correct position of the SVT wafers, and corresponds to the perfect alignment scenario. Hence, fits to simulated B_{CP} and B_{flav} samples provide the nominal value for $\sin 2\beta$ with perfect alignment. Possible misalignment scenarios in data are expressed in terms of transformations $(\mathfrak{R}_i, \mathfrak{T}_i)$, and are used to introduce a *known* misalignment in the reconstruction of simulated events. Variations in $\sin 2\beta$ in fits to *misaligned* B_{CP} and B_{flav}

samples provides an estimate of the systematic uncertainty due to the SVT alignment.

Variation $\delta \sin 2\beta$ for three different misalignment scenarios [128] with respect to the perfect alignment are summarized in Table 9.21. The uncertainty on $\delta \sin 2\beta$ takes into account the correlation ρ between the perfect and the misaligned samples, computed with the *Kin* variable [129]. The average of the three contributions is 0.004 ± 0.006 and the systematic uncertainty is taken to be 0.010. Note that the uncertainties in Table 9.21 are highly correlated and can not be used to compute a simple weighted average. The above value for the average variation has been computed by taking into account the correlations.

Alignment set	$\delta \sin 2\beta$
`Nov2001`	-0.003 ± 0.005
`OverlapRun2`	-0.004 ± 0.006
`DiffBlend`	0.004 ± 0.007

Table 9.21: Variations in $\sin 2\beta$ for three SVT-misalignment scenarios.

9.4.17 Monte Carlo bias

The measured value of $\sin 2\beta$ in data is corrected to account for an observed bias of +0.014, discussed in Section 8.4.3. In Section 8.4.4, it was shown that the correlation between $\langle \mathcal{D} \rangle$ and $\sigma_{\Delta t}$ accounts for +0.004 of this bias.

The difference of 0.010 between the total bias and the understood fraction is taken as the systematic uncertainty.

9.4.18 Doubly-CKM-suppressed decays

The flavor-tagging algorithm relies primarily on the correlation between the charge of the particles in the final state and the flavor of the parent B meson. The main sources of flavor-tag information were discussed in Section 6.1. It is usually assumed that the $D^{(*)-}\, X^{+}$ final states are produced in decays of B^0 while the conjugate modes $D^{(*)+}\, X^{-}$ are final states of $\overline{B}^0$. The diagram for the $B^0 \to D^{(*)-}\, X^{+}$ decay is shown in Figure 9.14a.

However, the $\overline{B}^0$ meson also contributes to this same final state as illustrated in Figure 9.14b, but the amplitude for this contribution is suppressed by

$$\mathcal{R} \equiv \frac{|\mathcal{A}(B^0 \to D^{*-} X^+)|}{|\overline{\mathcal{A}}(\overline{B}^0 \to D^{*-} X^+)|} = \frac{|V_{ub}^* V_{cd}|}{|V_{cb}^* V_{ud}|} = \lambda^2 \approx 0.04 \text{ [33]}. \tag{9.6}$$

The decay of B^0 is CKM-favored, while the decay of $\overline{B}^0$ is referred to as doubly-CKM-suppressed (DCS), since both CKM factors are suppressed by a factor λ.

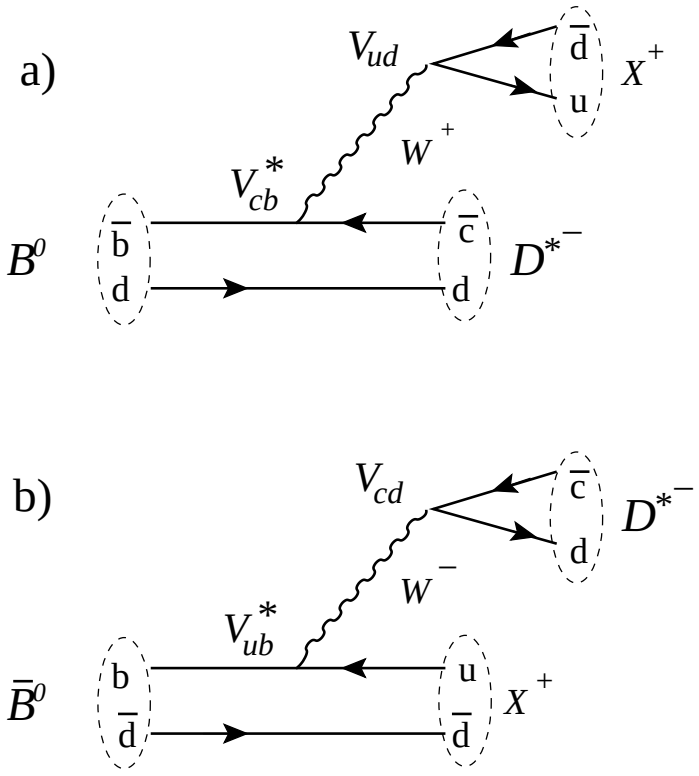

Figure 9.14: a) The CKM-favored decay $B^0 \to D^{*-} X^+$, and b) the doubly-CKM-suppressed decay $\overline{B}^0 \to D^{*-} X^+$.

The DCS decays affect the tagging B meson in the $B_{\rm CP}$ and the $B_{\rm flav}$ samples, and also the fully reconstructed B meson in the $B_{\rm flav}$ sample. Although the branching fractions for these decays are suppressed by about $\mathcal{O}(10^{-4})$, neglecting these decays can impact both the flavor tagging and the Δt distributions.

In terms of flavor tagging, these decays, to first order, increase the mistag fractions when kaons and pions are used to determine the flavor of the B meson, because the charge correlation has the opposite sign. Flavor tags using leptons are not affected because the semileptonic decays $B^0 \to X^- \ell^+ \nu_\ell$ do not have a DCS-related decay.

The Δt distributions for the events in the $B_{\rm CP}$ and the $B_{\rm flav}$ samples are modified due to the interference between amplitudes $\mathcal{A}$ and $\overline{\mathcal{A}}$ in (9.6). The complete derivation of these distributions can be found in Reference [130]. The distributions (8.3) and (8.4) for the $B_{\rm CP}$ sample, including the DCS decays can be written as

$$\begin{aligned} f_{B_{\rm tag}=\overline{B}^0}(\Delta t) \;\propto\; & e^{-\Gamma|\Delta t|}\left\{(1+\mathcal{R}^2) - 2\mathcal{R}\cos(2\beta)\cos(2\beta+\gamma'+\delta')\right. \\ & -\cos\Delta m\Delta t\left[2\mathcal{R}\sin(2\beta)\sin(2\beta+\gamma'+\delta')\right] \\ & \left.+\sin\Delta m\Delta t\left[(1-\mathcal{R}^2)\sin(2\beta)\right]\right\} \qquad (9.7) \\ f_{B_{\rm tag}=B^0}(\Delta t) \;\propto\; & e^{-\Gamma|\Delta t|}\left\{(1+\mathcal{R}^2) - 2\mathcal{R}\cos(2\beta)\cos(2\beta+\gamma'-\delta')\right. \\ & -\cos\Delta m\Delta t\left[2\mathcal{R}\sin(2\beta)\sin(2\beta+\gamma'-\delta')\right] \\ & \left.-\sin\Delta m\Delta t\left[(1-\mathcal{R}^2)\sin(2\beta)\right]\right\} \qquad (9.8) \end{aligned}$$

where $1/\Gamma = \tau_{B^0}$ and

$$\begin{aligned} A(B_{\rm tag}=B^0 \to D^{(*)-}X^+) &= \mathcal{A} \\ A(B_{\rm tag}=\overline{B}^0 \to D^{(*)-}X^+) &= \mathcal{A}\,\mathcal{R}\,e^{-i\gamma'}\,e^{i\delta'} \\ A(B_{\rm tag}=B^0 \to D^{(*)+}X^-) &= \mathcal{A}\,\mathcal{R}\,e^{+i\gamma'}\,e^{i\delta'} \\ A(B_{\rm tag}=\overline{B}^0 \to D^{(*)+}X^-) &= \mathcal{A}\,. \end{aligned}$$

Here, γ' and δ' are, respectively, the weak and the strong phase difference between the DCS and the CKM-favored diagrams, and vary for different final states $D^{(*)\pm}X^{\mp}$. The effect of the DCS decays is twofold: the amplitude of the sine term is reduced by a factor $(1-\mathcal{R}^2)$, and there is an additional cosine terms. As mentioned earlier, the reduced amplitude of the sine term is taken into account by the dilution factors. On the contrary, the new cosine term is out of phase with respect to the sine term by $\pi/2$ and modifies the oscillation amplitude. The effect of the cosine term is not accounted for by the dilution factors.

The variation in $\sin2\beta$, to good approximation, is given by [131, 132]

$$\delta\sin2\beta = -\mathcal{R}\sin(\gamma'-1.0)\cos\delta'\,, \qquad (9.9)$$

with γ' expressed in radians. Studies with toy Monte Carlo events have been performed for several values of γ' and δ' [133], and the systematic uncertainty on $\sin2\beta$ is estimated to be 0.008.

9.4.19 Summary of systematic uncertainties

The dominant contributions to the systematic uncertainty are from differences in the mistag fractions for the $B_{\rm CP}$ and the $B_{\rm flav}$ samples (0.012), and the composition of the background in

the $B_{\rm CP}$ sample (0.010). The latter, and all other contributions evaluated in data, are expected to decrease with enlarged data samples.

The second largest contribution is from the uncertainty on the bias in $\sin 2\beta$ observed in simulated events (0.010). Validation studies in the limit of infinite statistics and perfect detector do not show any bias. Hence, the origin of the bias is expected to be in detector effects such as the Δt resolution function, or other correlations similar to that between $\sigma_{\Delta t}$ and the mistag fractions.

The total systematic uncertainty $\sigma_{\rm sys}$ is computed to be 0.030, by adding in quadrature all contributions in Table 9.22, which are assumed to be uncorrelated. This uncertainty is more than a factor of two smaller than the statistical uncertainty $\sigma_{\rm stat} = 0.074$.

Source	Contribution
Signal parameters	
Common Δt resolution function [9.4.2]	± 0.002
Parameters of the Outliers component [9.4.2]	± 0.005
Tail scale factor [9.4.2]	± 0.002
Δt signal resolution model [9.4.3]	± 0.006
Wrong tag resolution function [9.4.4]	± 0.001
Signal dilutions [9.4.5]	± 0.012
Background parameters	
Signal probability: $B_{\rm CP}$ sample [9.4.6]	± 0.007
Signal probability: $B_{\rm flav}$ sample [9.4.6]	± 0.001
$m_{\rm ES}$ endpoint [9.4.7]	± 0.001
$B_{\rm CP}$ fraction of peaking background [9.4.8]	± 0.006
$B_{\rm CP}$ background CP content (combinatorial) [9.4.9]	± 0.012
$B_{\rm CP}$ background CP content (peaking) [9.4.9]	± 0.005
$B_{\rm CP}$ background lifetime [9.4.10]	± 0.002
Background Δt resolution function [9.4.11]	± 0.006
$B_{\rm flav}$ background model [9.4.12]	± 0.003
$B_{\rm flav}$ fraction of peaking background [9.4.8]	0
external parameters	
B^0 lifetime [9.4.13]	± 0.004
Δm_d [9.4.13]	± 0.003
detector effects	
z scale + boost [9.4.14]	± 0.001
Beam spot [9.4.15]	± 0.010
SVT alignment [9.4.16]	± 0.010
Monte Carlo correction [9.4.17]	-0.014 ± 0.010
Doubly-CKM-suppressed decays [9.4.18]	± 0.008
Total systematic error	± 0.030
Statistical error	± 0.074

Table 9.22: Summary of contributions to the systematic uncertainty on $\sin 2\beta$. The number in square brackets on each line is the subsection where the evaluation of the contribution is discussed.

9.5 Measurement of $\sin 2\beta$ in $J/\psi\ K^0_L$ and $J/\psi\ K^{*0}$ ($K^0_S\ \pi^0$) decay modes

In addition to the decay modes $J/\psi\ K^0_S$, $\psi(2S)\ K^0_S$, $\chi_{c1}\ K^0_S$, and $\eta_c\ K^0_S$, the *BABAR* collaboration has also measured $\sin 2\beta$ in the decay modes $J/\psi\ K^0_L$ and $J/\psi\ K^{*0}$ ($K^0_S\ \pi^0$). These results are briefly described in this section.

9.5.1 $B \to J/\psi K^0_L$

The $J/\psi\ K^0_L$ final state has opposite *CP* eigenvalue $\eta_{CP} = +1$ compared to $\eta_{CP} = -1$ modes used in this analysis. Although theoretically clean, this mode suffers from significantly higher backgrounds due to poor K^0_L reconstruction in *BABAR*.

The $J/\psi\ K^0_L$ selection is described in Reference [134]. Due to their long lifetime of $\tau_{K^0_L} = (5.17 \pm 0.04) \times 10^{-8}\,\mathrm{s}$ (compared to $\tau_{K^0_S} = (893.5 \pm 0.8) \times 10^{-13}$ for the K^0_S), K^0_L mesons are identified from their hadronic interactions in the electromagnetic calorimeter and in the muon chambers, but their energy $E_{K^0_L}$ is not completely measured. The K^0_L momentum $p_{K^0_L}$ is computed from the measured direction $\vec{d}_{K^0_L}$ and by using the relation

$$m_B^2 = (E_{J/\psi} + \sqrt{m_{K^0_L}^2 + p_{K^0_L}^2})^2 - (\vec{p}_{J/\psi} + p_{K^0_L}\,\vec{d}_{K^0_L})^2\,, \tag{9.10}$$

The energy difference ΔE (see Section 5.4) is computed from $p_{K^0_L}$ and the reconstructed J/ψ. Figure 9.15 shows the ΔE distribution in data. The signal region is defined by $|\Delta E| < 10\,\mathrm{MeV}$ and contains 988 events with purity $\mathcal{P} = 55\%$. The non-J/ψ background is due to random combinations of particles. The properties of this background are studied from the sidebands of the J/ψ mass distribution in data. The $B \to J/\psi\ X$ background is from events with a real J/ψ and a fake or incomplete K^0_L candidate. Simulated events are used to study the composition of this background. The likelihood fit to the Δt distributions of the $J/\psi\ K^0_L$ sample requires dedicated probability density functions to model the contribution of individual backgrounds, which are described in Reference [134].

In the selected sample of $J/\psi\ K^0_L$ events, $\sin 2\beta$ is measured to be

$$\sin 2\beta = 0.723 \pm 0.158\ (\mathrm{stat}) \pm 0.086\ (\mathrm{syst})\,. \tag{9.11}$$

The dominant contribution to the systematic uncertainty is from the composition of the background (0.081). The remaining contributions are estimated with the same procedure described in Section 9.4.

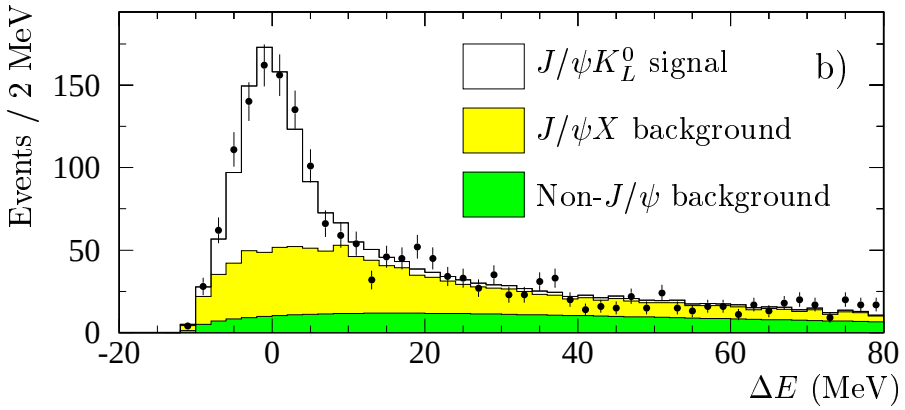

Figure 9.15: Distribution of ΔE for $B \to J/\psi\, K^0_L$ candidates in data. There are 988 events with $|\Delta E| < 10\,\mathrm{MeV}$ and purity $\mathcal{P} = 55\%$.

9.5.2 $B \to J/\psi\, K^{*0}(K^0_S\pi^0)$

The measurement of $\sin 2\beta$ in the $J/\psi\ K^{*0}$ decay mode is complicated by the presence of both *CP*-odd and *CP*-even eigenstates in the final state. The B meson is a spin-0 particle, while J/ψ and K^{*0} mesons have $S = 1$. The conservation of total angular momentum $J = L + S$ implies that orbital angular momentum L in the final state can be 0, 1, or 2. The states with $L = 0, 2$ have $\eta_{CP} = +1$ while those with $L = 1$ have $\eta_{CP} = -1$. The fraction $R_\perp$ of the L=1 component is measured to be $(16.0 \pm 3.5)\%$ [135].

The value of $\sin 2\beta$ can be measured by separating the three *CP* components with an angular analysis of the particles in the final state [136, 137]. When the angular information in the decay is ignored, the measured *CP* asymmetry is given by $(1 - 2R_\perp)\sin 2\beta$, which corresponds to an effective *CP* eigenvalue $\eta_{\mathrm{eff}} = 0.65 \pm 0.07$ for all $J/\psi\ K^{*0}$ candidates.

Figure 9.16 shows the m_{ES} distribution of $J/\psi\ K^{*0}$ events in data. There are 147 events in the signal region ($m_{\mathrm{ES}} > 5.27\,\mathrm{GeV}/c^2$) with purity $\mathcal{P} = 81\%$. The lower purity of this sample with respect to the $\eta_{CP} = -1$ modes is mainly due to the combinatorial background in the selection of π^0 candidates in the final state. From a fit to the Δt distributions of the selected events, and by using the effective *CP* eigenvalue η_{eff}, $\sin 2\beta$ is measured to be

$$\sin 2\beta = 0.224 \pm 0.516\ (\mathrm{stat}) \pm 0.068\ (\mathrm{syst})\ . \tag{9.12}$$

The dominant sources of systematic uncertainty are the uncertainty on the fraction of peaking background (0.031), and the uncertainty on η_{eff} (0.030) [133]. The other contributions are estimated according to the procedure described in Section 9.4.

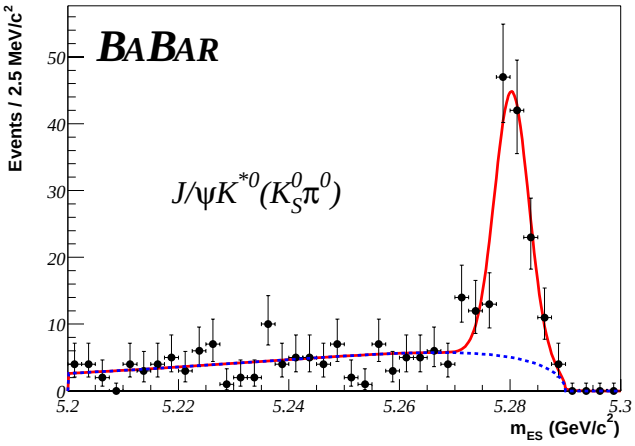

Figure 9.16: Distribution of $m_{\rm ES}$ for selected $J/\psi\ K^{*0}$ ($K^0_S\ \pi^0$) candidates after b-flavor tagging and vertex quality requirements.

9.6 $\sin 2\beta$ with all CP eigenstates

A simultaneous fit to all reconstructed CP eigenstates is performed to combine the measurements from individual CP decay modes. The results of all fits are summarized in Table 9.23 and compared in Figure 9.17. The value of χ^2, defined in Equation 9.4, for these three measurements is 1.0 with 2 degrees of freedom.

The systematic uncertainty for the combined result is evaluated according to the procedure discussed in Section 9.4 for the full data sample, with the addition of contributions specific to $J/\psi\ K^0_L$ and $J/\psi\ K^{*0}$ modes.

Sample	$N_{\rm sig}$	$\mathcal{P}$	$\sin 2\beta$
$J/\psi\ K^0_S$, $\psi(2S)\ K^0_S$, $\chi_{c1}\ K^0_S$, $\eta_c\ K^0_S$	1506	94	$0.755 \pm 0.074 \pm 0.030$
$J/\psi\ K^0_L$	988	55	$0.723 \pm 0.158 \pm 0.086$
$J/\psi\ K^{*0}$ ($K^0_S\ \pi^0$)	147	81	$0.224 \pm 0.516 \pm 0.068$
All	2641	78	$0.741 \pm 0.067 \pm 0.034$

Table 9.23: Number of events in the signal region $N_{\rm sig}$, purity $\mathcal{P}$, and the value of $\sin 2\beta$ for the individual samples of CP eigenstates, and the full sample. The first uncertainty is statistical, the second one is systematic.

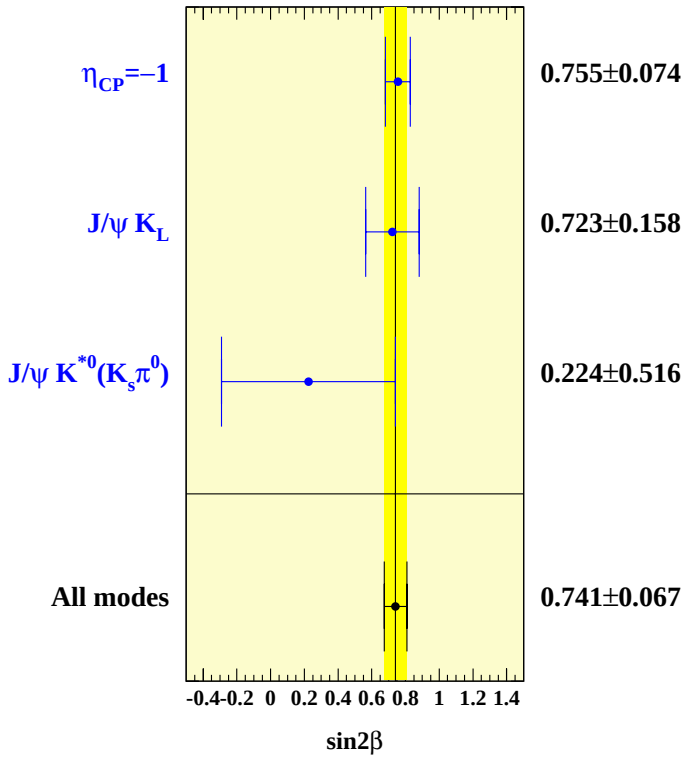

Figure 9.17: Measured $\sin 2\beta$ with samples of CP eigenstates and with the full sample. The value of χ^2 for the agreement between the measurements is 1.0 with 2 degrees of freedom.

The combined result is dominated by the measurement with the clean decay modes $J/\psi\ K^0_S$, $\psi(2S)\ K^0_S$, $\chi_{c1}\ K^0_S$, and $\eta_c\ K^0_S$, and more precisely by $J/\psi\ K^0_S$ (see Table 9.11).

The $J/\psi\ K^0_L$ mode has a large statistical uncertainty due to the high amount of backgrounds. The understanding of the composition of these backgrounds represents the largest contribution to the systematic uncertainty for this decay mode.

The uncertainty in the $J/\psi\ K^{*0}$ mode is expected to decrease by performing a full angular analysis. However, the statistical power of this sample is significantly smaller compared to the modes with $\eta_{CP} = -1$.

Chapter 10

Conclusions and outlook

About 88 million $\Upsilon(4S) \to B\bar{B}$ decays were collected between 1999 and 2002 with the *BABAR* detector at the PEP-II asymmetric-energy e^+e^- collider. In a sample of 1506 events, one B meson is fully reconstructed in CP eigenstates $J/\psi\ K^0_S$, $\psi(2S)\ K^0_S$, $\chi_{c1}\ K^0_S$, and $\eta_c\ K^0_S$, and the other B meson is determined to be a B^0 or $\overline{B}^0$ from its decay products. From a fit to the distributions of the decay-time difference Δt in these events, the amplitude of the CP asymmetry is measured to be

$$\sin 2\beta = 0.755 \pm 0.074\ (\mathrm{stat}) \pm 0.030\ (\mathrm{syst})\ . \tag{10.1}$$

In addition, 988 events in the $J/\psi\ K^0_L$, and 147 events in the $J/\psi\ K^{*0}$ ($K^0_S\ \pi^0$) decay modes have also been reconstructed in the same data sample by the *BABAR* collaboration. A simultaneous fit to the Δt distributions of all selected decay modes yields

$$\sin 2\beta = 0.741 \pm 0.067\ (\mathrm{stat}) \pm 0.034\ (\mathrm{syst})\ . \tag{10.2}$$

This result has appeared in the Physical Review Letters [138].

This measurement represents the first experimental observation of CP violation outside the kaon system [9]. Contrary to CP violation in kaons, which was of order $\mathcal{O}(10^{-3})$, the observed asymmetry in B mesons is of the order of unity. This is in agreement with the Standard Model predictions and represents a successful test of the Kobayashi-Maskawa mechanism of CP violation.

The significance of this result and the comparison with the existing measurements are discussed in Section 10.1. The measurement of $\sin 2\beta$ provides important constraints on the position of the apex of the Unitarity Triangle in the $(\bar{\rho}, \bar{\eta})$ plane (see Section 2.2). The agreement of this measurement with the Standard Model predictions and its impact on the Unitarity Triangle are discussed in Section 10.2. The PEP-II collider is expected to increase its luminosity in the near future. Prospects

for repeating this analysis with an enlarged data sample are summarized in Section 10.3. Consistency between independent measurements of $\sin 2\beta$ with different decay modes provides yet another important test of the Standard Model. This is briefly discussed in Section 10.4.

10.1 Significance of the result

The result presented here represents the most precise measurement of $\sin 2\beta$ available today. Measurements of $\sin 2\beta$ were previously reported by OPAL [139], ALEPH [140], CDF [141] and more recently BELLE [142] collaborations. The BELLE detector, similar to *BABAR* in design, is located in Japan, and collects data produced by the KEK asymmetric collider operating at the $\Upsilon(4S)$ energy. Figure 10.1 shows the comparison between all measurements and the current average value. The remarkable improvement in the precision in the last few years has been made possible by the e^+e^- colliders PEP-II and KEK operating at the $\Upsilon(4S)$ energy.

10.2 Constraint on the Unitarity Triangle

In Section 2.3 it was shown that $\sin 2\beta$ is related to the Wolfenstein parameters ρ, η, and λ by

$$\sin 2\beta = \frac{2\bar{\eta}(1-\bar{\rho})}{\bar{\eta}^2 + (1-\bar{\rho})^2} \ ,$$

where

$$\bar{\rho} = \rho\,(1 - \frac{\lambda^2}{2}) \quad \bar{\eta} = \eta\,(1 - \tfrac{\lambda^2}{2}) \ .$$

Since the value of λ is known with high precision [33], measurement of $\sin 2\beta$ provides a direct constraint on the position $(\bar{\rho}, \bar{\eta})$ of the apex of the Unitarity Triangle (see Figure 2.2), although there is a fourfold ambiguity on the value of angle β.

Figure 10.2 [143] shows the allowed region for the apex of the Unitarity Triangle in the $(\bar{\rho}, \bar{\eta})$ plane from measurements of

- CP-violating parameter ϵ_K in the kaon system,
- B^0 $\overline{B}^0$ oscillation frequency Δm_d,
- ratio of the CKM parameters $|V_{ub}/V_{cb}|$,

and limits on

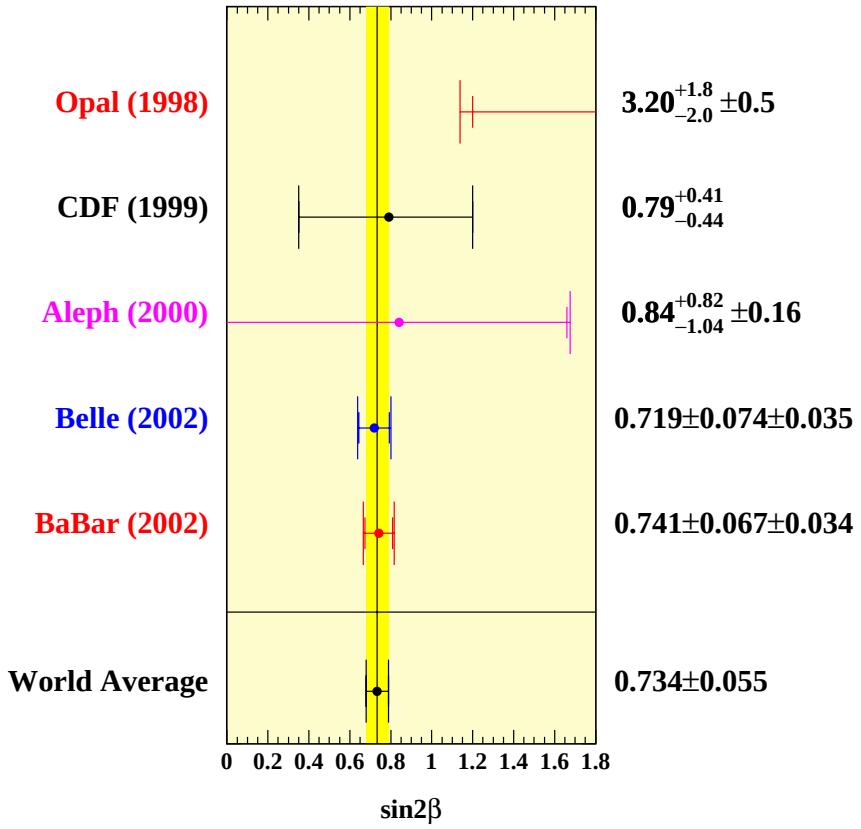

Figure 10.1: Current measurements of $\sin 2\beta$ and the new world average value.

- B_s $\overline{B}_s$ oscillation frequency Δm_s.

The four values of β corresponding to the measured value of $\sin 2\beta$ are also shown, and one of them overlaps with the existing indirect constraints.

The agreement between with the Standard Model prediction and the measured $\sin 2\beta$ implies that the complex phase $\delta_{\rm KM}$ of the CKM matrix is, most likely, the dominant source of CP violation in flavor-changing processes in weak interactions [146]. It excludes the proposed superweak model [144, 145] as a mechanism responsible for CP violation in B mesons. The expected magnitude of CP violation in this model is much smaller than the Standard Model prediction, and not consistent with the measured value of $\sin 2\beta$.

This measurement sharply constraints the position of the apex of the Unitarity Triangle in the $(\bar{\rho}, \bar{\eta})$ plane. Figure 10.3 shows the allowed region for the apex when the direct constraint from the value of $\sin 2\beta$ is combined with the indirect constraints from the other measurements.

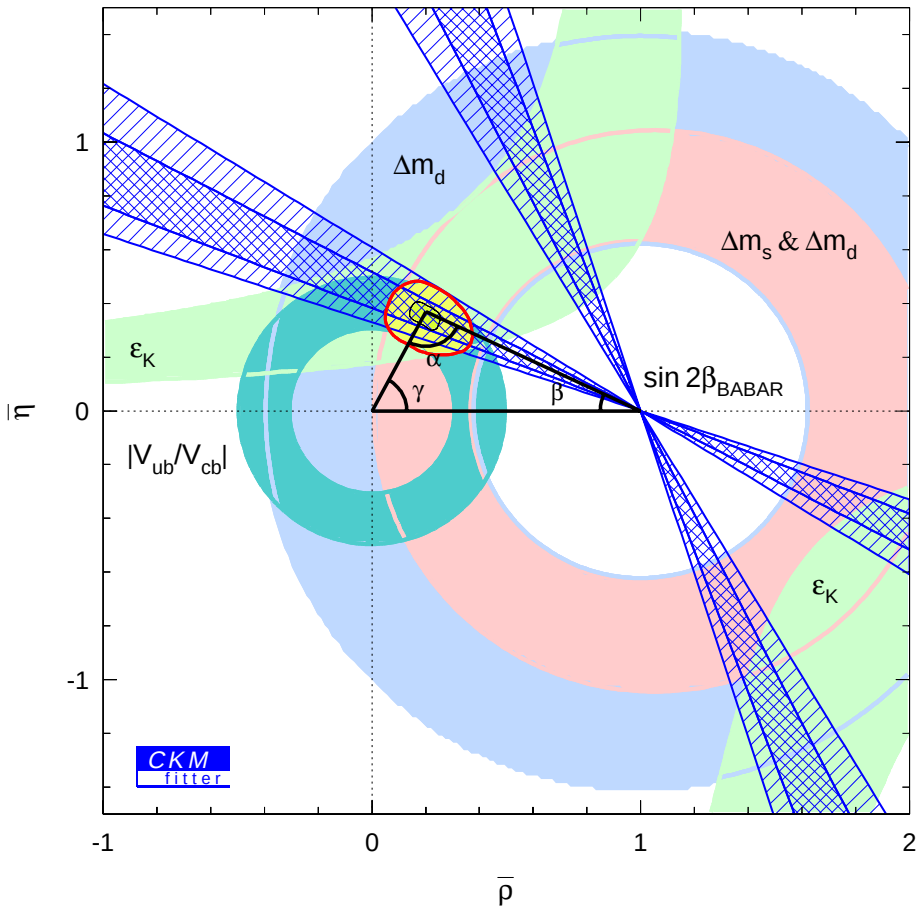

Figure 10.2: Comparison between the indirect constraints on the apex of the Unitarity Triangle from measurements of Δm_d, ϵ_k, $|V_{ub}/V_{cb}|$, and limits on Δm_s, and the region allowed by this measurement of $\sin 2\beta$. The cross-hatched (single-hatched) area corresponds to $\pm 1\sigma$ ($\pm 2\sigma$) uncertainty on the value of $\sin 2\beta$.

The allowed region for the apex corresponds to $\beta = 24^o \pm 4^o$ and is consistent with a value of $59^{\rm o} \pm 13^{\rm o}$ [33] for the angle γ of the Unitarity Triangle. In the Wolfenstein parameterization, the magnitude of γ is equal to the size of $\delta_{\rm KM}$. The large values of angles β and γ exclude models with approximate *CP* violation, where the size of $\delta_{\rm KM}$ is expected to be small.

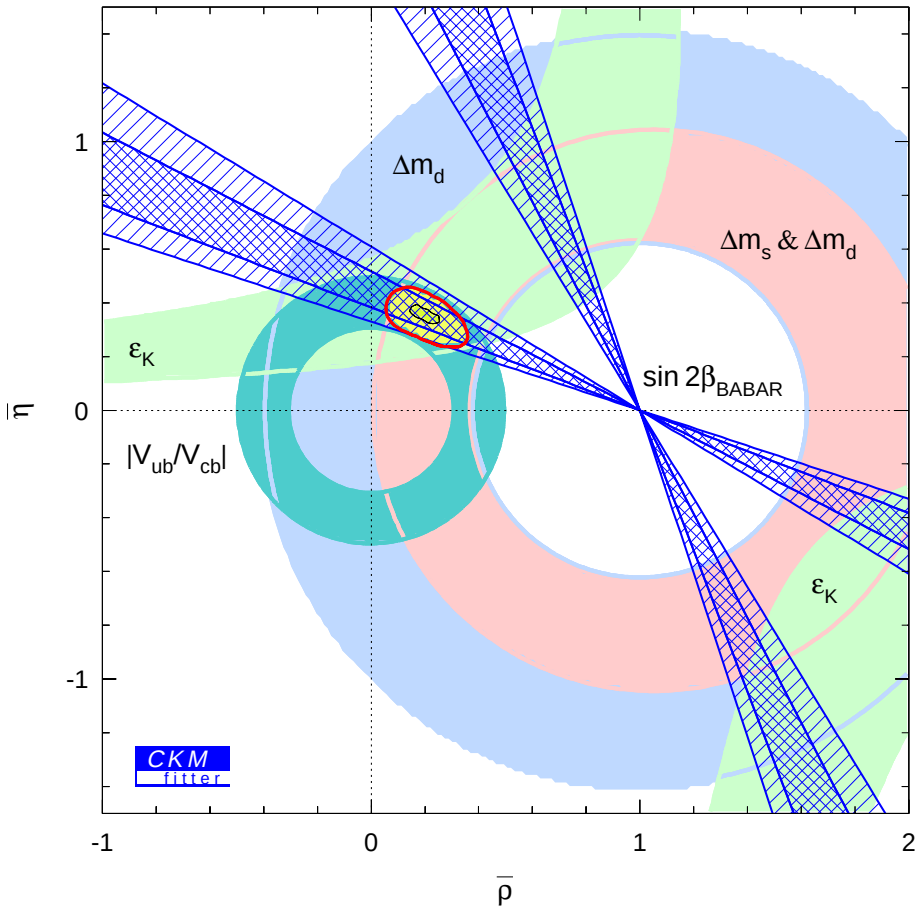

Figure 10.3: Constraints on the the apex of the Unitarity Triangle from measurement of $\sin 2\beta$, and from measurements of Δm_d, ϵ_k, $|V_{ub}/V_{cb}|$, and limits on Δm_s. The cross-hatched (single-hatched) area corresponds to $\pm 1\sigma$ ($\pm 2\sigma$) uncertainty on the value of $\sin 2\beta$.

10.3 Prospects for enlarged data sample

Current luminosity models for the PEP-II collider predict an accumulated data sample of about 500 fb^{-1} by the year 2005, five times larger than the sample used for this measurement. As the data sample increases, it is expected that improvements to the analysis technique will be necessary. For example, improvements in the flavor-tagging power Q increase the statistical power of the sample (see Section 8.5). In addition, detector upgrades can increase the overall reconstruction efficiency, or allow a more precise measurement of Δt, which directly affects the precision of the measurement. New decay modes can be added, although the measurement is, already, mainly dominated by the clean $J/\psi\ K^0_S$ mode.

A realistic estimate of the prospects of this measurement requires a detailed study of the above elements. However, under the assumptions that

- the analysis technique is unchanged,
- the event selection efficiency does not improve, and
- no other decay modes are added,

a statistical uncertainty of < 0.030 is expected, which is comparable to the current systematic uncertainty.

In this analysis, a very conservative approach has been used in the evaluation of the systematic effects, partly due to the larger statistical uncertainty. Moreover, many of the contributions described in Section 9.4 depend on the size of the data and simulated samples, and will decrease in the future. The following considerations can be made for the largest contributions at this time.

- **Common mistag fractions:** This contribution is evaluated with simulated events and will benefit from increased statistics. In addition, an improved b-flavor–tagging algorithm and understanding of sources of wrong-tag information will help reducing this contribution.
- **Monte Carlo correction:** The study of the correlations between mistag fractions and $\sigma_{\Delta t}$ explains about 1/4 of the observed bias. More detailed studies with simulated events are required to identify possible other sources of similar correlations, and reduce the current systematic uncertainty.
- **Composition of combinatorial CP background:** Due to the high purity of the sample, the properties of the background can not be measured with the small number of background

events in data. Very conservative assumptions are made to evaluate their systematic contribution. Hence, the evaluation of this contribution will certainly benefit from an enlarged data sample.

- **Contamination of CP modes (peaking background):** Currently the effect of the misreconstructed decay modes in CP eigenstates is evaluated by allowing for maximal CP asymmetry. A better understanding of the B decays to charmonium final states with an enlarged data sample will reduce this contribution. Similarly, the evaluation of the fraction of these events will benefit from a more detailed Monte Carlo simulation of B decays, and from the increase in the size of simulated events.

- **SVT alignment:** The current understanding of the alignment is considered very reliable. It is reasonable to assume that due to external factors, such as access to the detector, the SVT must be realigned a number of times during the same data-taking period. Given the stability of this estimate in the last year of data taking, the current 0.010 can be regarded as a realistic estimate for the coming years.

On the basis of these considerations, it is not unrealistic to assume that this measurement could still be statistically dominated by the year 2005.

10.4 Independent measurements of $\sin 2\beta$

The leading contribution to amplitudes for $B \to \phi^0 K_S^0$ and $\eta' K_S^0$ decays is the penguin diagram illustrated in Figure 10.4 (see Table 2.3). The absence of a second contribution at the order $\mathcal{O}(10^{-2})$ allows another theoretically clean measurement of $\sin 2\beta$ (Section 2.5.2). However, the absence of

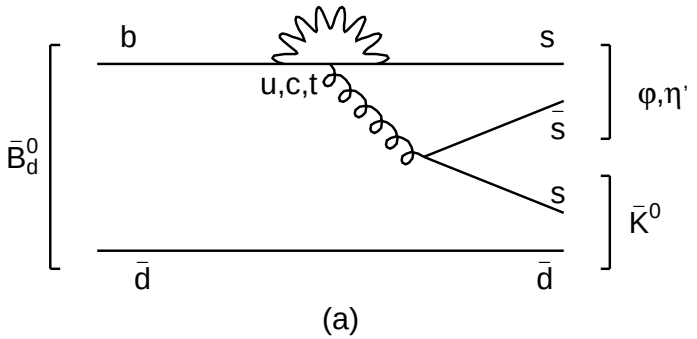

Figure 10.4: Penguin diagram for the $B \to \phi^0 K_S^0, \eta' K_S^0$ decays.

the tree diagram, results in smaller branching fractions for these decay modes, compared to the

$B \to J/\psi\, K^0_S$ decay.

Since the leading penguin diagram is suppressed in the Standard Model, these modes provide an important tool to probe the existence of additional sources of CP violation. Potential contributions from physics beyond the Standard Model could be comparable to the the penguin contribution, and result in discrepancies between the value of $\sin 2\beta$ in these modes and the measurement presented in this dissertation.

A preliminary measurement has been performed by the *BABAR* collaboration [57] and shows a discrepancy at the level of 2.7σ, but the statistical uncertainties are still large. Should the discrepancy persist, this could be a hint of New Physics.

Another independent measurement of $\sin 2\beta$ can be performed with the $B_s \to \phi K^0_S$ decays. The B_s mesons can not be produced at PEP-II and will be the subject of studies at CDF and D0 experiments at the Tevatron collider, located at Fermilab.

Appendix A

B-reconstruction software: BRecoUser, CharmUser, and DstarlnuUser

The fully reconstructed B mesons in hadronic, semileptonic, and CP final states constitute the primary ingredients of many of the analyses in *BABAR*.

The hadronic decay modes, discussed in Section 5.6, have been used for precise measurement of the B^0-$\overline{B}^0$ oscillation frequency Δm_d and the B^0 lifetime, and are **required** for all the time-dependent CP-violation studies. In fact, it was pointed out that the large sample of reconstructed B mesons in these decay modes are used to measure the Δt resolution function and the performance of the flavor-tagging algorithm in data. The large sample of fully reconstructed B^+ mesons is used for the lifetime measurement, as well as a control sample for the CP-violation studies.

Figure A.1 shows the distribution of the energy-constrained mass $m_{\rm ES}$ for the fully reconstructed B^0 and B^+ mesons in hadronic final states, described in Section 5.6. There are about

The decays to CP eigenstates with a Charmonium meson were discussed in Section 5.5 and have been used for measurements of branching fractions, as well as the measurement of $\sin 2\beta$ presented in this dissertation. The fully reconstructed B^+ candidates are used as a control sample and for the branching fraction measurement.

The distribution of $m_{\rm ES}$ for the $B^0 \to J/\psi\, K^0_S$, $\psi(2S)\ K^0_S$, $\chi_{c1}\ K^0_S$ and $\eta_c\ K^0_S$ candidates is

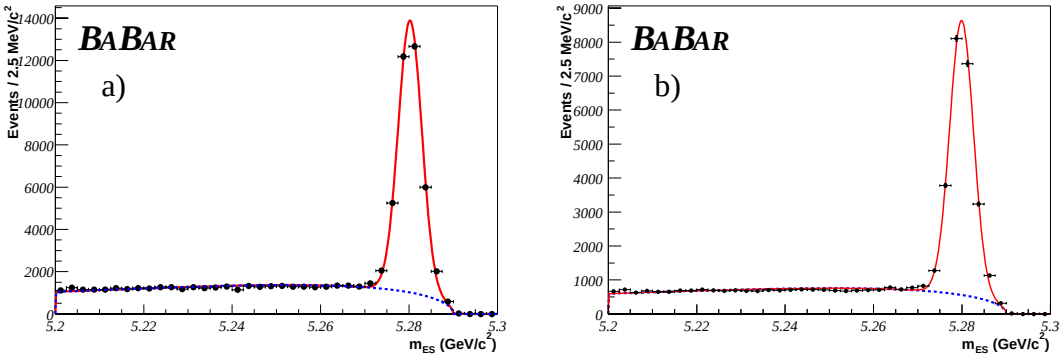

Figure A.1: Distribution of energy-constrained mass $m_{\rm ES}$ for fully reconstructed $B^0 \to D^{(*)-}\pi^+/\rho^+/a_1^+$ candidates in a), and for $B^+ \to D^{(*)0}\pi^+$ decay modes in b).

shown in Figure A.2a. A total of about 30 candidates are reconstructed in these modes in each fb^{-1} of data. Figure A.2b shows the distribution of $m_{\rm ES}$ for the fully reconstructed B^+ candidates in the $J/\psi\ K^+$, $\psi(2S)\ K^+$, $\chi_{c1}\ K^+$, and $J/\psi\ K^{*+}$ decay modes, which have a yield of about 120 candidates per fb^{-1} of data.

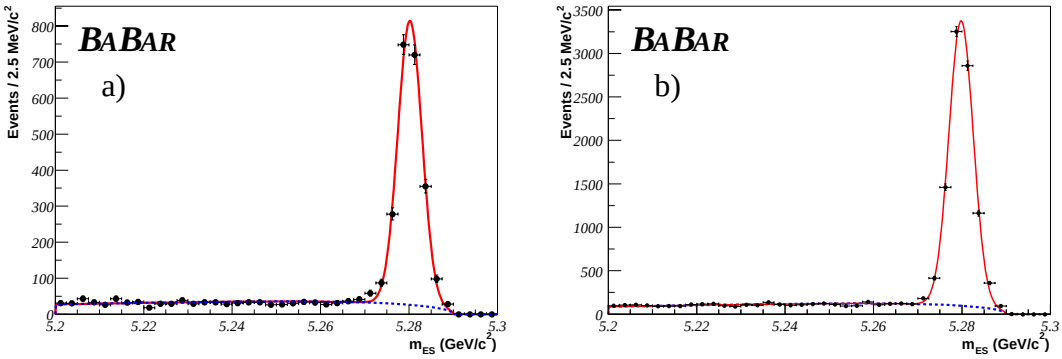

Figure A.2: Distribution of energy-constrained mass $m_{\rm ES}$ for fully reconstructed $B^0 \to J/\psi\, K^0_S$, $\psi(2S)\ K^0_S$, $\chi_{c1}\ K^0_S$, and $\eta_c\ K^0_S$ candidates in a), and for the $B^+ \to J/\psi\, K^+$, $\psi(2S)\ K^+$, $\chi_{c1}\ K^+$, and $J/\psi\ K^{*+}$ decay modes in b).

The semileptonic decays $B \to D^{*-}\ell^+\nu_\ell$ provide a sample of almost fully reconstructed B mesons, since the neutrino is not reconstructed, and have been used to measure the oscillation frequency and the B^0 lifetime. Currently about 820 $B \to D^{*-}\ell^+\nu_\ell$ candidates are reconstructed for each fb^{-1} of data. Figure A.3 shows the distribution of the mass difference $m(D^{*+}) - m(D^0)$

for reconstructed sample in about 38 fb^{-1} of data. The distributions are shown separately for the $B \to D^{*-} e^+ \nu_e$ and the $B \to D^{*-} \mu^+ \nu_\mu$ modes, because the particle-identification performance, and hence the sample purity are different.

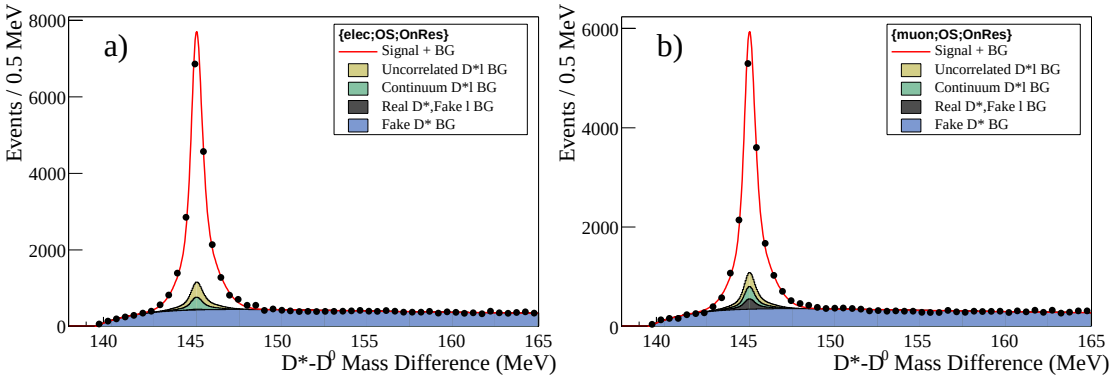

Figure A.3: Distribution of the mass difference $m(D^{*+}) - m(D^0)$ for the reconstructed $B \to D^{*-} e^+ \nu_e$ candidates in a), and for the $B \to D^{*-} \mu^+ \nu_\mu$ candidates in b).

The selection criteria for all the above modes were mainly studied in the period between 1999 and 2001. Given the need and the interest in reconstructed B mesons, a number of analysis applications are developed to provide standard lists of selected B candidates within the *BABAR* analysis framework `Beta`. The basic requirements for these applications are:

1. implementation of well-established selection criteria in order to provide all customers with the same sample of reconstructed B mesons;
2. addition of new decay modes must be easy;
3. a common ntuple structure; and
4. skimming capabilities to create collections of events with a fully reconstructed B meson.

Three distinct applications are available for reconstruction of different types of B decays:

1. **`BRecoUser`**: for the hadronic B decays. Initially, only the decays $B^0 \to D^{(*)-}\pi^+/\rho^+/a_1^+$ and $B^+ \to \overline{D}^{(*)0}\pi^+$ were reconstructed for the time-dependent analyses. Currently `BRecoUser` is used for a number of analyses, including:
   - branching fractions and CP violation measurements in $B^0 \to D^{*+}D^{(*)-}$ decays;
   - measurement of the branching fractions of the color-suppressed decays $B^0 \to \overline{D}^{(*)0}\pi^0/\rho/\omega/\eta/\eta'$;

- measurement of the branching fractions of $B^0 \to D^{(*)}D^{(*)}K$ decays;
- measurement of the branching fractions of $B^0 \to D_s^{(*)}\pi/K$ decays;
- measurement of $\sin 2\beta + \gamma$ with $B^0 \to D^{*-}\pi^+$ decays; and
- search for the modes $B \to D^{(*)}K_S^0/K^{*0}$ and $B \to DK\pi$, which could be used to measure the CKM angle γ.

2. **`CharmUser`**: for the CP eigenstates with a Charmonium meson, such as $B^0 \to J/\psi\, K_S^0$, $\psi(2S)\ K_S^0$, $\chi_{c1}\ K_S^0$, $J/\psi\ K^{*0}$, and $J/\psi\ K_L^0$.

3. **`DstarlnuUser`**: for the semileptonic $B^0 \to D^{*-}\ell^+\nu_\ell$ decays.

The structure and the organization of all three applications are similar and are described in this appendix. Since the *BABAR* software evolves quite rapidly, the reader is referred to the online documentation in References [147–149] for the technical details that are kept up to date with the latest *BABAR* software releases.

The *BABAR* analysis application `Beta` provides a common framework to access the event stores for data and Monte Carlo, and to utilize the reconstructed charged tracks and neutral particles. It also provides the interface to analysis tools such as particle-identification selectors [150] and vertex-reconstruction algorithms [151]. The core `Beta` code is organized in several packages, with `BetaUser` package representing the user front-end as described in Reference [152]. Users can implement their analysis within this package. The analysis code is organized in *modules* that must be appended to the executable of the package, `BetaApp`. The configuration of the modules is performed by using the **TCL** command line language.

In this picture, `BRecoUser`, `CharmUser`, and `DstarlnuUser` can be regarded as *clones* of `BetaUser`, specialized in B reconstruction. In the following, `BRecoUser` is used to illustrate the structure of these packages.

Figure A.4 illustrates the role of these packages in the offline software. The Online Prompt Reconstruction (OPR) processes the data collected with the data acquisition system (Section 4.4) and provides the collections in the Objectivity [84] database. These collections are also available as root-based **K**ind **AN**d **G**entle **A**nalysis (kanga) files [153].

Three types of output are currently used for these packages:

- **ntuples or rootuples**: this is probably the most common use of any analysis program. After a preliminary selection of events of interest, the output is saved in hbook-based ntuples, or root-based rootuples, for further analysis. This type of output is for example used when starting a new analysis where new selection criteria must be studied with very loose selection.

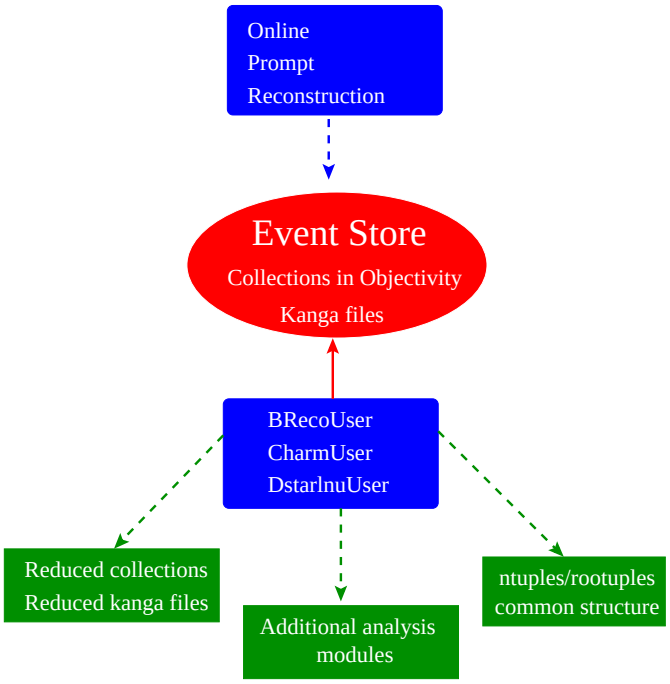

Figure A.4: The three packages `BRecoUser`, `CharmUser`, and `DstarlnuUser` implement the B reconstruction for hadronic, semileptonic, and CP final states.

A common structure and naming convention is used for all three packages as described in Reference [154] and discussed in the following.

- **reduced collections:** given the very large size of the data sample collected with the *BABAR* detector, it is preferable to create new collections containing only events of interest. These *reduced* collections present multiple advantages over the ntuples. While ntuples are static set of variables, the collections can be analyzed multiple times, taking advantage of all *BABAR* analysis tools. The size of these collections are at least 2 orders of magnitude smaller than the original collections produced by OPR, and therefore result in highly reduced use of CPU power for the analysis.

  These collections are particularly suitable for analyses with well established selection criteria, such as the selection of final states used in the $\sin 2\beta$ analysis. Since these criteria do not change often, if at all, the production of the collections can be ultimately integrated in OPR.

- **ASCII files for time-dependent fits:** the input to the fitting program used in the measurement of $\sin 2\beta$ are ASCII files, containing the Δt information of selected events, as described in the next chapter.

- **serialized analysis modules:** additional analysis modules can be appended to perform further analysis in events with a fully reconstructed B meson. An examples of such an analysis are the flavor-tagging studies. However, given the CPU constraints, it is better to perform this kind of analysis off the reduced collections, with significantly smaller number of events.

A.1 Structure of `BRecoUser`

The structure of `BRecoUser` is shown schematically in Figure A.5:

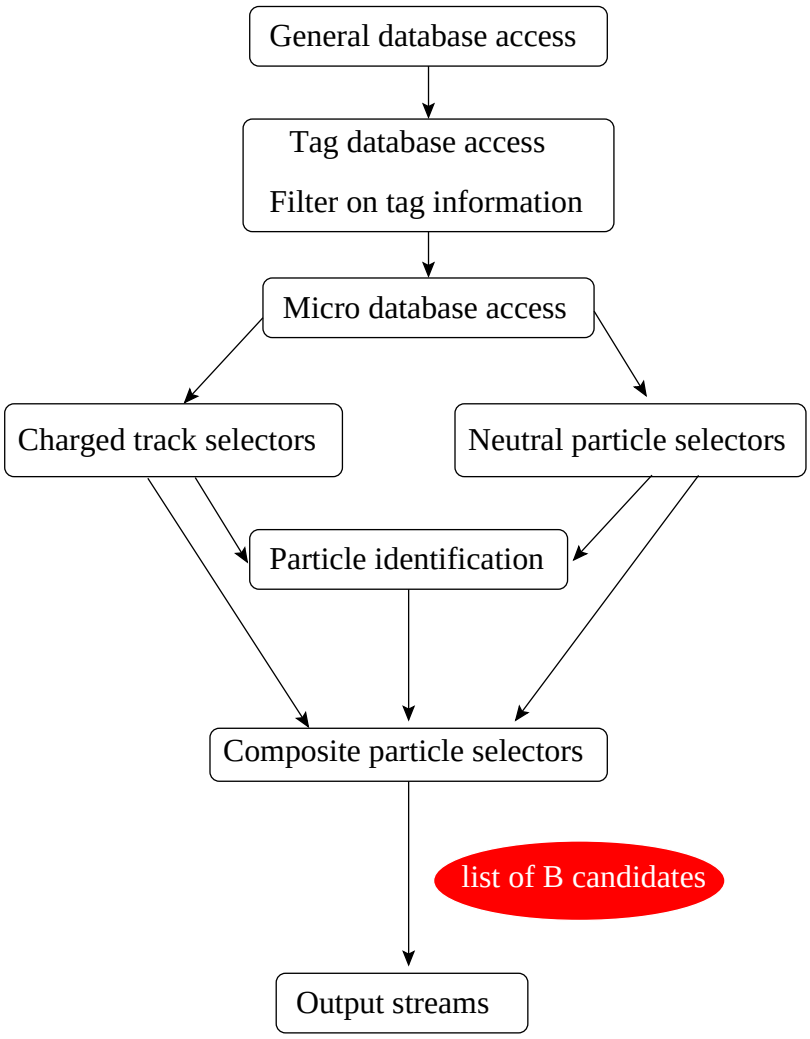

Figure A.5: Structure of `BRecoUser`. Each block corresponds to a set of sequences with specific tasks.

1. first, the connection with the event store is established. This allows to access the conditions database that contains the detector geometry constants, and the data taking conditions.

2. next, the content of the tag database is loaded and can be used to quickly filter the events. The tag database contains a number of float and boolean variables, mostly event variables, that can be used to discriminate different types of events.

   In particular, the tag database contains the *tagbits* for the various decay channels, set by OPR, and stored in the event store. These are boolean variables set to true in events which satisfy very loose selection requirements.

3. for the events passing the tag filter, the content of the micro database is loaded into memory and made available for analysis. The micro database contains the kinematic properties of the reconstructed charged and neutral particles at the interaction point and some of the detector variables, such as the number of hits in the tracking system and the deposited energy in the drift chamber or in the electromagnetic calorimeter. Using these information, the charged tracks and the neutral energy deposits are organized in hierarchical lists, as described in Sections 4.5.1 and 4.6.1.

4. the particle identification algorithms are used to identify electrons, muons, kaons, and protons among the reconstructed particles. For each species, several criteria, from very loose to very tight, are applied, which were described in Section 4.7.

5. the reconstruction of B mesons requires the selection of a number of intermediate states, including charmed mesons, charmonium states, and other resonances described in Section 5.3. The selectors used to reconstruct the large number of intermediate states are described in the next section.

6. a list of B candidates is created as a result of all composite particle selectors. This list is passed to the output streams to fill ntuples, create reduced collections, or produce ASCII files for fitting.

A.2 `CompositionTools` and the reconstruction of composite particles

The selection of all composite particles although differing in the specific species and the daughters in the final state, are characterized by a number of common features, shown schematically in Figure A.6:

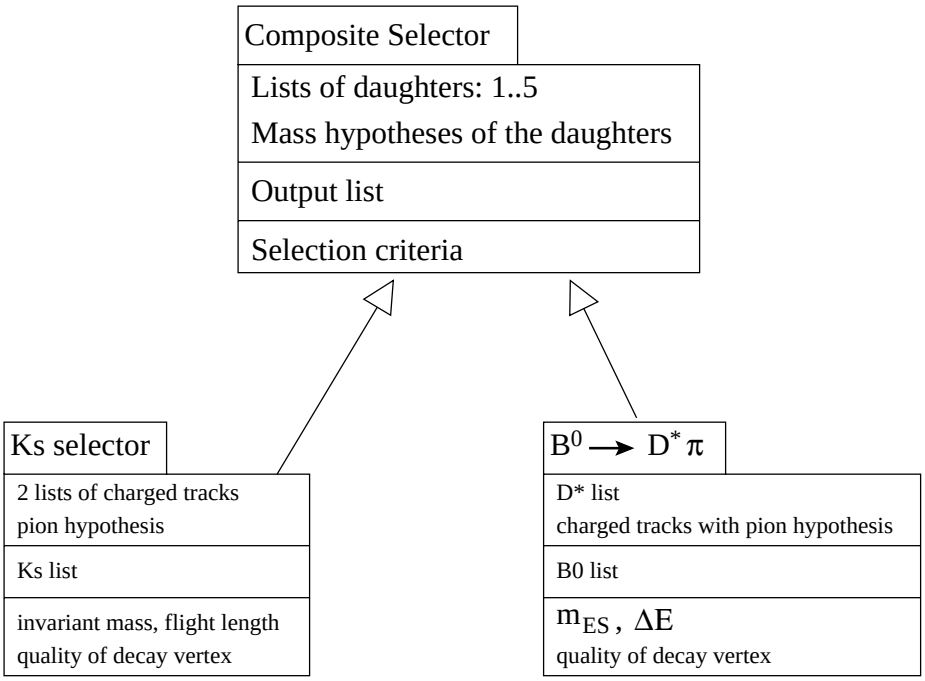

Figure A.6: The selectors of composite particles are characterized by up to 5 lists of daughters and their mass hypothesis, an output lists, and a set of selection criteria.

- lists of daughters in the final states;
- mass hypothesis for the daughter particles;
- output list containing the selected composite candidates; and
- selection criteria that vary for different types of composite particles.

The `CompositionTools` package provides general tools to perform the selection of any composite particle with a maximum of five daughters. In addition, it also provides selectors specialized

in the reconstruction of B^0, π^0, and D^{*-} candidates. A complete description of `CompositionTools` is given in Reference [155].

Furthermore, often it is necessary to apply slightly different selection criteria for the same composite particle. For example, in Section 5.3.2 it was explained that the $K^0_S \to \pi^+\pi^-$ candidates used to reconstruct CP and flavor eigenstates satisfy different requirements. This is easily achieved in the design of `CompositionTools`, by implementing each level of selection as a separate selector, as illustrated in Figure A.7.

The parameters of all selectors can be configured easily at runtime through the TCL language that provides the interface between the user and the analysis code.

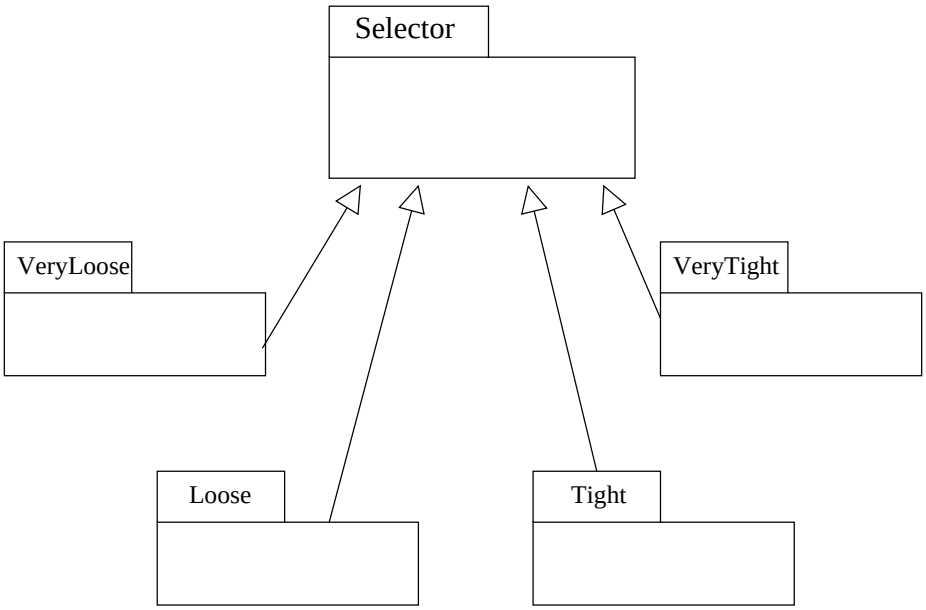

Figure A.7: The different selection criteria are implemented as independent copies of the same selector.

Figure A.8 shows schematically how the selectors are organized. Each block corresponds to all the selectors used to reconstruct each type of composite particles with different levels of requirements, and in all the final states described in Section 5.3.

A.3 Output streams

The output streams available in `BRecoUser` are illustrated in Figure A.9:

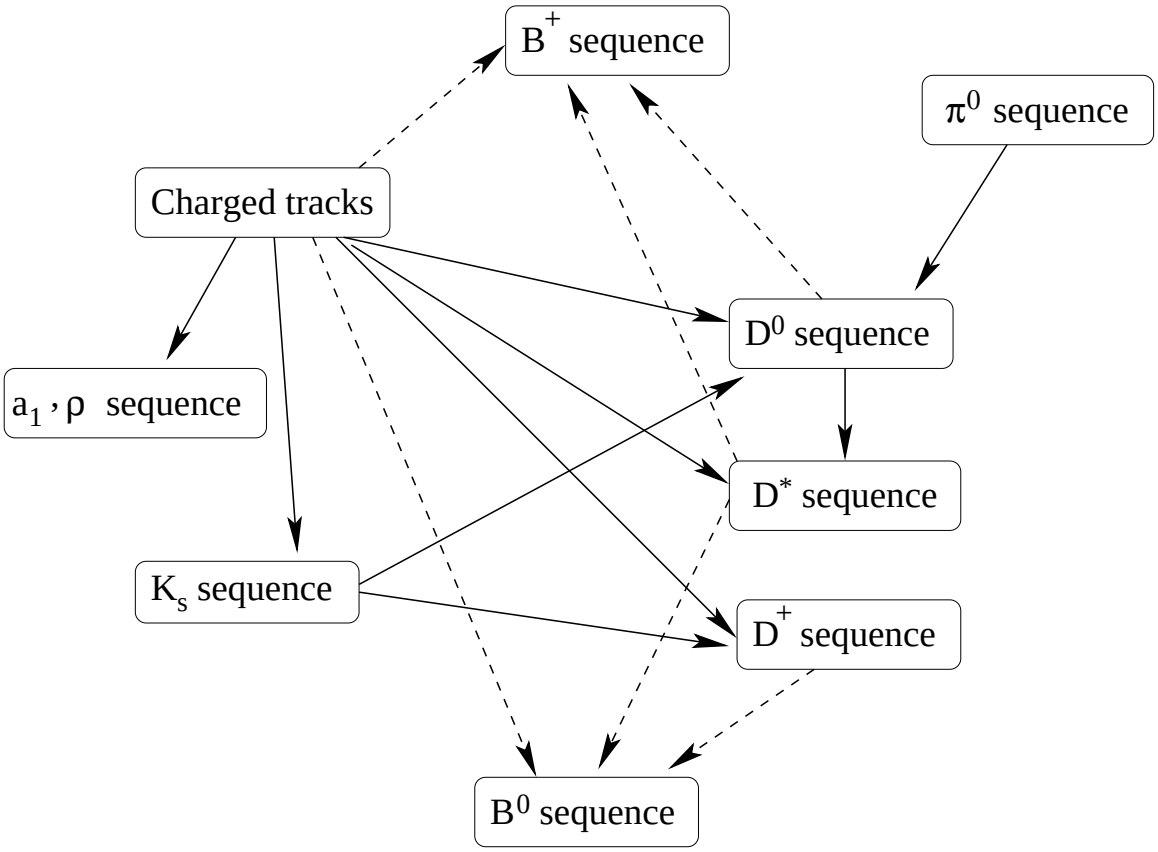

Figure A.8: The output of the sequences composed of the selectors are combined to reconstruct the B meson candidates.

- in the simplest scenario, the information about the reconstructed B candidates are stored in ntuples, using a common format that is described in the next section;

- for the $\sin 2\beta$ analysis, each B candidate is passed to the flavor-tagging algorithm (see Chapter 6), in order to determine its flavor content. The tagging information is then stored along with the information about the fully reconstructed B meson in the ntuples;

- in alternative to the ntuple, the information can be written into an ASCII file that is used by the *CP*-fitting programs. The format of the ASCII files and the variables stored in them are discussed in Appendix B.

- when processing the data for the first time, it is convenient to create reduced collections of events with at least one fully reconstructed B meson. Once such collections are available, one can quickly iterate over the selected events and save the output in one of the above formats.

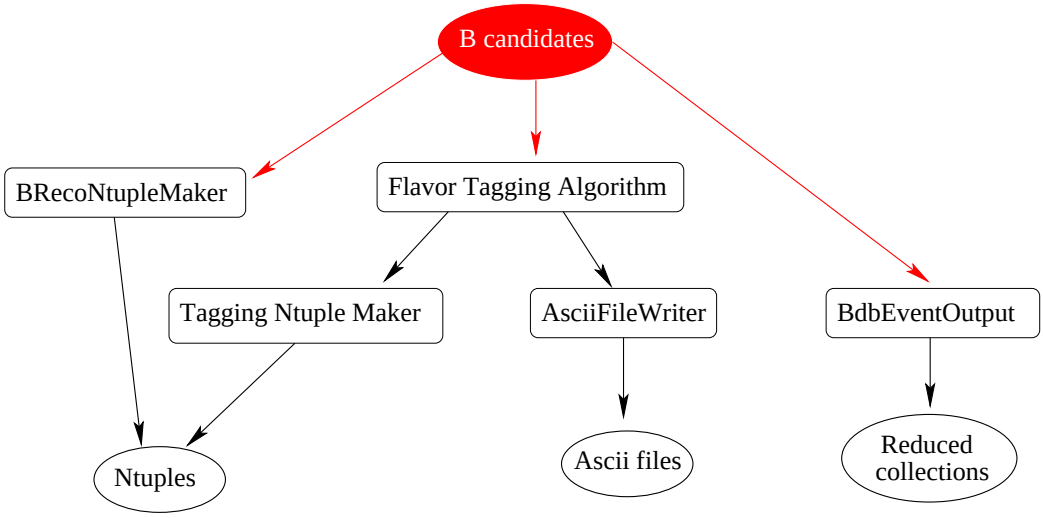

Figure A.9: The output streams available in `BRecoUser`.

A.4 Structure of the common ntuples

Kinematic and vertex fitting, as well as particle identification algorithms are applied within the `Beta` framework. None of these tools are available at ntuple level. Therefore it is important to store sufficient information from all the analysis tools in the ntuples.

Given the large number of decay channels reconstructed, it is helpful to define a common naming convention and a set of variables that are commonly used for charged tracks, neutral particles, and composite particles. These variables are extensively documented in Reference [154].

Due to the large data sample and the variety of the reconstructed final states, two requirements must be satisfied:

1. the genealogy of the particles, that is the relation between the reconstructed charged and neutral particles, and the selected composite particles must be stored in the ntuples; and

2. the storage must be efficient but with no redundancy in order to reduce the total size of the ntuples.

In order to meet the above conditions, column-wise ntuples are used, with one block of information for each type of particle. For example, there is a **TRK** block for the charged tracks, a **D0** block for selected D^0 candidates, and a **BCH** block for the B^+ candidates. The relation between the particles is stored through integer indices and Lund codes for each daughter of the composite candidates. This is shown in Figure A.10 for the $B^+ \to \overline{D}^0\pi^+$ candidates with $\overline{D}^0 \to K^+\pi^-$. The $\overline{D}^0$ block has pointers only to the block of the tracks. The B^+ block on the other hand has pointers

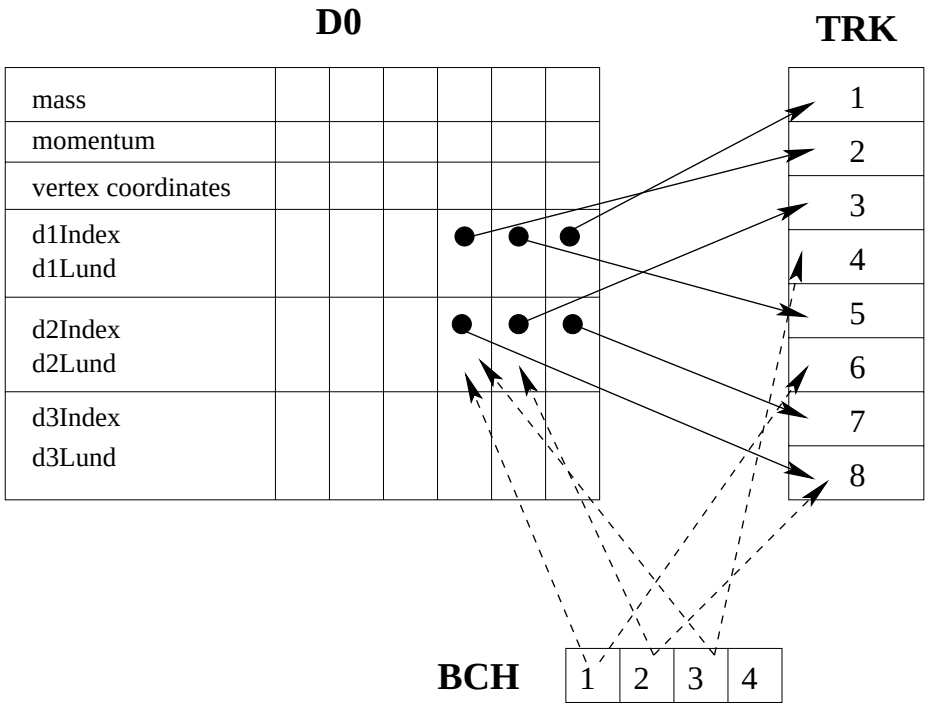

Figure A.10: Structure of the common ntuples. Each block of the column-wise ntuples corresponds to one type of particles. The genealogy of the particles is stored through integer pointers from the composite block to its daughters block. The Lund code, stored in the ntuple as well, removes any ambiguity.

to $\overline{D}^0$ and to the track blocks.

This approach allows to save each reconstructed particle only once. The pointers are the key to account for the overlaps between several composite candidates. In addition, only those particles used to reconstruct a B candidate are saved in the ntuple. This is done by saving first all the B candidates, then the D^{*-} candidates, followed by $\overline{D}^0$ all the way down to the charged tracks.

The combination of the integer indices and the Lund codes allows the users to quickly navigate the ntuples without any ambiguity. Moreover, this structure can be used for any arbitrary decay mode of the B mesons.

Appendix B

`tFit`: a fitting package for time-dependent studies

A dedicated fitting package, `tFit`, which uses Minuit [156] for minimization, is developed to perform the unbinned maximum likelihood fit described in detail in Chapter 8.

Although the primary goal of `tFit` was the the measurement of $\sin 2\beta$ described in this dissertation, `tFit` has been used for other time-dependent analyses, including:

- measurement of the direct CP violating parameter $|\lambda|$ (see Section 2.4.4) [133, 138];
- precise measurement of the B^0-$\overline{B}^0$ oscillation frequency Δm_d with hadronic flavor eigenstates [157, 158], described in Section 5.6;
- preliminary results on the oscillation frequency Δm_d with semileptonic decays $B^0 \to D^{*-}\ell^+\nu_\ell$ [159, 160];
- measurement of the decay-width difference $\Delta\Gamma$ (see Section 2.4.1) with fully reconstructed flavor eigenstates [161];
- measurement of $\sin(2\beta+\gamma)$ in $B^0 \to D^*\pi$ decays [162];
- measurement of CP-violating effects in $B \to J/\psi K^*$ decays [163];

All these analysis require the knowledge of the measured decay-time difference Δt and its uncertainty $\sigma_{\Delta t}$, as well as the flavor-tag information, but differ in the probability density function for the signal. Therefore `tFit` can be easily modified to implement new time-dependent analyses,

while taking advantage of the existing infrastructure, such as the toy Monte Carlo generators and convolution functions for different Δt resolution functions.

The user interface of `tFit` is implemented with the Kuip command processor, which is known to the users since it is used also in PAW. The fitting methods are therefore available as kuip commands. Users can configure the fitter at runtime via kumac files containing the required kuip commands. These commands are documented in Reference [164]. In the remainder of this chapter the available features of `tFit` are briefly described.

B.1 Format of the fitting ASCII files

A common format is used to store the information required by the various fitting programs in *BABAR* in ASCII files. This format is documented in detail in Reference [165].

The number of the measured quantities needed in the fit varies depending on the specific analysis that is considered. For example, the mixing analysis with semileptonic decays has many types of background whose fractions must be provided to the fitter, while the $\sin 2\beta$ analysis is relatively simpler due to the clean sample of CP final states with charmonium mesons.

The adopted format has sufficient redundancies to allow all the above measurement to use the same common format. The input variables to the fitter include:

- measured Δt and its uncertainty $\sigma_{\Delta t}$;
- measured flavor tag and the tagging category, e.g. lepton category;
- decay channel of the fully reconstructed B meson;
- flavor of the fully reconstructed hadronic flavor eigenstates;
- kinematic variables of the fully reconstructed B mesons, such as the energy-constrained mass $m_{\rm ES}$ and the energy difference ΔE; and
- the true values of the above variables in the simulated Monte Carlo samples.

B.2 Structure of `tFit`

The typical structure of a kumac to perform a fit is schematically shown in Figure B.1. The flow chart from the top to the bottom corresponds to the order of kuip commands, represented by blocks, in the kumac.

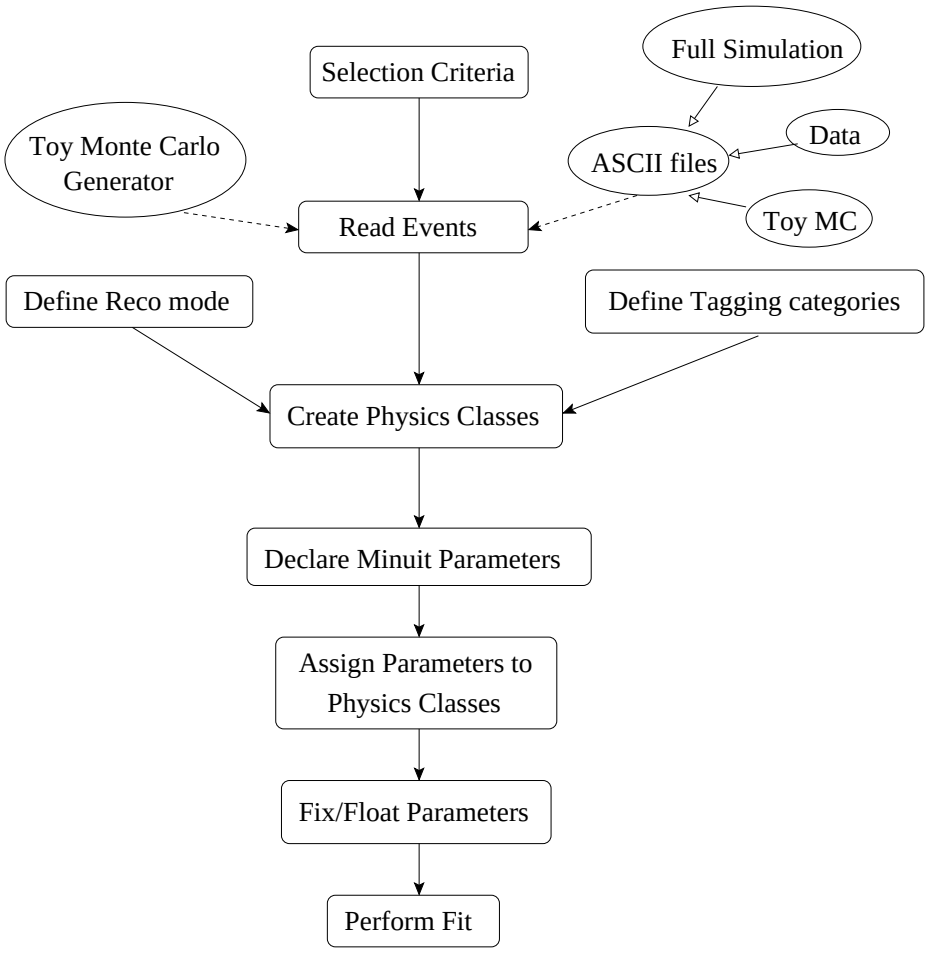

Figure B.1: Structure of a typical fit with `tFit`. The kuip commands are represented by the blocks, while the flow chart corresponds to their order in the kumac.

B.2.1 Sources of input

There are two types of input for the fit: the ASCII files or the realtime generation of fast parameterized Monte Carlo (toy MC) events.

ASCII files

The ASCII files are usually produced for the selected events in data or in full-simulation samples, but can also contain toy MC events generated at an earlier time.

Toy Monte Carlo generator

A toy Monte Carlo generator is available within `tFit` for all the analyses mentioned at the beginning of this Chapter. The generator can be invoked to generate events right before performing the fit. Alternatively, the generated events can be stored in ASCII files with the common format used in data and full simulation.

The properties of the generated events are specified by the user as illustrated in Figure B.2. It is

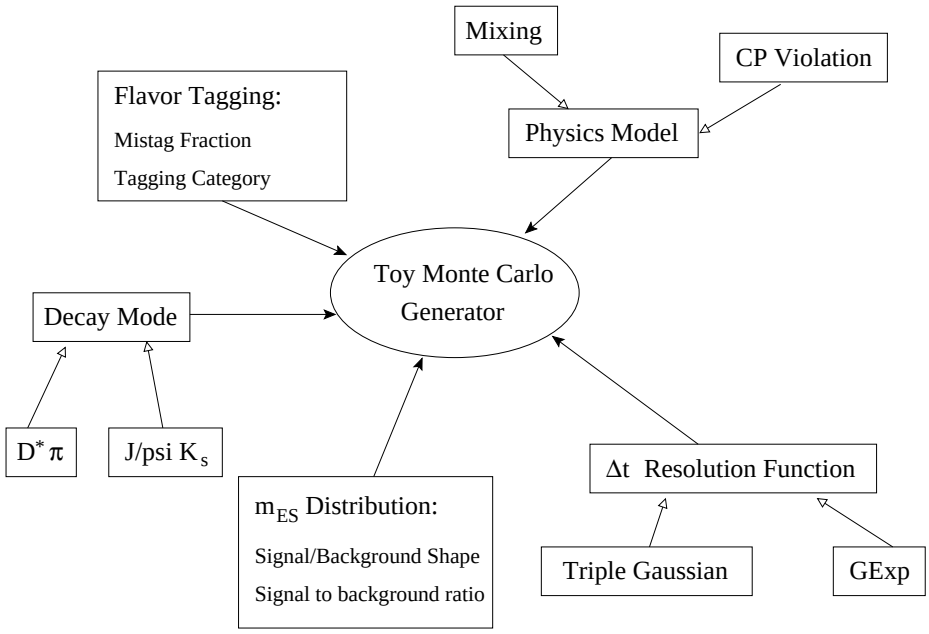

Figure B.2: The toy Monte Carlo generator is configured by users via kuip commands.

possible to specify:

- the theoretical Δt distribution (physics model) for each type of analysis, e.g. mixing or CP violation;
- the Δt resolution function model. Currently one can choose between the triple-Gaussian and the `GExp` models (see Section 9.4.3);
- a flavor-tagging category and its mistag fraction. This allows to simulate events with the same properties measured in data;
- the shape of the $m_{\rm ES}$ distribution and the signal to background ratio; and
- the decay mode of the fully reconstructed B.

It is possible to generate samples of events with the exact same properties of the events selected in data, by configuring the generator. This is important for example to determine the goodness of fit to the data, by generating a large number of data-like samples.

B.2.2 Input selection criteria

There are a total of 32 fields in the ASCII files that are read in for each event. It is possible to define selection criteria to filter on any of these variables when reading these files, as illustrated in Figure B.3. For example the vertex quality requirements of $|\Delta t| < 20$ ps and $\sigma_{\Delta t} < 2.5$ ps are applied at this stage.

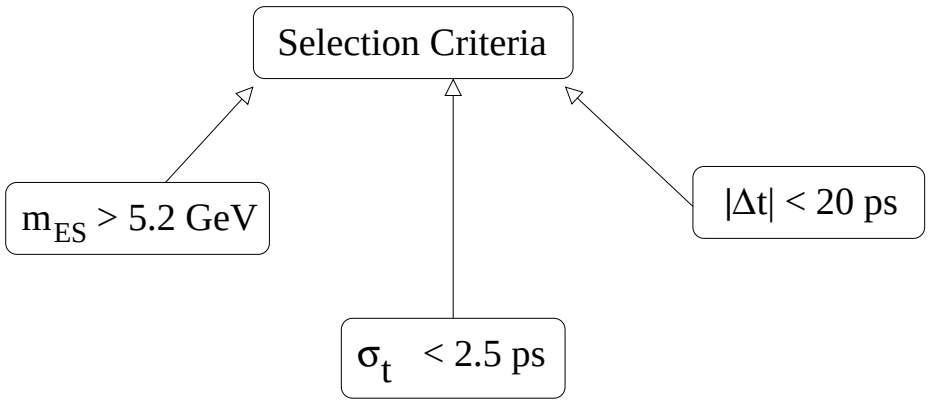

Figure B.3: It is possible to filter the events in input by defining selection criteria for any of the 32 fields in the ASCII files.

B.2.3 Reco modes, tagging categories, and physics classes

The decay mode of the fully reconstructed B meson and the flavor-tagging category of each event are stored in the ASCII files as integer variables. The values of these variables are defined in `BetaCoreTools/BtaExclusiveDecayList.hh` and in `AbsBTagging/AbsBTagger.hh` files, available in all *BABAR* offline software releases.

Since the assigned values can potentially change, `tFit` provides the possibility of defining internally decay modes and tagging categories. Using the stored information in the ASCII files, users can group the selected events regardless of the external definitions of categories and decay modes.

Events with similar theoretical Δt distributions can be grouped to form a physics class. For example, all CP eigenstate with a K^0_S in the final state are usually assigned to the `CharmKshort` class. Although the $J/\psi\ K^0_L$ events have the same Δt distribution, they are assigned to a separate physics class, `CharmKlong`, because of the special care required for the modeling of the background events.

Similarly the hadronic and semileptonic flavor eigenstates are divided in `ExclB` and `Dstarlnu` classes, since they differ significantly in the amount and the composition of background events.

Figure B.4 shows how a physics class is defined by a group of decay modes and tagging categories.

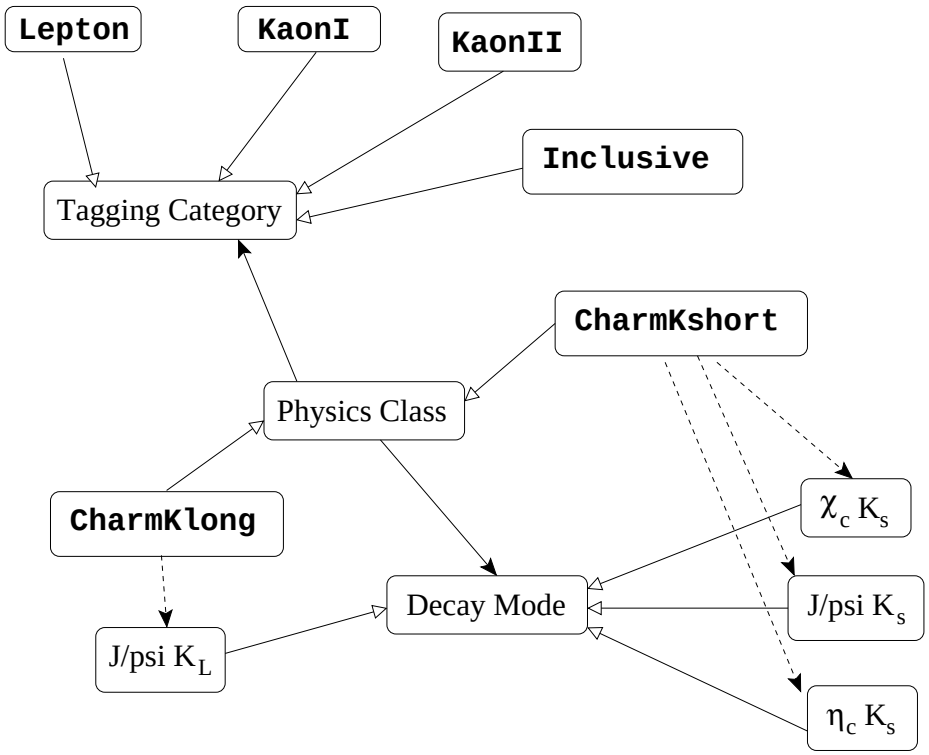

Figure B.4: A physics class is defined by assigning a group of decay modes and tagging categories.

B.2.4 Categories of Minuit parameters

All potential Minuit parameters in the fit are divided in several categories of parameters, such as dilution factors, lifetimes, resolution function scale factors, etc. In order to perform a simultaneous

fit to both the CP and to the flavor eigenstates it is necessary to build the probability density functions for the two different physics classes so that they share some of the parameters as illustrated in Figure B.5.

Users can define the maximum number of parameters of each type, and then assign them to the various physics classes. When the fit is performed, the events in each physics class constrain the value of the free parameters for that class.

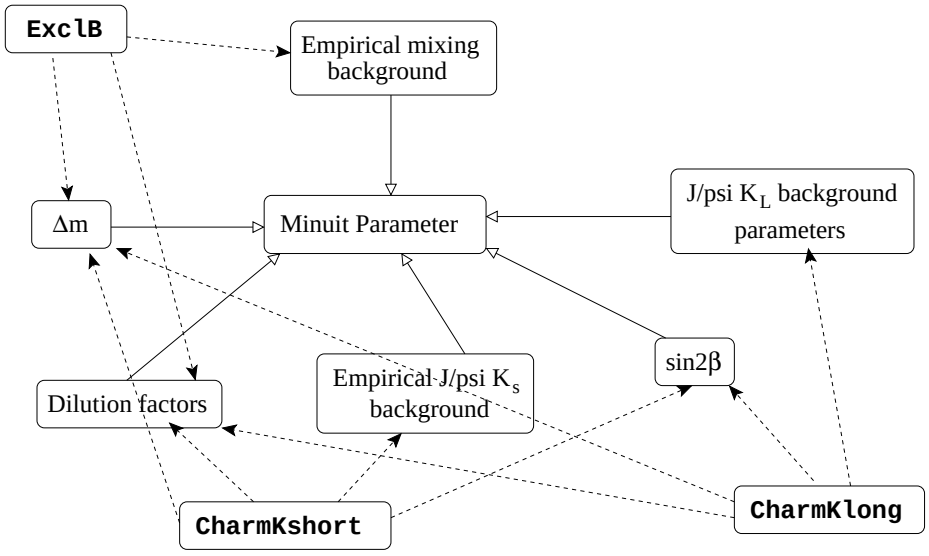

Figure B.5: The Minuit parameters can be shared between the physics classes and be determined in the simultaneous fit to all selected events.

B.2.5 Fixing and floating fit parameters

The fit parameters can be fixed or left floating at run time via kuip commands. In addition their initial values can also be changed prior to performing the fit.

B.2.6 Results and output

The results of the fit, including the correlation matrix elements are stored in an ntuple, while the likelihood curves are saved as histograms together with the data points.

References

[1] See for example Section 2.2 in M. E. Peskin and D.V. Schroeder, *An Introduction to Quantum Field Theory*, Addison-Wesley Publishing Company (1995) .

[2] See for example Chapter 1 in G. S. Branco, L. Lavoura, and J. P. Silva, *CP Violation*, Oxford Science Publications (1999) . Also Chapter 1 in I. I. Bigi and A. I. Sanda, *CP Violation*, Cambridge University Press (2000) .

[3] T. D. Lee and C. N. Yang, Phys. Rev. **104**, 254 (1956).

[4] C. S. Wu, E. Ambler, R. Hayward, D. Hoppes, and R. Hudson Phys. Rev. **105** 1413 (1957).

[5] M. Goldhaber, L. Grodzins, and A. Sunyar, Phys. Rev. **109**, 1015 (1958).

[6] J. I. Friedman and V. L. Telegdi, Phys. Rev. **105**, 1681 (1957).

[7] R. L. Garwin, L. M. Lederman, and M. Weinrich, Phys. Rev. **105** 1415 (1957).

[8] L. P. Roesch, V. L. Telegdi, P. Truttmann, A. Zehnder, L. Grenacs, and L. Palffy, *American Journal of Physics* **50**, 931 (1982).

[9] J. H. Christenson, J. W. Cronin, V. L. Fitch, and R. Turlay, Phys. Rev. Lett. **13** 138 (1964).

[10] M. Kobayashi and T. Maskawa, Prog. Th. Phys. **49**, 652 (1973).

[11] S.L. Glashow, Nucl. Phys. **22**, 579 (1961); S. Weinberg, Phys. Rev. Lett. **19**, 1264 (1967); A. Salam, in *Proc. 8th Nobel Symp.*, ed. N. Swartholm, Almquist and Wiksells, Stockholm (1968). For a general introduction see for example D. H. Perkins, *Introduction to High Energy Physics*, Addison-Wesley Publishing Company (1987) .

[12] S. W. Herb *et al.*, Phys. Rev. Lett. **39**, 252 (1977).

[13] W. R. Innes *et al.*, Phys. Rev. Lett. **39**, 1240 (1977).

[14] F. Abe *et al.*, Phys. Rev. Lett. **74**, 2626 (1995).

[15] A. Abachi *et al.*, Phys. Rev. Lett. **74**, 2632 (1995).

[16] G. Steigman, *Observational tests of antimatter cosmologies,* Ann. Rev. Astron. Astrophys. **14**, 339 (1976).

[17] A. Cohen, D. Kaplan, and A. Nelson, hep-ph/9607394 (1996).

[18] A simple discussion is given in Chapter 21 of I. I. Bigi and A. I. Sanda, *CP Violation*, Cambridge University Press (2000) .

[19] A. D. Sakharov, ZhETF Pis. Red. 5, 32 (1967); JETP Lett. 5, 24 (1956).

[20] P. Langacker, *CP Violation and Cosmology*, in *CP Violation*, edited by C. Jarlskog, World Scientific (1989). .

[21] W. Bernreuther, *CP VIOLATION and BARYOGENESIS*, hep-ph/0205279.

[22] G. S. Branco, L. Lavoura, and J. P. Silva, *CP Violation*, Oxford Science Publications (1999) .

[23] G. S. Branco, L. Lavoura, and J. P. Silva, *CP Violation*, Oxford Science Publications (1999) .

[24] D. H. Perkins, *Introduction to High Energy Physics*, Addison-Wesley Publishing Company (1987) .

[25] M. E. Peskin and D.V. Schroeder, *An Introduction to Quantum Field Theory*, Addison-Wesley Publishing Company (1995) .

[26] F. Mandel and G. Shaw, *Quantum Field Theory*, John Wiley and Sons Ltd. (1984) .

[27] See for example Chapter 4 in Reference [23].

[28] T. Muta, *Foundations of Quantum Chromodynamics*, World Scientific (1987).

[29] See for example Chapter 20 in Reference [25].

[30] A. Ali and B. Kayser, Quark Mixing and CP Violation, hep-ex/9806230 (1998).

[31] See for example Section 8.3 in Reference [23].

[32] N. Cabibbo, Phys. Rev. Lett. **10**, 531 (1963).

[33] Particle Data Group, K. Hagiwara *et al.*, Phys. Rev. **D66**, 010001 (2002).

[34] A complete and clear discussion of the parameterization can C. Jarlskog, *Introduction to CP Violation*, in *CP Violation*, edited by C. Jarlskog, World Scientific (1989). .

[35] L. L. Chau and W. Y. Keung, Phys. Rev. Lett. **53**,1802 (1984).

[36] A. J. Buras and R. Fleischer, Adv. Ser. Direct. High Energy Phys. **15**, 65 (1998).

[37] J. D. Bjorken, Phys. Rev. D **39**, 1396 (1989).

[38] C. Jarlskog and R. Stora, Phys. Lett. **B208**, 268 (1988).

[39] L. Wolfenstein, Phys. Rev. Lett. **51**, 1945 (1983).

[40] A. J. Buras, M.E. Lautenbacher and G. Ostermaier, Phys. Rev. D **50**, 3433 (1994).

[41] UA1 Collaboration, C. Albajar *et al.*, Phys. Lett. B **186**, 247 (1987).

[42] ARGUS Collaboration, H. Albrecht *et al.*, Phys. Lett. B **192**, 245 (1987).

[43] See for example Chapter 6 in Reference [22]. Also, Chapter 6 in Reference [23].

[44] I. I. Bigi, V. A. Khoze, N. G. Uraltsev and A. I. Sanda, in *CP Violation*, edited by C. Jarlskog, World Scientific (1989). .

[45] See for example Section 10.2.7 in Reference [23], and Section 18.3 in Reference [22].

[46] *The BABAR Physics Book*, edited by P. F. Harrison and H. R. Quinn, SLAC-R-504 (1998).

[47] Ya. I. Azimov, N. G. Uraltsev and V. A. Khoze Sov. J. Nucl. Phys. **45**, 878 (1987).

[48] W. Grimus, *Fortschr. Phys.* **36**, 201 (1988).

[49] A. B. Carter and A. I. Sanda, Phys. Rev. Lett. **45**, 952 (1980); Phys. Rev. D **23**, 1567 (1981).

[50] I. I. Bigi and A. I. Sanda, Nucl. Phys. B **193**, 85 (1981); Nucl. Phys. B **281**, 41 (1987).

[51] I. Dunietz and J. Rosner, Phys. Rev. D **34**, 1404 (1986).

[52] M. Bander, S. Silverman and A. Soni, Phys. Rev. Lett. **43**, 242 (1979).

[53] M. K. Gaillard and B. W. Lee, Phys. Rev. Lett. **33**, 108 (1974); G. Altarelli and L. Maiani, Phys. Lett. **52B**, 351 (1974); J. Ellis, M. K. Gaillard, and D. V. Nanopoulos, Nucl. Phys. **B100**, 313 (1975); A. I. Vainshtein, V. I. Zakharov, and M. A. Shifman, Pi'sma Zh. Exsp. Teor. Fiz. **22**, 123 (1975) [JETP Lett. 22, 55 (1975)].

[54] R. Fleischer, Z. Phys. C **62**, 81 (1994);
N. G. Deshpande and X.-G. He, Phys. Lett. B **336**, 471 (1994).

[55] S. L. Glashow, J. Illiopoulos, and L. Maiani, Phys. Rev. D **2**, 1285 (1970).

[56] M. Gronau, Phys. Lett. **B300**, 163 (1993).

[57] *BABAR* collaboration, Measurement of $\sin 2\beta$ in $B^0 \to \phi K^0_S$, hep-ex/0207070 (2002).

[58] M. Ciuchini *et al.*, Phys. Rev. Lett. **79**, 978 (1997).

[59] B. Aubert *et al.*, Measurement of time-dependent CP asymmetries and the CP-odd fraction in the decay $B^0 \to D^{*+}D^{*-}$, hep-ex/0207072 (2002).

[60] B. Aubert *et al.*, Measurement of branching fractions and CP-violating asymmetries in $B^0 \to \pi^+\pi^-, K^+\pi^-, K^+K^-$ decays, hep-ex/0207055 (2002), submitted to Phys. Rev. Lett. .

[61] B.K. Casey *et al.*, Charmless hadronic two-body B meson decays, hep-ex/0207090 (2002), submitted to Phys. Rev. D .

[62] K. Abe *et al.*, Study of CP-violating asymmetries in $B^0 \to \pi^+\pi^-$ decays, hep-ex/0204002 (2002), submitted to Phys. Rev. Lett.

[63] M. Gronau and D. London, Phys. Rev. Lett. **65**, 3381 (1990).

[64] B. Aubert *et al.*, A search for the decay $B^0 \to \pi^0\pi^0$, hepex/0207063 (2002).

[65] See for example Chapters 22-27 in G. S. Branco, L. Lavoura, and J. P. Silva, CP *Violation*, Oxford Science Publications (1999) . See also Chapters 16-21 in I. I. Bigi and A. I. Sanda, CP *Violation*, Cambridge University Press (2000) .

[66] Y. Nir and H. Quinn, CP *Violation in B Physics*, SLAC-PUB-5737 (1992).

[67] P. Oddone, *Proceedings of the UCLA Workshop: Linear Collider* $B\bar{B}$ *Factory Conceptual Design*, edited by D. Stork, World Scientific, 243 (1987).

[68] J. Seeman *et al.*, The PEP-II Storage Rings, SLAC-PUB-8786 (2001), submitted to Nucl. Instr. and Methods .

[69] J. Seeman *et al.*, Status Report on PEP-II Performance, *Proceedings of the 7th European Particle Accelerator Conference(EPAC 2000)*, Vienna, Austria, (2000).

[70] B. Aubert *et al.*, The *BABAR* Detector, Nucl. Instr. and Methods **A479**, 1-116 (2002).

[71] A. Foland and K. Bloom, *Introduction to CLEO* (1998).

[72] M. Sullivan, B-Factory Interaction Region Design, *Proceedings of the IEEE Particle Accelerator Conference (PAC97)*, Vancouver, BC, Canada (1997), SLAC-PUB-7563.

[73] Real-time information about the PEP-II integrated luminosity are available online at `http://www.slac.stanford.edu/grp/cd/soft/images/lum.gif`.

[74] G. Lynch, S. Schaffner, S. Wagner, G, Raven, and F. Wilson, *BABAR Drift Chamber Tracking Conventions*, *BABAR* Note 488, TNDC-NOTE-99-95 (1999).

[75] For a discusion of multiple scattering see for example W. R. Leo, *Techniques for Nuclear ad Particle Physics Experiments*, Springer–Verlag (1987).

[76] G-Link, Giga-bit Transmit/Receive Chip Set HDMP-1012/HDMP-1014, Hewlett-Packard, Inc., Palo Alto, CA, USA.

[77] Motorola model MVME2306 boards, each with a 300 mHz PowerPC 604 CPU, 32 mbytes of RAM, 5 mbytes of non-volatile flash memory, two PCI mezzanine card slots (only one of which is currently used), a 100 mbsps Ethernet interface, and a Tundra Universe II VME interface, Motorola Inc., Tempe, AZ, USA.

[78] The VxWorks realtime operating system and Tornado Development interface, Wind River Systems, Inc., Alameda, CA, USA.

[79] P. Grosso *et al.*, The *BABAR* Fast Control System, *Proceedings of the International Conference on Computing in High-Energy Physics* , Chicago, IL, USA (1998).

[80] R. Claus *et al.*, Development of a Data Acquisition System for the *BABAR* CP Violation Experiment, *Proceedings of the 11th IEEE NPSS RealTime Conference*, Santa Fe, NM, USA (1999), `http://strider.lansce.lanl.gov/-rt99/index11.html` .

[81] G. P. Dubois-Felsmann, E. Chen, and Yu. Kolomensky *et al.*, Flexible Processing Framework for Online Event Data and Software Triggering, IEEE Trans. Nucl. Sci. **47**, 353 (2000).

[82] T. Glanzman *et al.*, The *BABAR* Prompt Reconstruction System, *Proceedings of the International Conference on Computing in High Energy Physics*, Chicago, IL, USA (1998).

[83] F. Safai Tehrani, *The Babar Prompt Reconstruction Manager: A Real Life Example Of A Constructive Approach To Software Development*, Comput. Phys. Commun. **140**, 56 (2001).

[84] Objectivity, Inc., Mountain View, CA, USA. See for example `http://www.objectivity.com` .

[85] I. Gaponenko *et al.*, An Overview of the BaBar Conditions Database, *Proceedings of the International Conference on Computing in High Energy Physics*, Padova, Italy (2000).

[86] L. Dalesio *et al.*, The Experimental Physics and Industrial Control System Architecture: past, present and future, Nucl. Instr. and Methods A **352**, 179 (1994).

[87] B. Franek, C. Gaspar, SMI++ Object Oriented Framework for Designing and Implementing Distributed Control Systems, IEEE Trans. Nucl. Sci. **45**, 1946 (1998).

[88] A tour of the *BABAR* DAQ user interface is available online at `http://www.slac.stanford.edu/BFROOT/www/Detector/Operations/shifts/DAQDoc/tourConsole.html` .

[89] D. N. Brown, E. A. Charles, and D. A. Roberts, The *BABAR* Track Fitting Algorighm, *Proceedings of CHEP 2000*, Padova, Italy (2000).

[90] P. Billoir, Nucl. Instr. and Methods **A255**, 225 (1984).

[91] G. Raven *et al.*, Determination of the tracking efficiency for high momentum tracks, *BABAR* Analysis Document 61 (2000).

[92] E. Varnes *et al.*, Report of the Tracking Efficiency Task Force, *BABAR* Analysis Document 324 (2002).

[93] For a summary of all reconstructed lists see
`http://www.slac.stanford.edu/BFROOT/www/doc/workbook/nanomicro/newest/Micro/CandLists.html`

[94] B. Brabson *et al.*, Nucl. Instr. and Methods A **332**, 419 (1993).

[95] S. Menke *et al.*, Calibration of the *BABAR* Electromagnetic Calorimeter with π^0 s, *BABAR* Note 528 (2000).

[96] A. Drescher *et al.*, Nucl. Instr. and Methods **A237**, 464 (1985).

[97] S. Spanier and G. Mancinelli, Kaon Selection at *BABAR*, *BABAR* Analysis Document 116 (2001).

[98] G. Mancinelli and. S. Yellin, An Event Likelihood Algorithm for DIRC-Based Particle Identification, *BABAR* Analysis Document 165 (2001).

[99] R. Sinkus and T. Voss, Nucl. Instr. and Methods A **391**, 360 (1997).

[100] U. Langenegger, Cut-based Electron Identification, *BABAR* Analysis Document 90 (2001).

[101] L. Lista and F. Fabozzi, Muon Identification in the *BABAR* Experiment, *BABAR* Analysis Document 60 (2000).

[102] G.C. Fox and S. Wolfram, Phys. Rev. Lett. **41**, 1581 (1978).

[103] Paul Avery, *Applied Fitting Theory*, CLEO Note CBX 91-72 (1991). Available online at
`http://www.phys.ufl.edu/~avery/fitting.html`.

[104] See for example *Supporting document for the Moriond 2002* $\sin 2\beta$ *analysis*, *BABAR* Analysis Document 356. Also presentations by Steve Levy available at
`http://www.slac.stanford.edu/~levys/sin2b_0907`,
`http://www.slac.stanford.edu/~levys/sin2b_0924`,
`http://www.slac.stanford.edu/~levys/sin2b_1008` .

[105] The η_c group, *Supporting document for Moriond 2002* $\sin 2\beta$ *with* $B^0 \to \eta_c K^0_S$ *BABAR* Analysis Document 381 (2002).

[106] B. Aubert *et al.*, *Branching Fraction Measurements of the Decays* $B \to \eta_c K$*, where* $\eta_c \to K\overline{K}\pi$ *and* $\eta_c \to 4K$, hep-ex/0203040, SLAC-PUB-9170 (2002).

[107] The η_c group, *Branching Fraction Measurements of the Decays* $B \to \eta_c K$,$\eta_c \to K\overline{K}\pi$ *and* $\eta_c \to 4K$, *BABAR* Analysis Document 336 (2002).

[108] J. Smith, A. Soffer, and R. Waldi, *Reccomendation for Exclusive* B *Reconstruction Analysis Variables*, *BABAR* Note 497 (1999).

[109] ARGUS Collaboration, Z. Phys. **C48**, 543 (1990).

[110] N. Barlow *et al.*, *Measurements of branching ratios of charged and neutral* B *mesons into exclusive charmonium final states*, *BABAR* Analysis Document 113 (2001).

[111] B. Aubert *et al.*, Phys. Rev. D **D65**, 032001 (2002).

[112] BReco AWG, *Exclusive Reconstruction of Hadronic* B *Decays to Open Charm*, *BABAR* Analysis Document 150 (2001).

[113] ARGUS collaboration, Z. Phys. **C62**, 371 (1994).

[114] S. Versille and F. Le Diberder, *Cornelius: Multi-purpose fitting scheme*, *BABAR* Tagging Note 10 (1997).

[115] H. Hu *et al.*, *The NetTagger*, *BABAR* Analysis Document 103 (2000).

[116] J. Beringer *et al.*, *Cut Based Tagging*, *BABAR* Analysis Document 118 (2000).

[117] J. Beringer *et al.*, *B Tagging in BABAR: Status for the Run1* $\sin 2\beta$, *BABAR* Analysis Document 119 (2001).

[118] J. Beringer *et al.*, *BTagger — A Multivariate Tagging Algorithm with Categories Based on the Physics of the* $B_{\rm tag}$ *Decay*, *BABAR* Analysis Document 317 (2002).

[119] F. Martinez *et al.*, *The BABAR Vertexing*, *BABAR* Analysis Document 102 (2001).

[120] F. Le Diberder, CP *Violation as seen from the* Δz *Distribution*, *BABAR* Note 42 (1990).

[121] F. Martinez *et al.*, *Vetexing supporting document for summer 2001 conferences*, *BABAR* Analysis Document 254 (2001).

[122] C.-H. Cheng, *A measurement of the lifetime and mixing frequency of neutral* B *mesons with semileptonic decays with the BABAR detector*, PhD thesis, Stanford University (2002).

[123] C.-H. Cheng and P. Burchat, Correlation between mistag of kaon tag and calculated error on Δt, *BABAR* Analysis Document 349 (2002).

[124] A. Snyder, *Dilution vs. Error explained?*, available online at `http://www.slac.stanford.edu/~snyder/BaBar/dilerrIII.ps`.

[125] F. Le Diberder, *Precision on* CP*-Violation Measurements and Requirement on the Vertex Resolution*, *BABAR* Note 34 (1990).

[126] B. Dunwoodie *et al.*, *Radial and longitudinal length scale from beampipe structure* , presented at the *BABAR* collaboration meeting, December 2000. Available at `http://www.slac.stanford.edu/~wmd/beampipe/dec00.talk`

[127] D. Brown *et al.*, *Local Alignment of the SVT*, *BABAR* Analysis Document 486 (2002).

[128] S. Wagner, *SVT Misalignment Studies for* $\sin 2\beta$, presented at the *BABAR* collaboration meeting, 26 February 2002. Available at `http://www.slac.stanford.edu/BFROOT/www/Organization/CollabMtgs/2002/detFeb2002/Tues3a/wagner.pdf`.

[129] The *Kin* variable is described in F. Le Diberder, *The KIN variable*, 1996. The evaluation of the correlation between two samples is described in Section 9.6 of *Supporting document for the Moriond 2002* $\sin 2\beta$ *analysis*, edited by D. Lange, *BABAR* Analysis Document 356 (2002).

[130] R. Cahn and D. Kirkby, *A General Model for Neutral* B *Decay-Time Distributions*, *BABAR* Analysis Document 188 (2002).

[131] O. Long, *The Effect of Doubly-Cabibbo-Suppressed Decays on the* $\sin 2\beta$ *Analysis* (2002), available at `http://www.slac.stanford.edu/~owen/dcsd-problem.ps.gz`.

[132] R. Cahn, *The Influence of Doubly-Cabibbo-Suppressed Decays on Tagging*, 2002.

[133] *Supporting document for the summer 2002* $\sin 2\beta$ *analysis*, edited by O. Long and S. Prell, *BABAR* Analysis Document 442 (2002).

[134] B. Dahmes *et al.*, *Aspects of the summer 2002* $\sin 2\beta$ *analysis specific to the decay mode* $B^0 \to J/\psi\, K^0_L$, *BABAR* Analysys Document 452 (2002).

[135] B. Aubert *et al.*, Phys. Rev. Lett. **87**, 241801 (2001).

[136] I. Dunietz, H.R. Quinn, A. Snyder, W. Toki and H. J. Lipkin, Phys. Rev. D **43**, 2193 (1991).

[137] A.S. Dighe, I. Dunietz, H.J. Lipkin and J.L. Rosner, Phys. Lett. B**369**, 144 (1996).

[138] B. Aubert *et al.*, Phys. Rev. Lett. **89**, 201802 (2002).

[139] OPAL Collaboration, K. Ackerstaff *et al.*, Eur. Phys. Jour. **C5**, 379 (1998).

[140] ALEPH Collaboration, R. Barate *et al.*, Phys. Lett. B **492**, 259 (2000).

[141] CDF Collaboration, T. Affolder *et al.*, Phys. Rev. D **61**, 072005 (2000).

[142] BELLE Collaboration, K. Abe *et al.*, hep-ex/0207098 (2002).

[143] A. Höcker, H. Lacker, S. Laplace, and F. LeDiberder, Eur. Phys. Jour. **C21**, 225 (2001). See also `http://www.slac.stanford.edu/~laplace/`.

[144] J. Liu and L. Wolfenstein, Phys. Lett. B **197**, 536 (1987).

[145] A brief and clear discussion of the superweak is given in Section 7.4 of G. S. Branco, L. Lavoura, and J. P. Silva, *CP Violation*, Oxford Science Publications (1999) .

[146] Y. Nir, *CP Violation*, talk presented at the Internation Conference of High Energy Physics, Amsterdam, The Netherlands, 7/29/2002.

[147] The organization of `BRecoUser` and the QA plots are available online at: `http://www.slac.stanford.edu/BFROOT/www/Physics/ Analysis/AWG/EHBDOC/post-cpf/breco-tutorial.html`.

[148] The original `CharmUser` user guide is available at: `http://www.slac.stanford.edu/BFROOT/www/Physics/Analysis/AWG/Charmonium/CharmUser/CTGuide.html`. More recent instructions are available at: `http://www.slac.stanford.edu/BFROOT/www/Physics/CP/beta/doc/run2c/charmonium-ascii-instructions/s2b-instructions.html`.

[149] The implementation of `DstarlnuUser` is described in the original user guide available at: `http://www.slac.stanford.edu/ rahatlou/guide/DstarlnuUser.html`.

[150] The particle-identification selectors are described at: `http://www.slac.stanford.edu/BFROOT/www/Physics/Tools/Pid/pid.html`.

[151] The `VertexingTools` user guide is available online at: `http://www.slac.stanford.edu/BFROOT/www/Physics/Tools/Vertex/VtxGuide/index.html`.

[152] The `BetaUser` package is described in the user guide `BetaUser/doc/guide.ps`, available in the *BABAR* software releases. See for example `$BFROOT/dist/releases/analysis-13b/BetaUser/doc/guide.ps`.

[153] The kanga files are described in `http://www.slac.stanford.edu/BFROOT/www/Computing/Offline/Kanga/index.html`.

[154] The structure and the naming convntion of the variables in the ntuples are descibed in `http://www.slac.stanford.edu/`sim`rahatlou/guide/CommonVariables.html`.

[155] The implementation and the organization of `CompositionTools` is described in the user guide available online at:

http://www.slac.stanford.edu/BFROOT/www/Physics/Tools/Vertex/CompGuide/index.html.

[156] The reference manual for *Minuit, Function Minimization and Error Analysis* is available online at:
http://wwwinfo.cern.ch/asdoc/minuit/minmain.html .

[157] B. Aubert *et al.*, Phys. Rev. Lett. **88**, 221803 (2002).

[158] G. Raven *et al.*, Measurement of B^0 $\overline{B}^0$ Mixing with Fully Reconstructed Hadronic B Decays, *BABAR* Analysis Document 125 (2001).

[159] B^0-$\overline{B}^0$ *Mixing with fully reconstructed* B *Decays*, *BABAR* Analysis Document 64 (2000).

[160] Sh. Rahatlou, *Mixing studies with semileptonic* B *decays*, presented at the *BABAR* collaboration meeting, 13 December 2000. Available at:
http://www.slac.stanford.edu/BFROOT/www/Organization/CollabMtgs/2000/detDec2000/Wed4a/rahatlou.pdf.

[161] S. Prell and Sh. Rahatlou, *Measurement of* $\Delta\Gamma$ *with fully reconstructed hadronic* B *decays*, presented at the Lifetime and Mixing Workshop, 4–5 December 2001, Stanford University. Available online at:
http://www.slac.stanford.edu/BFROOT/www/Physics/Analysis/AWG/BBMixingHadr/Workshop/session4/prell.pdf.

[162] C. Voena, *Measurement of* $\sin(2\beta+\gamma)$ *in* $B^0 \to D^*\pi$ *decays* , presented at the *BABAR* collaboration meeting, 11 December 2001. Available at:
http://www.slac.stanford.edu/BFROOT/www/Organization/CollabMtgs/2001/detDec2001/Tues1a/cecilia.pdf.

[163] *Measurement of wrong-flavor to right-flavor amplitude ratio in* $B \to J/\psi K^*$ *decays*, *BABAR* Analysis Document 423 (2002).

[164] *tFit user guide*, *BABAR* Analysis Document 101 (2001).

[165] The format of the ASCII files are described in
http://www.slac.stanford.edu/BFROOT/www/Physics/CP/beta/doc/fitFormat.html .